

**STRUCTURE, FUNCTION, AND INHIBITION OF ENOYL
REDUCTASES**

A Dissertation

by

MACK RYAN KUO

Submitted to the Office of Graduate Studies of
Texas A&M University
in partial fulfillment of the requirements for the degree of
DOCTOR OF PHILOSOPHY

December 2006

Major Subject: Biochemistry

**STRUCTURE, FUNCTION, AND INHIBITION OF ENOYL
REDUCTASES**

A Dissertation

by

MACK RYAN KUO

Submitted to the Office of Graduate Studies of
Texas A&M University
in partial fulfillment of the requirements for the degree of
DOCTOR OF PHILOSOPHY

Approved by:

Chair of Committee, James C. Sacchettini

Committee Members, Michael Kladde

Andy C. Liwang

Paul A. Lindahl

Head of Department, Gregory D. Reinhart

December 2006

Major Subject: Biochemistry

ABSTRACT

Structure, Function, and Inhibition of Enoyl Reductases. (December 2006)

Mack Ryan Kuo, B.S., Baylor University

Chair of Advisory Committee: Dr. James C. Sacchettini

Malaria and tuberculosis constitute two of the world's deadliest infectious diseases. Together, they afflict over one third of the world's population. Once thought of as one of a group of nearly vanquished diseases only 50 years ago, malaria and tuberculosis have experienced renewed prominence due to issues such as multi-drug resistance and a lack of responsiveness by the global community. Fatty acid biosynthesis has been shown to be an essential pathway to the causative organisms of malaria and tuberculosis. One integral component of the fatty acid biosynthesis pathway, enoyl acyl-carrier-protein (ACP) reductase, has repeatedly been validated as an appropriate drug target in other organisms. The 2.4 Å crystal structure of the enoyl-ACP reductase from the human parasite *Plasmodium falciparum* (PfENR) reveals a nucleotide-binding Rossmann fold, as well as the identity of several active site residues important for catalysis. The 2.43 Å crystal structure of PfENR bound with triclosan, a widely utilized anti-bacterial compound, provides new information concerning key elements of inhibitor binding. Applying knowledge attained from these initial crystal structures, several triclosan derivatives were synthesized, and subsequently PfENR:inhibitor co-crystal structures were determined to extend our knowledge of protein:inhibitor interactions within the active site. Additionally, the crystal structures of the enoyl-ACP reductase from the mouse parasite *Plasmodium berghei* (PbENR), in apo-form and in complex with triclosan, were refined to 2.9 Å

and 2.5 Å resolution, respectively. These structures confirm the structural and active site conservation between the human and mouse parasite enoyl-ACP reductases, suggesting that utilizing a murine model for *in vivo* testing of promising inhibitors is viable. The 2.6 Å crystal structure of the enoyl-ACP reductase from *Mycobacterium tuberculosis* (InhA) in complex with triclosan reveals a novel configuration of triclosan binding, where two molecules of triclosan are accommodated within the InhA active site. Finally, high-throughput screening approaches using enoyl acyl-carrier-protein reductases as the targets were utilized to identify new lead compounds for future generations of drugs. The 2.7 Å crystal structure of InhA bound with Genz-10850 confirms the value of this technique.

DEDICATION

This thesis is dedicated to my family.

ACKNOWLEDGEMENTS

I would like to thank my adviser, Dr. James C. Sacchettini, for his guidance and for giving me the opportunity to conduct research in his lab. I would also like to thank past members of the lab, Dr. Donald Ronning, Dr. Thomas Klabunde, Dr. Vivek Sharma, Dr. Remo Perozzo, and Dr. Christoph Eicken, for their generosity with their time and expertise. The members of the Sacchettini lab, past and present, have all contributed to my graduate work, either by engaging in helpful discussions or by giving me the push I needed to finish my research. The staff of the Biochemistry & Biophysics Department have also been a valuable resource over the years. Finally, thanks to my friends and family for all their support.

TABLE OF CONTENTS

| | Page |
|---|------|
| ABSTRACT | iii |
| DEDICATION | v |
| ACKNOWLEDGEMENTS | vi |
| TABLE OF CONTENTS | vii |
| LIST OF FIGURES | ix |
| LIST OF TABLES | x |
| CHAPTER | |
| I INTRODUCTION TO MALARIA | 1 |
| History of Malaria | 1 |
| Characteristics and Pathogenesis | 5 |
| Chemotherapy and Treatment | 7 |
| Drug Resistant Malaria | 10 |
| Role of the Apicoplast | 11 |
| Fatty Acid Biosynthesis | 13 |
| <i>P. falciparum</i> Enoyl-ACP Reductase | 18 |
| II CRYSTALLOGRAPHIC STUDIES OF PFENR | 21 |
| Basic Crystallographic Theory | 21 |
| Phase Problem | 24 |
| Results and Discussion | 28 |
| III PFENR INHIBITOR STUDIES | 41 |
| Results and Discussion | 44 |
| Conclusion | 86 |
| IV CRYSTALLOGRAPHIC STUDIES OF PBENR | 92 |
| <i>Plasmodium berghei</i> Enoyl-ACP Reductase | 92 |
| Results and Discussion | 93 |
| Comparison to PfENR | 101 |

| CHAPTER | Page |
|---|------|
| V INTRODUCTION TO TUBERCULOSIS | 103 |
| History of Tuberculosis | 103 |
| The Tuberculosis Epidemic | 107 |
| Drug-resistant Tuberculosis | 108 |
| Characteristics and Pathogenesis | 112 |
| Defense Mechanisms | 114 |
| Mycobacterial Envelope | 116 |
| Mycolic Acid Synthesis | 123 |
| <i>M. tuberculosis</i> Enoyl Acyl-Carrier-Protein Reductase | 129 |
| VI CRYSTALLOGRAPHIC STUDIES OF INHA | 134 |
| Results and Discussion | 134 |
| Crystal Structure of InhA with Triclosan | 135 |
| Genzyme Inhibitors | 141 |
| Comparison of InhA and Other ENR Inhibitors | 146 |
| VII CONCLUSIONS AND FUTURE WORK | 150 |
| Discussion | 150 |
| Future Work | 154 |
| VIII EXPERIMENTAL: MATERIALS AND METHODS | 157 |
| <i>Plasmodium falciparum</i> Enoyl-ACP Reductase | 157 |
| <i>Plasmodium berghei</i> Enoyl-ACP Reductase | 169 |
| <i>Mycobacterium tuberculosis</i> Enoyl-ACP Reductase | 172 |
| REFERENCES | 177 |
| VITA | 192 |

LIST OF FIGURES

| FIGURE | Page |
|--------|---|
| 1 | Fatty acid biosynthesis pathway 15 |
| 2 | <i>Plasmodium falciparum</i> enoyl-ACP reductase reaction 18 |
| 3 | Sequence alignment of homologous enoyl reductases 31 |
| 4 | Tertiary structure of <i>Plasmodium falciparum</i> enoyl-ACP reductase . . 32 |
| 5 | Superposition of PfENR with homologous enzymes 34 |
| 6 | Quaternary structure of the PfENR tetramer 37 |
| 7 | Triclosan and its nomenclature 42 |
| 8 | Structural details of the triclosan binding site 48 |
| 9 | Isoniazid protrudes into a cavity not occupied by triclosan. 50 |
| 10 | Isoniazid ring-stacks with Tyr ²⁶⁷ in PfENR 51 |
| 11 | Structures of triclosan derivatives tested for inhibitory activity 52 |
| 12 | Structures of B13 and B24 bound to PfENR 54 |
| 13 | Triclosan derivative JPC-2305 ring stacks with Tyr ²⁶⁷ of PfENR 62 |
| 14 | Structural details of the PfENR:4'-inhibitor binding site 71 |
| 15 | Structural details of the PfENR:JPC-2153 complex 73 |
| 16 | Chemical structure of the GSK aminopyridine lead compound 75 |
| 17 | PfENR docked with ChemBridge compound 7682275 80 |
| 18 | Stick models of ZINC lead compounds 85 |
| 19 | PfENR:NADH docked with ZINC compound 68769 87 |
| 20 | PfENR:NADH docked with ZINC compound 1911861 88 |
| 21 | Sequence alignment of PfENR, PbENR, and PvENR 94 |

| FIGURE | Page |
|--|------|
| 22 Structural details of the PbENR binding site | 99 |
| 23 Comparison of PbENR and PfENR structures with co-factor | 102 |
| 24 Structure of the mycobacterial cell wall skeleton | 120 |
| 25 Structure of the arabinogalactan-mycolate cluster | 121 |
| 26 Chemical structures of mycolic acids | 125 |
| 27 FAS-II fatty acid biosynthesis by <i>M. tuberculosis</i> | 128 |
| 28 <i>M. tuberculosis</i> enoyl-ACP reductase reaction | 130 |
| 29 Structure of the InhA:triclosan complex | 137 |
| 30 Superposition of the two forms of the InhA:triclosan complex | 139 |
| 31 Superposition of the InhA:C ₁₆ -NAc and InhA:triclosan complexes | 140 |
| 32 Stick models of newly discovered InhA inhibitors | 141 |
| 33 Structure of the InhA:Genz-10850 complex | 145 |
| 34 Active sites of <i>M. tuberculosis</i> and homologous ENRs | 147 |

LIST OF TABLES

| TABLE | | Page |
|-------|---|------|
| 1 | Observed K_M and V_{max} values for ENRs | 35 |
| 2 | Effects of substitution at the 1-position of triclosan | 56 |
| 3 | Inhibitory effects of 5-substituted derivatives | 58 |
| 4 | Inhibitory effects of selected 5-alkyl derivatives | 58 |
| 5 | Inhibitory properties of selected 5-aryl and heteroaryl derivatives . . . | 59 |
| 6 | Inhibitory effects of substitution at the 6-position of triclosan | 64 |
| 7 | Inhibitory effects of selected 2'-substituted derivatives | 65 |
| 8 | Inhibitory effects of 2'-substituted derivatives with a 4'-hydrogen . . . | 66 |
| 9 | Inhibitory effects of 2'-substituted derivatives with a 4'-chloride . . . | 66 |
| 10 | Inhibitory effects of 2'-substituted derivatives: <i>p</i> -Cl-benzylamines . . | 67 |
| 11 | Inhibitory effects of 2'-substituted derivatives: selected amines | 68 |
| 12 | Inhibitory effects of selected 4'-substituted derivatives | 69 |
| 13 | Inhibitory effects of selected 4'-amide derivatives | 70 |
| 14 | Inhibitory effects of selected 4'-aniline derivatives | 70 |
| 15 | Selected Chemical Diversity compounds, assay comparison | 79 |
| 16 | Molsoft-ICM ChemBridge compounds, screen results | 81 |
| 17 | Selected ZINC compounds, docking comparison | 84 |
| 18 | InhA:Genz-10850 structure-activity relationship | 142 |
| 19 | InhA:Genz-8575 structure-activity relationship | 144 |
| 20 | PfENR:NADH and PfENR:inhibitor crystallographic statistics | 164 |
| 21 | PbENR:NADH and PbENR:triclosan crystallographic statistics . . . | 173 |

| TABLE | Page |
|---|------|
| 22 InhA:Genz-10850 and InhA:triclosan crystallographic statistics | 178 |

CHAPTER I

INTRODUCTION TO MALARIA

History of Malaria

Malaria, or a disease resembling malaria, has plagued humanity for more than 4,000 years. The earliest recorded evidence of malaria was discovered in the form of antigens detected in skin and lung samples (Miller *et al.*, 1994) from mummified remains dating from between 3200 and 1304 B.C. Enlarged, blackened spleens and livers, indicative of malaria, were discovered in 3,000 year old Egyptian mummified remains. Several ancient works of literature vividly described diseases possessing the characteristics of malaria. Clay tablets inscribed with cuneiform writing around 2000 B.C. also described deadly, malaria-like periodic fevers, indicating that over 4,000 years ago Egypt already had a malarial presence. In 2700 B.C., several characteristic symptoms (chills, fevers, and a third or fourth day periodicity) fever associated with spleen enlargement of what would later be named malaria were described in the ancient Chinese medical text, *Nei Ching*, The Canon of Medicine.

Several prominent Greek and Roman historical figures referenced malaria between 500-200 B.C. Homer's *Iliad*, Aristotle's writings (382-322 B.C.), Plato (428-347 B.C.), and Sophocles (496-406 B.C.). Hippocrates (460-370 B.C.), in his treatise *Book of Epidemics*, clearly described the quartan (every fourth day) and tertian (every third day) fevers symptomatic of malaria. He also noted that quartan malaria was the less dangerous of the two and the uncovered the association between enlarged spleens and marshes. In 200 B.C., the Roman medical literature contains accurate descriptions of malaria and references to stagnating bodies of water as the sources of disease.

This condition, described as “Roman fever”, eventually gave rise to the Italian word mal’aria, translating to “bad air”, erroneously describing the cause of the sickness.

Between 300-500 A.D., Indian and Chinese physicians also had breakthroughs regarding malaria. Susruta, an Indian physician (380-450 AD), authored a medical text describing malaria and attributing the symptoms to the bites of certain insects. In China, during the second century B.C., the Qinghao plant was described in the medical text, 52 Remedies, found in the Mawangdui Tomb. In 340 A.D., the anti-fever properties of qinghaosu were described by Ge Hong, and the active ingredient of qinghaosu was isolated by Chinese scientists in 1971. Known as artemisinin, it is presently a very potent and effective antimalarial drug, especially when administered in combination therapy with other medicines.

By the 12th century, malaria had progressed as far west as Spain, and to Poland and Russia in the east. By the 15th century, intermittent fevers were recorded as being common in eastern Europe. In England, seasonal fevers called “agues” were common in the 14th, 15th, and 16th centuries and were described by writer Geoffrey Chaucer (1340-1400) and the playwright William Shakespeare (1564-1616). Spanish Jesuit missionaries in Peru learned of a medicinal bark from the indigenous Incas that was used to treat fevers and chills. With powder from the bark, the Countess of Chinchon, was cured of her fever. The bark from the tree was then called Peruvian bark and the tree was named Cinchona in honor of the countess. The active ingredient from the bark is now known as the antimalarial quinine. Along with artemisinin, quinine is one of the most effective anti-malarial drugs available today.

Charles Louis Alphonse Laveran, a French army surgeon stationed in Algeria, was the first researcher to attribute the symptoms of malaria to parasites in the blood. His examination of blood from feverish artillerymen revealed unusual microscopic bodies, some with mobile filaments, on his microscope slides. Laveran eventually identified

four different forms of the parasite: crescent shaped bodies, spherical bodies actively moving flagella, spherical bodies with pigment and without movement, and much smaller spherical bodies that also had pigment. These later were identified as separate stages of the parasite development (male and female gametocytes, segmenter, and trophozoite stages). For his discovery, Laveran was awarded the Nobel Prize in 1907.

In 1897, Ronald Ross, a British officer in the Indian Medical Service, was the first to demonstrate that malaria parasites could be transmitted from infected patients to mosquitoes. In further work with bird malaria, Ross showed that mosquitoes could transmit malaria parasites from bird to bird (Ross, 1923). This necessitated a sporogonic cycle (the time interval during which the parasite developed in the mosquito). Thus, the nature of malaria transmission was determined. For his discovery, Ross was awarded the Nobel Prize in 1902.

In 1899, led by Giovanni Batista Grassi, a team of Italian investigators, which included Amico Bignami and Giuseppe Bastianelli, collected *Anopheles claviger* mosquitoes and fed them on malarial patients. Mosquitoes infected by feeding on a patient in Rome were transported to London where they fed on two volunteers, both of whom developed benign tertian malaria, unequivocally demonstrating human-to-human malaria transmission. The complete sporogonic cycle of *P. vivax*, and *P. malariae* was demonstrated.

The construction of the Panama Canal demarcated the beginning of US efforts to control malaria by targeting the disease vector, the anopheline mosquito. At the inception of construction, 1906, there were over 26,000 employees working on the Panama Canal, and over 21,000 were hospitalized for malaria at some time within the duration of the project. After 6 years, the number of employees increased to over 50,000 people, but the number of hospitalized workers dramatically decreased to less than 6,000 cases, showing the promise of vector targeting as a method of malaria

control. In 1933, this strategy experienced renewed success when U.S. President Franklin D. Roosevelt signed a bill that created the Tennessee Valley Authority (TVA). This gave the federal government a centralized body to take advantage of the Tennessee river's potential for hydroelectric power, as well as improve the land and waterways for development of the region. An organized and effective malaria control program stemmed from this new authority in the Tennessee River valley. Malaria affected 30 percent of the population in the region when the TVA was established, but by 1947, the disease was essentially eliminated. Mosquito breeding sites were reduced by controlling water levels and liberal applications of insecticide to target the mosquito vector.

In 1934, the anti-malarial drug chloroquine was discovered by a German researcher, Hans Andersag at Bayer. Chloroquine was recognized and established as an effective and safe anti-malarial in 1946 by British and U.S. scientists, and quickly became the most widely deployed front-line anti-malarial drug. In 1874, Othmer Zeidler synthesized dichlorodiphenyltrichloroethane (DDT), but the insecticidal property of DDT was not discovered until 1939 by Paul Müller in Switzerland, who later won the Nobel Prize for Medicine in 1948 for his discovery. DDT was widely used for malaria control at the end of World War II after it had proved effective against malaria-carrying mosquitoes by British, Italian, and American scientists. However, the rise in incidence of insecticide-resistant mosquitoes, as well as public concerns about the effect of DDT on the environment, caused the demise of DDT application for insect control.

1946 marked the inception of the Communicable Disease Center's (CDC) mission to combat malaria. Much of the early work done by the CDC was focused on the control and eradication of malaria in the United States. With the successful reduction of malaria in the United States, the CDC switched its malaria focus from eradication

efforts to a strategy based on prevention and surveillance. By the end of 1949, over 4.6 million housespray applications had been made, and malaria incidence drop from 15,000 reported malaria cases in 1947 to only 2,000 cases in 1950. By 1951, malaria was widely considered to be eradicated from the United States.

With the success of DDT, the advent of less toxic, more effective synthetic antimalarials, and the enthusiastic and urgent belief that time and money were of the essence, the World Health Organization (WHO) submitted at the World Health Assembly in 1955 an ambitious proposal for the eradication of malaria worldwide. Eradication efforts began and focused on house spraying with residual insecticides, anti-malarial drug treatment, and surveillance. Successes included eradication in nations with temperate climates and seasonal malaria transmission. Some countries such as India and Sri Lanka had sharp reductions in the number of cases, followed by increases to substantial levels after efforts ceased. Other nations had negligible progress (such as Indonesia, Afghanistan, Haiti, and Nicaragua), and some nations were excluded completely from the eradication campaign (most of sub-Saharan Africa). The emergence of drug resistance, widespread resistance to available insecticides, wars and massive population movements, difficulties in obtaining sustained funding from donor countries, and lack of community participation made the long-term maintenance of the effort untenable. Completion of the eradication campaign was eventually abandoned in preference to a strategy of control.

Characteristics and Pathogenesis

Recent estimates of the incidence of malaria in the year 2002 place the number of clinical episodes at 515 million, with a range of 300-660 million, placing approximately 2.2 billion people at risk (Snow *et al.*, 2005). Malaria remains one of the

top ten killers worldwide, with mortality rates between 1-2 million people annually. Resistance to the most prevalent antimalarials is widespread, while it is developing in others (Winstanley, 2002). Although four species of the genus *Plasmodium* cause human malaria (*P. falciparum*, *P. vivax*, *P. ovale*, and *P. malariae*), the deadliest of these is *Plasmodium falciparum*, a protozoan parasite transmitted from host to host by an infected anopheline mosquito. Hours after the resultant infection, severe *P. falciparum* infection is characterized by paroxysms (chills and fevers). *P. falciparum* is capable of causing acute life-threatening encephalopathy also referred to as cerebral malaria. Cerebral malaria is the most severe form, resulting in 80% of children's death. The diagnostic features of cerebral malaria are unrousable comas and seizures.

Normal development of the parasite requires the presence of two hosts: the *Anopheles* mosquito vector (the definitive host, where sexual recombination occurs), and humans (the intermediate host). The life cycle of malaria begins in the definitive host when a female *Anopheles* mosquito ingests gametocytes (the first sexual stages of parasites) from a malaria-infected vertebrate host. Microgametocytes (male forms of gametes) and macrogametocytes (female forms of gametes) fertilize in the mosquito midgut to form zygotes. About 18-24 hours post blood feeding, zygotes further differentiate into motile ookinetes. Ookinetes migrate through the mosquito gut wall and differentiate into oocysts on the external gut wall. The oocysts increase in size until they rupture, releasing thousands of sporozoites destined for the mosquito salivary glands.

Transmission occurs when the infected mosquito bites an uninfected host. Sporozoites from the infected mosquito salivary ducts are transmitted to human host, and travel within the bloodstream to the liver, ultimately entering the hepatocytes. The sporozoites reproduce asexually over an approximately one-week time interval and

develop into schizonts, containing 30,000 to 50,000 “daughter” parasites called merozoites. Upon rupture of the schizonts, merozoites are subsequently released from the liver to the blood where they invade the erythrocytes. Merozoites reproduce asexually over the next 48-72 hours, completing another round of multiplication, devouring hemoglobin in the process and forming a red blood cell (RBC) with a ring-shaped morphology termed the trophozoite. The trophozoites mature into schizonts, which burst synchronously and release the merozoites into the bloodstream. This release coincides with the periodic rises in body temperature associated with the attacks seen in malaria infections. Significant numbers of RBCs are destroyed, resulting in the paroxysms characteristic of malaria infections. The released merozoites also can invade other RBCs and continue the cycle of RBC destruction.

While the majority of invading merozoites develop into asexual schizonts, some differentiate into male (microgametocyte) and female (macrogametocyte) gametocytes. The infective sporozoites are released into the mosquito haemocoel (midgut) and move to the salivary gland, where they await injection into another human host, thus completing the life cycle. Some plasmodial species (*Plasmodium ovale* and *Plasmodium vivax*) can produce a dormant form, a hypnozoite, which can cause relapses of the disease months and even years after the original disease (relapsing malaria), once triggered from its dormant state within the liver cells (Oaks *et al.*, 1999; Warrell and Gilles, 2002; Sherman, 1998).

Chemotherapy and Treatment

In the 1940s, the administration of chloroquine (CQ) ushered in the age of malaria chemotherapy. Chloroquine was highly effective (3 doses with a 48 hour therapy duration), easily administered, inexpensive, and had good safety and tolerability.

An intra-erythrocytic parasite would ingest host cell hemoglobin, which rapidly degraded within a food vacuole within the parasite. Upon hemoglobin cleavage, free heme would be released, resulting in toxicity. *P. falciparum* contends with this problem of heme toxicity by polymerizing free heme into an insoluble crystalline material termed hemozoin. Chloroquine inhibits the parasitic enzyme heme polymerase that converts the toxic heme into non-toxic hemozoin, thereby resulting in the accumulation of toxic heme within the parasite. However, chloroquine resistance in *P. falciparum* quickly arose in Thailand and Colombia in the 1950s, and emerged in New Guinea and sub-Saharan Africa in the 1970s. By 1973, chloroquine treatment had failure rates in excess of 30% in parts of Africa, and between 46-85% in Asia. Subsequently, chloroquine monotherapy was replaced by sulfadoxine-pyrimethamine cocktails in 1971 and became the standard second-line therapy against chloroquine resistant malaria due to its superior safety and tolerability, and required only single-dose chemotherapy. This combination acts synergistically against folate synthesis, inhibiting dihydropteroate synthase (DHPS) and dihydrofolate reductase (DHFR). DHFR is required for the synthesis of thymidylate, purine nucleosides, methionine and other metabolic intermediates, and disrupts DNA synthesis when inhibited. Again, resistance to the sulfadoxine-pyrimethane combination was observed at the Thai-Cambodian border in the 1960s, and failures occurred in refugee camps in Thailand in the 1970s. Mefloquine emerged as a successor to chloroquine in the 1980s. Resistance occurred at the Thai-Cambodian border within a few years once again. Quinine emerged as an effective anti-malarial drug that requires 21 doses administered over a 7 day period. Quinine exerts its effects by inhibiting the α -subunit of DNA gyrase and topoisomerase IV, leading to inhibition of nucleic acid synthesis. Primaquine, developed during World War II, remains the only licensed tissue-stage schizonticide for the prevention of relapse after infection. It has a uniquely broad

spectrum, killing liver stages, asexual blood stages, and sexual blood stages. Despite 50 years of use in millions of people, primaquine and its mechanism of action are poorly understood. Artemisinin, a sesquiterpene endoperoxide extracted from the weed *Artemisia annua*, was developed by China in the 1960s and appears to be a very promising anti-malarial because of its ability to rapidly clear parasites and its demonstrated tolerance in humans. Artemisinins are among the newest and most effective of all anti-malarial drugs, and are effective against blood-stage parasites in nanomolar concentrations. The mode of action appears to occur in two steps, with the first step requiring activation of artemisinin derivatives to produce radicals, followed by alkylation of heme and specific malaria proteins. Heme-artemisinin adducts were demonstrated in parasite-infected mice (Robert *et al.*, 2005), supporting the notion of activation.

Combined drug therapy, a strategy useful in treating the diseases tuberculosis, leprosy, and infection with the human immunodeficiency virus (HIV), has recently been applied to malaria chemotherapy. The purpose is to take advantage of the synergistic and additive potential of individual drugs, thus increasing efficacy and retarding the development of resistance to each individual drug. This strategy ideally involves agents with separate mechanisms of action against the same stage of parasite, so a sulfadoxine-pyrimethamine combination would not fit this criteria because both are folate antagonists. Similarly, combining a blood-stage schizonticide with primaquine is not considered combined therapy, since the drugs attack different stages of the parasite. The combination of atovaquone-chloroguanide, which affects mitochondrial electron transport and folate metabolism in asexual blood stages, represents true combination therapy. Artemisinin Combination Therapy (ACT) provides the best present effort in treating malaria. The combination of artesunate and mefloquine has been utilized in Thailand for 10 years, with no diminution of its effi-

cacy (Wongsrichanalai *et al.*, 2001). ACT has the following characteristics: (i) rapid and substantial reduction of the parasite biomass (ii) rapid parasite clearance (iii) rapid resolution of clinical symptoms (iv) effective action against multidrug-resistant *P. falciparum*.

Drug Resistant Malaria

Treatment of malaria has been complicated in recent years by a surge in the resistance of malaria to commonly dispensed antimalarials, particularly to the affordable mainstays chloroquine and sulfadoxine-pyrimethamine. Molecular studies have identified several mutations associated with chloroquine resistance. Polymorphisms in the *P. falciparum* chloroquine resistance transporter (*pfcr1*) gene, located on chromosome 7, were reported to be important in chloroquine resistance. A Ser⁷⁶ to Thr mutation is tightly linked to resistance (Fidock *et al.*, 2000; Djimdé *et al.*, 2001a). Polymorphisms in the *P. falciparum* multidrug resistance 1 gene (*pfmdr1*) have been shown to modulate higher levels of chloroquine resistance, and also to affect mefloquine and quinine resistance (Djimdé *et al.*, 2001b; Sidhu *et al.*, 2002). The molecular basis of resistance to pyrimethamine and sulfadoxine has been more clearly defined. Polymorphisms in the dihydrofolate reductase (*dhfr*) gene have been shown to confer resistance to pyrimethamine. Additional polymorphisms at amino acid positions 50, 51, 59, and 164 combined with Asn¹⁰⁸ confer increasing levels of pyrimethamine resistance. Similarly, polymorphisms in the dihydropteroate synthase (*dhps*) gene confer resistance to sulfadoxine (Foote *et al.*, 1990). The polymorphism Gly⁴³⁷ in *dhps* encodes lower level resistance to sulfadoxine. Subsequent polymorphisms at positions 436, 540, 581, and 613 confer increasing levels of resistance to this drug (Syafuruddin *et al.*, 2005). Quinine resistance has been traced to mutations in the

pfmdr1 gene, 162 kDa transporter protein that is a parasite homolog of the mammalian multidrug resistance gene family. A significant role in resistance has been ascribed to N1042D mutation. The triple mutation S1034C/N1042D/D1246Y also has been shown to enhance parasite susceptibility to mefloquine, halofantrine, and artemisinin (Sidhu *et al.*, 2005). Artemisinin, a promising drug against malaria, has had well documented problems in availability and synthesis (Enserink, 2005). Most recently, there have been studies identifying specific polymorphisms that result in increased resistance to artemisinin (Jambou *et al.*, 2005). Jambou *et al.* discovered six of seven isolates with increased resistance to an artemisinin derivative shared a single polymorphism, S769N in *PfATPase6*, a gene encoding a sarco/endoplasmic reticulum calcium-dependent ATPase.

Every malaria drug administered has resulted in resistant strains of *P. falciparum*, so research continues to focus on the development of new anti-malarial compounds. It is clear that researchers must find more effective therapeutics that have a rapid mode of action. New drugs must be developed that inhibit enzymes that have not previously been targeted, to ensure that low level resistance is not already present in some strain of *P. falciparum*, so as not to compromise the success of any new drugs.

Role of the Apicoplast

P. falciparum was recently discovered to have contain a unique plastid organelle, surrounded by four membranes and containing its own genome. This organelle, termed the apicoplast (McFadden *et al.*, 1996; Wilson *et al.*, 1996; Kohler *et al.*, 1997) , was discovered to be quite similar to plant chloroplasts, except it lacks chlorophyll and the photosynthetic machinery necessary to create food from carbon dioxide (CO₂) and sunlight. The apicoplast is a characteristic feature of the apicomplexan parasites

(Gornicki, 2003), and in *Plasmodium falciparum* contains a highly reduced genome, comprised of 68 genes on a 35 kb circular DNA (Wilson *et al.*, 1996). The apicoplast is thought to have originated from an ancestral endosymbiotic relationship (Kohler *et al.*, 1997; Palmer and Delwiche, 1996; McFadden and Waller, 1997), involving the assimilation of an ancient bacteria that lost its autonomy once engulfed by an ancestral apicomplexan predecessor. In the case of *P. falciparum*, the apicoplast has lost all photosynthetic function, but still serves to provide the host with other metabolic services that render them indispensable. The apicoplast has recently been found to be essential to normal development of apicomplexan parasites (Fichera and Roos, 1997; He *et al.*, 2001). Mutant parasites lacking an apicoplast are not viable (He *et al.*, 2001). It has been proposed that the lack of a functional apicoplast causes parasites to fail to re-infect subsequent host cells and die, due to their inability to synthesize a parasitophorous vacuole, which is useful for re-invasion of erythrocytes (Fichera *et al.*, 1995). The nature of the defect is not known, but these results are consistent with the delayed-death phenotype observed for parasites treated with antibiotics targeting apicoplast house-keeping functions.

The apicoplast functions as a fairly self-contained “cell-within-a-cell”, housing the cell processes of DNA replication, transcription, translation, post-translational modification, catabolism, and anabolism. Parasites die after treatment with drugs that interrupt apicoplast genome replication, transcription, or translation (Ralph *et al.*, 2001; Fichera and Roos, 1997). A number of interesting pathways exist: non-mevalonate isoprenoid synthesis, ferredoxin-dependent electron transport, lipoate synthesis, iron-sulfur cluster formation, several steps of heme synthesis and *de novo* fatty acid synthesis (Ralph *et al.*, 2004). Each of these processes is bacterial in nature, and potentially a drug target because of their differences from the eukaryotic host pathways. It was recently demonstrated that the *P. falciparum* apicoplast con-

tains a functional fatty acid biosynthesis system (Waller *et al.*, 1998), a pathway that has been targeted for inhibition by several anti-bacterials and presents new opportunities for drug targets. Genome sequencing of *P. falciparum* revealed the presence of a *de novo* FAS-II fatty acid biosynthesis system (Gardner *et al.*, 2002), a type not predicted to occur in a protozoan. Plant-like and prokaryote-like biochemical pathways which are not present in the parasite host or which differ significantly from host pathways could be exploited in the control of malaria.

Proteins that are targeted to the apicoplast possess an amino-terminal leader peptide capable of targeting nuclear-encoded proteins to the stroma of the apicoplast. This requires traversal of four membranes needed to reach its destination. Apicoplast-targeted proteins possess a leader peptide has a distinct bipartite architecture comprised of a hydrophobic signal peptide followed by a basic transit peptide (Gardner *et al.*, 2002; Foth *et al.*, 2003; Zuegge *et al.*, 2001). The signal peptide mediates co-translational import into the lumen of the endoplasmic reticulum and is cleaved in the process. The transit peptide is responsible for subsequent import into the stroma of the apicoplast and is also cleaved. Studies with chimeric mutants show that leader peptides are sufficient to target other proteins to the apicoplast (Waller *et al.*, 2000, 1998; van Dooren *et al.*, 2002). It is now thought that nearly 500 nuclear-encoded proteins may be targeted to the stroma of the apicoplast.

Fatty Acid Biosynthesis

Fatty acid biosynthesis is an essential pathway (Zhang and Cronan, 1998; Egan and Russell, 1973) present in all bacteria sequenced thus far, and provides the essential building blocks for membrane phospholipid formation. Metabolites of fatty acid biosynthesis form major constituents of the protective cell wall, as well as key cellular

components such as quorum sensing molecules and a diverse variety of fatty and lipoic acids. Fatty acids also provide a source of metabolic energy. Moreover, the cell wall / membrane component fatty acyl chains are essential to microbe division and metabolism, and microbial pathogens are apparently unable to survive simply by scavenging host fatty acids. These factors combine to make the fatty acid biosynthesis pathway an attractive target for anti-bacterial development.

Fatty acid biosynthesis can be classified into two systems: FAS-I and FAS-II. Typically, FAS-II systems are found in plants, bacteria, and other microorganisms, while FAS-I are found in higher eukaryotes such as humans (Smith, 1994). In FAS-I, a large, multifunctional enzyme catalyzes all the reactions necessary for fatty acid biosynthesis (Smith *et al.*, 2003). In contrast, in the FAS-II system each of the individual enzymatic activities are carried out by discrete enzymes (Rock and Cronan, 1996; Harwood, 1996; Magnuson *et al.*, 1993). The reactions of the fatty acid biosynthesis pathway are identical in each individual step (Figure 1) between the two systems. Although the chemical reactions involved in fatty acid biosynthesis are identical, the chemical reactions responsible for fatty acid biosynthesis are organized differently in humans. The differences between the systems afford an opportunity to specifically target microorganisms without harming the human host.

Most of the groundwork for understanding of the FAS-II pathway came from work first initiated in *Escherichia coli*, and the remarkable wealth of knowledge gained from these experiments made *E. coli* the model system for research into FAS-II biochemistry (Rock and Cronan, 1996). This work uncovered the production of fatty acids as a repeating cycle of reactions involving the condensation, reduction, dehydration, and the final reduction of carbon-carbon bonds. Later, searches of newly available microbial genome databases revealed that the component genes and proteins of the FAS-II pathways were well conserved, with a significant degree of

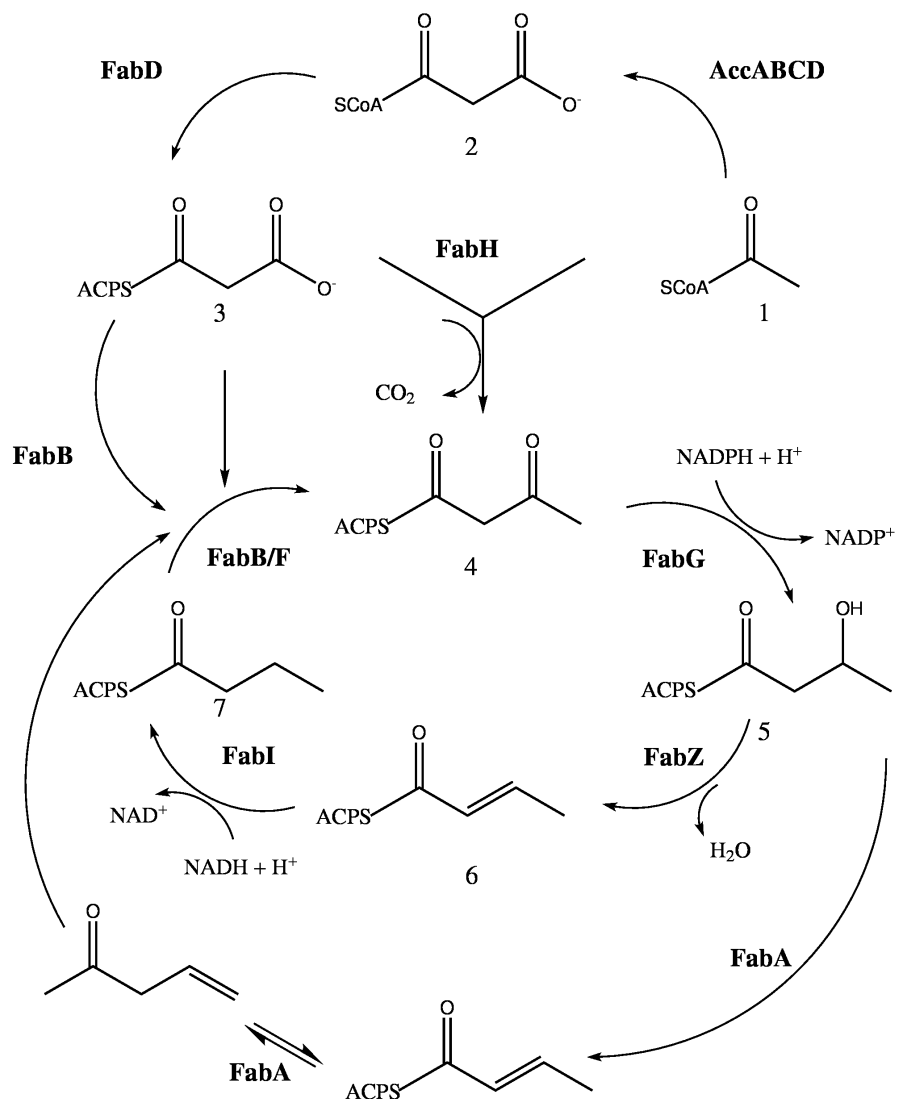


Figure 1: Fatty acid biosynthesis pathway. Acetyl-CoA (1) is converted into malonyl-CoA (2) by ACC and then to malonyl-ACP (3) by FabD. The resulting malonyl-ACP condenses with another molecule of acetyl-CoA to form b-oxoacyl-ACP (4) catalyzed by b-oxoacyl ACP synthase III (FabH). This is then converted into b-hydroxyacyl-ACP (5) by b-oxoacyl ACP reductase (FabG) and then dehydrated by b-hydroxyacyl ACP dehydratases (FabZ/FabA). The synthesis of unsaturated fatty acids branches out at this step catalyzed first by FabA and then by FabB. The dehydrated product, enoyl-ACP (6) is then reduced by enoyl-ACP reductase (FabI) to form butyryl-ACP (7). This product re-enters the FAS cycle and the growing chain is elongated by two carbon units per cycle. The condensing enzymes involved in elongation are FabB and FabF.

sequence identity to the *E. coli* counterparts.

The first evidence of a FAS-II pathway in malaria parasites came from the genomics database analysis work of Waller *et al.* These investigators (Waller *et al.*, 1998) reported the presence of *P. falciparum* nuclear genes encoding proteins identified as the FAS-II enzymes *acpP*, *fabH*, and *fabZ*, encoding acyl-carrier protein (ACP), β -ketoacyl-ACP synthase III, and β -hydroxy-ACP dehydratase, respectively. FAS-II initiation is catalyzed by the enzyme complex acetyl-CoA carboxylase (AccABCD), which catalyzes a key step in intermediary metabolism that diverts acetyl-CoA to malonyl-CoA. The overall ACC reaction requires the coordinate action of four gene products, AccA, AccB, AccC, and AccD. The malonyl group of malonyl-CoA is transferred to acyl-carrier protein (ACP) by malonyl-CoA:ACP transacylase (FabD) to produce malonyl-ACP. All of the subsequent intermediates in FAS are attached to the terminal sulfhydryl of ACP, making this protein a co-factor partner in all subsequent reactions. Each of the intermediates in fatty acid biosynthesis is persistently bound to acyl-carrier protein (ACP). β -ketoacyl-ACP synthase III (FabH) catalyzes the first condensation step in the pathway using acetyl-CoA as the primer and malonyl-CoA as the acceptor, resulting in a β -ketoacyl-ACP product (acetoacetyl-ACP in the first cycle of fatty acid biosynthesis).

The acetoacetyl-ACP formed by FabH then enters the next step of biosynthesis, the elongation cycle. This cycle consists of four core enzyme activities that progressively elongate the acyl chain attached to ACP by two carbons through each revolution. β -ketoacyl-ACP reductase (FabG) is a ubiquitously expressed, NADPH-dependent reductase that gives rise to β -hydroxyacyl-ACP from the preceding β -ketoacyl-ACP reductase. This intermediate is dehydrated by the β -hydroxyacyl-ACP dehydratases (FabA and FabZ). In *P. falciparum*, the enoyl-ACP is reduced by enoyl-ACP reductase (PfENR) to complete the elongation cycle.

Many FAS-II enzymes (the elongating condensation enzymes FabB, FabF, and FabH and the enoyl-reductase FabI) have already been identified as the targets of several widely utilized anti-bacterials. Inhibitors of the condensing enzymes include cerulenin (Omura *et al.*, 1967) and thiolactomycin (Jackowski *et al.*, 1989; Nishida *et al.*, 1986; Tsay *et al.*, 1992). Cerulenin is synthesized by the fungus *Cephalosporium ceruleans* and irreversibly inhibits fatty acid synthases from a variety of prokaryotes and eukaryotes. FabB is the major cerulenin target in *E. coli*, but unfortunately it also is able to inhibit the essential mammalian fatty acid synthase enzyme. Thiolactomycin is specific for type II synthases, exhibiting anti-bacterial activity towards gram-negative and gram-positive bacteria, *M. tuberculosis* (Kremer *et al.*, 2000), and *P. falciparum* (Waller *et al.*, 1998). FabB is the major target for thiolactomycin in *E. coli*, although FabF and FabH are also affected. BP1 is an inhibitor of the multi-subunit acetyl-CoA carboxylase (Blanchard *et al.*, 1999), targeting the biotin carboxylase subunit AccC. Inhibitors of enoyl-ACP reductase include triclosan (Heath *et al.*, 1998), diazaborines (Roujeinikova *et al.*, 1999b), isoniazid (Banerjee *et al.*, 1994), SB-627696, SB-663042, SB-633857 (Fan *et al.*, 2002), and the pro-drug NB2001 (Li *et al.*, 2002). Triclosan is a noncovalent inhibitor of NADH/NADPH dependent enoyl-ACP reductases (FabI) that is widely utilized as a broad spectrum anti-bacterial and incorporated into several consumer products. Diazaborines and isoniazid both covalently modify the NADH co-factor in order to form an adduct that potently inhibits enoyl-ACP reductases. The GlaxoSmithKline compounds SB-627696, SB-663042, and SB-633857 noncovalently inhibit *S. aureus* FabI. NB2001 is a compound consisting of triclosan linked to a cephalosporin scaffold, which is cleaved by bacterial β -lactamases. FAS-II is absent in humans, superseded by a FAS-I system that is insensitive to many FAS-II inhibitors. The enzyme target of most of the known FAS-II antimicrobial compounds is ENR, which catalyzes the final enzymatic

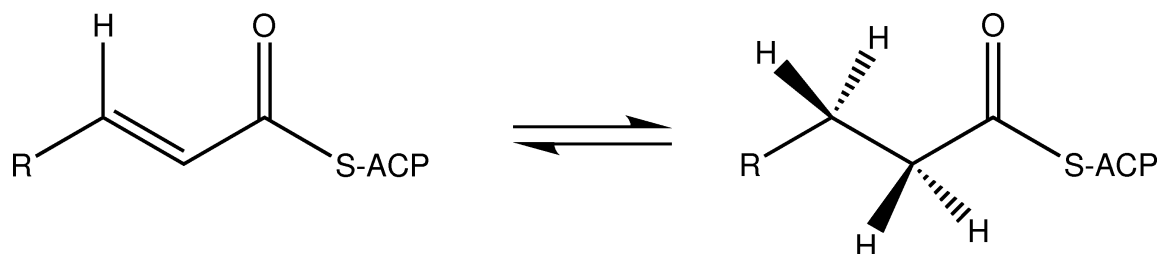


Figure 2: *Plasmodium falciparum* enoyl-ACP reductase reaction. The substrate is a 2-*trans*-enoyl-ACP, which is reduced to yield a saturated chain in a NADH-dependent manner. The mechanism is via a transfer of a hydride ion from the NADH co-factor to the substrate.

step in the elongation cycle of the fatty acid biosynthesis. Thus far, only enoyl-ACP reductase inhibitors have achieved *in vivo* efficacy.

***P. falciparum* Enoyl-ACP Reductase**

The focus of this study is *Plasmodium falciparum* enoyl-ACP reductase (PfENR), an enzyme that catalyzes the final reduction in the elongation cycle of FAS-II fatty acid biosynthesis (Figure 2). From prior enzymatic studies with the homologous enzymes *E. coli* FabI (Ward *et al.*, 1999) and *M. tuberculosis* InhA (Quemard *et al.*, 1995), they were determined to follow a sequential kinetic mechanism, with NADH preferred as the first substrate. The chemical mechanism involves the stereospecific hydride transfer of the 4*S* hydrogen of NADH to the C3 position of 2-*trans*-enoyl substrate, followed by the protonation at C2 of an enzyme-stabilized enolate intermediate. Subsequent studies with PfENR showed it catalyzed an identical reaction (Surolia and Surolia, 2001). PfENR is a nuclear-encoded, apicoplast-targeted protein and has become an excellent anti-malarial candidate for a myriad of reasons. Many inhibitors have been identified that specifically target enoyl-reductases in a wide variety of organisms. There have also been many enzymatic characterizations of

these enoyl reductases. Preliminary indications are that the inhibition of PfENR is a reasonable anti-malarial target, with a mode of action separate from existing classes of anti-malarial drugs.

It has been observed that enzyme inhibitors exert their effects in various manners. They have been divided into four categories according to the strength of their interaction with the enzyme and the rate at which equilibrium involving enzyme and inhibitor is achieved. The categories are classical, slow-binding, tight-binding, and slow-tight-binding. Historically, classical inhibitors have been the most well characterized, while only a few studies have examined tight-binding inhibitors. From investigations into the homologous enzymes *E. coli* FabI, *B. napus* ENR, and *M. tuberculosis* InhA with the inhibitors triclosan and isoniazid, it was evident that these two inhibitors exerted their effects in a manner termed slow, tight-binding inhibition. The tight-binding designation stemmed from the observations that inhibition was stoichiometric, *i. e.* all of the inhibitor was bound to the enzyme whenever the inhibitor concentration decreased below that of the binding sites. The slow designation referred to the slow-onset of the inhibited complex, since it was observed that the degree of inhibition increased gradually over several minutes (Ward *et al.*, 1999). Recently, triclosan has been shown to be a slow, tight-binding, reversible inhibitor of PfENR (Kapoor *et al.*, 2004). Kapoor *et al.* reported that inhibition by triclosan with PfENR also exhibited slow onset, as the formation of the enzyme:inhibitor complex took a long time to form relative to the catalytic rate of the enzyme. Triclosan bound to PfENR in two steps, where the first step involved a rapid formation of a weak initial enzyme:inhibitor complex, which slowly transforms to a more stable and tightly bound enzyme:inhibitor complex from which the inhibitor dissociates in a very slow manner (Kapoor *et al.*, 2004).

The information available concerning enoyl reductases from other organisms will

be incredibly beneficial in pursuing PfENR as an anti-malarial drug target. Given the knowledge that PfENR is a critical component of the FAS-II pathway, that the FAS-II pathway is essential to the function of the apicoplast, and that the apicoplast is required for the viability of the malaria parasite, it is clear that FAS-II enzymes including PfENR are important targets for anti-malarial drug discovery. Structural information concerning the PfENR protein and insight gained from PfENR:inhibitor complexes will advance our understanding of the key elements necessary for the design of potent inhibitors that target this critical enzyme.

CHAPTER II

CRYSTALLOGRAPHIC STUDIES OF PFENR*

Basic Crystallographic Theory

Determining the three dimensional structure of a protein is a labor-intensive procedure that is dependent upon overcoming several hurdles. Purified, homogeneous, soluble protein is just the first step in x-ray crystallography. Once an appreciable amount of protein is obtained, the protein is concentrated to an appropriate solubility and used for crystal screening experiments. Crystals are necessary because single protein atoms do not sufficiently diffract an x-ray. This problem is circumvented by irradiating a crystal, a repeating array of proteins oriented in discrete directions. The identically oriented proteins diffract the impinging x-rays identically, serving to augment and cumulatively provide a detectable diffracted x-ray beam.

Crystal screens consist of a variety of buffers, precipitants, and salts designed to produce crystals by providing a starting point for optimization. This is a trial-and-error process, since predicting crystallization conditions is currently not feasible. Once a condition is discovered that produces crystals, the condition is optimized amongst each component to produce larger, diffraction-quality crystals. When suitably-sized crystals are obtained, it is important to find a cryoprotectant capable of protecting the crystal from radiation damage while preserving the integrity of the crystal throughout the data collection process. Then, the crystals are prepared for x-ray diffraction experiments.

*Part of the data reported in this chapter is reprinted with permission from "Structural elucidation of the specificity of the antibacterial agent triclosan for malarial enoyl acyl carrier protein reductase" by Perozzo *et al.*, 2002. *J Biol Chem*, **277**, 13106-14. 2006 by the American Society for Biochemistry and Molecular Biology.

Data collection is initiated by exposing the cryo-preserved crystal to x-rays over a small oscillation angle, usually about one degree. Over a given duration of x-ray exposure, the crystal is rotated about its center to record reflections onto an x-ray detector, resulting in one frame of data collection.

The conditions that produce diffraction are given by Bragg's law:

$$2d_{hkl}\sin\theta = n\lambda$$

where d_{hkl} refers to the distance between two parallel planes of lattice points, θ is the angle of the impinging x-ray on the plane, n is an integer, and λ is the wavelength of the incident x-ray. To summarize, a reflection is produced only when the difference in path length for rays reflected from successive planes is equal to an integral number of wavelengths of the impinging x-rays. Only when this condition is satisfied will the rays reflected from successive planes emerge in phase with each other, constructively interfering to produce a measurable diffracted beam. In all other cases the angles of incidence produce waves emergent from successive planes that are out of phase, so that they destructively interfere and no diffracted beam is recorded on the x-ray detector. Bragg's law simply states that all atoms on a set of equivalent, parallel lattice planes diffract in phase with each other. Therefore, only a subset of reflections are collected over a given oscillation range. To collect the entire range of unique reflections, rotation of the crystal around its center (through manipulation of the goniometer head) is necessary for a complete data set, resulting in the collection of several successive frames. Each frame consists of numerous reflections comprising a diffraction pattern, with each reflection having a position and intensity. Each frame of data is processed to index each reflection and calculate its intensity. The intensities of identical reflections collected on separate frames of data are compared

and a scaling factor is applied to each frame. Afterwards, post-refinement scaling commences to recover information from partially recorded reflections (reflections that span consecutive frames). The result of scaling and post-refinement is that every measurement of a particular Bragg reflection is averaged together, yielding a reduced data set containing the index (hkl) and its averaged intensity (I).

The next step is to translate the diffraction data to electron density. A structure factor equation is a Fourier series that describes a reflection, containing one term corresponding to the contribution of each atom (or volume element) in the unit cell.

$$F_{hkl} = \sum_{j=1}^n f_j e^{2\pi i(hx_j + ky_j + lz_j)}$$

In short, the structure factor equation that describes reflection hkl is a Fourier series in which each term is the contribution of one atom. The contribution of each atom j to F_{hkl} depends on the type of element, which determines the amplitude of the contribution (f_j), and its position in the unit cell (x_j, y_j, z_j), which establishes the phase of its contribution. In turn, the electron density is described by a Fourier series in which each term is a structure factor. The Fourier transform is used to convert the structure factors to $\rho(x, y, z)$, the desired electron density equation:

$$\rho(x, y, z) = \frac{1}{V} \sum_h \sum_k \sum_l F_{hkl} e^{-2\pi i(hx + ky + lz)}$$

A full description of a diffracted ray must contain three parameters: amplitude, frequency, and phase. In data collection, only the indices of each reflection and its corresponding intensity are observable. The only measurable variable in the above electron density equation is F_{hkl} , and the measured intensity of a reflection does not completely define F_{hkl} . However, useful information can still be extracted.

The structural amplitudes are directly obtainable from a single measurement of the reflection intensity, in the following manner:

$$I_{hkl} \propto |F_{hkl}|^2$$

Simply put, the amplitude of the F_{hkl} is related to the intensity of I_{hkl} . In order to compute $\rho(x, y, z)$ from the structure factors, we must obtain, in addition to the intensity of each reflection, the phase of each diffracted ray. This inability to measure phase directly is addressed as the phase problem.

Phase Problem

The phase problem can be circumvented through several techniques. These include molecular replacement (MR), multiple isomorphous replacement (MIR), multi-wavelength anomalous dispersion (MAD), and other variants using the anomalous scattering properties of heavy atoms such as single isomorphous replacement (SIR), and single anomalous dispersion (SAD). There are differing requirements for these types of experiments. For example, MR requires an observed native data set and a closely related phasing model. MIR requires a native data set and two or more heavy metal derivatives. MAD typically requires incorporation of a heavy atom into the protein of interest and data collection of up to four different wavelengths, with increased data collection requirements. So there are numerous variations available to circumvent the phase problem. For *P. falciparum* enoyl-ACP reductase, molecular replacement was utilized as the most efficient technique for solving this particular structure, since the structures of closely-related homologs were available.

Molecular Replacement

Molecular replacement (Rossmann and Blow, 1962) is a computational technique used to determine the phases, and therefore the three-dimensional structure, of a protein using structural knowledge obtained from a homologous protein. This technique requires only a native data set and a structurally related phasing model. The underlying principle of molecular replacement is to utilize the phases from the existing model, given by the location of the atoms, and insert the model into the unit cell of the new protein. This step is typically divided into separate rotation and translation functions for reasons of speed. Several programs including AMORE, Phaser, CNS, MOLREP, and BRUTE, are commonly utilized to search for molecular replacement solutions.

The searches are typically undertaken via Patterson searches. Simply put, the coordinates of the known structure are used to compute the Patterson function:

$$P(uvw) = \frac{1}{V} \sum_h \sum_k \sum_l |F_{hkl}|^2 e^{-2\pi i(hu+kv+lw)}$$

Then the diffraction pattern of the protein of interest is used to calculate its transform. The calculated transform from the known structure is compared to the observed transform from the unknown structure, rotated through all possible orientations, and a correlation coefficient calculated. Once the rotation and translation searches are successfully accomplished, then it is possible to place the known molecule in the crystallographic unit cell of the unknown molecule so that its atoms approximately assume the putative coordinates of the corresponding unknown atoms. Using the structure factor equation, the coordinates of the known molecule can be used to calculate phases for the F_{hkl} of the unknown crystal, providing first estimates of the phases.

Model Building

Model building is the process of constructing a protein model consistent with the observed data, and proceeds after phasing. Several types of difference Fourier maps are useful. The most accurate electron density maps (least subject to model bias) are MAD and MIR maps. They are unbiased because the phases are not calculated from a protein model, but empirically determined. These are typically most useful for building novel proteins. Typical Fourier maps represent the difference between observed structure factors (F_{obs} or F_o) and calculated structure factors (F_{calc} or F_c). $2F_o - F_c$ maps represent the electron density around the model, while $F_o - F_o$ and $F_o - F_c$ maps are useful in finding discrepancies between the model and the collected data and are most useful in determining the location of inhibitors in initial models. For molecular replacement experiments, a homologous protein with known structure is used to provide estimates of the initial phases for the new protein. Structure factors can be calculated from the known protein model. Computing the structure factors from a model of the unit-cell contents is an essential part of crystallography, for several reasons. First, this computation is useful in obtaining phases. This process starts by obtaining rough estimates of initial phases, then undertaking an iterative process to improve the estimates. This process entails two alternating steps: (1) computed an estimated $\rho(x, y, z)$ with the observed intensities (I_{obs}) and the estimated phases (α_{calc}), and then calculating new structure factors F_{calc} - either with the the crude model of $\rho(x, y, z)$ or a partial atomic model of the molecule containing only those atoms that can definitively be located. The second computation produces a new set of estimated phases, and the cycle is repeated: a new estimated $\rho(x, y, z)$ (a more complete model) is used to obtain new phases. With each cycle, the intent is to obtain better phases, and better estimates of $\rho(x, y, z)$ which means more complete

and accurate models of the desired structure.

Electron density calculation is simply the Fourier transform of the structure factors:

$$\rho(x, y, z) = \frac{1}{V} \sum_h \sum_k \sum_l F_{hkl} e^{-2\pi i(hx+ky+lz)}$$

Refinement

Refinement is the iterative process of correcting the model to be consistent with the observed diffraction data. This can be accomplished by fixing protein geometry errors, and as a final step adding ordered water molecules to the model. This process is monitored at each cycle of refinement with R_{factor} and a cross-validated data set, R_{free} . This R_{free} is a cross-validation data set that excludes up to 10% of the collected data and is used to prevent over-refinement of the model. This was necessary because it was shown previously that it was possible to incorrectly place atoms into electron density and artificially reduce the R_{factor} , resulting in a misleading model. Programs used for refinement include the least-squares, reciprocal-space based program XPLOR, which has been superseded by the maximum-likelihood based refinement programs CNS or REFMAC.

To monitor the correctness of the model building, to see if it is converging towards improved phases and improved electron density $\rho(x, y, z)$, the F_{calc} and F_{obs} are compared. A statistical value gauging the accuracy of the model to the observed data is calculated as follows:

$$R_{factor} = \frac{\sum_{hkl} ||F_{obs}| - |F_{calc}||}{\sum_{hkl} |F_{obs}|}$$

In each step of refinement, the R_{factor} and R_{free} are monitored to ensure that

the intensities (I_{obs} and I_{calc} present in the structure factors) are moving towards convergence. When cycles of computation provide no further improvement in correspondence between calculated and measured intensities, then this process is complete.

Results and Discussion

Initial crystallization trials utilized incomplete factorial screens purchased from Hampton Research. The screens contained 98 different conditions containing varying combinations of salt, precipitant, and buffer within a pH range of 4-10. PfENR protein was screened at 20 mg/mL in the presence of NADH cofactor, and microcrystals were discovered in a condition containing ammonium sulfate and 100 mM sodium acetate, pH 5.6. Subsequently grid screening was performed to optimize the conditions to that most favorable for large crystal growth. Over the course of 14 days, good quality crystals were produced that resulted in diffraction to approximately 3 Å in initial tests using $\text{CuK}\alpha$ radiation from a rotating anode.

After screening several crystals to determine the highest quality one, a 95% complete data set was collected to a resolution of 2.4 Å. The crystal was of the $P4_32_12$ space group with unit cell dimensions of $a = b = 134.0$ Å, $c = 84.0$ Å, and $\alpha = \beta = \gamma = 90^\circ$. Molecular replacement was performed using the cross rotation and translation protocols in CNS (Brünger *et al.*, 1998) using the structure of *Brassica napus* ENR as the search model. The results indicated two possible rotation and translation solutions, consistent with a Matthews coefficient calculation predicting two molecules within the asymmetric unit. These solutions were subjected to rigid body refinement protocols, where each monomer was initially treated as a rigid body for the purpose of refinement. After rigid body refinement, the refine protocol from CNS was uti-

lized to subject the model to successive steps of simulated annealing, minimization, B-factor refinement, and to calculated sigma-A weighted $2F_o - F_c$ maps and $F_o - F_c$ difference maps. Sigma-A weighting attempts to present a more accurate model of the error by multiplying the F_o term by m , representing the estimated correctness of the phases, and multiplying the F_c term by D , applying a “blur” factor to the phasing model. The starting temperature for the simulated annealing was 2500° K, and the default settings for the energy minimization and B-factor refinement were used for the initial refinement.

The $2F_o - F_c$ maps were of high quality, and matched well with the refined protein model. Inspection of the $F_o - F_c$ difference electron density maps revealed strong density consistent with NADH, so the cofactor was included into the model for future calculations. Two cofactors were located, one within each of the substrate binding sites of each monomer. Ultimately, after further refinement to correct errors in the protein backbone and side-chains, water molecules were added to the model using CNS water picking protocols that selected peaks greater than 3σ in the $F_o - F_c$ electron density maps. Waters were inspected manually, and structure validation was performed with the PROCHECK/WHATIF suite of programs.

PfENR Sequence Characteristics

pfenr encoded a predicted protein of 432 amino acids with an expected molecular mass of 49.8 kDa. Sequence alignments (Figure 3) revealed that PfENR showed much greater overall sequence similarity to plant ENRs than to microbial ENRs. Regions of homology with plant enzymes were interrupted by a 43-amino acid insert (residues 325-367) that was enriched in the polar residues asparagine (30%), lysine (12%), glutamine (9%), and serine (9%). This low complexity insertion was demonstrated to be coding, because it was routinely identified in cDNA libraries, it did not have typ-

ical splice acceptor and donor sequences, and it maintained the same A/T content as the other coding regions. Similar insertions have previously been reported in *P. falciparum* enzymes and are thought to generally have minimal impact on function (Gardner *et al.*, 1998; Gilberger *et al.*, 2000). PfENR has a long N-terminal extension (similar in length to plant ENRs) that is characteristic of bipartite N-terminal pre-sequences found in *Plasmodium* and *Toxoplasma* parasite proteins targeted to the apicoplast (Waller *et al.*, 1998, 2000). Using prediction programs SIGNALP (Bendtsen *et al.*, 2004) and PSORT (Nakai and Horton, 1999), a putative cleavage site for the signal peptide could be detected between residues Cys²⁰ and Phe²¹ (Claros *et al.*, 1997; Nielsen *et al.*, 1997). The size of the adjacent apicoplast translocation signal was recently discovered to be 56 amino acids long, with Glu⁷⁸ being the first amino acid of the mature enzyme (Surolia and Surolia, 2001). Sequence alignments revealed 33 completely conserved and 44 highly conserved residues in the PfENR sequence when compared with the ENRs of *E. coli*, *B. napus*, and *Mycobacterium tuberculosis*. Mapping of the completely conserved residues onto the three-dimensional structure of PfENR showed Gly¹⁰⁴, Tyr²⁷⁷, Met²⁸¹, Lys²⁸⁵, Ala³¹², and Pro³¹⁴ located immediately adjacent to the nicotinamide ring of NADH. These residues are likely to play an important role in substrate recognition and/or the catalytic function of the enzyme. The remaining conserved residues were dispersed throughout the structure, occurring mainly at the interfaces between the subunits of the tetramer or in positions where they were predicted to stabilize the orientation of secondary structure.

Tertiary Structure of PfENR

Overall, the structure contained a Rossmann fold (Rossmann *et al.*, 1974) and was similar to all other structurally defined homologous enzymes. The PfENR subunit comprised a single domain of 55 x 50 x 50 Å (Figure 4). Each subunit was composed

| | | |
|--------|-----|---|
| Plafal | 1 | MNKISQRLFLFLHFYTI VCFIQNNTQKTFHNVLQNEQIRGKEKAFYRKE |
| Branap | 1 | ---MAATAAASSLQMATTRPSISAASSKARTYVVGANPRNAYKIACTPHL |
| Esccol | 1 | ----- |
| Myctub | 1 | ----- |
| | | |
| Plafal | 51 | KRENIFIGNKMKHLNNMNNTHNNNHMEKEEQDASNINKIKEENK NEDIC |
| Branap | 48 | SNLGCLRNDSPASKKSFSTKAMSESESKASSGLPIDLRGKR---A |
| Esccol | 1 | -----MGFLSGKR---I |
| Myctub | 1 | -----MTGLLDGKR---I |
| | | |
| Plafal | 101 | FIAGIGDNGYGWGI AKELSKRNVKII FGIWPPVYNIFMKNYKNGKFDND |
| Branap | 95 | FIAGIADDNGYGWAVAKSLAAAGAEILVGTWVPALNIFETSLRRGKFDQS |
| Esccol | 10 | LVTGVASKLSIAYGIAQAMHREGAELAF-----TYQNDKLGK- |
| Myctub | 11 | LVSGLIITDSSIAFHIAARVAQEQAQLVLT-----GFDRLRLIQ- |
| | | |
| Plafal | 151 | MIIDKDKKMNILDMLPFDASFDTANDIDEETKNNKRYNMLQNYTIEDVAN |
| Branap | 145 | RVLDPDGLMEIKKVYPLDAVFDNPEDVPEDVKANKRYAGSSNWTVQEAEE |
| Esccol | 47 | -----RVEEFAAQLGSDIVLQC--DVAEDASIDTMFAELG----- |
| Myctub | 49 | -----RITDRLPAKAPLLELDVQNEEHLASLAGRVTEAIG----- |
| | | |
| Plafal | 201 | LIHQKYGKINMLVHSLANAKEVQKD---LLNTRKGYLDALSKSSYSLIS |
| Branap | 195 | CVRQDFGSIDILVHSLANGPEVSKP---LLET SRKGYLAAISASSYSFVS |
| Esccol | 80 | ---KVWPKFDGFVHSIGFAPGDQLDGDYVNAVTRREGFKIAHDISSYSFVA |
| Myctub | 84 | ---AGNKLDGTVHHSIGFMPQTGMGINPFFDAPYADVSKGIHISAYSYS |
| | | |
| Plafal | 248 | LCKYFVNIMKPPQSSIISLTYHASQKVVPGYGGGMSSAKAALES DTRVLAY |
| Branap | 242 | LLSHFLPIMNPPGASISLTYIASERIIPGYGGGMSSAKAALES DTRVLAF |
| Esccol | 127 | MAKACRSMLNPPGSALLTLSYLGAERAIPNYN-VMGLAKASLEANVRYMAN |
| Myctub | 130 | MAKALLPIMNPPGGSIVGMDFD-PSRAMPAYN-WMTVAKSALESVNR FVAR |
| | | |
| Plafal | 298 | HLGRNYNIRINTISAGPLKSRAATAINKLNNTYENNTNQNKNRNSHDVHN |
| Branap | 292 | EAGRKQNI RVNTISAGPLGSRAAKAIG----- |
| Esccol | 176 | AMGPE-GVRVNAISAGPIRTLAASGIKD----- |
| Myctub | 178 | EAG-KYGVRSNLVAAGPIRTLAMSAIVG----- |
| | | |
| Plafal | 348 | <u>IMNNSGEKEEKNSASQNYTFIDYAI EYSEKYAPLRQKLL-STDIGSVAS</u> |
| Branap | 319 | -----FIDTMIEYSYNNAPIQKTLT-ADEVGNAAA |
| Esccol | 203 | -----FRKMLAHCEAVTPIRRTVT-IEDVGNAAA |
| Myctub | 205 | -----GALGEEAGAQLQLLEEGWDQRAPIGWNMKDATPVAKTVC |
| | | |
| Plafal | 397 | FLLSRESRAITGQTIYVDNGLNIM--FLPDDIYRNEE |
| Branap | 348 | FLVSPLASAITGATIYVDNGLNSMGVALDSPVFKDLNK |
| Esccol | 231 | FLCSDLSAGISGEVVHVDGCF SIA--AMNELELK---- |
| Myctub | 244 | ALLSDWLPATTGDIYADGCAHTQLL----- |

Figure 3: Sequence alignment of PfENR with homologous enoyl reductases. The degree of sequence identity was 48, 16, and 30%, for *B. napus*, *E. coli*, and *M. tuberculosis*, respectively. Green indicates completely conserved residues, and yellow indicates two or more highly conserved residues. The secondary structure of *P. falciparum* ENR is shown above the sequences. The putative signal sequence cleavage site is located between Cys²⁰ and Phe²¹. The first amino acid of the mature, cleaved enzyme is Glu⁷⁸. The residues proposed to be catalytically important are indicated by asterisks (*). The 43-amino acid low complexity region is underlined in red.

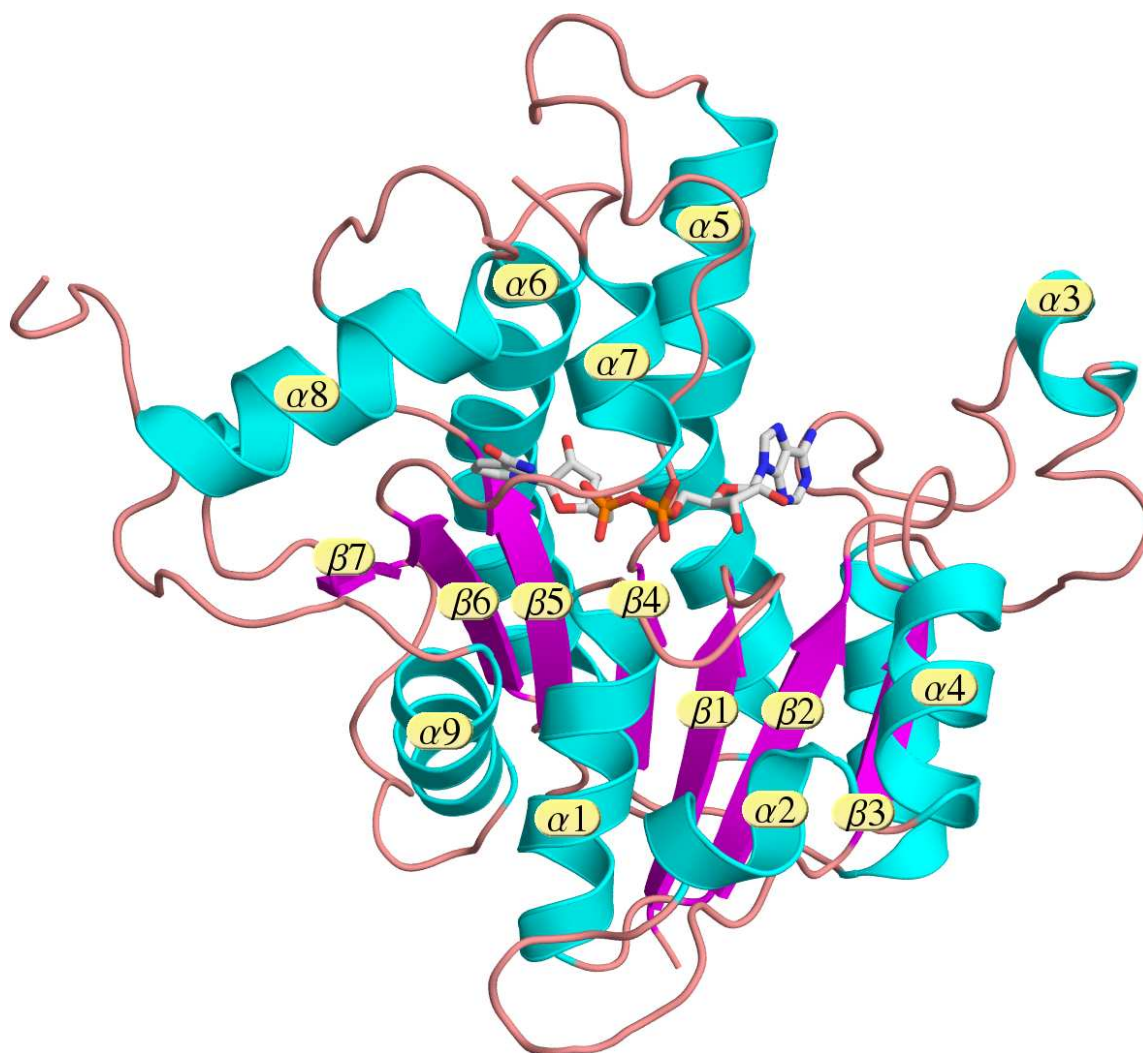


Figure 4: Tertiary structure of *Plasmodium falciparum* enoyl-ACP reductase. Representation of subunit B of the PfENR tetramer with the co-factor NADH bound to their active sites. Helices are shown in blue, the β -strands in purple, NADH is represented as sticks, colored by atom type. The tertiary structure shows the Rossmann fold typical of dinucleotide-binding enzymes. The chain break visible at the top of the inhibitor binding site between $\alpha 7$ and $\alpha 8$ is due to the PfENR substrate binding loop that was not resolved in the crystal structures.

of seven β -strands (β 1- β 7) that formed a parallel β -sheet and nine α -helices (α 1- α 9) that were connected to the β -strands by a number of loops of varying length. The parallel β -sheet was flanked by helices α 1, α 2, α 4, α 5, α 6, and α 9, with α 3 arranged along the top of α 2 and α 4. Helix α 8 was located at the C-termini of strands β 6 and β 7. Comparison of the C_α positions of the *E. coli*, *M. tuberculosis*, and *B. napus* ENRs showed that the overall structure of all enzymes was very similar (the C_α root mean square deviation for superimposition of PfENR with ENR from *B. napus*: 0.30 Å; from *E. coli*: 0.78 Å; from *M. tuberculosis*: 0.75 Å; Figure 5, a, c, and e). Whereas the core region built of the β -sheet was nearly identical in all structures, major differences were nevertheless discernible between PfENR and the ENRs of *E. coli*, *M. tuberculosis*, and *B. napus*, (Figure 5). The loop regions between α 2- β 3, β 3- α 3- β 4, and β 4- α 5 of PfENR were longer due to insertions in the sequence, and helix α 2 was shifted away from the protein, toward the solvent, relative to the bacterial ENRs. Helix α 3, a small helix in the loop region between β 3 and α 4, was not observed in the microbial structures but was present in the plant ENR. The aforementioned 43-amino acid low complexity insertion in PfENR sequence localized to an important loop region (α 7 and α 8), near the catalytic center of the protein. This region is thought to be a determinant in substrate specificity, because it participates in acyl substrate binding, as shown in the *M. tuberculosis* structure in which the bound fatty acyl substrate was held in place by the substrate binding loop (Rozwarski *et al.*, 1999). Only 3 amino acids of the low complexity insertion were visible in the electron density maps, indicating that most of this region was disordered even in the presence of bound substrate and inhibitor. Nonetheless, the last visible amino acids just before (Lys³²⁵) and after (Tyr³⁶⁶) the low complexity region were in nearly the exact same position as the comparable loop residues in the *E. coli* enzyme structure (Figure 5d). For the *E. coli* ENR, this loop was disordered

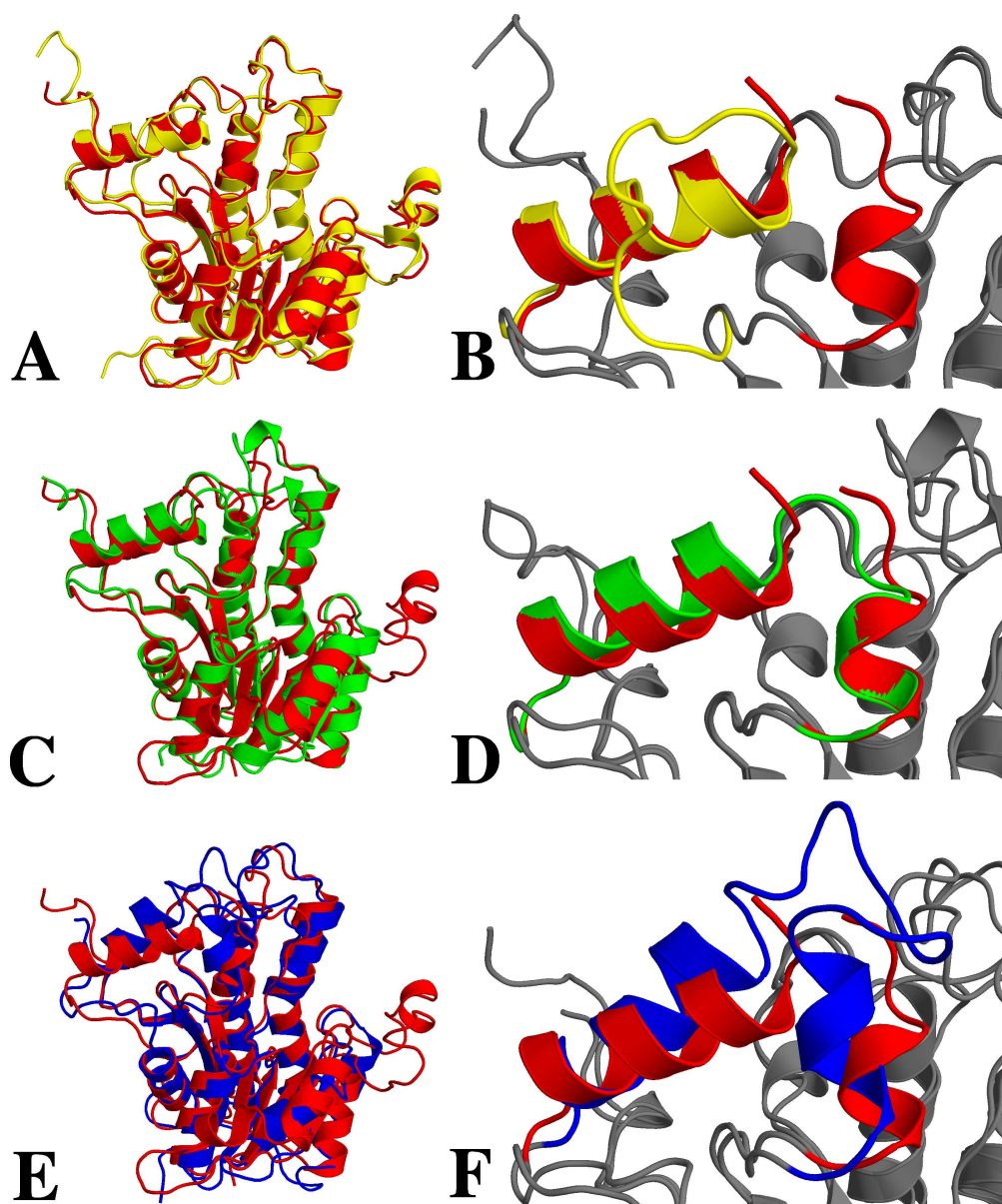


Figure 5: Superposition of PfENR with homologous enzymes. A, overall structures of PfENR (red) and *B. napus* ENR (yellow) revealed a major difference occurring in the lid region (magnified view in B), for which the loop of the *B. napus* enzyme made a turn in the direction opposite to that found in *P. falciparum*, *M. tuberculosis*, and *E. coli* ENRs. C, comparison of PfENR (red) and the *E. coli* ENR (green) is shown on the left, whereas the lid region has been magnified and is presented in D. Both lid regions adopted very similar orientations and conformations. E, major structural differences were found for the lid region when the ENR of *P. falciparum* (red) and *M. tuberculosis* (gold) were superimposed.

Table 1: Observed K_m and V_{max} values for ENRs

| Organism | K_m | V_{max} |
|----------------------|---------------|-------------------------------|
| | μM | $\mu\text{M}/\text{min}^{-1}$ |
| <i>P. falciparum</i> | 48 ± 3 | 16 ± 2 |
| <i>B. napus</i> | 178 | NA |
| <i>E. coli</i> | 2,700 | 10 |
| <i>S. oleracea</i> | 40 | 11 |

when NAD^+ was bound, but became ordered upon binding of the inhibitor triclosan (Roujeinikova *et al.*, 1999a; Qiu *et al.*, 1999). In the *M. tuberculosis* ENR this loop was displaced away in a more open conformation (Figure 5f), presumably for the binding pocket to accommodate the binding of the longer fatty acid substrates (C_{16} - C_{56} , precursors of mycolic acid) used by the mycobacterial enzyme. The loop region of *B. napus* ENR was very different because $\beta 6$ makes a turn in the opposite direction when compared with all other structures, and connects $\beta 6$ with $\alpha 7$ of *B. napus* ENR, resulting in a substrate binding pocket that is considerably more solvent exposed (Figure 5b). Earlier investigations into *E. coli*, *B. napus*, and *M. tuberculosis* ENRs have found a correlation between the length of the substrate binding loop and the fatty acyl substrate chain length (Rozwarski *et al.*, 1999). If this held for *P. falciparum* ENR, one could expect that very long-chain fatty acids would serve as substrate and, by analogy to the *M. tuberculosis* ENR, the PfENR would not use very short-chain acyl-CoAs as substrate. However, kinetic studies indicated that the *P. falciparum* ENR can use crotonoyl-CoA ($\text{C}_4:1$) (Table 1), with kinetics in line with those observed for *S. oleracea* and *B. napus* ENRs.

Quaternary Structure of PfENR

In gel filtration studies, PfENR formed a tetramer in solution, in agreement with all other bacterial and plant ENRs reported to date. In support of this, the packing

in the crystal showed an obvious homotetramer possessing internal 222 symmetry (Figure 6). The estimated dimensions for the tetramer were 60 x 85 x 85 Å . The solvent-accessible surface areas for the subunits and the tetramer were calculated using DSSP (Kabsch and Sander, 1983) and were determined to be about 15,000 Å² for each subunit and 43,000 Å² for the tetramer. Approximately 1600 Å² (11%) of the surface area of subunit A was buried, making intermolecular contacts with subunit B, 1700 Å² (12%) with subunit C, and 900 Å² (6%) with subunit D. Thus, the total surface area involved in intermolecular contacts of each subunit was 4200 Å² or 29%. This type of organization for PfENR was comparable to the crystal structures elucidated for enoyl-ACP reductases from *E. coli* (Baldock *et al.*, 1996), *B. napus* (Rafferty *et al.*, 1995), and *M. tuberculosis* (Rozwarski *et al.*, 1999).

Analysis of the Nucleotide Binding Site

Both the ENR:NADH binary complex and the ENR:NAD⁺/NADH inhibitor ternary complexes showed excellent electron density for the co-factors. NAD⁺ and NADH were localized to the enzyme in an extended conformation at the C-terminal end of the β -sheet with both ribose sugar rings found as C2'-endo conformers and the nicotinamide moiety in the *syn* conformation. The adenine ring was located in a pocket on the surface of the protein, formed by the side chains of Trp¹³¹, Phe¹⁶⁷, Ala¹⁶⁹, Ser¹⁷⁰, Asn²¹⁸ and the main chain between residues Phe¹⁶⁷ and Asp¹⁶⁸. Hydrogen bonds were formed between the adenine nitrogen atoms at position N1 with the peptide nitrogen atom of Ala¹⁶⁹ and at position N6 with the side chain of Asp¹⁶⁸. Both the 2' and 3' adenine ribose hydroxyl groups were hydrogen-bonded to the same ordered water molecule, which in turn was hydrogen-bonded with the peptide nitrogen of Trp¹³¹. This mode of hydrogen bonding in *P. falciparum* was different from many NAD⁺/NADH-linked dehydrogenases for which the common mechanism

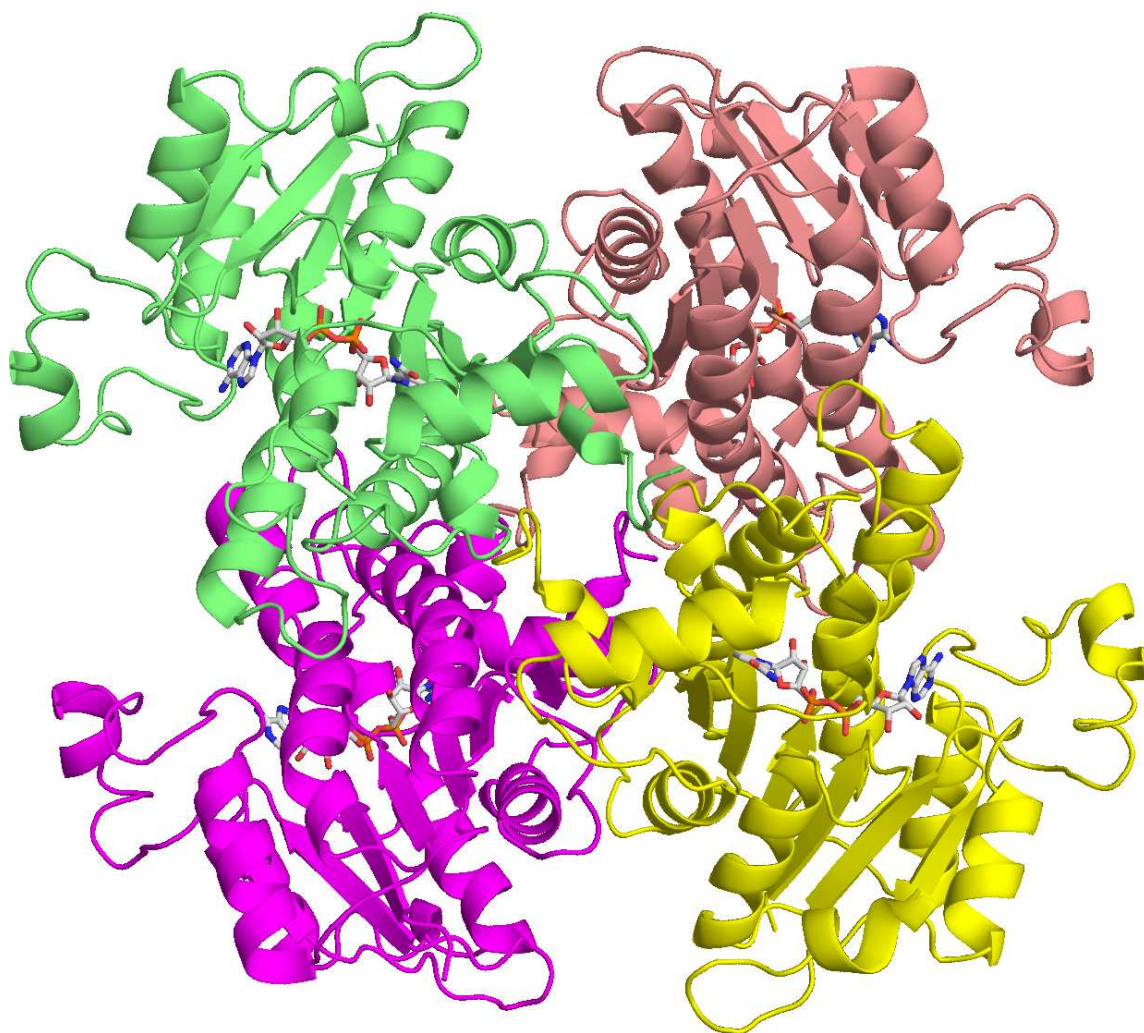


Figure 6: Quaternary structure of the PfENR tetramer. Front view of the PfENR biological tetramer, in which each subunit is represented as a differently colored ribbon. The bound NADH is colored by atom type. Three perpendicular 2-fold symmetry axes intersect in the center, creating a molecule of internal 222 symmetry.

for co-factor recognition involves hydrogen bonding between an acidic residue and both ribose hydroxyl groups (Wierenga *et al.*, 1985). However, the recognition of the adenine ribose hydroxyl groups was similar to that observed in *B. napus* and *E. coli* ENRs. In PfENR, the 2'-hydroxyl group of the adenine ribose occupied a small depression flanked by Gly¹⁰⁶, Trp¹³¹ and Val¹³⁴, which resulted in a tight fit for the NAD⁺/NADH co-factor. This spatial arrangement leaves no room for the extra phosphate group of NADPH and is consistent with the previous observation that NADH was a much more efficient co-factor than NADPH for PfENR function (Surolia and Surolia, 2001). The pyrophosphate moiety of NAD⁺(NADH) lay close to the C-terminal part of the β -sheet and interacted with the glycine-rich region of the loop connecting β 1 and α 1, with α 1 being the nucleotide binding helix. Contacts through hydrogen bonds were made by the pyrophosphate oxygen atoms with the peptide nitrogen of Tyr¹¹¹ and, mediated by a solvent molecule, with the main-chain carbonyl of Gly¹⁰⁴, the peptide nitrogen of Gly¹¹² and the side-chain hydroxyl of Ser²¹⁵. By way of an additional water molecule, hydrogen bonding also occurred with the peptide nitrogen of Gly¹⁰⁴. The co-factor was bound by this series of hydrogen bonds and was not further supported by positively charged side chains close to the nucleotide binding site. The nicotinamide binding pocket was composed of the side chains of Tyr¹¹¹, Leu²⁶⁵, Tyr²⁶⁷, Tyr²⁷⁷, Ala³¹², Gly³¹³, Pro³¹⁴, Leu³¹⁵, and Ile³⁶⁹. Both 2'- and 3'-ribose hydroxyl groups hydrogen-bonded to the amino group of the Lys²⁸⁵, whereas only the 3'-group interacted with a solvent molecule that was contacted by the side chain of His³¹⁴. The nicotinamide ring was completely ordered on the enzyme, where it interacted via specific hydrogen bonds formed by the oxygen and nitrogen of the carboxamide moiety and the Leu³¹⁵ peptide nitrogen and co-factor pyrophosphate moiety. These interactions appeared to stabilize the packing of the A-face of the nicotinamide ring against the phenolic ring of Tyr¹¹¹,

exposing the B-face to the active site. Thus, the co-factor adopted the same conformation for stereospecific hydride transfer via the *pro*-4S hydrogen of NADH as that observed with *E. coli*, *B. napus*, and *M. tuberculosis* ENRs (Rozwarski *et al.*, 1999; Roujeinikova *et al.*, 1999a; Qiu *et al.*, 1999; Rafferty *et al.*, 1995; Dessen *et al.*, 1995; Stewart *et al.*, 1999; Roujeinikova *et al.*, 1999b; Ward *et al.*, 1999).

Location of the Fatty Acyl Binding Pocket

Earlier structural studies of *M. tuberculosis* ENR complexed to the C₁₆ fatty acyl substrate analog and NAD⁺ revealed that the C₁₆ substrate bound in a U-shaped conformation, with the *trans*-double bond position directly adjacent to the nicotinamide ring of NAD⁺ and the side chain of Tyr²⁷⁷ interacting directly with the C₁₆ substrate thioester carbonyl oxygen (Rozwarski *et al.*, 1999). The binding crevice for the fatty acyl portion of the substrate was built of hydrophobic residues that were derived primarily from the substrate binding loop. The ENR structures from *P. falciparum*, *B. napus*, and *E. coli* showed a similar patch of predominantly hydrophobic side chains adjacent to the position of the nicotinamide ring and the fatty acid chain binding area. With PfENR, the corresponding amino acids and side chains flanking the putative binding site were Tyr²⁶⁷, Gly²⁷⁶, Tyr²⁷⁷, Met²⁸¹, Pro³¹⁴, Ala³¹⁹, Ala³²⁰, Ala³²², Ile³²³, Ile³⁶⁹, and Ala³⁷². Most residues were located in helices α 7 and α 8 and formed a hydrophobic finger-shaped cavity with the approximate dimensions of 10 x 8 x 6 Å. One side of the cavity was accessible to solvent. Based on volumetric measurements of the fatty acyl binding cavity in the PfENR:NADH binary complex, there was only enough space to accommodate a substrate of six to eight carbon atoms in length. This implies that there must be sufficient flexibility in the PfENR pocket to bind longer substrates (up to at least C₁₆), which probably occurs via an opening movement of the flexible loop. In view of the present biochemical and structural

information, it is possible that the extensive substrate binding loop of PfENR, which includes the low complexity region, would allow for broader specificity in the fatty acyl chain.

CHAPTER III

PFENR INHIBITOR STUDIES*

To advance our knowledge of interactions concerning PfENR and inhibitors within the active site, *in vitro* enzyme assays, co-crystallization experiments, and x-ray diffraction experiments were conducted. Based on prior reports concerning homologous enoyl reductases, we targeted our initial research at understanding triclosan and its interactions with PfENR. We directed our energies towards rational drug design of triclosan, followed by generation of a comprehensive structure-activity relationship (SAR) by substituting atoms at several positions on the molecule.

We were interested in the commercially available compound 5 - chloro - 2 - (2,4 - dichlorophenoxy) phenol, commonly known as triclosan, (Figure 7) for several reasons. Triclosan inhibits *P. falciparum* in a stage specific manner, preventing trophozoites from invading erythrocytes after 48 hours (Surolia and Surolia, 2001). Triclosan has been reported to inhibit the growth of drug-resistant and drug-sensitive *P. falciparum* in *in vitro* whole cell assays with IC₅₀ values of 0.2-0.9 μ M (Kuo *et al.*, 2003). This activity was significantly better than that of the antibiotic thiolactomycin, which is thought to act on FAS-II enzymes including β -ketoacyl-ACP synthase, showed an IC₅₀ value of approximately 50 μ M against *P. falciparum* (Waller *et al.*, 1998). Triclosan was also reported to be effective in clearing *Plasmodium*

*Part of the data reported in this chapter is reprinted with permission from *Bioorg Med Chem Lett*, Vol 15, Freundlich JS, Anderson JW, Sarantakis D, Shieh HM, Yu M, Valderramos JC, Lucumi E, Kuo M, Jacobs WR, Fidock DA, Schiehser GA, Jacobus DP, Sacchetti JC, "Synthesis, biological activity, and X-ray crystal structural analysis of diaryl ether inhibitors of malarial enoyl acyl carrier protein reductase. Part 1: 4'-substituted triclosan derivatives", 5247-5252, Copyright (2005), with permission from Elsevier, and from *Bioorg Med Chem Lett*, Vol 16, Freundlich JS, Yu M, Lucumi E, Kuo M, Tsai HC, Valderramos JC, Karagoyzov L, Jacobs WR, Schiehser GA, Fidock DA, Jacobus DP, Sacchetti JC, "Synthesis, biological activity, and X-ray crystal structural analysis of diaryl ether inhibitors of malarial enoyl acyl carrier protein reductase. Part 2: 2'-substituted triclosan derivatives", 2163-2169, Copyright (2006), with permission from Elsevier.

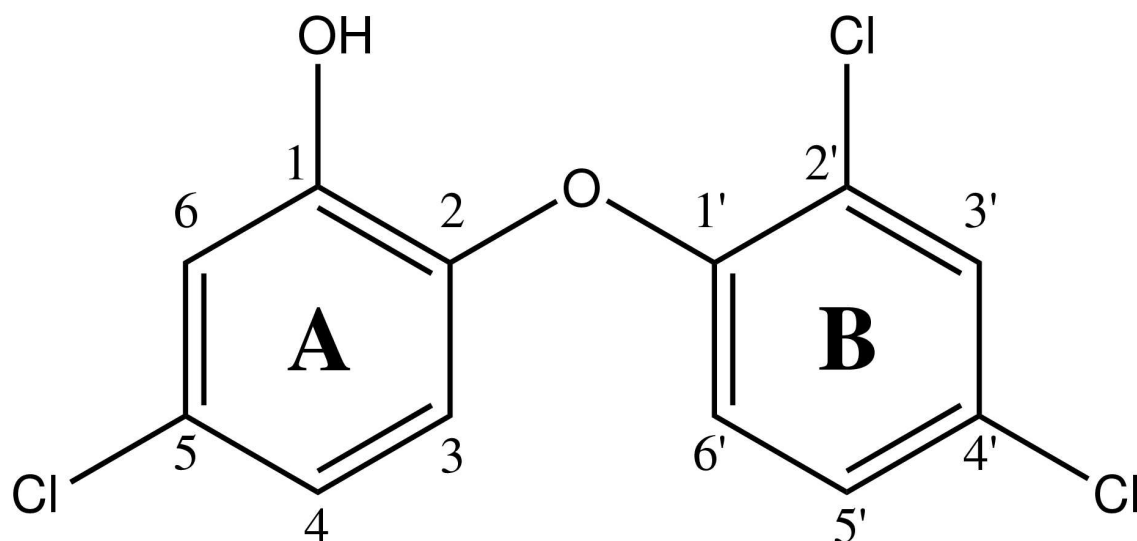


Figure 7: Triclosan and its nomenclature. 5-chloro-2-(2,4-dichlorophenoxy)phenol, commonly known as triclosan, is a hydroxy diphenyl ether that has been employed for years in anti-bacterial products. Because of its favorable safety profile and effectiveness, its scaffold was adopted as a basis for derivatization, with the goal of generating new compounds with improved pharmacological properties.

berghei from mice with a single subcutaneous 38 mg/kg injection of triclosan, with no apparent toxic side effects (Surolia and Surolia, 2001). Liver and kidney function were normal at this dose, as measured in assays for serum glutamate-pyruvate transaminase and glutamate-oxaloacetate transaminase activities, as well as urea, glucose, and creatinine levels. Triclosan has also been reported to specifically inhibit the enoyl reductase from *P. falciparum* (Surolia and Surolia, 2001), as well as the homologous FAS-II enoyl reductases from other organisms such as *Mycobacterium tuberculosis* (Parikh *et al.*, 2000), *Staphylococcus aureus* (Heath *et al.*, 2000b), *Escherichia coli* (Heath *et al.*, 1998), *Bacillus subtilis* (Heath *et al.*, 2000a), *Brassica napus* (Roujeinikova *et al.*, 1999a), *Haemophilus influenzae*, (Marcinkeviciene *et al.*, 2001) and *Pseudomonas aeruginosa* (Hoang and Schweizer, 1999). Triclosan possesses a favorable long-term safety profile (Jones *et al.* 2000), and has been incorporated into many household items, including toothpaste, soaps, mouthwash, and even children's toys (Bhargava and Leonard, 1996) as an antimicrobial agent. It has been utilized for over 40 years in the United States and is recognized by the Food and Drug Administration (FDA) as either an over-the-counter or prescription drug (Jones *et al.*, 2000). Observation of the enzyme activity assay is straightforward, requiring only the spectrophotometric monitoring of the A_{340} to follow interconversion of NADH to NAD^+ that accompanies the transfer of a hydride from the co-factor to the substrate. All these factors led us to pursue triclosan as a potential anti-malarial agent.

The dramatically different binding affinities of triclosan for each of the enoyl-ACP reductases (10,000-fold difference between *E. coli* FabI and *M. tuberculosis* InhA, in particular) (Sivaraman *et al.*, 2003) also suggested that tailoring the triclosan scaffold to each specific enzyme was a reasonable endeavor. A multiple sequence alignment of the various enoyl reductases (Figure 3) exhibited regions of low conservation within

the substrate binding loop that were believed to be structurally adjacent to the triclosan binding site. This allowed us to speculate that the differences could be exploited by developing a triclosan derivative with exquisite specificity for the FAS-II enoyl-ACP reductase for a particular organism. While triclosan was very effective against the enoyl-ACP reductases *in vitro*, it was unsuitable in this configuration as an ingestible antibacterial. Limited studies regarding triclosan metabolism have shown that triclosan is subject to modification through glucuronidation and sulfonation at a key position, the phenolic hydrogen of the A ring (Wang *et al.*, 2004). Previous studies have also shown that triclosan was primarily excreted as the glucuronide following application of a 1% formulation to guinea pig or rat skin (Black *et al.*, 1975). Yet another study showed that topically applied triclosan formed sulfate and glucuronide conjugates in human as well as rat skin (Moss *et al.*, 2000). Finally, another study showed that polar bear livers sulfonate triclosan (Sacco and James, 2005). Despite the observation that triclosan is subject to modification *in vivo*, the basic triclosan scaffold holds promise as a starting point to modify, to increase potency and specificity, as well as pharmacokinetic profiles.

Results and Discussion

The structure of the binary complex of PfENR:NADH gave us a starting point for protein:co-factor:inhibitor ternary complex structural studies. Hundreds of vapor diffusion experiments based on the optimized crystallization conditions were set up, in order to obtain the largest, well-ordered, best-diffracting crystals possible. Inhibitors were typically solubilized in acetonitrile, a solvent that was determined to be compatible with the protein crystals in early solvent-screening trials. Inhibitors were allowed to soak undisturbed into the crystals for 14 to 21 days, before being subjected to

X-ray diffraction experiments. Provided that the crystals diffracted to sufficient resolution, complete data sets were collected on the PfENR:NAD⁺:inhibitor complexes. Although the crystals generally suffered minor damage, the cell parameters of these ternary complexes were isomorphous to the native crystals, greatly simplifying each successive step of model building and refinement. A model of PfENR containing only protein atoms was subjected to rigid body refinement and minimization using the newly collected data, and sigma-A weighted $2F_o - F_c$ and $F_o - F_c$ electron density maps were calculated using the crystallographic refinement package CCP4 (Collaborative Computational Project, Number 4, 1994). Inspection of the electron density maps was performed with the molecular modeling program XtalView (McRee, 1999). If the electron density maps exhibited peaks consistent with the presence of NADH cofactor, the cofactors were built into the model and another round of restrained refinement and map calculations performed. If the electron density maps exhibited significant peaks consistent with a conformer of the incubated inhibitor, the inhibitor was built into the model. Another cycle of restrained refinement and new electron density map calculation followed. Waters were first automatically placed, subsequently manually inspected, then waters were added or deleted with the molecular modeling program XtalView.

Analysis of the Triclosan Binding Site

Three distinct classes of chemically synthesized agents have been shown to act by inhibiting this enzyme in the bacterial FAS-II pathway. Isoniazid targets the ENR homolog, InhA, from *M. tuberculosis*, after activation and covalent attachment to the nicotinamide ring of NADH (Rozwarski *et al.*, 1998). The mechanism of inhibition of the diazaborines is through a covalent bond between a boron atom in the diazaborine and the 2'-hydroxyl group of the nicotinamide ribose moiety in this

enzyme (Kater *et al.*, 1994; Bergler *et al.*, 1994; Baldock *et al.*, 1996). Another extremely potent bacterial ENR inhibitor is triclosan, which, in contrast to the other antimicrobials, forms a non-covalent complex with NAD^+ and protein primarily via hydrogen bonds. The crystal structure of PfENR solved with protein incubated with NAD^+ and triclosan revealed the mode of triclosan binding (Figure 8). Comparison of the *P. falciparum* ENR: NAD^+ :triclosan structure with the corresponding *E. coli* and *B. napus* structures (Roujeinikova *et al.*, 1999a; Stewart *et al.*, 1999) demonstrated that, for the malaria enzyme, the binding mode for triclosan was very similar, showing the same stacking interaction with the nicotinamide ring of NAD^+ and comparable hydrogen-bonding pattern with the 2'-hydroxyl group of the nicotinamide ribose and with Tyr²⁷⁷. Ring A (the phenol ring) of the inhibitor interacted face-to-face with the nicotinamide ring of NAD^+ allowing π -cation interactions. The same ring formed additional van der Waals interactions with the side chains of Tyr²⁶⁷, Tyr²⁷⁷, Pro³¹⁴, Phe³⁶⁸, and Ile³⁶⁹. The phenolic hydroxyl hydrogen-bonded to the 2'-hydroxyl moiety of the nicotinamide ribose and the oxygen atom of Tyr²⁷⁷, and the amino nitrogen of Lys²⁸⁵ was within 4.6 Å. These residues are completely conserved in all known ENRs and have been implicated in the enzyme's catalytic mechanism (Rafferty *et al.*, 1995; Parikh *et al.*, 1999). The 4-chloro atom of ring A was surrounded by mainly hydrophobic residues making van der Waals contacts with the side chains of Tyr²⁶⁷, Pro³¹⁴, and Phe³⁶⁸. The ether oxygen atom of triclosan interacted with the 2'-hydroxyl group of the nicotinamide ribose, and it approached to within 3.65 Å of one of the oxygen atoms of the nicotinamide ribose phosphate group. Ring B (2,4-dichlorophenoxy ring) of triclosan was located in a pocket bounded by the pyrophosphate and nicotinamide moieties of NAD^+ , by the peptide backbone residues 217-231 and by the side chains of Asn²¹⁸, Val²²², Tyr²⁷⁷, and Met²⁸¹. Although the 4-chloro atom of ring B was placed adjacent to the side chains of Val²²²

and Met²⁸¹ and residues 218-219, the 2-chloro atom was surrounded by the α -carbon atom, the side chain of Ala²¹⁷, and atoms of the nicotinamide ribose pyrophosphate moiety. One ordered water molecule was observed in the inhibitor binding site of the binary ENR:NADH complex, interacting through hydrogen bonds with the 2'-hydroxyl group of the nicotinamide ribose and with Tyr²⁷⁷. This water molecule was very close to the position of the phenolic hydroxyl group of the inhibitors and was displaced upon triclosan binding. Superposition of the binary and ternary complex structures revealed subtle conformational changes in the protein upon inhibitor binding, with the most pronounced change being a slight shift of helix $\alpha 7$ by 0.5 Å towards the solvent.

Isoniazid

Isonicotinic acid hydrazide (INH), commonly known as isoniazid, has been used as an effective first-line anti-tubercular agent for over 50 years. The target of isoniazid was discovered to be InhA (Banerjee *et al.* 1994), a *Mycobacterium tuberculosis* enoyl-ACP reductase enzyme homologous to PfENR. The structure of *M. tuberculosis* InhA in complex with isoniazid (Rozwarski *et al.*, 1998) revealed new interactions in a vicinity distinct from where triclosan occupies upon binding. Isoniazid itself is a prodrug that is activated by the catalase-peroxidase enzyme KatG (Zhang *et al.*, 1992) within *M. tuberculosis*, and covalently attaches to the nicotinamide ring of the cofactor NADH to generate a tightly bound and potent adduct. The structure of InhA:isoniazid showed that isoniazid binding is accompanied by an approximately 90° rotation of a catalytic residue (Phe¹⁴⁹) to optimize aromatic ring stacking interactions with the pyridine ring of the isonicotinic acyl group. While *P. falciparum* lacks a homologous catalase-peroxidase enzyme to activate isoniazid, we crystallized the PfENR:INH complex to enable us to characterize the analogous interactions in the

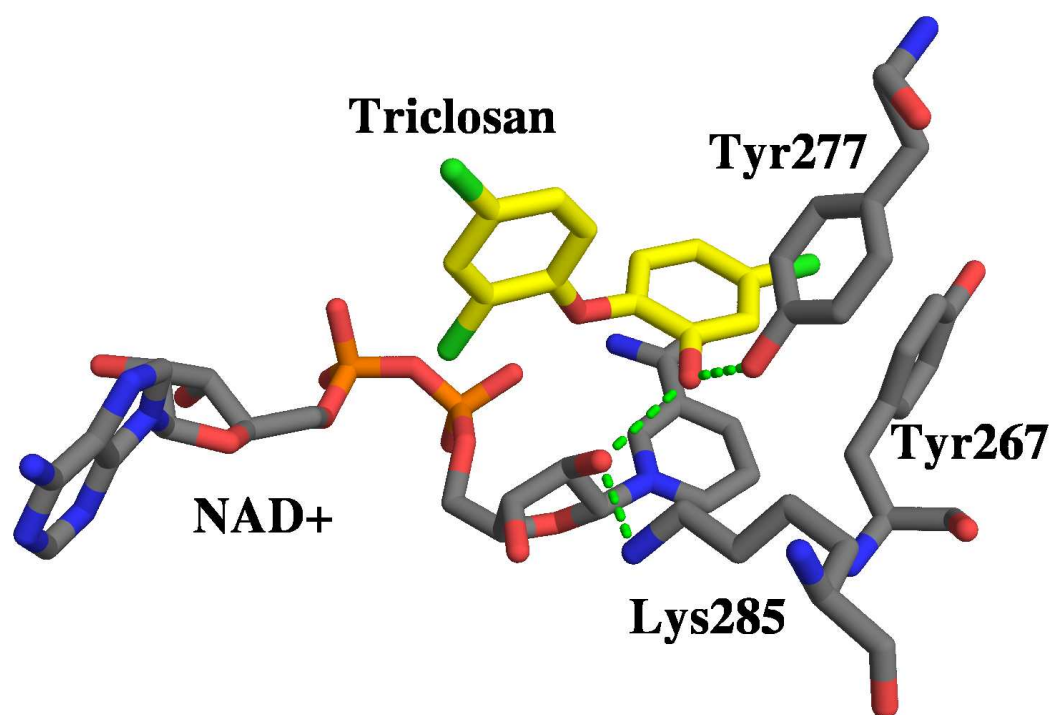


Figure 8: Structural details of the triclosan binding site. Close-up view of the PfENR active site. The hydroxyl-substituted ring of triclosan forms aromatic ring-stacking interactions with the nicotinamide moiety of the NAD⁺ co-factor. Triclosan also forms a conserved hydrogen-bonding network with Tyr²⁷⁷ and the 2'-ribose of the NAD⁺ co-factor. Lys²⁸⁵ serves to position NAD⁺ within the binding site.

malarial enoyl-ACP reductase. The structure of PfENR:INH showed the isonicotinyl group protruding into a hydrophobic cavity bordered by the residues Phe³⁶⁸, Ser³¹¹, Ala³¹², Gly³¹³, Pro³¹⁴, Ala³⁷², Ser³⁷⁶, and Asp⁴¹⁴ (Figure 9), in a manner similar to that of InhA:INH. Isoniazid also formed an additional aromatic ring stacking interaction with Tyr²⁶⁷ of PfENR (Figure 10) as expected, and we chose to leverage this knowledge to inspire new triclosan derivatives.

The Triclosan Analogs B13 and B24

Recently, the antibacterial activities of several 2-hydroxydiphenylethers as well as hexachlorophene and 2-hydroxy-diphenylmethanes were determined (Ward *et al.*, 1999) against the FAS-II enoyl-ACP reductase from *E. coli*. Studies with a *des*-hydroxyl analog of triclosan showed a more than 10,000-fold reduced affinity for *E. coli* FabI and implicated a critical antibacterial role for the triclosan hydroxy group (Ward *et al.*, 1999). Moreover, it was proposed that the ether oxygen of triclosan might be critical to the formation of the ternary complex, because corresponding 2-hydroxy-diphenylmethanes did not result in tight binding (Heath *et al.*, 2000b), while the replacement of the ether oxygen with sulfur abolished the inhibitory activity (Heath *et al.*, 1998). Ring B of triclosan was considered to be of lesser importance, because variations in this region had less effect on inhibitor activity. Synthesis of 20 triclosan analogs followed by screening against purified PfENR revealed that PfENR inhibition was sensitive to the hydroxyl group at the 1-position in ring A, which could not be replaced with methoxy groups or sulfur derivatives, as observed for the bacterial ENRs. These studies led us to identify a diphenylamine derivative (B13, Figure 11) with moderate inhibitory activity (K_i 14.3 \pm 1.4 μ M) against PfENR. This inhibitor, which carried nitrogen as a bridging atom, adopted a very similar conformation compared with triclosan (2,4-dichloroaniline ring) (Figure 12).

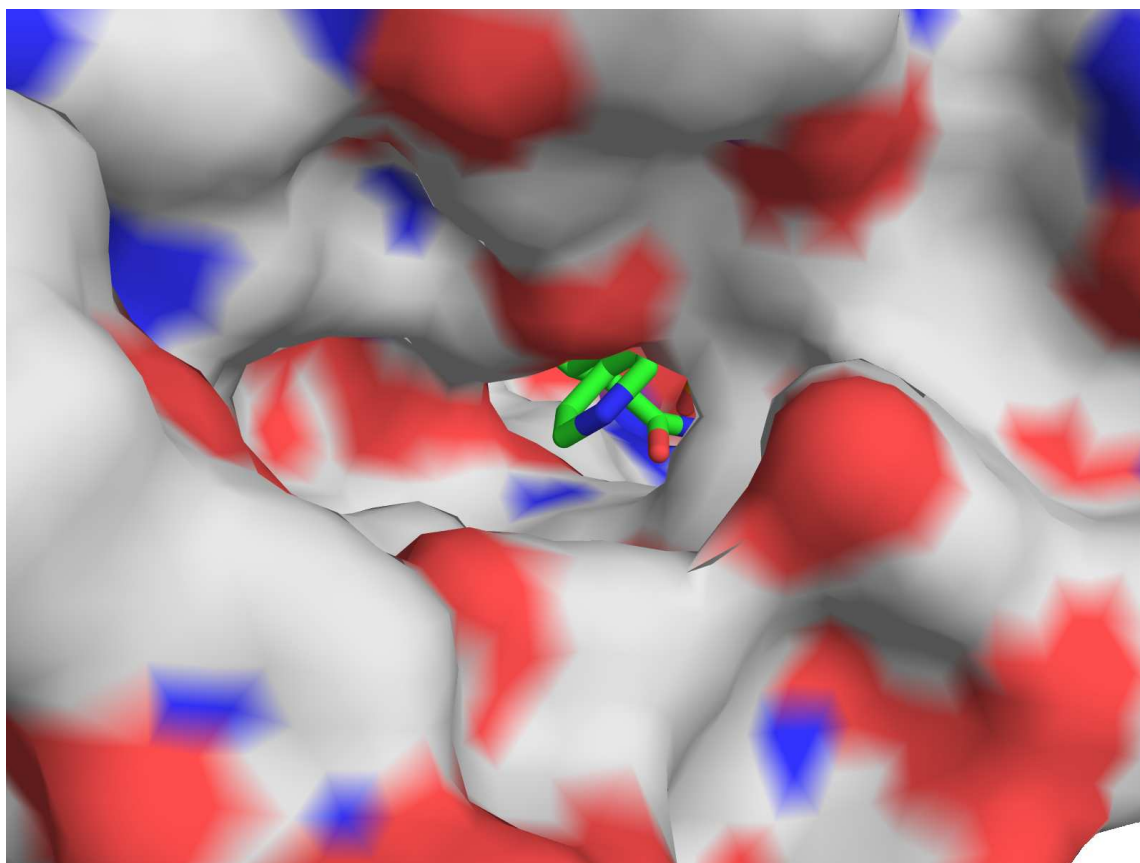


Figure 9: Isoniazid protrudes into a cavity not occupied by triclosan. PfENR is indicated as a molecular surface, colored by electrostatic potential. The just-visible isoniazid moiety (colored with green carbons) is covalently attached to the NADH co-factor, and the isonicotinyl group protrudes into an open cavity not typically occupied by substrate or triclosan. The residues Phe³⁶⁸, Ser³¹¹, Ala³¹², Gly³¹³, Pro³¹⁴, Ala³⁷², Ser³⁷⁶, and Asp⁴¹⁴ serve as the border of the hydrophobic cavity.

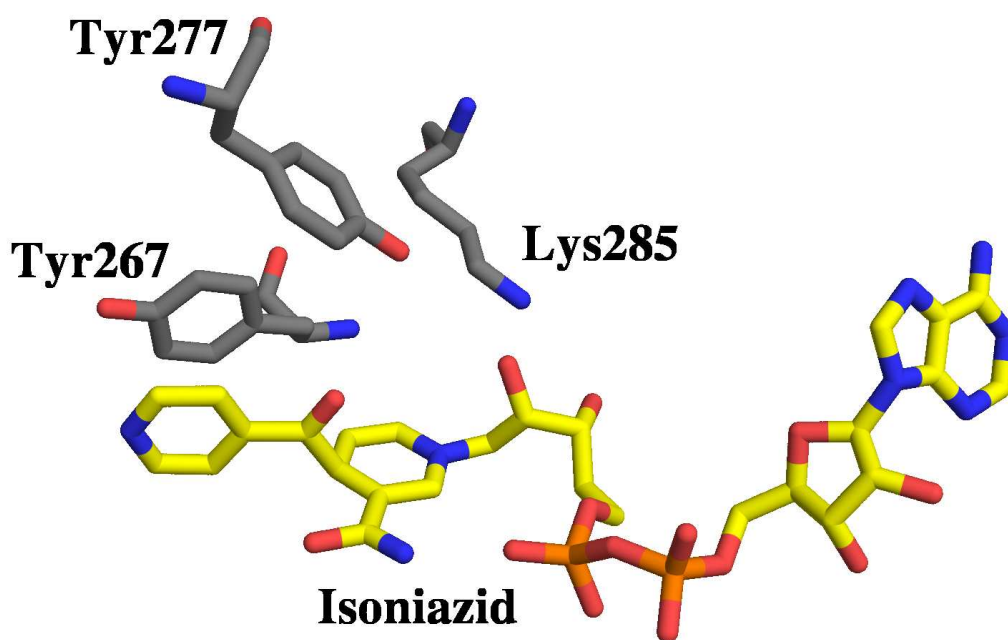


Figure 10: Isoniazid ring-stacks with Tyr²⁶⁷ in PfENR. Isoniazid covalently modifies NADH to create an INH-NADH adduct, and forms aromatic ring-stacking interactions with Tyr²⁶⁷, and binds to the active site in an area separate from that typically occupied by triclosan or substrate. Tyr²⁷⁷ does not form hydrogen bonds with isoniazid, while Lys²⁸⁵ maintains its conserved interaction with the NADH co-factor.

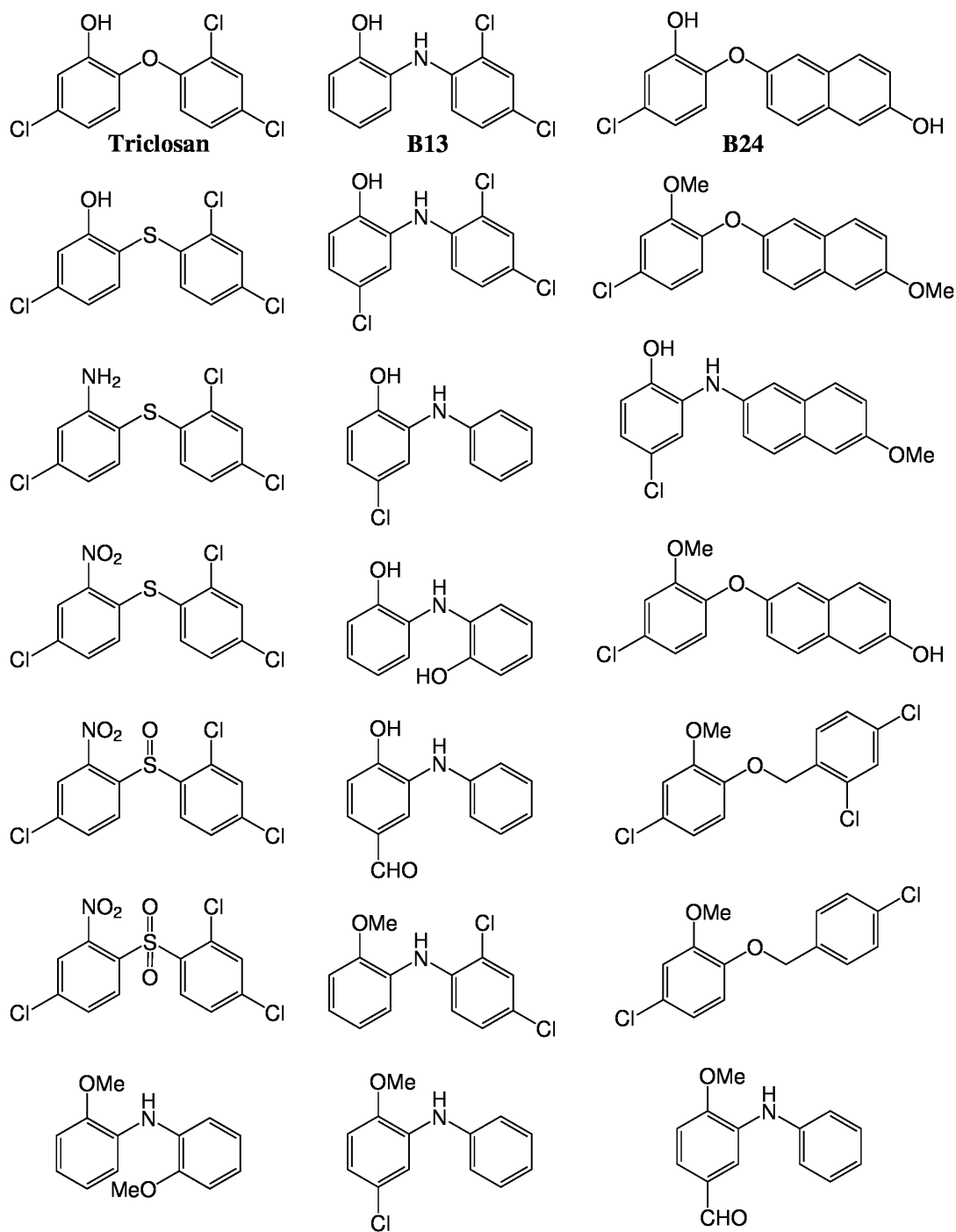


Figure 11: Structures of triclosan derivatives tested for inhibitory activity. Biochemical activity assays were performed using purified recombinant PfENR. Out of the presented compounds, only triclosan, B13, and B24, showed significant biochemical inhibition (cut-off 100 μM) of purified PfENR.

The extensive hydrogen bonding network involving the 1-hydroxy group of ring A and the π - π stacking interaction with the nicotinamide ring system were completely maintained, emphasizing the importance of these interactions. An analog designed through molecular modeling studies, B24, was found to have a K_i of 150 ± 14 nM against purified PfENR, close to the 50 ± 6 nM K_i observed with triclosan. Structural analysis of this 6-hydroxy naphthalene derivative complexed to PfENR in the presence of NAD^+ revealed an electron density that was clearly detectable after the first round of refinement, showing strong and continuous difference density for inhibitor in both monomers of PfENR. Ring A of B24 again stacked to the nicotinamide ring system in the same manner as observed for triclosan. The extended ring B of B24 was oriented in the same direction as the corresponding ring in triclosan but was tilted by 10 degrees out of the plane found for ring B of triclosan and B13. This now allowed for three potential new hydrogen bonds mediated through the hydroxyl group of the naphthalene ring, the side-chain nitrogen of Asn²¹⁸ and the main-chain oxygen and nitrogen of Ala²¹⁹ (Figure 12). Reduced affinity of B24 for PfENR may be a result of the missing chlorine in this analog. Because most bacterial ENRs have a Phe at the position comparable to Asn²¹⁸ of PfENR, it is likely that B24 will be specific for the malarial protein.

Jacobus Pharmaceuticals Triclosan Analogs

To gain greater insight into the structure-activity relationship of the triclosan scaffold, we substituted the atoms at several positions on the triclosan scaffold, on both ring A and ring B. Molecular modeling studies identified two hydrophobic cavities capable of being filled, one where the substrate binds, and one where the isonicotinyl group from the isoniazid-NADH adduct protrudes. There were also several possibilities for aromatic ring-stacking, van der Waals, hydrophobic, and hydrogen-bonding

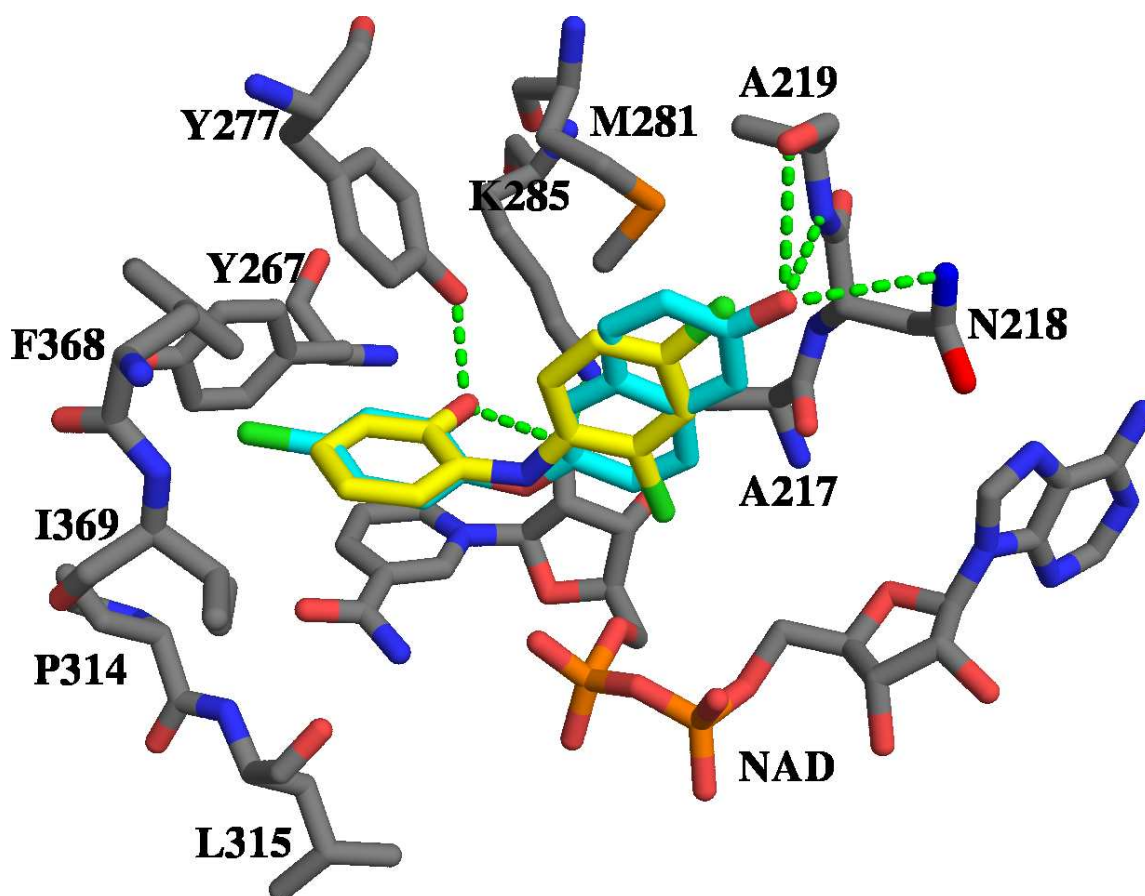


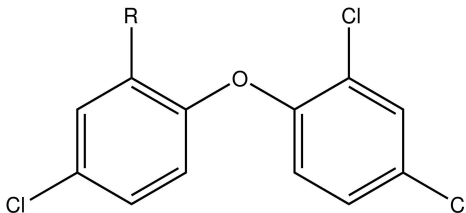
Figure 12: Structures of B13 and B24 bound to PfENR. B13 (yellow carbons) and B24 (cyan carbons) maintained the hydrogen-bonding network observed when tri-closan binds to PfENR. However, the extra length of the naphthol ring of B24 puts the hydroxyl group within hydrogen-bonding distance of the backbone carbonyl and nitrogen of Ala²¹⁹, as well as the side chain of Asn²¹⁸.

interactions distributed throughout the binding cavity. Our intent was to discern which interactions were reasonably available for inhibitor optimization. Several triclosan analogs, with a variety of substituents at the 1, 5, 6, 2', and 4' positions were synthesized for testing in *in vitro* enzyme assay systems. PfENR enzyme assays were conducted in the presence of 50 μM inhibitor as an initial screen, and any candidates exhibiting at least 50% inhibition were further subjected to IC_{50} determination experiments, to elicit information about the relative potencies of each derivative. Promising inhibitors were selected based on *in vitro* assay results, and then incorporated into co-crystallization experiments.

1-position Inhibitors

The hydroxyl group on ring A of triclosan is a critical interaction, forming a 2.5 Å hydrogen bond to Tyr²⁷⁷ of the enzyme as well as a 2.7 Å hydrogen bond to the NAD⁺ co-factor. This pattern of hydrogen bonding, along with a hydrogen bond from Lys²⁸⁵ to the 2'-hydroxyl of the NAD⁺ co-factor, is conserved in most structures of enoyl-reductases, with the exception of inhibitors that covalently modify the co-factor such as diazaborines (Baldock *et al.*, 1996) and isoniazid (Rozwarski *et al.*, 1998). While triclosan is an extremely potent inhibitor *in vitro*, the A-ring hydroxyl group of triclosan is rapidly glucuronidated or sulfonated in live animal studies with rats, rendering it ineffective. Triclosan is then quickly excreted as glucuroconjugates. Our strategy was to remove or replace the hydroxyl group at the 1-position with a functional group that would not be subject to *in vivo* modification, while maintaining inhibitor potency. Dozens of 1-substituted triclosan derivatives were synthesized and assayed for potency at 50 μM inhibitor concentration, using the percent inhibition to gauge the relative effectiveness of each substitution. IC_{50} values were determined only if the initial assays showed a moderate degree of inhibition.

Table 2: Effects of substitution at the 1-position of triclosan



| Compound | R | PfENR IC ₅₀ (μM) |
|----------|-----------------------------------|-----------------------------|
| JPC-2642 | OMe | >50 |
| JPC-2548 | CF ₃ | >50 |
| JPC-1093 | OCO ₂ H | >50 |
| JPC-2063 | NH ₂ | >50 |
| JPC-2064 | NO ₂ | >50 |
| JPC-2025 | OCH ₂ CN | >50 |
| JPC-2070 | NHSO ₂ CH ₃ | >50 |
| JPC-2078 | NHSO ₂ Ph | >50 |
| JPC-2068 | NHC(O)CH ₃ | >50 |
| JPC-2082 | NHC(O)Ph | >50 |

Substitution of the hydroxyl group at the 1-position with any other group resulted in a dramatic loss of inhibitor potency in the *in vitro* PfENR enzyme activity assays. Table 2 shows a selection of triclosan analogs synthesized and screened against PfENR. Regardless of the nature of the substitution, the triclosan analogs had no significant inhibitory effect on the activity of the enzyme, implying that substitutions at the 1-position were not tolerated. Structurally, modifications at this position would disrupt the hydrogen bonding interaction of triclosan with the catalytically important residue Tyr²⁷⁷ in the active site of the enzyme, as well as hydrogen bonding interactions to the NAD⁺ co-factor. Modeling studies with a sample of these inhibitors revealed that in order to accommodate 1-position substituted inhibitors, the catalytic residues in PfENR could not adopt a conformation normally seen when enoyl-ACP reductases are bound to substrates. Due to the low efficacy of these 1-position modified triclosan analogs, co-crystallization of PfENR with these inhibitors

was unsuccessful.

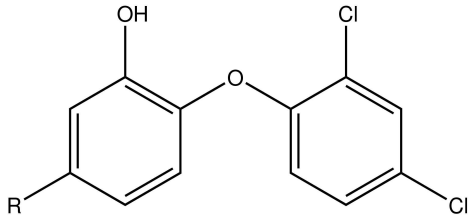
5-position Inhibitors

5-position inhibitors (Tables 3, 4, and 5) were pursued due to knowledge we transferred from the structure of the FAS-II enoyl-ACP reductase from *M. tuberculosis* InhA complexed with isoniazid, as well as the structure of PfENR:INH. The isoniazid moiety of the INH:NADH adduct projected into a hydrophobic cavity separate from the area that triclosan or substrate would occupy, and formed an additional ring stacking interaction with Tyr²⁶⁷ of PfENR. We chose to create a triclosan derivative to utilize this additional pocket and attempt to engineer an isoniazid:triclosan chimera taking advantage of these favorable interactions with various substitutions at the 5-position of triclosan. If a significant gain in potency could be achieved at the 5-position, then the removal or replacement of the A-ring phenol could be facilitated.

Enzymatic assays confirmed the feasibility of this guided design process. We surmised that effective substitutions here could possibly lead to greater affinity of the inhibitor for PfENR and subsequently more potent inhibition, just as in *M. tuberculosis* InhA. The initial results of the 5-position inhibitor screens indicated that increasing lengths of carbon chains were acceptable, while some aromatic rings vectoring off the 5-position were also tolerated. A preference for hydrophobic atoms was also notable. Modeling studies showed that the carbon chain allowed protrusion into a small cavity bordered by Phe³⁶⁸, Ser³¹¹, Ala³¹², Gly³¹³, Pro³¹⁴, Ala³⁷², Ser³⁷⁶, and Asp⁴¹⁴. Determination of the structure of PfENR in complex with JPC-2305 was pursued to test these suppositions.

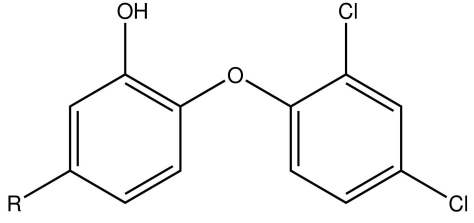
Table 3 shows the biological activity of a range of differentially substituted 5-position analogs. Clearly, hydrophobic groups such as methyl (JPC-2131) and phenyl (JPC-2589) were preferred in the enzyme assays. JPC-2131 ($IC_{50} = 200 \pm 60$ nM)

Table 3: Inhibitory effects of 5-substituted derivatives



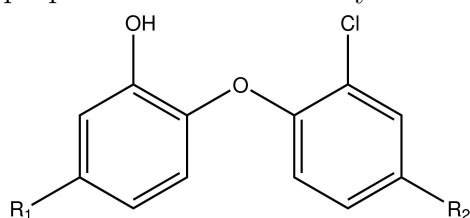
| Compound | R | PfENR IC ₅₀ (nM) |
|-----------|---------------------|-----------------------------|
| Triclosan | Cl | 73 ± 20 |
| JPC-2131 | CH ₃ | 200 ± 60 |
| JPC-2589 | Ph | 140 ± 40 |
| JPC-2590 | CN | 940 ± 100 |
| JPC-2285 | 2H-tetrazol-5-yl | >50,000 |
| JPC-2287 | C(O)NH ₂ | 21,000 ± 9,000 |
| JPC-2286 | COOH | >50,000 |

Table 4: Inhibitory effects of selected 5-alkyl derivatives



| Compound | R | PfENR IC ₅₀ (nM) |
|-----------|---|-----------------------------|
| Triclosan | Cl | 73 ± 20 |
| JPC-2131 | CH ₃ | 200 ± 60 |
| JPC-2573 | CH ₂ CH ₃ | 110 ± 30 |
| JPC-2572 | (CH ₂) ₂ CH ₃ | 210 ± 60 |
| JPC-2571 | (CH ₂) ₃ CH ₃ | 480 ± 80 |
| JPC-2489 | CH ₂ CH(CH ₃) ₂ | 180 ± 80 |
| JPC-2591 | CH ₂ CH(CH ₃)CH ₂ CH ₃ | 290 ± 20 |
| JPC-2590 | (CH ₂) ₂ CH(CH ₃) ₂ | 120 ± 50 |

Table 5: Inhibitory properties of selected 5-aryl and heteroaryl derivatives



| Compound | R ₁ | R ₂ | PfENR IC ₅₀ (nM) |
|----------|------------------------------------|----------------|-----------------------------|
| JPC-2589 | Ph | Cl | 140 ± 40 |
| JPC-2305 | <i>o</i> -CH ₃ -Ph | Cl | 440 ± 100 |
| JPC-2551 | <i>o</i> -CH ₃ -Ph | CN | 410 ± 100 |
| JPC-2279 | <i>m</i> -CH ₃ -Ph | Cl | 230 ± 70 |
| JPC-2264 | <i>p</i> -F-Ph | Cl | 27 ± 8 |
| JPC-2472 | CH ₂ Ph | H | 78 ± 20 |
| JPC-2448 | (CH ₂) ₂ Ph | Cl | 87 ± 10 |
| JPC-2592 | (CH ₂) ₃ Ph | Cl | 660 ± 90 |
| JPC-2530 | 2-pyridyl | CN | 720 ± 70 |
| JPC-2491 | 3-pyridyl | Cl | 33,000 ± 5,000 |
| JPC-2522 | 4-pyridyl | CN | 3,600 ± 2,000 |
| JPC-2492 | CH ₂ (2-pyridyl) | Cl | 640 ± 100 |
| JPC-2501 | CH ₂ (3-pyridyl) | Cl | 840 ± 300 |
| JPC-2575 | CH ₂ (4-pyridyl) | CN | 530 ± 100 |

and phenyl JPC-2589 ($IC_{50} = 140 \pm 40$ nM) were approximately as potent against the enzyme when compared to triclosan ($IC_{50} = 73 \pm 20$ nM). Analogs with polar functionality such as carboxylic acid (JPC-2286, $IC_{50} > 50,000$ nM), carboxamide (JPC-2287, $IC_{50} = 21,000 \pm 9,000$ nM), and tetrazole (JPC-2285, $IC_{50} > 50,000$ nM) were much less efficacious. These observations are consistent with the view of the 5-position binding pocket derived from the x-ray crystal structure of triclosan bound to the PfENR:NAD⁺ complex. Analogs JPC-2131 and JPC-2589 were deemed reasonable origins from which to initiate medicinal chemistry efforts.

Various alkyl-substituted triclosan derivatives are shown in Table 4. It is interesting to note that the introduction of a cyclic constraint did not significantly improve potency in the enzyme assays. While some inhibitors improved on the enzymatic potency of JPC-2131, none of these alkyl analogs were more potent against the enzyme than triclosan with no clear trend being discernible to the best of our abilities.

Derivatives of JPC-2589 are shown in Table 5. Placement of a methyl group around the phenyl ring of JPC-2589 had a detrimental effect on the enzyme activity. Substitution of 2-, 3-, and 4-pyridine for the 5-phenyl moiety in JPC-2589 led to a decrease in activity in the *in vitro* enzyme assays. Noticeably, 3-pyridyl analog is the least active of the trio. The benzyl and phenethyl derivatives were slightly more potent against PfENR than phenyl JPC-2131, whereas phenylpropyl was much less active.

The results of our exploration of the 5-position SAR and, in particular the data presented in Table 5, are complemented by an x-ray crystal structure of *o*-tolyl derivative JPC-2305 bound to the PfENR:NAD⁺ complex (Figure 13). Comparison of the structure to that of triclosan bound clearly shows that the 5-*o*-tolyl better fills the enzyme hydrophobic pocket into which triclosan's 5-chloro group projects. An increase in surface area of interaction of approximately 50 \AA^2 between JPC-2305

and the enzyme active site results, compared to the binding of triclosan. The *o*-tolyl group has enhanced van der Waals interactions with Pro³¹⁴ and Phe³⁶⁸. Phe³⁶⁸ has rotated approximately 60° from its conformation in the triclosan structure to engage in an edge-to-face interaction with the *o*-tolyl moiety. Tyr²⁶⁷ is now engaged in a face-to-face interaction with the *o*-tolyl group and has been pushed away from C6 of the triclosan A-ring by approximately 0.5 Å. JPC-2305 also is engaged in van der Waals interactions with Ile³²³ and Ala³⁷² due to the *o*-tolyl moiety; the chloro group of triclosan is incapable of making these interactions.

6-position Inhibitors

The rationale behind developing 6-position inhibitors (Table 6) was an indirect measure to undermine the enzyme-catalyzed glucuronidation or sulfonation of the 1-position of triclosan. We surmised that placing a bulky substituent at the 6-position could conceivably occlude the hydroxyl group from being modified, due to steric clashing with the modifying enzymes. While molecular modeling studies predicted that modifications at the 6-position would cause steric interference with the catalytic residue Tyr²⁷⁷ as well as other active site residues, this was surprisingly tolerated, albeit with a slight loss of potency. Several inhibitors were tested in our *in vitro* enzyme assay system, as shown in Table 6. Conservative and small substitutions, such as JPC-2626 and JPC-2635, slightly diminished inhibitor potency. The addition of a carbonyl group at the 6-position decreased inhibitor effectiveness further, but replacement of methylene recovered much of the potency. This implies that a degree of flexibility is important at this position. JPC-2624, with a benzyl group projecting off the 6-position, yielded the best results. Possibly a ring-stacking interaction, perhaps with Phe³⁶⁸ or Tyr²⁶⁷ in the vicinity, is important in this analog. Another explanation is that JPC-2624 may have an alternative mode of binding,

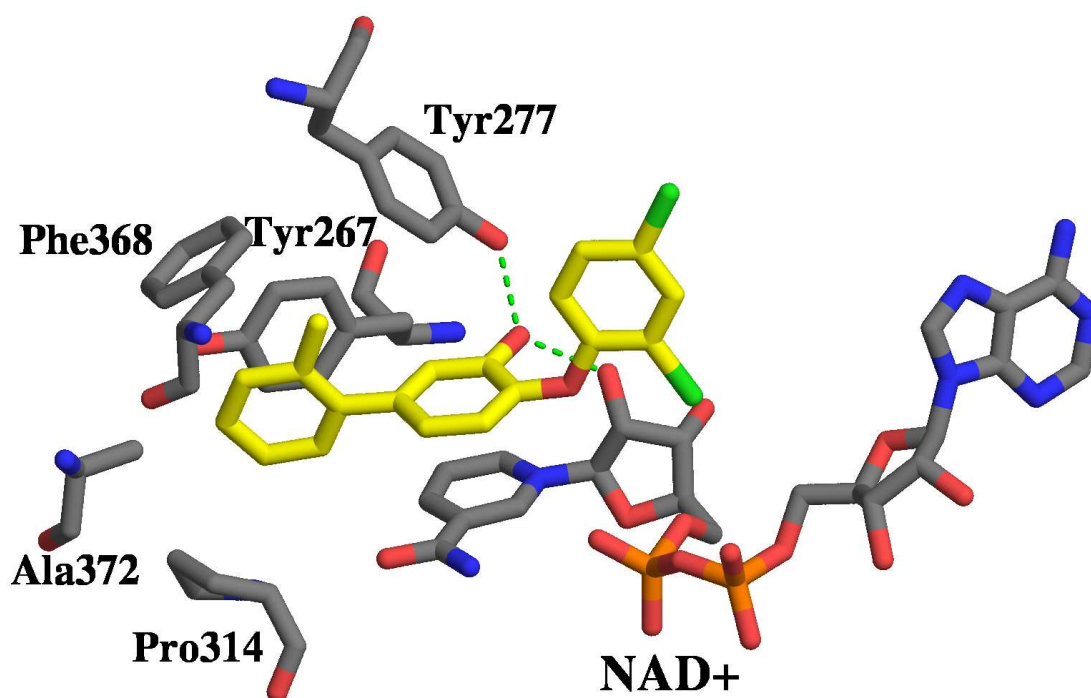


Figure 13: Triclosan derivative JPC-2305 ring stacks with Tyr²⁶⁷ of PfENR. The *o*-tolyl group binds in a portion of the enzyme distinct from triclosan binding. The structure of PfENR:JPC-2305 showed the *o*-tolyl group protruding into a small hydrophobic cavity bordered by the residues Ile³²³ (not shown), Phe³⁶⁸, Ala³⁷², Pro³¹⁴. JPC-2305 ring-stacked with Tyr²⁶⁷ and retained the conserved hydrogen-bonding network seen in other enoyl-ACP reductases bound to triclosan.

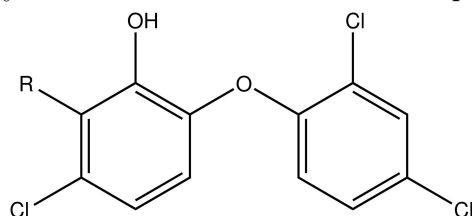
where the 6-position benzyl ring occupies the position where either the A or B ring of triclosan typically binds. X-ray structural studies are necessary to unambiguously determine the mode of binding. While none of the analogs had activity comparable to triclosan, occluding the 1-position by modifying the 6-position may be a feasible technique to prevent the host from forming glucuroconjugates that are summarily excreted before they can act against the malarial parasite. While the potency of 6-position substitutions did not increase, this detriment could be overcome by optimization of the B ring to the PfENR binding cavity, and these were subsequently analyzed. Substitutions at the A ring that decrease inhibitor potency could conceivably be compensated for with modifications of the B ring.

2'-position Inhibitors

The B ring of triclosan was also modified at two positions (Freundlich *et al.*, 2006). Several possible hydrogen bonding interactions were also apparent in this area of the binding cavity. Examination of the PfENR:NAD⁺:triclosan ternary structure revealed that the 2'-chloro group projected towards the pyrophosphate portion of NAD⁺ and was approximately 4 Å away from two of the negatively charged oxygens. We proposed that a properly placed positively charged amine off the 2'-position could favorably interact with one or both of these oxygens. In addition, a hydrophobic substituent on the amine could participate in favorable interactions with proximal enzyme residues such as Ala³¹⁹ and Arg³¹⁸. 2'-position analogs with these features could have enhanced interactions, both with co-factor and enzyme, thus, conferring greater binding ability for the enzyme:co-factor complex and potentially enhanced parasitic activity.

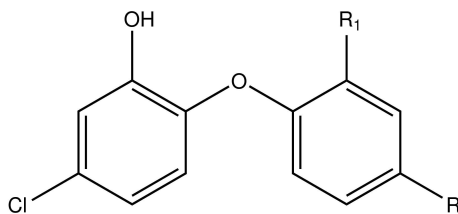
In keeping with our design hypothesis, we examined the effect of placing hydrophobic groups off the amine terminus of JPC-2210 (Figure 7) in order to improve

Table 6: Inhibitory effects of substitution at the 6-position of triclosan



| Compound | R | PfENR IC ₅₀ (μM) |
|----------|--------------------------------------|-----------------------------|
| JPC-2621 | C(O)NH ₂ | 1.6 |
| JPC-2622 | C(O)NHCH ₃ | 2.11 |
| JPC-2623 | C(O)N(CH ₃) ₂ | 2.07 |
| JPC-2640 | C(O)CH ₃ | 2.93 |
| JPC-2651 | C(O)Ph | 2.21 |
| JPC-2625 | COOH | 10.48 |
| JPC-2626 | CH ₃ | 0.195 |
| JPC-2635 | CF ₃ | 0.419 |
| JPC-2639 | Ph | 0.554 |
| JPC-2646 | CH ₂ OH | 0.772 |
| JPC-2624 | CH ₂ Ph | 0.187 |
| JPC-2637 | CH(OH)CH ₃ | 1.83 |
| JPC-2650 | CH(OH)Ph | 2.21 |
| JPC-2643 | 2-Cl-Ph-CH ₂ | 2.93 |
| JPC-2644 | 3-Cl-Ph-CH ₂ | 0.894 |
| JPC-2645 | 4-Cl-Ph-CH ₂ | 1.32 |

Table 7: Inhibitory effects of selected 2'-substituted derivatives



| Compound | R ₁ | R ₂ | PfENR IC ₅₀ (μM) |
|-----------|---------------------------------|----------------|-----------------------------|
| Triclosan | Cl | Cl | 0.073 ± 0.021 |
| JPC-2205 | NH ₂ | H | 7 ± 2 |
| JPC-2210 | CH ₂ NH ₂ | H | >50 |

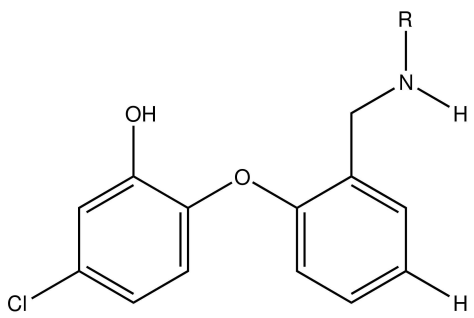
its enzyme and anti-parasitic potencies over that of triclosan. Shown in Tables 7,8, 9, 10, and 11 are the IC₅₀ results of several 2'-substituted triclosan analogs.

Most attempts to substitute the 2'-position were met with greater than 10-fold decreases in binding affinity. The chloro at the 2'-position appears to be already well-suited for the local PfENR binding environment. Attempts to substitute at this position apparently perturbed interactions in the halogen binding pocket enough to turn a nanomolar inhibitor into a micromolar inhibitor. Interestingly, compounds JPC-2311 and JPC-2265 differed by only the addition of a chloro group at the 4'-position, but this resulted in a significant increase in binding affinity (35 μM versus 7.2 μM). This was a minor surprise, considering that a 5-chloro-2-phenoxyphenol analog of triclosan lacking the ring B chlorines bound *E. coli* FabI 7-fold more tightly than triclosan (Sivaraman *et al.*, 2003).

4'-position Inhibitors

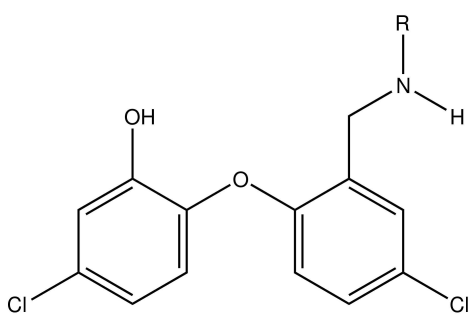
The x-ray crystal structures of aniline JPC-2136, nitro JPC-2137, urea JPC-2153, and methylamide JPC-2166, bound to PfENR in the presence of co-factor, were resolved as expected (Freundlich *et al.*, 2005). The only significant difference in

Table 8: Inhibitory effects of 2'-substituted derivatives with a 4'-hydrogen



| Compound | R | PfENR IC ₅₀ (μ M) |
|----------|---|-----------------------------------|
| JPC-2210 | H | >50 |
| JPC-2239 | CH ₂ Ph | 10 \pm 3 |
| JPC-2309 | CH ₂ (<i>p</i> -ClC ₆ H ₄) | 35 \pm 4 |
| JPC-2240 | (CH ₂) ₃ Ph | 19 \pm 5 |
| JPC-2242 | 1-naphthyl | 11 \pm 4 |
| JPC-2243 | 2-naphthyl | 46 \pm 14 |

Table 9: Inhibitory effects of 2'-substituted derivatives with a 4'-chloride



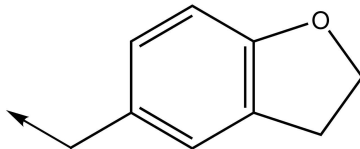
| Compound | R | PfENR IC ₅₀ (μ M) |
|----------|---|-----------------------------------|
| JPC-2613 | CH ₃ | >50 |
| JPC-2549 | C(O)Ph | 18 \pm 8 |
| JPC-2490 | SO ₂ Ph | 15 \pm 7 |
| JPC-2265 | CH ₂ (<i>p</i> -Cl-C ₆ H ₄) | 7.2 \pm 1.4 |
| JPC-2301 | CH ₂ (<i>p</i> -Ph-C ₆ H ₄) | 35 \pm 15 |
| JPC-2302 | 1-naphthyl | >50 |
| JPC-2303 | 2-naphthyl | 26 \pm 7 |
| JPC-2247 |  | 9 \pm 3 |

Table 10: Inhibitory effects of 2'-substituted derivatives: *p*-Cl-benzylamines

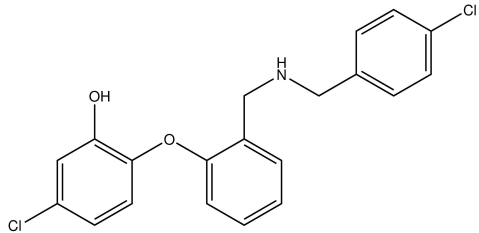
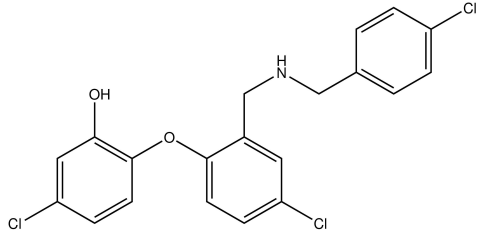
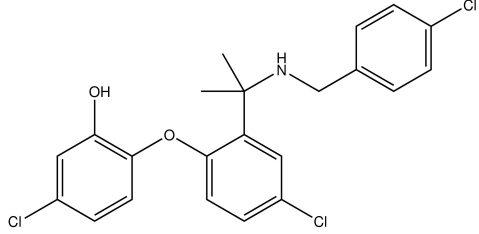
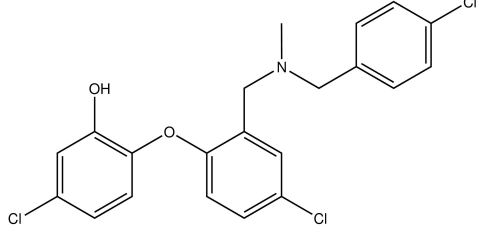
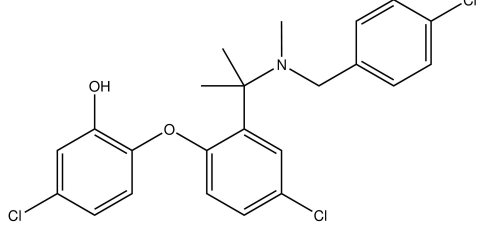
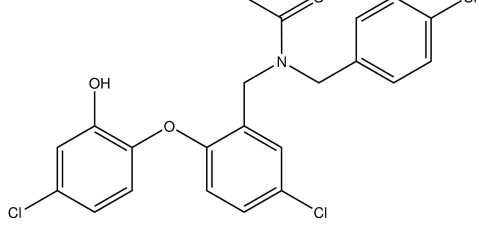
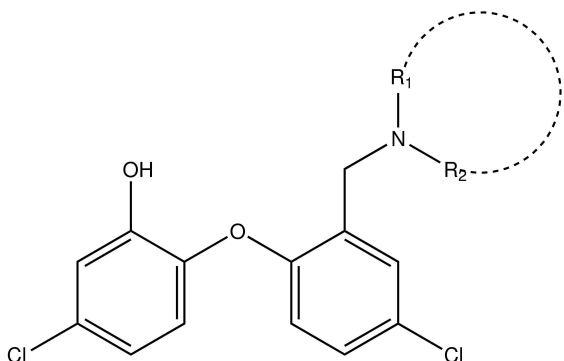
| Compound | Structure | PfENR IC ₅₀ (μM) |
|----------|--|-----------------------------|
| JPC-2311 |  | 35 ± 4 |
| JPC-2265 |  | 7.2 ± 1.4 |
| JPC-2333 |  | 7.2 ± 1.6 |
| JPC-2308 |  | 22 ± 2 |
| JPC-2446 |  | 27 ± 4 |
| JPC-2307 |  | 28 ± 3 |

Table 11: Inhibitory effects of 2'-substituted derivatives: selected amines



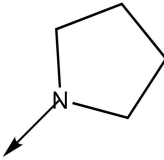
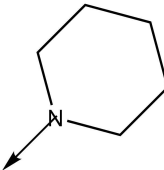
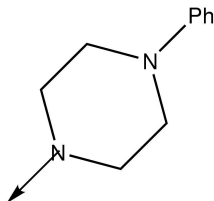
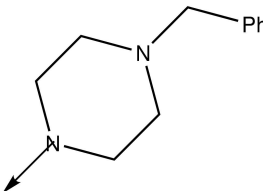
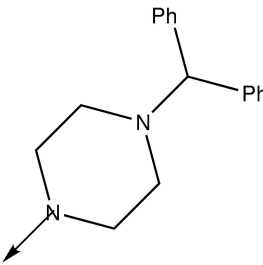
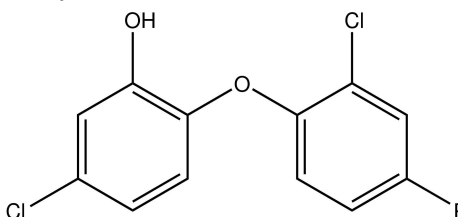
| Compound | NR ₁ R ₂ | PfENR IC ₅₀ (μ M) |
|----------|---|-----------------------------------|
| JPC-2613 | N(H)Me | 27 \pm 9 |
| JPC-2614 | NMe ₂ | 19 \pm 5 |
| JPC-2468 |  | >50 |
| JPC-2469 |  | >50 |
| JPC-2442 |  | 6.1 \pm 1.0 |
| JPC-2444 |  | 11 \pm 2 |
| JPC-2470 |  | >50 |

Table 12: Inhibitory effects of selected 4'-substituted derivatives

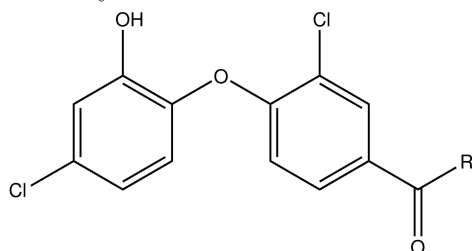


| Compound | R | PfENR IC ₅₀ (nM) |
|-----------|---------------------|-----------------------------|
| triclosan | Cl | 30 |
| JPC-2181 | OH | 177 |
| JPC-2137 | NO ₂ | 201 |
| JPC-2136 | NH ₂ | 189 |
| JPC-2149 | CN | 80 |
| JPC-2283 | CH ₂ CN | 295 |
| JPC-2154 | COOH | 553 |
| JPC-2150 | 1H-tetrazol-5-yl | 1180 |
| JPC-2212 | C(O)NH ₂ | 52 |
| JPC-2211 | C(O)NHOH | 1220 |

all of these structures is the interaction of the 4'-substituent with the surrounding enzyme residues. Other interactions of the triclosan core with co-factor and enzyme were preserved. Displayed in Figure 14, JPC-2136 utilized its aniline hydrogens to form weak hydrogen bonds to the side chain carbonyl of Asn²¹⁸ ($d_{C=O-N} = 3.4 \text{ \AA}$) and the main chain carbonyl of Ala²¹⁹ ($d_{C=O-N} = 3.7 \text{ \AA}$). The aniline nitrogen's lone pair may be engaged in a favorable interaction with the main chain N-H group of Ala²¹⁹ ($d_{N-N} = 2.7 \text{ \AA}$). JPC-2137 binds in a conformation similar to JPC-2136 (Figure 14). The only significant change in the enzyme active site is the rotation of the Asn²¹⁸ side chain to allow its carboxamide N-H to interact with one of the nitro oxygens. The other nitro oxygen forms a hydrogen bond with the main chain N-H group of Ala²¹⁹ ($d_{N-O} = 3.2 \text{ \AA}$).

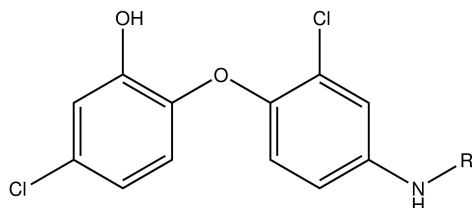
Methylamide derivative JPC-2166 utilized its amide carbonyl to form a hydrogen bond with the side chain N-H of Asn²¹⁸ ($d_{N-O=C} = 3.2 \text{ \AA}$) and the carbonyl may

Table 13: Inhibitory effects of selected 4'-amide derivatives



| Compound | R | PfENR IC ₅₀ (nM) |
|----------|------------------|-----------------------------|
| JPC-2212 | NH ₂ | 52 |
| JPC-2166 | N(H)Me | 435 |
| JPC-2164 | N(H)Bn | 4380 |
| JPC-2167 | NMe ₂ | 401 |
| JPC-2171 | N-pyrrolidine | 309 |
| JPC-2168 | N-piperidine | 537 |
| JPC-2169 | N-morpholine | 187 |

Table 14: Inhibitory effects of selected 4'-aniline derivatives



| Compound | R | PfENR IC ₅₀ (nM) |
|----------|---------------------------------|-----------------------------|
| JPC-2136 | H | 189 |
| JPC-2182 | Ac | 103 |
| JPC-2170 | Bz | 143 |
| JPC-2159 | C(O)NH ₂ | 44 |
| JPC-2153 | C(O)N-morpholine | 909 |
| JPC-2160 | SO ₂ Ph | 550 |
| JPC-2190 | SO ₂ (1-naphthyl) | 665 |
| JPC-2191 | SO ₂ (2-naphthyl) | 4160 |
| JPC-2200 | SO ₂ CF ₃ | 206 |
| JPC-2170 | CH ₂ Ph | 2120 |
| JPC-2192 | CH ₂ (2-CNPh) | 331 |
| JPC-2176 | CH ₂ (2-HOPh) | 299 |

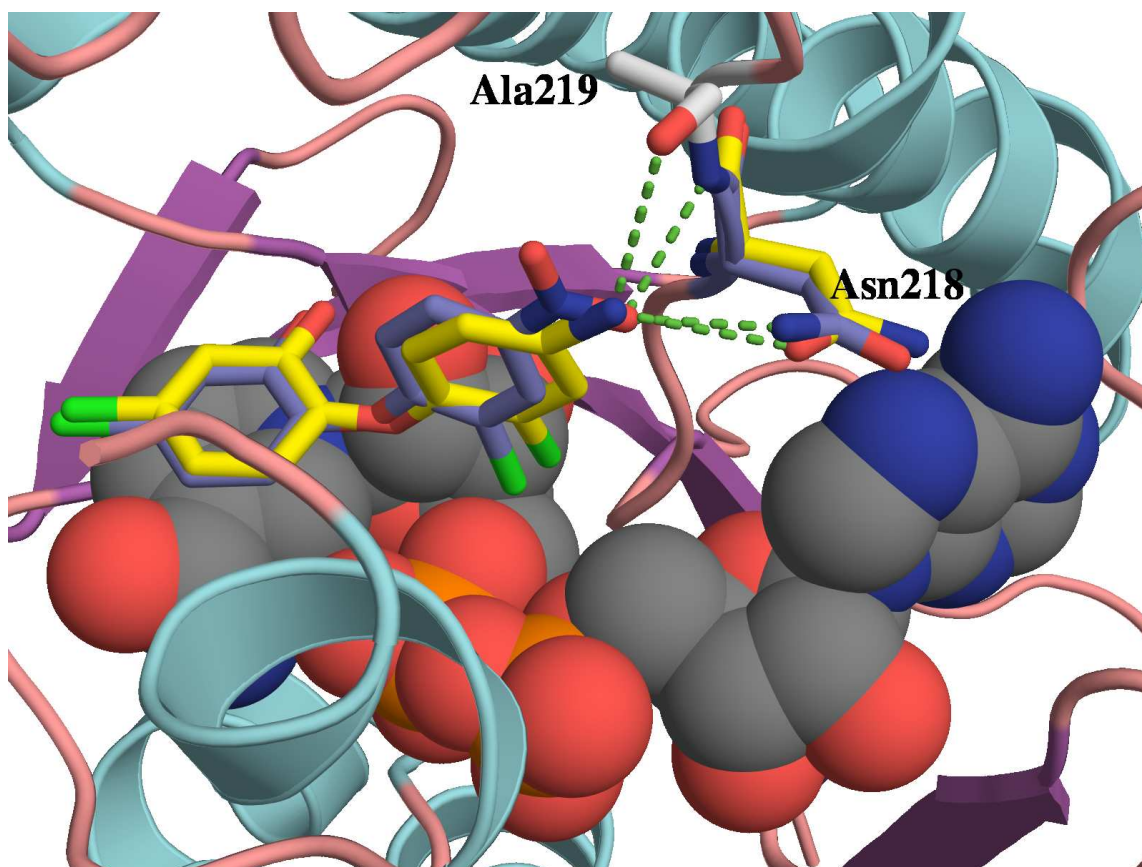


Figure 14: Structural details of the PfENR:4^l-inhibitor binding site. X-ray structure of JPC-2136 (yellow carbons) and JPC-2137 (slate blue carbons) in the PfENR active site (ribbon and tube with key residues in stick format) with bound co-factor (space-fill). The JPC-2137 nitro group makes a hydrogen bond with the side chain N-H of Asn²¹⁸ and it may also be engaged in a weak hydrogen bond with the backbone N-H of Ala²¹⁹.

also make a weak hydrogen bond with the main chain N-H group of Ala²¹⁹ ($d_{N-O=C} = 4.0 \text{ \AA}$). Its *N*-methyl group appears to act favorably with the *i*-propyl side chain of Val²²². Depicted in Figure 15, the urea derivative JPC-2153, in contrast did not have significant interactions between the appended morpholino group and the enzyme, projecting instead towards solvent. The urea carbonyl moiety is hydrogen bonded to the Asn²¹⁸ side chain N-H group ($d_{N-O=C} = 2.8 \text{ \AA}$) and the Ala²¹⁹ main chain N-H ($d_{N-O=C} = 3.0 \text{ \AA}$).

Clearly, the crystal structures of JPC-2136, JPC-2137, JPC-2166, and JPC-2153 demonstrated the ability to append hydrogen-bonding functionality off the 4'-position through interactions with Asn²¹⁸ and Ala²¹⁹. However, from the enzyme data in Tables 12, 13, and 14, it was exceedingly clear that overall losses in binding affinity for the enzyme were realized. The reasons for these decreases in enzyme binding are not clear at this moment. One can speculate that, in the structurally characterized analogs, replacement of the chloro with a more polar group such as anilino, nitro, carboxamido, or ureido may result in the loss of hydrophobic interactions with Val²²² and Met²⁸¹. Subtle rearrangements in the enzyme complex with co-factor and ligand may also be responsible for the observed decreases in ligand affinity. Perhaps the binding pocket is already well optimized for a halogen.

In conclusion, a series of 4'-substituted triclosan derivatives have been prepared and assayed for the inhibition of purified PfENR and cultured *P. falciparum*. While the effort did not result in compounds more potent than triclosan against the enzyme, it did provide an understanding of which groups could be substituted for the 4'-chloro to provide nanomolar inhibitors of PfENR with demonstrated anti-parasitic activity. X-ray crystallographic studies demonstrated the ability of a subset of the prepared compounds to expand upon triclosan's interactions with PfENR via hydrogen-bonding networks with Asn²¹⁸ and Ala²¹⁹. This examination of the

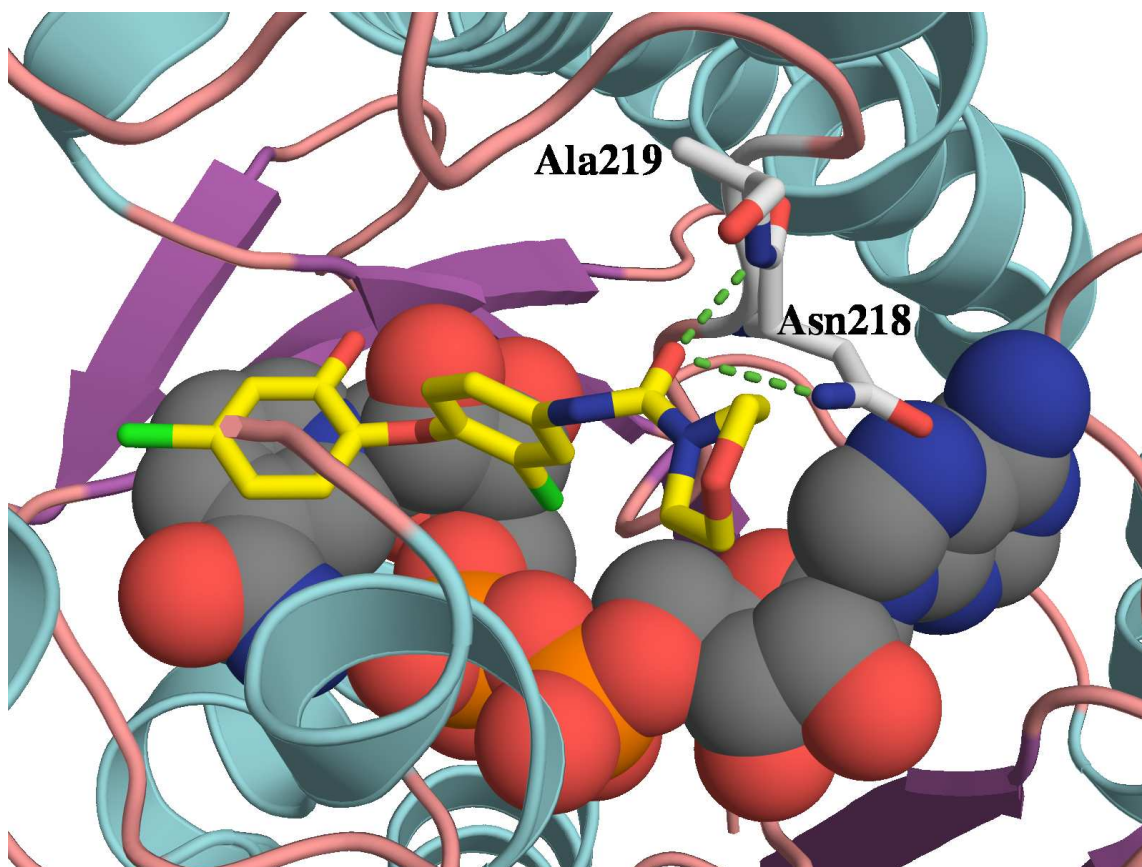


Figure 15: Structural details of the PfENR:JPC-2153 complex. X-ray structure of JPC-2153 in the PfENR active site (ribbon and tube with key residues in stick format) with bound co-factor (space-fill). The urea carbonyl moiety is hydrogen bonded to the Asn²¹⁸ side chain N-H group and the Ala²¹⁹ main chain N-H.

4'-position will aid future efforts guided towards improving the potency and pharmacokinetic profiles of this diarylether class of anti-malarials.

GlaxoSmithKline Compounds

A large scale high throughput screen was initiated with GlaxoSmithKline, using PfENR as the drug-screening target. A class of proprietary inhibitors from their screens were identified as effective, and all of these compounds were confirmed as sub micromolar inhibitors against PfENR. These were built and docked into the active sites of

PfENR with the docking program GOLD Jones *et al.* (1997). SB508982 was one of the initial hits identified from the target-focused screening. The molecular modeling studies carried out with this derivative suggested that this class of compounds could interact by forming a hydrogen bond with Tyr²⁶⁷ at the PfENR active site. In this scaffold, there is a potential hydrogen bonding interaction with Tyr²⁶⁷, a possible hydrogen bond to Tyr²⁷⁷, and a π -stacking interaction between the amide and the nicotinamide portion of NAD⁺. An acrylamide is needed to enforce a planar disposition within the active site, to direct a terminal benzyl ring towards the potential hydrogen bonding interactions with Ala²¹⁹ and Asn²¹⁸.

SB643152, SB628749, and SB618268

The compounds SB643152, SB628749, and SB618268 were based on aminopyridine compounds (Figure 16) first reported as low micromolar inhibitors against *Staphylococcus aureus* and *Haemophilus influenzae* FabI (IC₅₀ = 16.5 and 6.9 μ M, respectively) (Miller *et al.*, 2002). The aminopyridine derivatives appear to have a mode of binding similar to that of triclosan. The linking amides in SB643152, SB628749, and SB618268 are engaged in the same interactions as the phenolic ring of triclosan, namely, π -ring stacking with the nicotinamide of the NAD⁺ co-factor, with the carbonyl oxygen interacting with Tyr²⁷⁷ of PfENR as well as the ribose 2'-hydroxyl from the co-factor. In the x-ray crystal structure, the phenol subunit of triclosan appears to function as a transition state enolate mimetic, taking the place of the enolate that results from hydride delivery from the cofactor to the β - position of the natural substrate, crotonoyl-ACP.

Previous studies from Miller *et al.* implied that the indole position was the minimal pharmacokinetic moiety necessary for inhibition. Therefore, modifications to the rest of the moiety were considered for synthesis. The idea was to maximize

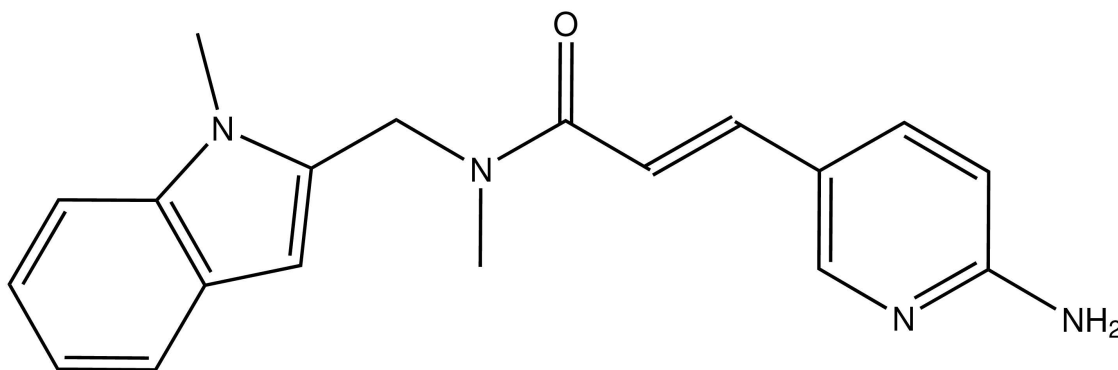


Figure 16: Chemical structure of the GSK aminopyridine lead compound. This GlaxoSmithKline aminopyridine compound was identified in high throughput screens against the enoyl-ACP reductases for *Staphylococcus aureus* and *Haemophilus influenzae*. Derivatives of this backbone were synthesized using the active site of PfENR to guide design of the inhibitors.

interactions with the phosphate oxygens on NAD^+ , however, this was not the result. Instead, the compounds make additional hydrogen bonding interactions with the backbone of PfENR.

GSK508982, GSK585309, GSK626808, and GSK626814

The proprietary GlaxoSmithKline compounds GSK508982, GSK585309, GSK626808, and GSK626814 (structures not shown) were based upon a similar aminopyridine backbone, with minor substitutions in the terminal benzyl ring. Several of these inhibitors were soaked into PfENR:NADH binary crystals, and after 14 days of incubation, data was collected. The structure of PfENR:NAD⁺:GSK585309 diffracted the best of all the inhibitors, to a maximum resolution of 2.2 Å. This data set was well refined with a maximum resolution of 2.2 Å and good statistics. The central amide in the inhibitor is within hydrogen bonding distance of the catalytic residue Tyr²⁷⁷ (2.7 Å) and the 2'-hydroxyl group of the NAD⁺co-factor (2.8 Å). The terminal aniline of the inhibitor may participate in weak hydrogen bonding interactions with

the backbone carbonyl of Ala²¹⁹, with a distance of 3.0 Å. On the opposite end of the inhibitor, the chloro-phenoxy ring protrudes into a hydrophobic pocket flanked by Phe³⁶⁸, Ala³⁷², Val²⁷⁴, and Pro³¹⁴. The oxygen between the benzyl and piperidine rings does not appear to interact with Tyr²⁶⁷, approaching within a distance of 4.1 Å at its closest point. As the only substitutions occurred in the terminal benzyl ring that projects towards the exterior of the enzyme, the other GSK inhibitors did not exhibit significant deviation of position within the active site of PfENR.

High Throughput Screens

In parallel with experiments centered around derivatives of the triclosan scaffold, high throughput screens were initiated to identify lead compounds with broader chemical diversity. The experiments incorporated both *in vitro* high throughput screening assays as well as virtual screening techniques directed against PfENR.

In vitro Enzyme Assays

High throughput screening of a 50,000 compound library (ChemDiv) from Chemical Diversity Labs was undertaken at Southern Research Institute. The 50,000 compounds within the library were screened at 10 μ M inhibitor concentration, and of these, 350 selected based on several criteria. First of all, due to several anomalies over the course of the screen, we filtered the initial results by selecting only those compounds that inhibited PfENR greater than 20% and had χ^2 values of 0.99 or greater. This step was added to ensure that any potential hits stemmed from actual measurement of initial velocity, instead of unusual occurrences or fluctuations in the wells during absorbance readings. This resulted in a subset of approximately 1,000 compounds meeting both criteria. From the 1,000 compounds that passed this step of filtering, the top 350 compounds were selected and purchased, based on greatest

enzyme inhibition and adherence to Lipinski rules. The Lipinski rules or “the rule of 5” predicts that poor absorption or permeation is more likely when there are more than 5 hydrogen-bond donors, 10 hydrogen-bond acceptors, the molecular weight is greater than 500, and the calculated Log P (ClogP, a measure of solubility) is greater than 5. If the compound violated two or more of these rules, the compound was not included in this final set. This resulted in a set of 300 compounds being purchased, possessing enzyme inhibition of between 46-100% at 10 μ M. Of this pared down set, 55 were randomly selected and screened in *in vitro* enzyme assays at 10 μ M to confirm the results of the initial high throughput screen. The HTS screen performed at Southern Research Institute and the *in vitro* screen performed at Texas A&M gave considerably different results for the same compounds, as summarized in Table 15 . The distribution was also noticeably in disagreement, with the HTS conducted at Southern Research Institute yielding much more potent inhibitors, with all 55 compounds tested inhibiting between 40-100%. Only 7 of the 55 compounds were within this range in the *in vitro* enzyme assays performed at Texas A&M. There was not a discernible pattern to normalize one assay to another. Several problems were noted during the execution of these assays. First, the ChemDiv compounds were not all completely soluble in the HTS plates, leading to fluctuating and erroneous readings from the inhibitor suspension remaining in the well. Second, the crotonoyl-CoA substrate originated from two different sources, leaving open the possibility that early runs would not be comparable to later runs. Third, equipment problems were identified that resulted in an incorrect amount of dispensed enzyme, as well as technical glitches with the armature used to automatically change plates. Fourth, the triclosan controls were manually added, and it was evident that there were inaccuracies here because the percent inhibition varied substantially from plate to plate. Finally, the technical problems caused the high-throughput screen to be drawn out over a period

of seven months, and there is no guarantee that the enzyme provided during this time had equivalent activity.

MolSoft-ICM Virtual Screening

Molsoft-ICM docking software was utilized to search and score 336,000 compounds from Chembridge. From 336,000 compounds, the program selected the top 750 docked compounds. These top 750 scoring compounds were submitted for absorption, distribution, metabolism, and excretion (ADME) prediction by preADME (<http://preadme.bmdrc.org/preadme>), and two measures indicating cell permeability, Caco-2 and MDCK, were considered for further filtering of results. This program can predict permeability for Caco-2 cell (measures the net flux of a compound over a cellular barrier), MDCK cell and BBB (blood-brain barrier), HIA (human intestinal absorption), skin permeability, and plasma protein binding. The model for predicting Caco-2 is based on more data points, and is reportedly more accurate than MDCK. Selecting for compounds with high Caco-2 scores (>7) yielded a list of 260 compounds. Further screening of that list for compounds with high MDCK scores (>50) yielded a list of 169 compounds. These 169 compounds were ordered from ChemBridge, and a subset of 88 compounds were randomly selected and screened at 10 μM of inhibitor in PfENR *in vitro* enzyme assays. These 88 compounds weakly inhibited PfENR, with only 4 compounds decreasing enzyme activity by over 10%.

Because of these lackluster results at 10 μM inhibitor, a more comprehensive screen was performed. These initial screens were repeated one time at 50 μM of inhibitor with the entire set of 169 compounds. 95 of these compounds inhibited PfENR activity 10% or less, 31 compounds inhibited PfENR between 10-20%, 14 compounds inhibited PfENR between 20-30%, 11 compounds between 30-40%, 2 compounds between 40-50%, and 8 compounds between 50-60%. The remaining 6

Table 15: Selected Chemical Diversity compounds, assay comparison

| ChemDiv ID | SRI % Inhibition | TAMU % Inhibition |
|------------|------------------|-------------------|
| 2534-6551 | 100 | -15 |
| 0272-0165 | 100 | -4 |
| 3448-6741 | 100 | 0.8 |
| 4593-2742 | 100 | 1.8 |
| 4424-0922 | 100 | 3.3 |
| 3578-0866 | 100 | 4.6 |
| 3330-2686 | 100 | 5.3 |
| 2534-6536 | 100 | 9.0 |
| 3330-2700 | 100 | 11.0 |
| 4424-0668 | 100 | 26.0 |
| 4341-0545 | 100 | 30.4 |
| 3572-6013 | 100 | 34.0 |
| 1694-0068 | 100 | 84.2 |
| 4490-0017 | 85.7 | 15.4 |
| 2028-0074 | 73.0 | 78.1 |
| 4297-0723 | 71.3 | 33.3 |
| 4413-0020 | 68.6 | -8.0 |
| 0488-0124 | 67.2 | -4.1 |
| K889-0658 | 66.3 | -0.2 |
| 3699-1233 | 64.6 | 27.9 |
| 3336-0955 | 64.0 | 11.5 |
| 4393-0144 | 63.9 | -1.0 |
| K205-1682 | 63.4 | 10.0 |
| 1180-0297 | 63.2 | 21.5 |
| 4249-0088 | 60.2 | 3.0 |
| 4491-0983 | 59.5 | -3.4 |
| 4300-0119 | 58.8 | 35.5 |
| 3232-0432 | 57.4 | -2.0 |
| 3132-0181 | 57.2 | 1.3 |

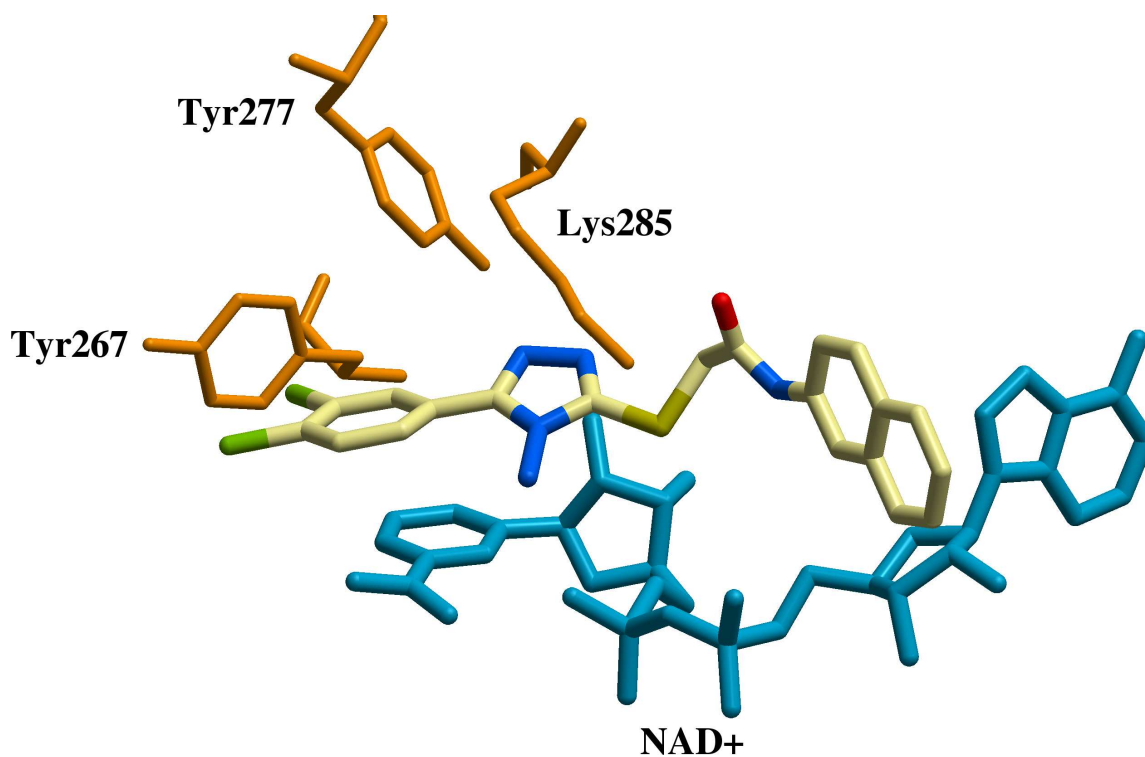
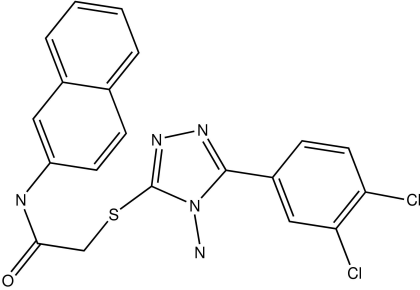
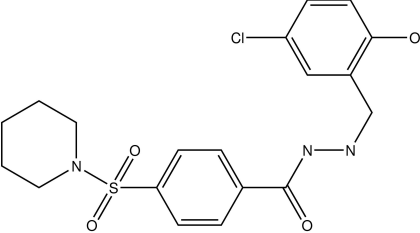
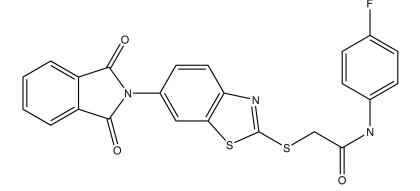
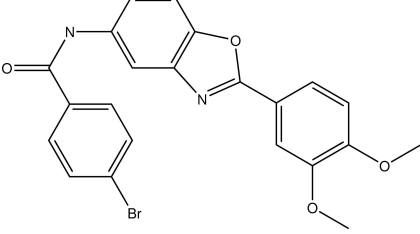
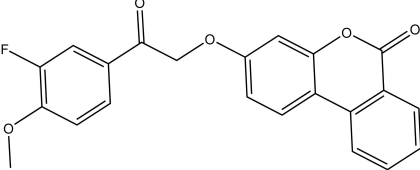
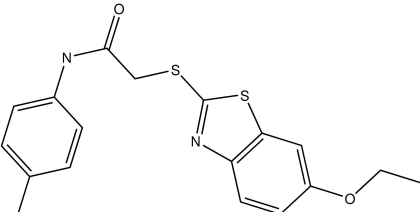


Figure 17: PfENR docked with ChemBridge compound 7682275. This compound maintains an element of stacking with the NAD⁺ co-factor, but does not appear to form any hydrogen bonds. The hydrogen bonding distances and geometries, to either the co-factor or Tyr²⁷⁷, are unfavorable. The dichloro-substituted ring is also predicted to sterically interfere with Tyr²⁶⁷, making it a less than ideal candidate for an initial drug design scaffold.

compounds inhibited PfENR between 75-97% and were subjected to IC₅₀ determinations (Table 16). Only one compound, 7682275, exhibited an IC₅₀ value less than 50 μ M, at 33 μ M. This compound was soaked into PfENR:NAD⁺ binary crystals for 14 days, but was not present in the crystal structure after data collection. This compound maintains an element of stacking with the NAD⁺ co-factor, but does not appear to form any hydrogen bonds. The hydrogen bonding distances and geometries, to either the co-factor or Tyr²⁷⁷, are unfavorable. The dichloro-substituted ring is also predicted to sterically interfere with Tyr²⁶⁷, making it a less than ideal candidate for an initial drug design scaffold.

Table 16: Molsoft-ICM ChemBridge compounds, screen results

| Compound | Structure | PfENR IC ₅₀ (μ M) |
|----------|---|-----------------------------------|
| 7682275 |  | 33.0 |
| 5217961 |  | 57.5 |
| 5964423 |  | 58.4 |
| 6401523 |  | 91.6 |
| 6842511 |  | 101.6 |
| 5344752 |  | 112.7 |

ZINC Virtual Screening

Virtual High Throughput Screening (vHTS) experiments were conducted with FlexX docking software and the ZINC 3.3 million compound library of commercially available small molecules (Irwin and Shoichet, 2005). This database was advantageous for several reasons: (i) all chemicals are commercially available through various vendors; (ii) biologically relevant protonation states have already been assigned; (iii) chemicals are annotated with molecular weight, calculated logP values, and number of rotatable bonds; (iv) compounds are prepared in multiple protonation states and tautomeric forms; (v) database has been pre-filtered to conform to current opinion in the field about eligible compounds for screening; (vi) the database is free. The crystal structure of the ternary complex PfENR:NAD⁺:triclosan was used for vHTS. All crystallographic waters were removed. Atom typing of protein residues and addition of hydrogens to them was carried out by reference to standard Biopolymer libraries keyed to residue type available in SYBYL 7.0. Terminal rotors such as methyl and hydroxyl groups were then relaxed to avoid distortion of scores by spurious steric clashes with the added hydrogen atoms. Charges were assigned to both protein and ligand atoms as described by Gasteiger and Marsili. Binding sites were defined for all scoring functions as including all atoms in protein residues where at least one atom was within 6.5 angstroms of any atom in the inhibitor, triclosan, as found in the parent crystal structure. Triclosan was then removed from the model and the effective binary complex of PfENR and NADH was used for docking purposes. FlexX docking runs utilized the default parameters provided in SYBYL 7.0. Afterwards, they were scored with the consensus scoring technique (Clark *et al.*, 2002) to give a score in five separate categories, namely FlexX, DOCK, PMF, GOLD, and ChemScore. The FlexX scoring function considered the number of rotatable bonds

in the ligand, hydrogen bonds (including atom types and geometry of interaction), ion pairing, aromatic interactions, and the lipophilic contact energy (Rarey *et al.*, 1996). DOCK considered both electrostatic and hydrophobic contributions to the binding energy, but did not include entropic terms (Meng *et al.*, 1993). The PMF scoring function was simply a summation over all pairwise interaction terms (Muegge and Martin, 1999). The magnitude and sign of each interaction potential was based on the atom types of the interacting pair and the intervening distance. Potential curves for each atom type pairing were derived from a survey of crystal structures retrieved from the Protein Data Bank. The GOLD evaluation function was the sum of hydrogen bonding stabilization energy calculated from donor/acceptor pair atom types and geometries; internal van der Waals energy for the ligand conformer in question; and the strength of steric interactions between ligand and protein (Jones *et al.*, 1995, 1997). ChemScore used four terms that estimate contributions to binding energy from lipophilic interactions, metal-ligand binding, hydrogen bonding, and loss of ligand flexibility (Eldridge *et al.*, 1997). The concept of consensus scoring was to identify those ligand conformations that have the highest score in most of the scoring functions. Subsequently, the top candidates were selected as the intersection of the top scoring 2% of each of the five categories. This resulted in 68 hits, which were manually inspected before obtaining these compounds from each vendor for *in vitro* enzyme assays. The results are given below in Table 17. For each category, lower numbers (more negative) represent better scores. Triclosan was docked and scores calculated for comparison, but was not selected amongst the top hits via the consensus scoring technique.

Manual inspection of the docked compounds revealed some points of interest. First, only 4 of the 68 docked compounds (selected compounds in Figure 18)

that were visualized with the molecular modeling program SPOCK retained

Table 17: Selected ZINC compounds, docking comparison

| ZINC ID | FlexX | DOCK | PMF | GOLD | ChemScore |
|-----------|--------|----------|--------|---------|-----------|
| Triclosan | -8.18 | -498.80 | -22.95 | -55.08 | -14.09 |
| 68769 | -20.13 | -2182.79 | -10.19 | -210.47 | -17.99 |
| 105449 | -20.59 | -2180.37 | -10.12 | -213.44 | -18.30 |
| 105523 | -19.53 | -2176.66 | -9.20 | -201.11 | -17.66 |
| 414098 | -20.87 | -2316.14 | -16.88 | -243.79 | -23.87 |
| 1911861 | -29.80 | -281.92 | -10.54 | -208.84 | -17.93 |
| 152008 | -17.89 | -2339.46 | -8.33 | -240.14 | -19.89 |
| 246330 | -18.62 | -3719.36 | -10.80 | -269.31 | -22.05 |
| 279738 | -10.98 | -3536.22 | -8.31 | -215.03 | -17.61 |
| 152008 | -17.89 | -2339.46 | -8.33 | -240.14 | -19.89 |
| 488570 | -28.09 | -2258.78 | 43.73 | -236.81 | -18.01 |
| 537682 | -28.63 | -2242.43 | -12.30 | -219.49 | -14.59 |
| 618454 | -10.63 | -3808.40 | -18.42 | -234.28 | -18.02 |
| 703599 | -31.44 | -3852.98 | 21.23 | -234.24 | -18.19 |
| 741814 | -30.04 | -2187.29 | 63.88 | -239.18 | -19.21 |
| 752290 | -13.70 | -2370.04 | -8.49 | -211.60 | -18.31 |
| 793428 | -28.45 | -3858.68 | 53.10 | -210.28 | -18.09 |
| 858779 | -11.97 | -3696.84 | -10.01 | -276.71 | -19.16 |
| 920638 | -32.37 | -2210.12 | 55.92 | -272.07 | -18.55 |
| 1010182 | -31.88 | -2196.22 | 52.55 | -282.87 | -19.71 |
| 1010193 | -29.38 | -2191.45 | 38.56 | -260.66 | -20.53 |
| 1010201 | -29.31 | -2323.91 | 32.14 | -288.36 | -22.23 |
| 1157902 | -11.94 | -3656.32 | -8.38 | -273.26 | -20.79 |
| 1205257 | -30.44 | -3795.04 | 7.67 | -216.55 | -19.04 |
| 1226158 | -13.61 | -2369.98 | -8.50 | -226.21 | -18.35 |
| 1236811 | -13.80 | -3577.27 | -6.82 | -250.90 | -17.47 |

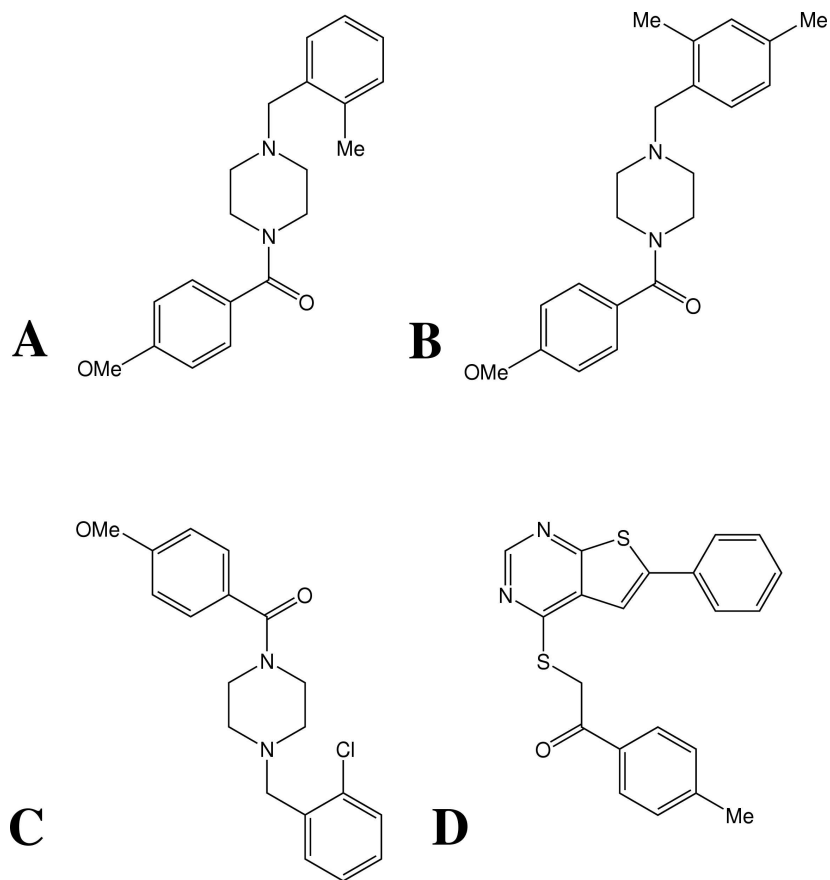


Figure 18: Stick models of ZINC lead compounds. A, B, C, and D correspond to ZINC compounds 67689, 105549, 105523, and 1911861, respectively.

atoms capable of hydrogen-bonding with the catalytic residue Tyr²⁷⁷. Three of these compounds, 68769, 105449, and 105523 (Figure 19) were based on the same backbone, and had small changes in the terminal aromatic ring. The other ZINC compound was 1911861 (Figure 20), which could possibly form an additional edge-to-face ring stacking interaction with Tyr²⁶⁷. Of the complete set of 68 top hits, FlexX did however preserve the aromatic ring-stacking property with the nicotinamide moiety of the NADH co-factor in virtually every case, and also selected compounds that were within hydrogen bonding distance of the PfENR backbone between residues 217-219. FlexX also seemed to prefer molecules that would form hydrogen bonds with the co-factor, and molecules that would completely fill the binding cavity. FlexX had one outlier in this group, ZINC 1346103, which did not bind to the active site at all. Instead, it was docked to the outer perimeter of the protein. None of the hits protruded into the hydrophobic cavity that isoniazid occupies. No compounds were docked that took advantage of both the ring-stacking interactions as well as hydrogen-bonds or van der Waals interactions to the residues 217-219. Compounds of interest were then ordered from the vendor for future *in vitro* enzyme assays.

Conclusion

Our systematic modification of triclosan scaffolds, as well as co-crystal structures with the GlaxoSmithKline compounds, helps shed light on the possibilities for modification to the triclosan scaffold and its impact on the surrounding residues. While we did not achieve a more potent triclosan derivative, we have discerned areas of the triclosan scaffold where modifications are tolerated to increase the value of the pharmacokinetic profile, as well as characteristics necessary to maintain inhibitor potency, such as hydrogen bonding to Tyr²⁷⁷, aromatic ring stacking with co-factor,

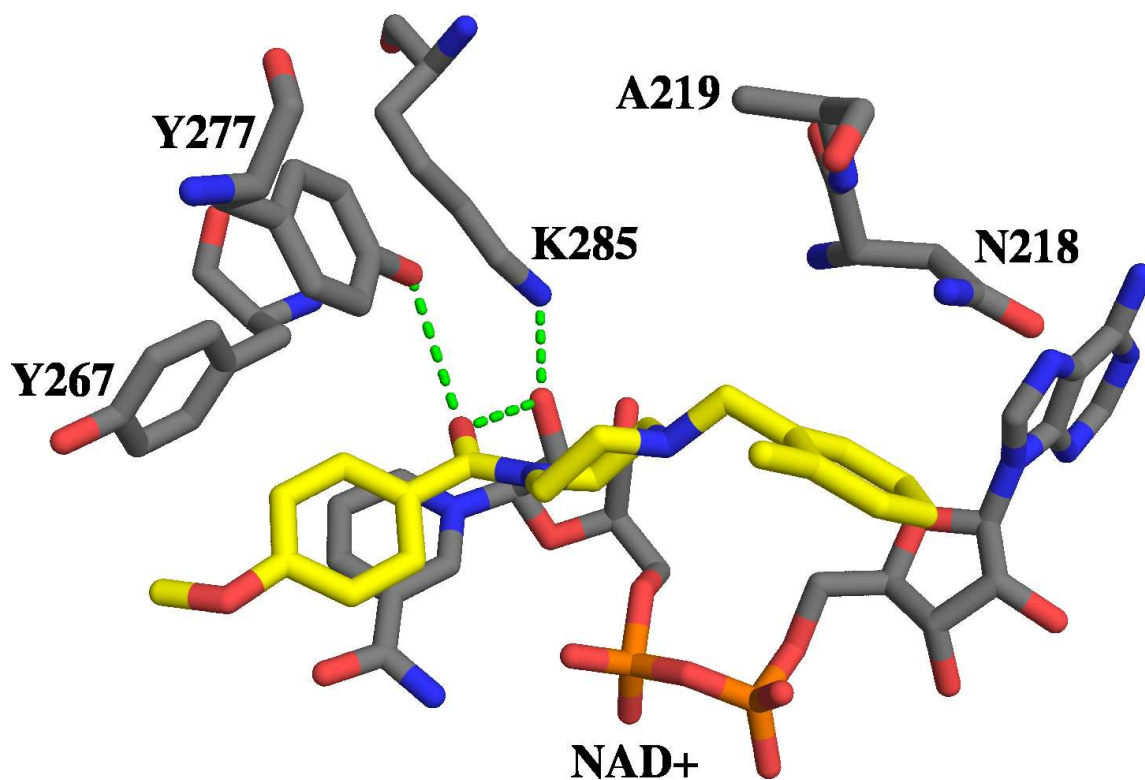


Figure 19: PfENR:NADH docked with ZINC compound 68769. ZINC 68769 is indicated in yellow carbons. This compound maintains the conserved hydrogen bonding network common to triclosan as well as the aromatic ring stacking with the nicotinamide moiety of the co-factor. Compounds 105449 and 105523 were docked in a similar fashion, with minor changes on the terminal aromatic ring facing the backbone of PfENR.

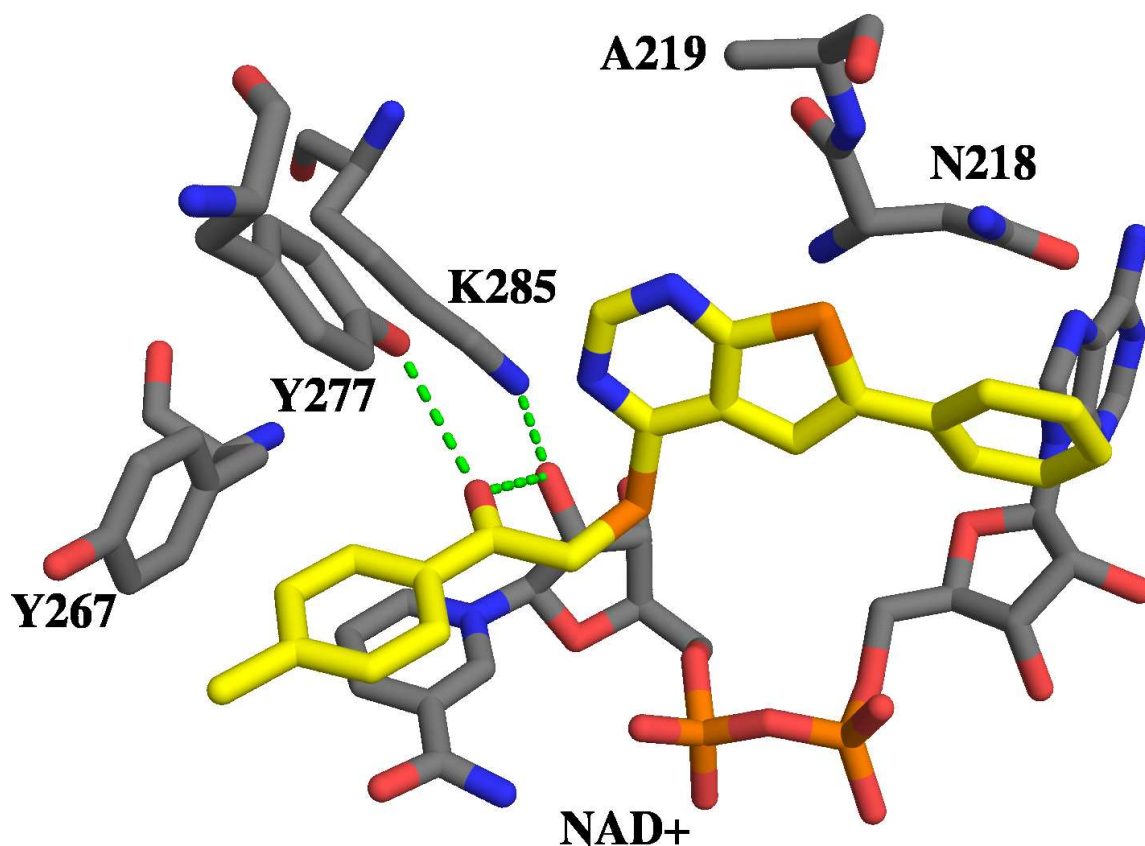


Figure 20: PfENR:NADH docked with ZINC compound 1911861. ZINC 1911861 is indicated in yellow carbons. This compound maintains the conserved hydrogen bonding network common to triclosan as well as the aromatic ring stacking with the nicotinamide moiety of the co-factor. There's a possible edge-to-face stacking interaction between ZINC 1911861 and Tyr²⁶⁷.

and hydrophobic interactions with the remainder of the active site.

Our data corresponds nicely with studies conducted by Kapoor *et al.* While we approached the problem of understanding the critical interactions within the binding site by modifying triclosan, Kapoor *et al.* modified the protein to measure the net effects of mutations at several positions. They made the following mutations at Ala²¹⁷, to A217V and A217G, changes that would be predicted to affect the B ring of triclosan. The A217V mutation resulted in a reduced affinity in excess of 7,700-fold. Thus it seems reasonable to conclude that in the case of PfENR, the mutation of Ala²¹⁷ to Val leads to unacceptable steric contacts between the side chain of valine and the B ring of triclosan, leading to reduced affinity of triclosan for the enzyme. The 2'-chloro atom of ring B of triclosan is positioned close to the side chain of Ala²¹⁷. The A217G mutation resulted in a reduced affinity of 19-fold with respect to the wild-type. The decrease in the affinity of the A217G mutant for triclosan could be due to loss of hydrophobic contacts between triclosan and the side chain of alanine. In contrast, the *E. coli* enzyme has a glycine at the corresponding position, and its replacement by alanine reduced the affinity considerably for triclosan. Thus, despite having nearly identical tertiary structure and the binding pocket, the malaria enzyme differs drastically from its bacterial counterpart.

Kapoor *et al.* also introduced mutations at the Asn²¹⁸ position, from N218A and N218D. Ring B of triclosan was located in a pocket interacting with the pyrophosphate and nicotinamide moieties of NAD⁺, by peptide backbone residues 217-231 and by side chains of Asn²¹⁸, Val²²², Tyr²⁷⁷, and Met²⁸¹. The mutation of Asn²¹⁹ to aspartic acid (N218D) led to a 50-fold decrease in the affinity of the malarial enzyme for triclosan. The mutation M281T had 333-fold reduced affinity for triclosan. This could be caused by the loss of van der Waals contacts between the 4-chloro atom of ring B and hydrophobic side chain of Met²⁸¹. In order to rule out the possibility that

the addition of the β -branched threonine could introduce indirect effects due to the perturbation of the local structure, the M281A mutant was made, and showed K_i similar to M281T. Our crystal structure data with the 4'-position triclosan inhibitors also revealed the significance of interactions with Asn²¹⁸, as well as Ala²¹⁹.

As observed from the crystal structure of the ternary complex of *P. falciparum* with triclosan and NAD⁺, ring A of triclosan makes van der Waals interactions with the side chain of Phe³⁶⁸. Also the 4-chloro atom of ring A of triclosan makes several van der Waals contacts with Phe³⁶⁸. The F368A mutation and F368I mutation led to 240- and 210-fold (respectively) decreases in the affinity of enzyme for the inhibitor, highlighting the importance of stacking and the van der Waals interactions between ring A of triclosan and Phe³⁶⁸ of the enzyme. Kapoor *et al.* also indicated that the loss of the ring B chlorines substantially decreases the potency of triclosan. The Ala²¹⁷ mutations project directly into ring B of triclosan, while the N218 mutations are near the 4'-position of the B ring, an area we identified as a possible new interaction area for hydrogen bonds. Met²⁸¹ lies near one of the chlorines on the B ring, suggesting the loss of hydrophobic interactions is also detrimental. Phe³⁶⁸ occupies an area near the A ring of triclosan and could possibly flip out of the way, suggesting that Phe³⁶⁸ ring stacks or forms hydrophobic interactions with something.

Thus, to conclude, the strong affinity of PfENR for triclosan is discernible via specific residues at the catalytic center of the protein. Because of the subtle but significant contributions observed in these studies for the contribution of key residues to the binding affinity of PfENR for triclosan, in contrast to its bacterial counterparts, it should be possible to design better and specific analogs of triclosan as antimalarial agents that do not target the host pathways. Our assays of hundreds of triclosan analogs, along with Kapoor *et al.* investigations into PfENR mutations, help to define which interactions are critical to inhibitor potency, and serve as a basis for

future drug studies.

CHAPTER IV

CRYSTALLOGRAPHIC STUDIES OF PBENR

Plasmodium berghei Enoyl-ACP Reductase

Malarial parasites are extremely species specific. Plasmodial species able to infect humans are unable to infect non-primate animal models, posing problems for transferring knowledge from *in vitro* to *in vivo* experiments. However, recently published studies demonstrated a high level of conservation of genome organization between rodent and human plasmodial parasites. Comparative mapping of genes located in the central regions of the chromosomes has shown that both linkage and gene order appear to be well conserved between human and rodent parasites, resulting in significant level of homology between these species. These similarities between human and rodent Plasmodial parasites have significant consequences and benefits for anti-malarial drug research, providing researchers with a model organism from which critical information can be learned. Compounds that are effective against the *P. falciparum* enoyl-ACP reductase *in vitro* could be subjected to testing in the murine model, with a reasonable expectation that the results would be relevant to humans. The similarity also provides a cost-effective and abundant experimental source for further studies, as data obtained from our understanding of malaria in rodents can be used to combat malaria in humans. To this end, we embarked upon determining the structure of *Plasmodium berghei* enoyl-ACP reductase (PbENR).

Results and Discussion

PbENR Sequence Characteristics

pbenr encoded a predicted protein of 396 amino acids with an expected molecular mass of 44.8 kDa. Sequence alignments (Figure 21) revealed that PbENR showed 76% overall sequence identity to PfENR when comparing the mature enzyme sequences. Regions of significant homology with PfENR were interrupted by a 15-amino acid deletion (residues 333-348 in PfENR are absent in PbENR) and a 6-amino acid deletion (residues 358-363 in PfENR are absent in PbENR), in a segment known as the low-complexity region in PfENR (residues 325-368). PbENR has a long N-terminal extension (similar in length to plant ENRs) that is characteristic of bipartite N-terminal pre-sequences found in *Plasmodium* and *Toxoplasma* parasite proteins targeted to the apicoplast (Waller *et al.*, 1998, 2000). The apicoplast targeting sequence prediction programs PATS (Zuegge *et al.*, 2001) and PlasmAP (Foth *et al.*, 2003) predicted the first 23 N-terminal amino acids to be an apicoplast targeting sequence, with the following ~51 residues are the adjacent transit peptide. This segment of polypeptide shared little similarity with the bipartite N-terminal pre-sequence found in the *Plasmodium falciparum* ENR protein. Using prediction programs SIGNALP (Bendtsen *et al.*, 2004) and PSORT (Nakai and Horton, 1999), a putative cleavage site for the signal peptide could be detected between residues Cys²¹ and Phe²² (Claros *et al.*, 1997; Nielsen *et al.*, 1997). Sequence alignments revealed 220 completely conserved residues in the PbENR sequence when compared with the closely related ENRs of *P. falciparum* and *P. vivax*. Interestingly, the three available sequenced *Plasmodial* ENR proteins (*Plasmodium berghei*, *Plasmodium falciparum*, and *Plasmodium vivax*) have no significant identity over the N-terminal bi-partite extension or in the low complexity region, but are well conserved in the remainder

```

P. falciparum 1 -MNKISQRLLFLFLHFYTIIVCFIQN-NTQKTFHNVLQNEQIRGKEKAFYRKEKRENIFIG
P. berghei 1 MYKKLIVFLTILIFNYLKITCF TNNGYEKKTFSSLRMKNENYWKNKILRKKKNENLRIN
P. vivax 1 MHVRRRVQLATLLYIASVSAMLRSAKGGGQPKWEIERRGNSREMQFITSKAIKGVAHK

P. falciparum 59 NKMKHLNMMNTHNNHMEKEEQDASNINKI KEENKNE DICFIAGIGDTNGYGWGIAKE
P. berghei 61 VESNQNDKIDNIKN-----KNENENE-ICFIAGVGDSDNGYGWGIAKE
P. vivax 61 RKISQHSSPAHEMVSEQSQQAEGING-----KGEPLGD-ICFIAGVGDSDNGYGWGIAKE

P. falciparum 119 LSKRNVKIIIFGIWPPVYNIFMKNYKNGKFDNDMIIDKD--KKMNIIDMLPFDASFDTAND
P. berghei 102 LSKRNVKVIIFGVWPPVYNIFIKNLESKGFDDKMIINNDNSKRMQILDVLPDAGFDNYDD
P. vivax 114 LSKKNVKIILGVWPPVYNIFMKNLQSGKFDSDMIIGEG--KKMELLDILPDAAFDSASD

P. falciparum 177 IDEETKNNKRYNMLQNYTIEDVANLIHQKYGKINMLVHSLANAKEVQKDLLNTSRKG YLD
P. berghei 162 IDEETKNNKRYNMLKNYSIEEVANLIYNKYGKISMLVHSLANGREVQKSLDTSRDGYLD
P. vivax 172 VDEETRKNKRYASLDSYSIEEVANLVYKKGKINMLVHSLANGREVERSLLETSRGGYLD

P. falciparum 237 ALSKSSYSLSLCKYFVNIMKQPSSIIISITYHASQKVVPGYGGGMSAKAALES DTRVLA
P. berghei 222 AISKSSYSLSLCKHFCKFMNSGGSVVSLTYQASQKVVPGYGGGMSAKAALES DTRVLA
P. vivax 232 ALSKSSYSLSLCKHFCKIMHPQSSVISISYASQKVVPGYGGGMSAKAALES DTRTLA

P. falciparum 297 YHLGRNYNIRINTISAGPLKSRAATAINKLNNTYENN TNQNKNRNSHDVHNIMNNSGEKE
P. berghei 282 YYLGRKYNIRINTISAGPLKSRAATAINKFNNNQKNN-----MNSSGETD
P. vivax 292 YHLGRKHKIRVNTISAGPLKSRAATAIKKATPQSGGN-----EGEK-

P. falciparum 357 EKKN SASQNYTFIDYAI EYSEKYAPLRQKLLSTDIGSVASFLLSRESRAITGQTIYVDNG
P. berghei 327 K-----QNYSFIDYAI DYSEKYAPLKKLLSTDVGSVASFLLSKESAVTGQTIYVDNG
P. vivax 333 -----KNLAFIDYAI DYSEKYAPLQQKLYSTDVGAVAAFLLSKESRAV TGQTIYVDNG

P. falciparum 417 LNIMFLPDDIYRNE
P. berghei 381 LNIMFGPDDLFQSSDS
P. vivax 386 LNIMFGPDDLFQGGAA

```

Figure 21: Sequence alignment of PfENR, PbENR, and PvENR. The proteins *Plasmodium falciparum* ENR, *Plasmodium berghei* ENR, and *Plasmodium vivax* ENR show great conservation, with a few notable differences. Completely conserved residues are indicated in green. Note the differing low-complexity region lengths, indicated in red underline. PbENR lacks approximately 30 residues that are present in PfENR. The N-terminal bi-partite extensions also show little sequence conservation.

of the sequence.

Tertiary Structure

The tertiary structure of PbENR is presented in Figure 4, and is virtually identical to that of PfENR. Overall, the structure was reminiscent of the Rossmann fold (Rossmann *et al.*, 1974) and was similar to all other structurally defined homologous enzymes. The PbENR subunit comprised a single domain of 55 x 50 x 50 Å (Figure 4). Each subunit was composed of seven β -strands (β 1- β 7) that formed a parallel β -sheet and nine α -helices (α 1- α 9) that were connected to the β -strands by a number

of loops of varying length. The parallel β -sheet was flanked by helices $\alpha 1$, $\alpha 2$, $\alpha 4$, $\alpha 5$, $\alpha 6$, and $\alpha 9$, with $\alpha 3$ arranged along the top of $\alpha 2$ and $\alpha 4$. Helix $\alpha 8$ was located at the C-termini of strands $\beta 6$ and $\beta 7$. The aforementioned 10-amino acid low complexity insertion in PbENR sequence localized to an important loop region ($\alpha 7$ and $\alpha 8$), near the catalytic center of the protein. This region was thought to be a determinant in substrate specificity, because it participates in acyl substrate binding, as shown in the *M. tuberculosis* structure in which the bound fatty acyl substrate was held in place by the substrate binding loop (Rozwarski *et al.*, 1999). Only 3 amino acids of the low complexity insertion were visible in the electron density maps, indicating that most of this region was disordered even in the presence of bound co-factor. Nonetheless, the last visible amino acids just before (Lys³³²) and after (Tyr³⁴⁹) the low complexity region were in virtually the exact same position as the comparable loop residues in the *E. coli* enzyme structure. Earlier investigations into *E. coli*, *B. napus*, and *M. tuberculosis* ENRs have found a correlation between the length of the substrate binding loop and the fatty acyl substrate chain length (Rozwarski *et al.*, 1999). If this held for *P. berghei* ENR, one could expect that long-chain fatty acids would serve as substrate and, by analogy to the *M. tuberculosis* ENR, the PbENR would not use very short-chain acyl-CoAs as substrate. However, kinetic studies indicated that the *P. berghei* ENR can utilize crotonoyl-CoA (C4:1), much like *P. falciparum* ENR which contains a substantially longer low-complexity insertion of 43 amino acids. The 43 amino acid low-complexity insertion in PfENR and the 13 amino acid insertion in PbENR (compared to *E. coli* FabI) do not appear to affect the substrate chain-length specificity. This observation, coupled with the unusually high polar residue content, raises questions about the role of the low-complexity insertion in *Plasmodial* enzymes.

Quaternary Structure

In gel filtration studies, PbENR formed a tetramer in solution, in agreement with all other bacterial and plant ENRs reported to date. In support of this, the packing in the crystal showed an obvious homotetramer possessing internal 222 symmetry. The estimated dimensions for the tetramer were 60 x 85 x 85 Å . The solvent-accessible surface areas for the subunits and the tetramer were calculated using DSSP (Kabsch and Sander, 1983) and were determined to be about 15,000 Å² for each subunit and approximately 43,000 Å² for the tetramer. Approximately 1600 Å² (11%) of the surface area of subunit A was buried, making intermolecular contacts with subunit B, 1700 Å² (12%) with subunit C, and 900 Å² (6%) with subunit D. Thus, the total surface area involved in intermolecular contacts of each subunit was 4200 Å² or 29%. Again, these figures are virtually identical to those of PfENR. This type of organization for PbENR was comparable to the crystal structures elucidated for enoyl-ACP reductases from *E. coli* (Baldock *et al.*, 1996), *B. napus* (Rafferty *et al.*, 1995), *M. tuberculosis* (Rozwarski *et al.*, 1999), and *Plasmodium falciparum* (Perozzo *et al.*, 2002).

Analysis of the Nucleotide Binding Site

The PbENR:NADH binary complex showed excellent electron density for the co-factor NAD⁺ and was localized to the enzyme in an extended conformation at the C-terminal end of the β-sheet with both ribose sugar rings found as C2'-endo conformers and the nicotinamide moiety in the *syn* conformation . The adenine ring was located in a pocket on the surface of the protein, formed by the side chains of Trp¹¹⁴, Leu¹⁵², Ala¹⁵⁴, Gly¹⁵⁵, Asn²⁰³ and the main chain between residues Leu¹⁵² and Asp¹⁵³. Hydrogen bonds were formed between the adenine nitrogen atoms at

position N1 with the peptide nitrogen atom of Ala¹⁵⁴ and at position N6 with the side chain of Asp¹⁵³. In PbENR, the 2'-hydroxyl group of the adenine ribose occupied a small depression flanked by Gly⁸⁹, Trp¹¹⁴ and Val¹¹⁷, which resulted in a tight fit for the NAD⁺/NADH co-factor. This spatial arrangement leaves no room for the extra phosphate group of NADPH and is consistent with the notion that NADH was a much more efficient co-factor than NADPH for PbENR function. The pyrophosphate moiety of NAD⁺(NADH) lay close to the C-terminal part of the β -sheet and interacted with the glycine-rich region of the loop connecting β 1 and α 1, with α 1 being the nucleotide binding helix. Contacts through hydrogen bonds were made by the pyrophosphate oxygen atoms with the peptide nitrogen of Tyr¹¹¹ and, mediated by a solvent molecule, with the main-chain carbonyl of Gly⁸⁹, the peptide nitrogen of Gly⁹⁵ and the side-chain hydroxyl of Ser²⁰⁰. The co-factor was bound by this series of hydrogen bonds and was not further supported by positively charged side chains close to the nucleotide binding site. The nicotinamide binding pocket was composed of the side chains of Tyr⁹⁴, Leu²⁵⁰, Tyr²⁵², Tyr²⁶², Ala²⁹⁷, Gly²⁹⁸, Pro²⁹⁹, Leu³⁰⁰, and Ile³³³. Both 2'- and 3'-ribose hydroxyl groups hydrogen-bonded to the amino group of the Lys²⁷⁰, whereas only the 3'-group interacted with a solvent molecule that was contacted by the side chain of His¹⁹⁹. The nicotinamide ring was completely ordered on the enzyme, where it interacted via specific hydrogen bonds formed by the oxygen and nitrogen of the carboxamide moiety and the Leu³⁰⁰ peptide nitrogen and co-factor pyrophosphate moiety. These interactions appeared to stabilize the packing of the nicotinamide ring against the phenolic ring of Tyr¹¹¹, exposing the B-face to the active site. Thus, the co-factor adopted the same conformation for stereospecific hydride transfer via the *pro*-4S hydrogen of NADH as that observed with *E. coli*, *B. napus*, *M. tuberculosis*, and *Plasmodium falciparum* ENRs.

Location of the Fatty-Acyl Binding Pocket

The binding site for the fatty acyl portion of the substrate was built with hydrophobic residues that were derived primarily from the substrate binding loop. The ENR structures from *P. falciparum*, *B. napus*, *M. tuberculosis*, and *E. coli* showed a similar patch of predominantly hydrophobic side chains adjacent to the position of the nicotinamide ring and the fatty acid chain binding area, as would be expected with a fatty acyl binding enzyme. With PbENR, the corresponding amino acids and side chains flanking the putative binding site were Tyr²⁵², Gly²⁶¹, Tyr²⁶², Met²⁶⁶, Pro²⁹⁹, Ala³⁰⁴, Ala³⁰⁵, Ala³⁰⁷, Ile³⁰⁸, Ile³³³, and Ala³³⁶. Most residues were located in helices $\alpha 7$ and $\alpha 8$ and formed a hydrophobic finger-shaped cavity. One side of the cavity was accessible to solvent. Based on volumetric measurements of the fatty acyl binding cavity in the PbENR:NADH binary complex and structural similarity to PfENR, there was only enough space to accommodate a substrate of six to eight carbon atoms in length.

Analysis of the Triclosan Binding Site

Triclosan has been previously demonstrated to inhibit a variety of ENR from homologous organisms, including the closely related *Plasmodium falciparum* ENR. To confirm the similarities between PbENR and PfENR, we co-crystallized PbENR with triclosan and determined the crystal structure. The crystal structure of PbENR solved with protein incubated with NAD⁺ and triclosan (Figure 22) revealed the mode of triclosan binding. Comparison of the *P. berghei* ENR:NAD⁺:triclosan structure with the closely related *Plasmodium falciparum* enzyme as well as the corresponding *E. coli* and *B. napus* structures demonstrated that, for PbENR, the binding mode for triclosan was identical, showing the same aromatic ring stacking interaction with the

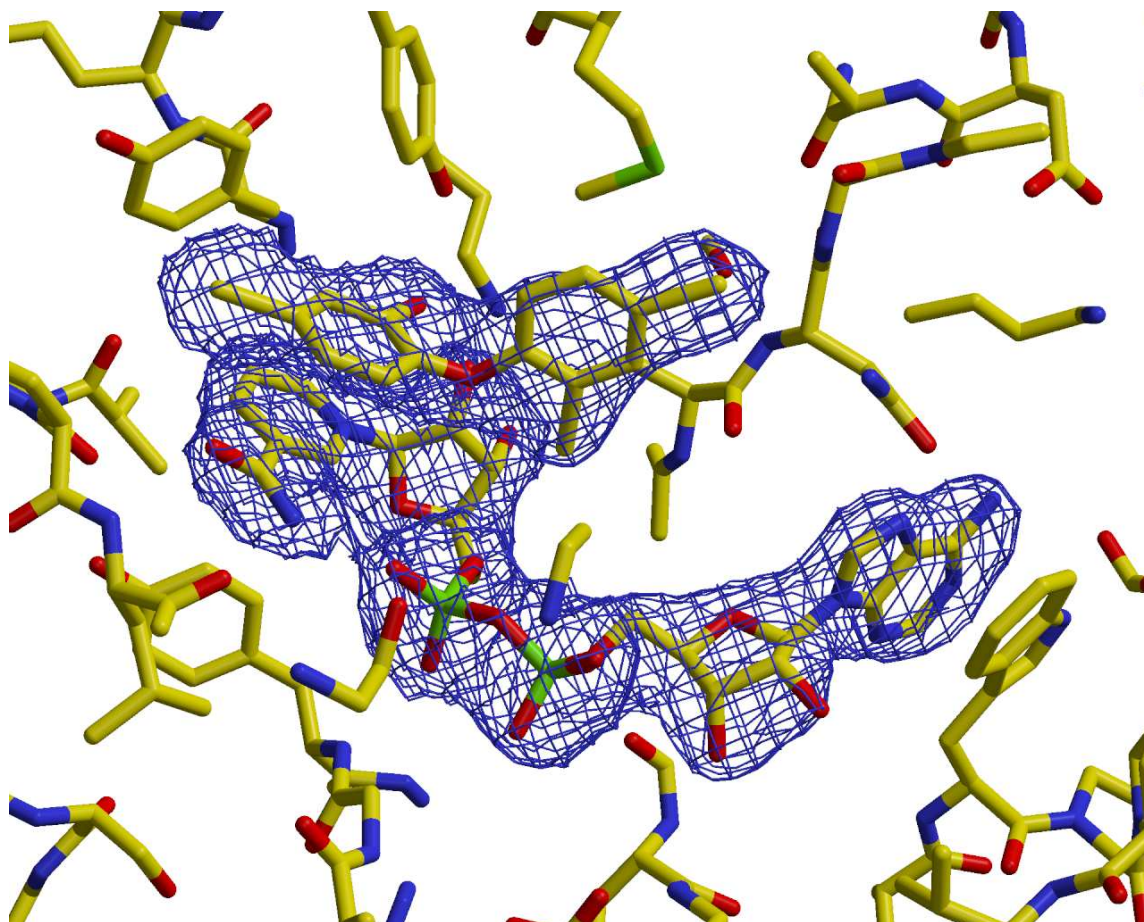


Figure 22: Structural details of the PbENR binding site. Indicated in blue wire frame is a $2F_o - F_c$ electron density map centered around the triclosan and NAD^+ co-factor within the PbENR active site. The presence of triclosan is clearly indicated within the electron density map. The mode of binding of triclosan is identical to that of PfENR complexed with triclosan.

nicotinamide ring of NAD^+ and comparable hydrogen-bonding pattern with the 2'-hydroxyl group of the nicotinamide ribose and with Tyr²⁶². Ring A (the phenol ring) of the inhibitor interacted face-to-face with the nicotinamide ring of NAD^+ allowing π -cation interactions. The same ring formed additional van der Waals interactions with the side chains of Tyr²⁵², Tyr²⁶², Pro²⁹⁹, Phe³²², and Ile³²³. The phenolic hydroxyl hydrogen-bonded to the 2'-hydroxyl moiety of the nicotinamide ribose and the oxygen atom of Tyr²⁶², and the amino nitrogen of Lys²⁷⁰ was within 4.6 Å. These residues are completely conserved in all known ENRs and have been implicated in the enzyme's catalytic mechanism (Rafferty *et al.*, 1995; Parikh *et al.*, 1999). The 4-chloro atom of ring A was surrounded by mainly hydrophobic residues making van der Waals contacts with the side chains of Tyr²⁵², Pro²⁹⁹, and Phe³³². The ether oxygen atom of triclosan interacted with the 2'-hydroxyl group of the nicotinamide ribose, and it approached to within 3.65 Å of one of the oxygen atoms of the nicotinamide ribose phosphate group. Ring B (2,4-dichlorophenoxy ring) of triclosan was located in a pocket bounded by the pyrophosphate and nicotinamide moieties of NAD^+ , by the peptide backbone residues 202-216 and by the side chains of Asn²⁰³, Val²⁰⁷, Tyr²⁶², and Met²⁶⁶. Although the 4-chloro atom of ring B was placed adjacent to the side chains of Val²⁰⁷ and Met²⁶⁶ and residues 203-204, the 2-chloro atom was surrounded by the α -carbon atom, the side chain of Ala²⁰², and atoms of the nicotinamide ribose pyrophosphate moiety. Superposition of the binary and ternary complex structures revealed subtle conformational changes in the protein upon inhibitor binding, with the most pronounced change being a slight shift of helix $\alpha 7$ by 0.5 Å toward the solvent.

Comparison to PfENR

The tertiary structure of PbENR is virtually identical to that of PfENR (Figure 23). The only significant differences are within the N-terminal bipartite pre-sequence, which is cleaved from the mature enzyme, and a smaller low-complexity region within the substrate-binding loop of PbENR, between helices $\alpha 7$ and $\alpha 8$. There is also a small, two residue insertion between loop $\alpha 3$ and $\alpha 4$. However, these differences do not cause significant differences in the binding of triclosan or NADH, giving credence to the possibility that inhibitors effective against PbENR would also have utility against PfENR, due to the extremely high level of sequence identity and structural similarity (less than 0.6 angstroms r.m.s.d.). This would allow researchers to circumvent the problems of extremely high species specificity posed by the *Plasmodial* parasites and more directly apply their research towards treating malaria infections of humans. Researcher could screen inhibitors against PfENR in *in vitro* enzyme assays, and test effective candidates in *in vivo* experiments against mice infected with *Plasmodium berghei*, with a reasonable expectation that the mouse model closely approximated human *Plasmodium falciparum* infection. This information would significantly benefit malaria research in humans.

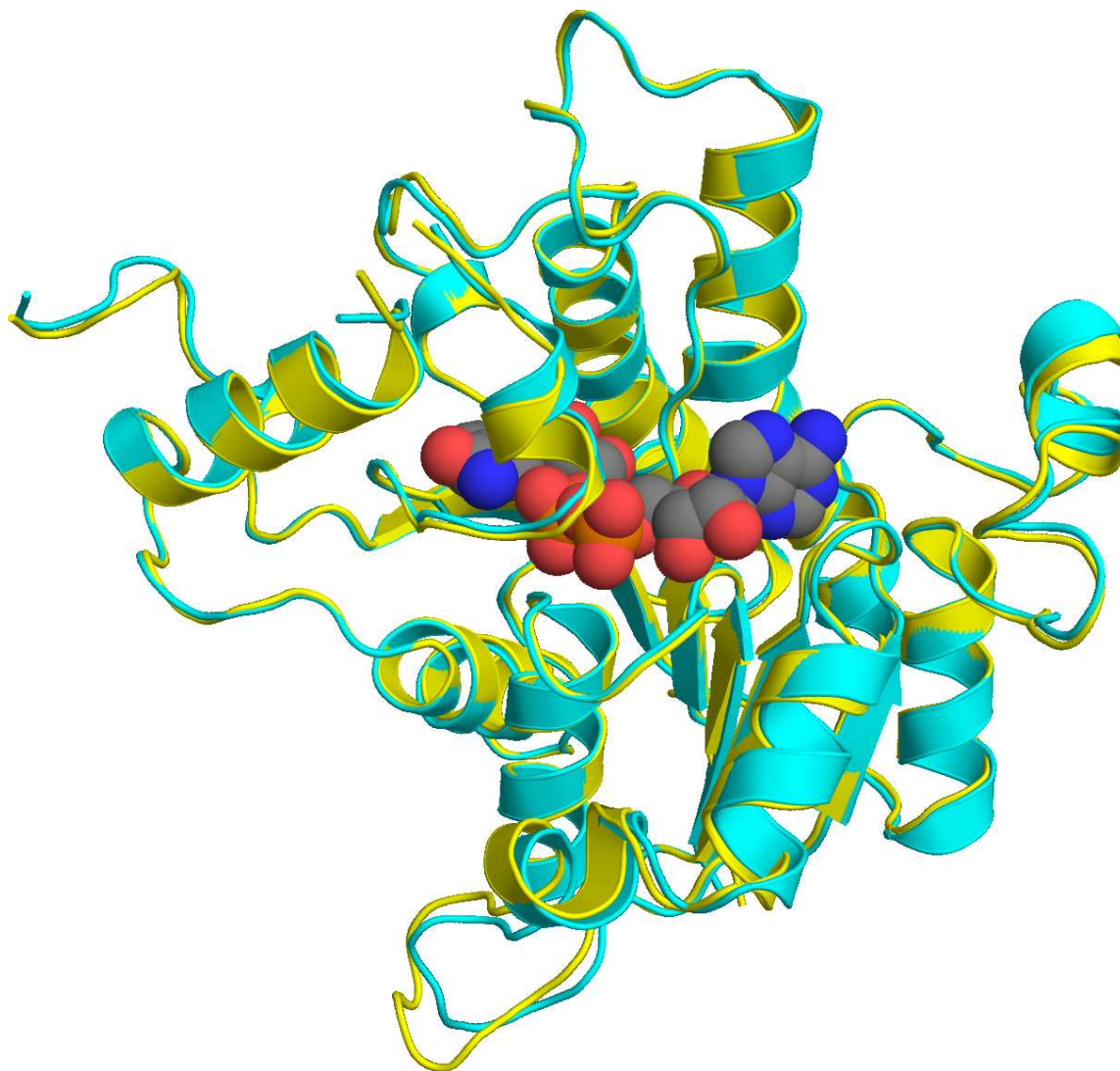


Figure 23: Comparison of PbENR and PfENR structures with co-factor. *Plasmodium berghei* ENR, indicated in blue ribbons, and *Plasmodium falciparum* ENR, indicated in yellow ribbons are virtually identical when superimposed, with a root mean square deviation of 0.56 angstroms. NADH co-factor is represented with spheres, and the atoms are colored by element.

CHAPTER V

INTRODUCTION TO TUBERCULOSIS

History of Tuberculosis

The disease tuberculosis (TB), historically referred to as consumption, wasting disease, phthisis, or white death, has afflicted humans for thousands of years. The earliest recorded evidence of tuberculosis was discovered in the 10,000 year old skeletal remains in Germany. Fragments of spinal columns of Egyptian mummies dating back to 2400 B.C. showed definitive signs of tubercular decay. The term phthisis appeared first in Greek literature. Around 460 B.C., the Greek physician Hippocrates identified phthisis as the most widespread disease of the times, and noted that it was almost always fatal. Due to common phthisis-related fatalities, he admonished his colleagues against visiting victims in late stages of the disease.

Exact pathological and anatomical descriptions of the disease began to appear in the seventeenth century. In his *Opera Medica* of 1679, the Dutch physician Franciscus Sylvius was the first to identify actual tubercles as a consistent and characteristic change in the lungs and other areas of consumptive patients. He also described their progression to abscesses and cavities. In 1702, French researcher John Jacobus Manget described the pathological features of miliary tuberculosis, an acute form of tuberculosis that is characterized by very small tubercles in various body organs, caused by the spread of tubercle bacilli through the bloodstream. The earliest references to the infectious nature of the disease appeared in seventeenth century Italian medical literature. An edict issued by the Republic of Lucca in 1699 recommended that personal effects belonging to the victim be destroyed after a tuberculosis-related

fatality, followed by quarantine of the deceased individual's home.

In 1720, the English physician Benjamin Marten was the first to conjecture, in his publication, *A New Theory of Consumption*, that tuberculosis could be caused by microorganisms and transmitted through shared foods or close contact. He postulated that microorganisms, once established within the host, could generate the lesions and symptoms of the disease. He stated, moreover, that prolonged exposure or close contact with individuals manifesting symptoms of tuberculosis was sufficient to transmit the disease to a healthy person.

It was not until the 1800s that tuberculosis could begin to be treated. In contrast to the significant level of understanding about the process of consumption, which enabled prevention and a break in the cycle of infection, those attempting to cure the disease were still far from a solution. The introduction of the sanatorium provided the first real step against tuberculosis. Hermann Brehmer, a botany student suffering from tuberculosis, was instructed by his doctor to seek out a healthier climate. He traveled to the Himalayas where he could pursue his botanical studies, while trying to rid himself of the disease. He returned home cured of tuberculosis and began to study medicine. In 1854, he presented his doctoral dissertation ambitiously entitled, *Tuberculosis is a Curable Disease*. In the same year, he built an institution in Germany where, in the midst of fir trees, and with good nutrition, patients were exposed on their balconies to continuous fresh air. This configuration inspired the subsequent development of sanatoria, a powerful weapon in the battle against tuberculosis. In 1865, the French military doctor Jean-Antoine Villemin demonstrated species-to-species transmission, by showing that tuberculosis could be passed from humans to cattle and from cattle to rabbits. On the basis of this revolutionary evidence, he postulated a specific microorganism as the cause of the disease, laying to rest the centuries-old notion that consumption arose spontaneously in each affected

individual. In 1882, Robert Koch discovered a staining technique that enabled him to see *Mycobacterium tuberculosis*. What excited the world was not so much the scientific brilliance of Koch's discovery, but the accompanying certainty that now the fight against humanity's deadliest enemy could really begin. The causative microorganism had been identified. The treatments available to doctors were still modest, consisting of improved social and sanitary conditions, and adequate nutrition. These factors were all that could be done to strengthen the body's defenses to stave off the bacillus. Sanatoria, now commonly established throughout Europe and the United States, provided a dual function: they quarantined the sick, the source of infection, from the general population, while the enforced rest, together with a proper diet and the well-regulated hospital life assisted the healing processes.

These efforts were reinforced by the observation by Carlo Forlanini, that lung collapse tended to have a favorable impact on the outcome of the disease. With the introduction of artificial pneumothorax and surgical methods to reduce the lung volume, the depressing era of helplessness in the face of advanced tuberculosis was over, and active therapy had begun. A diagnostic milestone occurred in 1895, when Wilhelm Konrad von Rontgen discovered the radiation that bears his name. Now the progress and severity of a patient's disease could be accurately followed and reviewed, examining the chest x-rays of individuals to determine the progress of infection. Another important development was provided by the French bacteriologist Calmette, who, together with Guerin, used specific culture media to lower the virulence of the bovine TB bacterium, creating the basis for the BCG vaccine still in widespread use today. Then, in the middle of World War II, came the final breakthrough, the greatest weapon to the bacterium that had ravaged humanity for thousands of years - chemotherapy.

Chemotherapy of infectious diseases using sulfonamide and penicillins, had been

underway for several years, but these molecules were ineffective against *Mycobacterium tuberculosis*. Selman Waksman had been systematically screening soil bacteria and fungi, and in 1939 discovered the marked inhibitory effect of certain fungi on bacterial growth. In 1940, he and his team were able to isolate an effective anti-tubercular antibiotic, actinomycin. However, toxicity problems relegated it to less prominent use in humans. In 1943, Waksman achieved success in the form of streptomycin, which combined maximal inhibition of *M. tuberculosis* with relatively low toxicity. A year later, the antibiotic was administered for the first time to a critically ill tuberculosis patient. The effect was almost immediate, and impressive. His advanced disease was visibly arrested, the bacteria disappeared from his sputum, and he made a rapid recovery. This discovery proved that *M. tuberculosis* could be combated successfully within the human body. Waksman was awarded the Nobel Prize in Medicine and Physiology in 1952 for his discovery of streptomycin.

A rapid succession of anti-tuberculosis drugs appeared in the following years. These were important because with only streptomycin therapy, resistant mutants began to appear with a few months, endangering the success of antibiotic therapy. Soon afterwards it was demonstrated that this problem could be overcome with drug cocktails of a combination of two or three drugs. Following streptomycin, *p*-aminosalicylic acid (1946), isoniazid (1952), pyrazinamide (1954), cycloserine (1955), ethambutol (1962) and rifampin (also known as rifampicin; 1963) were introduced as anti-tubercular agents. Aminoglycosides such as capreomycin, viomycin, kanamycin and amikacin, and the newer quinolones (e.g. ofloxacin and ciprofloxacin) were only used in drug resistance situations. Strategies of drug cocktails in concert with combinations of a β -lactam antibiotic with a β -lactamase inhibitor enhanced treatment effectiveness, but the newer drugs, including the macrolides, had not received much clinical testing.

In the United States alone, the number of tuberculosis cases in the United States declined steadily between 1920 and 1985, when the rate of newly reported cases hit a low of 9 deaths per 100,000. In the 1980s, however, tuberculosis experienced a resurgence, with the advent of AIDS, while new, drug-resistant forms of the disease emerged.

The Tuberculosis Epidemic

Today, one third of the world's population, two billion people, have latent tuberculosis infection, with approximately 7-8 million new cases arising each year. Disease rates were expected to rise in excess of 10 million by 2005. Annually, three million people fall victim to this disease, and it is the second leading cause of death from an infectious disease (4% of all deaths), for a disease that is widely perceived as treatable and curable. There is a correlation of the registered number of new cases of TB worldwide with economic conditions: 95% of those newly infected victims reside in developing countries. In industrialized countries, the steady drop in tuberculosis incidence leveled off in the mid-1980s, and then began to increase. Ominously, the number of incurable cases due to multi-drug resistant mutants is rising.

A great influence in the rising incidences of tuberculosis is the proliferation of Human Immunodeficiency Virus (HIV) infection. Epidemiological statistics indicate that only one out of ten immunocompetent people infected with *M. tuberculosis* will succumb to tuberculosis in their lifetimes, but among those with compromised immune systems, one in ten per year will develop active tuberculosis. In many industrialized countries this is a tragedy for the patients involved, but these cases make up only a small minority of cases. In developing countries, the impact of HIV infection on the TB situation is far more severe. A final factor contributing

to the resurgence of tuberculosis is the emergence of multi-drug resistance. Several errors have been made in allowing the threat of drug resistant tuberculosis: (i) administration of a single drug instead of more effective drug cocktail combinations, (ii) sub-therapeutic dosage below the pharmacologically required minimum inhibitory concentration (MIC), (iii) treatment applied for too short a duration, (iv) socio-economic problems under which poor people strive to obtain medical assistance, (vi) insufficient regional drug availability, (vii) lack of dispensation facilities and professional pharmaceutical care (Crofton *et al.*, 1997).

First-line antibiotics in use today are isoniazid (isonicotinic acid hydrazide, INH), rifampicin (rifampin, RMP), pyrazinamide (PZA), ethambutol (EMB), and streptomycin (SM). These drugs are effective against actively metabolizing bacilli. Second line drugs are protionamide (PTA), ethionamide (ETA), thiacetazone, thiocarlide, cycloserine, capreomycine, and ρ -aminosalicylic acid (PAA), which are all bacteriostatic in nature and are utilized to strengthen the treatment of drug-resistant disease or when bactericidal drugs are prohibited because of toxicity. These were developed in the 1940s and 1950s, and all of these have since given rise to a drug-resistant clinical isolates when singly-administered during pharmacotherapy.

Drug-resistant Tuberculosis

After the development of useful TB drugs in the 1940's and 1950's, the number of deaths from tuberculosis in the U.S. dropped precipitously, about 6% annually for the next 30 years. It was widely perceived that the threat of tuberculosis was under control, and that it was a foregone conclusion that tuberculosis would be eradicated. Over the years increasing apathy led to a reduction of government funding for tuberculosis research and public health programs. Alarmingly, in the mid 1980's, the

number of active TB cases in the U.S. surged, and this upward trend continued into the 1990's. In hindsight, several factors were identified for the sharp increase. Tuberculosis enjoys a synergistic relationship with AIDS, where the progression of the HIV/AIDS epidemic leaves the immuno-compromised individuals more susceptible to TB infection. Lagging interest in tuberculosis as a public health threat led to the decay of the infrastructure necessary to monitor the disease within the population, due to budget restrictions. The rise in prominence of multiply-drug resistant strains of *M. tuberculosis* (MDR-TB) accompanied the lack of vigilance in combating TB. Even in the 1950's, resistance to singly-administered tuberculosis drugs was quite common. Due to the protracted duration necessary to clear tuberculosis infection (6-12 months), patient noncompliance to the complex drug regimens led to the appearance of a number of *M. tuberculosis* strains that gained resistance to many of the first line TB drugs. The World Health Organization (WHO) responded by developing a new public health strategy named Directly Observed Therapy-Short Course (DOTS) which centered around vigilant monitoring of the ingestion of each drug dose throughout the entire course of treatment. Briefly, the DOTS program consisted of a two-month treatment duration with a combination of four antibiotics including isoniazid, rifampicin, and pyrazinamide, complemented with either streptomycin or ethambutol, followed by a 6-month treatment with either ethionamide or ethambutol, or a 4-month treatment with isoniazid and rifampicin. This program resulted in a decrease of active cases each year beginning in 1993, culminating in less than 19,000 reported cases of TB in 1998. However, in this same time period, there were documented incidences of MDR-TB in virtually every US state. Globally, in regions such as Eastern Europe, Latin America, Africa, and Asia, MDR-TB accounted for more than 4% of new TB cases. This is a significant financial burden, as the cost of treating MDR-TB can approach \$250,000, roughly 10-15 times the cost of treating

a case of fully drug-sensitive tuberculosis (McKinney *et al.*, 1998).

The mechanism of drug resistance for some of the first line anti-tubercular drugs has been determined. Streptomycin (SM), the first successful drug against TB, is an aminoglycoside with broad-spectrum bactericidal properties, and targets the ribosomal machinery, eventually inhibiting translation. Resistance quickly arose against streptomycin, and the long-term detrimental side effects (liver damage) and inconvenient delivery system (injection) of streptomycin also relegated it to a lesser role for treatment of tuberculosis. Currently, the appearance of MDR-TB has renewed interest in SM administration as an anti-tubercular strategy. SM binds to the 30s ribosomal subunit near the ribosomal protein S12 and 16S rRNA, and disruption of these interactions allows SM to interfere with the formation of an initiation complex with mRNA, therefore inhibiting protein synthesis. The majority of SM-resistant strains is ascribed to a mutation in the *rpsL* gene that encodes for the S12 protein. Isoniazid (INH), the most effective and least toxic first-line tuberculosis drug, was widely distributed for anti-tubercular use in the 1950's. Drug-resistant strains began to emerge soon afterwards, with Gardner Middlebrook isolating and characterizing the nature of the first isoniazid-resistant mutations of *M. tuberculosis* in 1954. Middlebrook observed a loss of catalase-peroxidase activity in these mutants (Middlebrook, 1954), and indeed, a large percentage of the clinical isolates today have lost catalase-peroxidase activity. Isoniazid-resistant strains cause mortality in 70 to 90% of AIDS-stricken patients who develop tuberculosis (Snider and Roper, 1992). In 1992, it was confirmed that the loss of the catalase-peroxidase activity was due to mutation or deletion of the protein KatG that has been shown to activate INH (Zhang *et al.*, 1992), and some 25 to 50% of the MDR-TB strains are attributable to *katG* inactivation (Zhang *et al.*, 1992; Heym *et al.*, 1994; Stoeckle *et al.*, 1993). Between 20 to 25% of INH resistant strains have also been shown to possess mutations

in another gene, *inhA* (Heym *et al.*, 1994). Mutations in *inhA* were found in 30% of resistant *M. tuberculosis* isolates and were never found in sensitive isolates (Heym *et al.*, 1994; Morris *et al.*, 1995; Musser *et al.*, 1996; Ristow *et al.*, 1995; Telenti *et al.*, 1997). This gene encodes an enoyl-ACP reductase essential to mycolic acid biosynthesis. Genetic and structural data indicated that a KatG-activated isoniazid metabolite binds to the active site of InhA and forms an isonicotinic acyl-NADH adduct. This product remains bound to the active site of the enzyme, disrupting a pathway essential to mycolic acid biosynthesis. Mutations in the *inhA* gene result in a protein possessing reduced NADH binding affinity (Quemard *et al.*, 1995). Up to 80% of all INH resistant strains have mutations occurring in the *katG* or *inhA* genes (Scior *et al.*, 2002). As the formation of the isonicotinic acyl-NADH requires NADH to bind InhA before the fatty acid substrate, the slightly decreased affinity for NADH by the mutant protein hinders the formation of the covalent adduct, while still maintaining enzymatic activity (Quemard *et al.*, 1995). Pyrazinamide, discovered in 1952, is a paradoxical and unconventional drug. It is not effective against actively growing tuberculosis, unlike conventional antibiotics. Instead, it is more active against old non-growing bacilli (Zhang *et al.*, 2002). Its mode of action is still unclear, but it has been proposed to disrupt membrane transport and energetics (Zhang *et al.*, 2003). Resistance most often occurs through mutations in the *pncA* gene encoding pyrazinamidase (PZase), an enzyme that converts PZA into pyrazinoic acid, the presumed active form of PZA against bacteria (Raynaud *et al.*, 1999). Ethambutol is used as a bacteriostat to prevent the growth of drug resistant strains during treatment. The use of ethambutol was shown to inhibit arabinogalactan synthesis (Deng *et al.*, 1995), eventually leading to cell death. This inhibition has been shown to make the bacilli more susceptible to other anti-tubercular drugs such as isoniazid, streptomycin, and rifampin. A majority of the mutations leading to EMB

resistance have been traced to amino acid substitutions at position 306 or 406 the gene *embB* (Ramaswamy *et al.*, 2000).

Every primary-line TB drug administered via monotherapy has resulted in resistant strains of *M. tuberculosis*, so it is imperative research continues to focus on the discovery and development of new anti-tubercular compounds. Due to the appearance of MDR-TB and the synergistic relationship between HIV and tuberculosis infection, there is a greater threat than ever before. While wealthy industrialized countries with modern and more advanced public health care systems can be expected to contain tuberculosis, much of the developing world cannot effectively manage a tuberculosis crisis. Thus, there is a critical need for effective drugs that are not only effective, but also affordable, to globally combat MDR-TB.

Characteristics and Pathogenesis

The progression of tuberculosis infection has been classified into five distinct stages, beginning with the initial infection.

Stage 1 commences when contagious sputum from infected individuals are inhaled. These droplet nuclei are readily transmissible as aerosols, and are generated through seemingly innocuous activities such as talking, sneezing, or coughing. Infected individuals can produce up to 3,000 aerosol droplets per cough attack, and droplet nuclei can be spread to individuals ranging up to 10 feet away, and can persist for relatively long periods of time.

Stage 2, also called the symbiotic stage, is accompanied by a logarithmic growth of bacteria within immature macrophages, beginning 7-21 days after initial infection. *M. tuberculosis* multiplies virtually unrestricted within unactivated macrophages until the macrophages lyse. Other macrophages begin to extravasate from peripheral

blood to replace the destroyed macrophages and phagocytose *M. tuberculosis*, but they are also unactivated and cannot curtail infection.

Stage 3, beginning 2-3 weeks after initial infection, is delineated as the interval when destruction of tissue surrounding the site of infection first occurs. At this point lymphocytes begin to infiltrate and recognize processed and presented *M. tuberculosis* antigens. This results in T-cell activation and the liberation of cytokines including gamma interferon (IFN), which in turn initiates the activation of macrophages. These activated macrophages are now capable of destroying *M. tuberculosis*. Consequently, the individual becomes tuberculin-positive, and tubercle formation begins. The center of the tubercle is characterized by tissue destruction (fibrosis), presenting focal areas with necrotic cells, forming an amorphous granular cheese-like mass. The conditions within these tubercles are unfavorable to *M. tuberculosis* multiplication, because of low pH and anoxic environment. *M. tuberculosis* can, however, persist within these tubercles until conditions favor reactivation.

Stage 4 is a critical juncture, determining whether the infection is halted, or whether disease progresses. Although many activated macrophages can be found surrounding the tubercles, the remainder may remain unactivated or poorly activated. *M. tuberculosis* uses these macrophages to replicate and hence the tubercle grows, possibly invading a bronchus and spreading to other parts of the lung. Similarly, the tubercle may invade an artery, vein, or other blood supply line. The hematogenous spread of *M. tuberculosis* may result in extrapulmonary tuberculosis otherwise known as miliary tuberculosis. The secondary lesions caused by miliary tuberculosis can occur at virtually any anatomical location, but usually involve the genitourinary system, bones, joints, lymph nodes, and peritoneum.

Stage 5 is characterized by liquefaction of the tubercle surrounding the bacilli, and may occur several years after initial infection. Usually, the immune system is

not prepared for this contingency. For unknown reasons, the caseous centers of the tubercles begin to liquefy, liberating material conducive to growth. The organism begins to rapidly multiply extracellularly. After time, the large antigen load causes the walls of nearby bronchi to become necrotic and rupture, forming cavities and allowing entrance into other airways and rapid spreading to other parts of the lung.

Only a very small percent of tuberculosis infections result in disease, and an even smaller percentage of infections progress to an advanced stage. Usually the host will begin to control the infection at some point. When the primary lesion heals, it becomes fibrous and calcifies, becoming what is termed the Ghon complex. Depending on the size and severity, the Ghon complex may never subside and is readily visible upon chest x-ray. Small metastatic foci containing low numbers of bacillus may also calcify. However, in many cases these foci will contain viable organisms and are referred to as Simon foci. The Simon foci are also visible upon chest X-ray, and are often the nucleation site of disease reactivation.

Defense Mechanisms

Mycobacterium tuberculosis is very well optimized for host invasion and survival, but does so largely without the benefit of classical bacterial virulence factors such as toxins, capsules and fimbriae. However, a number of structural and physiological properties of the bacterium are beginning to be recognized for their contribution to bacterial virulence and the pathology of tuberculosis. *Mycobacterium tuberculosis* has specialized mechanisms to facilitate cell entry. The tubercle bacillus can bind directly to mannose receptors on macrophages *via* the cell wall-associated mannosylated glycolipid, LAM, or indirectly via certain complement receptors or Fc receptors. *M. tuberculosis* can grow intracellularly, providing an effective means of evading the

immune system. In particular, antibodies and complement are ineffective in this location. Once phagocytosed, *M. tuberculosis* can inhibit phagosome-lysosome fusion. The exact mechanism utilized to accomplish this is not known but it is thought to be the result of a protein secreted by bacterium that modifies the phagosome membrane. The bacterium may remain in the phagosome or escape from the phagosome, in either case finding a protected environment for growth in the macrophage. *M. tuberculosis* also interferes with the toxic effects of reactive oxygen intermediates (ROI) produced in the process of phagocytosis by two mechanisms: (i) Compounds including glycolipids, sulfatides and LAM down regulate the oxidative cytotoxic mechanism; (ii) macrophage uptake via complement receptors may bypass the activation of a respiratory burst. There also exists an antigen 85 complex that is composed of a group of secreted proteins known to bind fibronectin. These proteins may aid in walling off the bacteria, barricading it from the immune system and may also facilitate tubercle formation. The slow generation time can also be considered a defense mechanism. Because of the slow generation time of *M. tuberculosis*, the immune system may not readily recognize the bacteria or may be weakly triggered, to an extent insufficient to eliminate them. Many other chronic diseases are caused by bacteria with slow generation times, for example, slow-growing *M. leprae* causes leprosy, *Treponema pallidum* causes syphilis, and *Borrelia burgdorferi* causes Lyme disease. The high lipid concentration in cell wall accounts for impermeability and resistance to antimicrobial agents, resistance to killing by acidic and alkaline compounds in both the intracellular and extracellular environment, and resistance to osmotic lysis via complement deposition and attack by lysozyme. Cord factor is another defense mechanism, although poorly understood. The cord factor is primarily associated with virulent strains of *M. tuberculosis*. It is known to be toxic to mammalian cells, but its exact role in tuberculosis virulence is unclear.

Mycobacterial Envelope

The mycobacterial envelope provides a unique and formidable defense mechanism, and can be subdivided into three discrete units: the capsule, the cell wall, and the cell membrane. While the plasma membrane of mycobacteria is very similar to that found in other bacteria such as *Escherichia coli*, the unique mycobacterial cell wall is distinguished by its great enrichment of covalently linked mycolic acids, and possession of a disordered capsule. These two additions distinguish mycobacteria from gram positive bacteria, that typically contain peptidoglycan as the dominant component of the cell wall. The cell wall and capsule in particular provide a waxy, highly impermeable defense mechanism against antibiotic agents, as well as the host organisms' defenses.

Capsule

The first discrete unit, the capsule, is composed of a mixture of polysaccharide, protein, and lipid, and forms the outermost and most complex layer of the mycobacterial cell envelope. Electron micrograph studies illustrated that the capsule is a heterogeneous and fluid component of the cell envelope. Closer examination of the capsule revealed that there were several elements that give *M. tuberculosis* both passive and active defense mechanisms against the host cell. The highly impermeable nature of the capsule contributes to passive resistance to acids, alcohols, alkaline conditions, and reactive oxygen intermediates. However, the capsule also contains protein and lipid components (such as β -lactamases, cord factor, host cell disruption enzymatic activities) that give *M. tuberculosis* active resistance against host defenses. Thus, the capsule provides a significant amount of protection to the bacillus by not only passively limiting the influx/efflux/access of the host cell (or antibacterial drugs) to the

bacillus, but also actively allowing the bacillus to hinder the action of host enzymes, modulate the host immune response, and process host-derived materials for use by the mycobacterium. These unique abilities allow *M. tuberculosis* to survive and even thrive within the harsh environment of macrophages, where immune system threats are typically destroyed. In conditions inhospitable to TB proliferation, the bacillus can also enter a dormant stage and linger until conditions are favorable for growth.

Electron microscopy and chemical extraction experiments have allowed researchers to better characterize the contents of the capsule as an extensive conglomerate of non-covalently attached lipids, acyl trehaloses, polysaccharides, proteins, and glycopeptidolipids. The capsular components exist in a fairly conserved fashion amongst all mycobacteria, but the envelope varies in thickness depending on species. Specifically, analysis of extracted capsule material indicates conservation of many neutral polysaccharides, small amounts of various lipids, and proteins. However, the relative proportions of the capsular components vary considerably among different species. The most prominent components of the *M. tuberculosis* capsule are a glucan, arabinomannan, and a mannan, along with other as yet uncharacterized oligo- and polysaccharides (Daffé and Etienne, 1999). The glucan, the most prevalent capsular polysaccharide, is similar to internal glycogen found in mycobacteria, consisting of short, branched chains of 4-linked α -D-glucosyl residues substituted at position 6 with mono- or di-glucosyl residues. The arabinomannan is formed by chains of 6-linked mannosyl residues (occasionally branching at the 2 position) attached to arabinose chains similar to those found in the cell wall, but are capped by oligomannosides in slow growing mycobacteria.

The outer surface of the capsule consists primarily of protein and carbohydrates, with approximately 2-5% of the material being lipid. Most of the lipid appears to be in the inner portion of the capsule. Because of this arrangement, there is little or

no interaction of lipids with the host immune system before lysis of the bacteria by immune cells. However, there are limited number of capsular lipids that appear to have very important effects on host cells. Sulfatides are acidic glycolipids that seem to interfere with the host immune response, including inhibition of phagosome/lysosome fusion, inhibition of macrophage activation, stimulation of tumor necrosis factor- α , and stimulation of neutrophils.

An important capsular lipid, trehalose dimycolate (TDM or cord factor) still has no clear function ascribed to it. However, TDM has been implicated in the pathogenicity of tuberculosis and is thought to be vital to the structural integrity of the cell wall. TDM has been shown to be highly toxic in mice when prepared as an emulsion, and the toxicity of TDM is also synergistically enhanced *in vivo* by the presence of the major sulfatide of *M. tuberculosis*.

Several important capsule-associated proteins have been identified. Thus far, only a limited number have been fairly well characterized and indicate a role in either pathogenicity or cell wall biosynthesis. These include proteins involved in β -lactam antibiotics resistance, cell wall biosynthesis, lectin binding, phospholipids degradation, hemolytic activity, nitrogen assimilation, host cell scavenging, reactive oxygen intermediate (ROI) detoxification, resistance to oxygen limitation, and mycobacterial aggregation. The class A β -lactamase BlaC, which destroys β -lactam based antibiotics such as penicillin and cephalosporins, possesses a lipid attachment site to localize it to either the capsule or the cell wall (Cole *et al.*, 1998). PstS1, a 38 kDa lipoprotein, may be responsible for scavenging environmental phosphate, as expression is upregulated during phosphate starvation (Espitia *et al.*, 1992). FAP-B is a glycoprotein that has been implicated in binding human fibronectin, efficient invasion of epithelial cells, and possibly also in molybdate uptake (Cole *et al.*, 1998). Superoxide dismutase (SOD) protects the bacteria from oxidative stress through the

destruction of ROI. The antigen 85 complex is responsible for the biosynthesis of trehalose dimycolate.

The capsule-associated proteins help ensure enhanced survival through various means by acting against the host immune response as well as having the responsibility for cell wall maintenance. The passive permeability barrier constructed from a diverse collection of lipids is augmented by capsule-associated proteins that actively synthesize compounds that interfere with specific pathways in the host. There are yet to be identified factors within the capsule that allow *M. tuberculosis* to enter the host cell, multiply within the environment of the host tissues, resist host defense mechanisms, and cause damage to the tissues of the host.

Cell Wall

The second discrete unit of the mycobacterial envelope is the cell wall of *M. tuberculosis*, a truly unique work of architecture. Over the past 50 years, our understanding of the structure of the mycobacterial cell wall and its associated lipids has been enhanced by recent developments in NMR and mass spectral studies, as well as sequencing of the genome. The cell wall is composed of two segments, an upper layer and a lower layer. The upper layer is centered around a massive core comprised of peptidoglycan covalently attached via a diglycosylphosphate linker unit (L-Rha-D-GlcNAc-P) to a linear galactofuran, in turn attached to several strands of a highly branched arabinofuran, in turn attached to their signature mycolic acids, with their long (up to C₆₀) meromycolate chains and shorter α -chains (Brennan, 2003), depicted in Figure 24.

This cell wall core is termed the mycolyl arabinogalactan-peptidoglycan complex (mAGP). The mycolic acids are oriented perpendicular to the plasma membrane, and form a highly impermeable lipid barrier responsible for the physiological

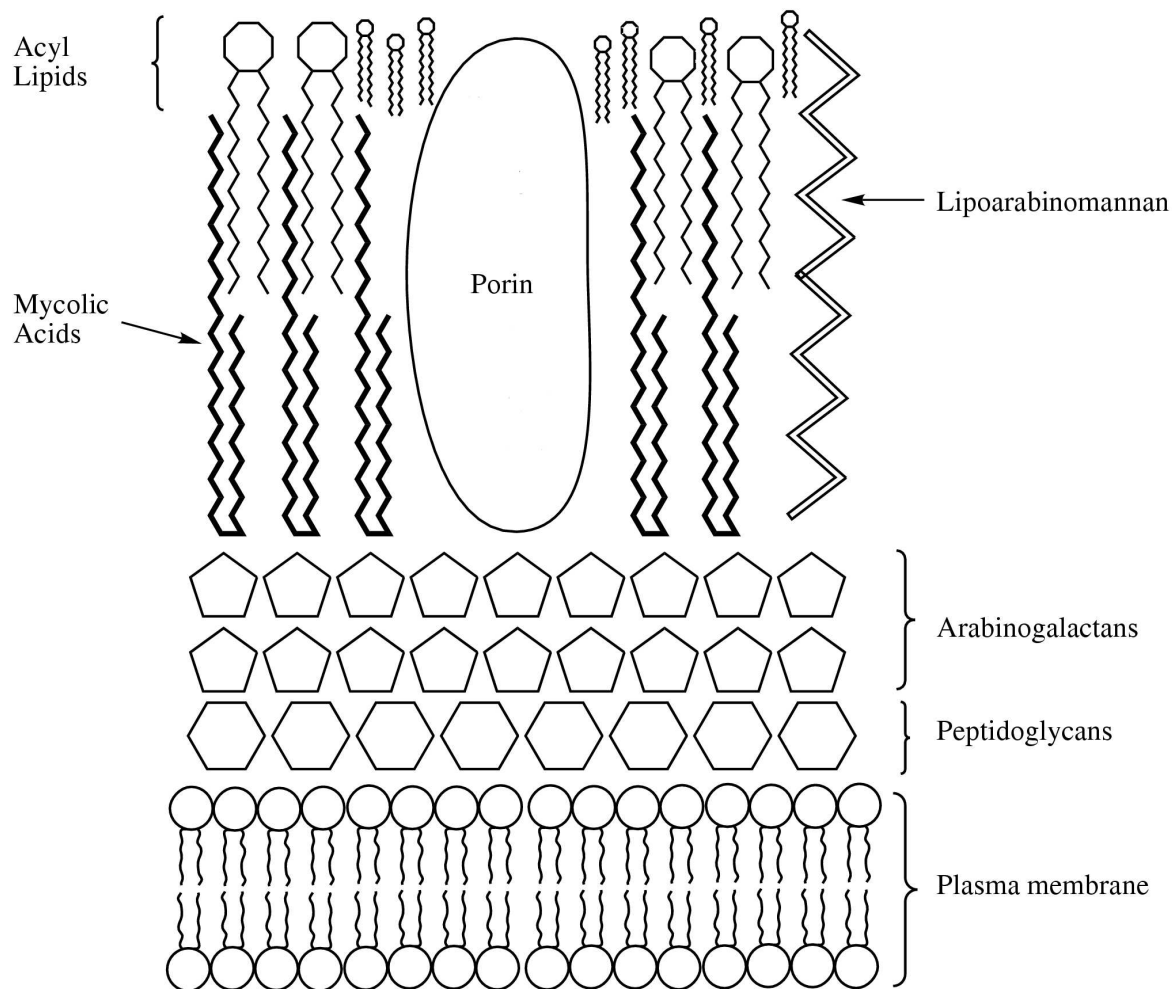


Figure 24: Structure of the mycobacterial cell wall skeleton. The core of the mycobacterial cell wall is the mycolyl-arabinogalactan-peptidoglycan complex (mAGP). The mycolic acids form a thick, highly hydrophobic, and impermeable barrier, and are covalently linked to the arabinogalactan layer, which is in turn linked to the peptidoglycan layer. The mycobacterial cell wall is also reduced in porin content. These factors allow the mycobacterial cell wall to function as a highly efficient permeability barrier.

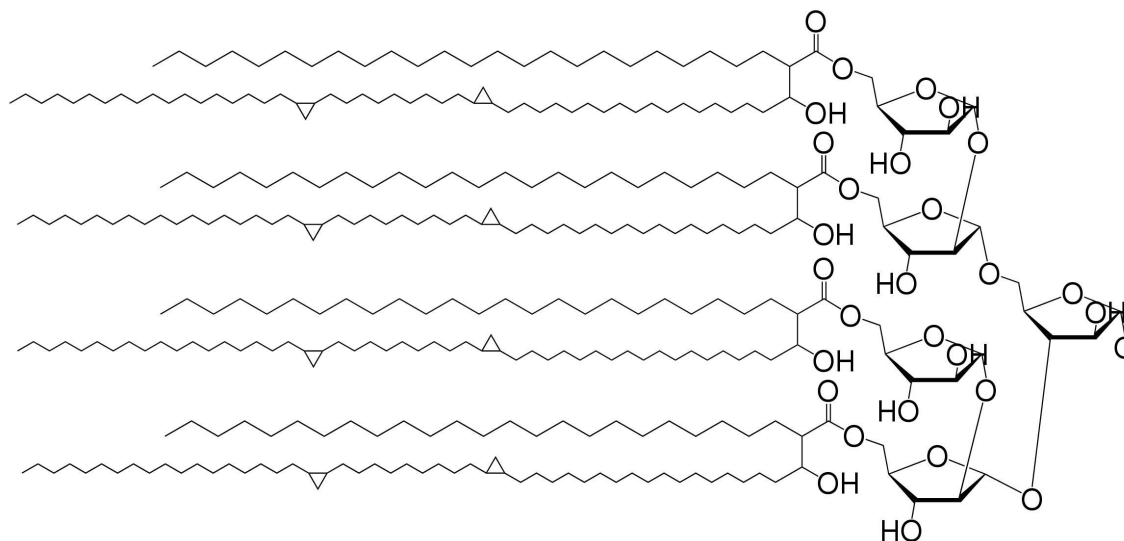


Figure 25: Structure of the arabinogalactan-mycolate cluster. The structure of the arabinogalactan-mycolate cluster is shown above. The β -branch of the α -mycolate is reduced in scale for clarity. Mycolic acids are shown covalently linked to the terminal arabinose residues *via* an ester linkage. The α - and β -branches are able to pack virtually parallel with each other, allowing the formation of a highly hydrophobic, tightly stacked, and extremely impermeable barrier.

and disease-inducing aspects of *M. tuberculosis*. The fine structure of the mycolyl-arabinogalactan cluster is illustrated in Figure 25. Interspersed throughout are several types of lipids, including phthiocerol dimycocerosate, cord factor / dimycolyl-trehalose, the sulfolipids, the phosphatidylinositol mannosides (PIMs), lipomannan (LM), and lipoarabinomannan (LAM). These lipids have been implicated in signaling events, in pathogenesis, as well as the immune response. Also intercalated in this layer are several cell-wall proteins.

When mycobacterial cell walls are disrupted through chemical extraction, the free lipids, proteins, LAM, and PIMs are solubilized, and the mycolic acid-arabinogalactan-peptidoglycan complex remains as the insoluble remnants. These soluble lipids, proteins, and lipoglycans, can be considered the signaling and effector molecules in tuberculosis progression, whereas the insoluble core is essential for the viability of

the cell. For example, cord factor (trehalose dimycolate) exerts considerable toxic effects when injected in small amounts (10 μg) peritoneally into mice. Death is associated with intense peritonitis and acute pulmonary hemorrhage. Sulfolipids were reportedly highly represented in the most virulent strains of mycobacteria, whereas the attenuated strains were deficient in these components. Phthiocerol dimycolate is a waxy, major lipid of the tubercle bacillus, and also reported to be implicated in *M. tuberculosis* virulence. Also present are the free lipids PIM, LM, and LAM. They are based on phosphatidyl inositol (PI), and attached to the inositol there may be as many as 6 mannose molecules. These lipids are of interest because LAM from *M. tuberculosis* has short mannose-containing oligosaccharide caps that allow it to bind to the mannose receptor on macrophages. LAM can bind to Toll receptors and physically insert itself into membranes, inducing numerous types of signal transduction events important in the host response in tuberculosis.

The peptidoglycan (lower layer) of the cell wall is quite similar to that of other gram-positive bacteria. In the most common form of peptidoglycan, chains of alternating residues of N-acetylglucosamine (NAG) and N-acetylmuramic acid (NAM), covalently attached through a $\beta 1 \rightarrow 4$ glycosidic linkage, are cross-linked by a tetrapeptide chain (L-alanyl-D-isoglutaminyl-*meso*-diaminopimelyl-D-alanine). The crosslink between the tetrapeptide chains occurs between the diaminopimelic acid of one chain and the D-alanine of a neighboring chain. The mycobacterial peptidoglycan differs from the common type in two ways. First, the muramic acid is N-glycosylated rather than N-acetylated. Secondly, some of the muramic acid crosslinks involve bonds between diaminopimelic acid groups of different tetrapeptides. The minor differences are of unknown significance.

Plasma Membrane

The third component of the mycobacterial cell envelope is the plasma membrane, which bears great similarity to the plasma membranes of other bacteria. Lying below the capsule and cell wall, the mycobacterial plasma membrane is composed primarily of asymmetrically distributed polar lipids possessing a fatty acyl chain and a hydrophilic head group. Its composition is very similar to typical bacterial plasma membranes, and not thought to play a vital role in pathological processes (Daffé and Etienne, 1999). Phospholipids in the form of phosphatidylinositol mannosides (PIMs), phosphatidylglycerol, cardiolipin, and phosphatidylethanolamine, comprise the majority of the lipid content of the plasma membrane. However, some lipids, notably phosphatidylinositol mannosides and phosphatidylethanolamine, are also present in purified cell walls and on the capsular surfaces of all mycobacterial species examined. While the locations of various mycobacterial molecules can be generalized, the envelope is in reality a dynamic entity, where mycobacterial molecules are moving within and throughout the envelope and even the cell wall skeleton is being reconstructed.

Mycolic Acid Synthesis

Mycolic acids are the major constituent of *M. tuberculosis* cell wall structure. They form a highly impermeable protective layer, and are involved other important roles such as forming the structural components of the cell wall and envelope. As mycolic acids possess such critical roles in tuberculosis for host cell evasion, enzymes involved in their biosynthesis offer attractive targets in the battle against tuberculosis. Mycolic acids, defined as α -alkyl, β -hydroxy long chain fatty acids, are proposed to be synthesized via a five stage pathway: (i) synthesis of C₂₀ to C₂₆ straight-chain

saturated fatty acids to provide the α -alkyl branch; (ii) synthesis of the meromycolic acid chain to provide the main carbon backbone, (iii) modification of this backbone to introduce other functional groups, (iv) the final Claisen-type condensation step followed by reduction; and (v) various mycolyltransferase processes to cellular lipids (Schroeder *et al.*, 2002). At the heart of this process is fatty acid biosynthesis, essential for producing the precursors of mycolic acids. Mycolic acids typically exist as a homologous series of fatty acids differing by two-carbon units and are characterized by very hydrophobic C₅₄ to C₆₃ fatty acids with C₂₂ to C₂₄ α -side chains. There are three distinct structural classes of mycolic acids found in *M. tuberculosis*, and they are the α -, methoxy-, and keto-mycolic acids (Figure 26). The α -mycolic acid is the most abundant form (>70%), whereas the methoxy- and keto-mycolic acids are the minor components (10-15%). Cyclopropane rings incorporated into mycolic acids contribute to the structural integrity of the cell wall complex and protect the bacillus from oxidative stress. Deletion of the proximal cyclopropane ring in of α -mycolic acid or of methoxy- and keto-mycolates in *M. tuberculosis* leads to a significant attenuation in growth of the two mutants in the mouse model of infection. A deletion of the keto-mycolates leads to restricted growth of this mutant in macrophages. Thus, the fine structure of mycolic acids is associated with virulence of *M. tuberculosis*. Inhibition of mycolic acid synthesis has been shown to induce the lysis of *M. smegmatis* cells (Vilcheze *et al.*, 2000), emphasizing the importance of its role in forming the highly impermeable and protective barrier. The process of fatty acid biosynthesis holds the central role in the production of mycolic acids. Two distinct types of fatty acid biosynthesis, FAS-I and FAS-II, have been characterized within *M. tuberculosis*.

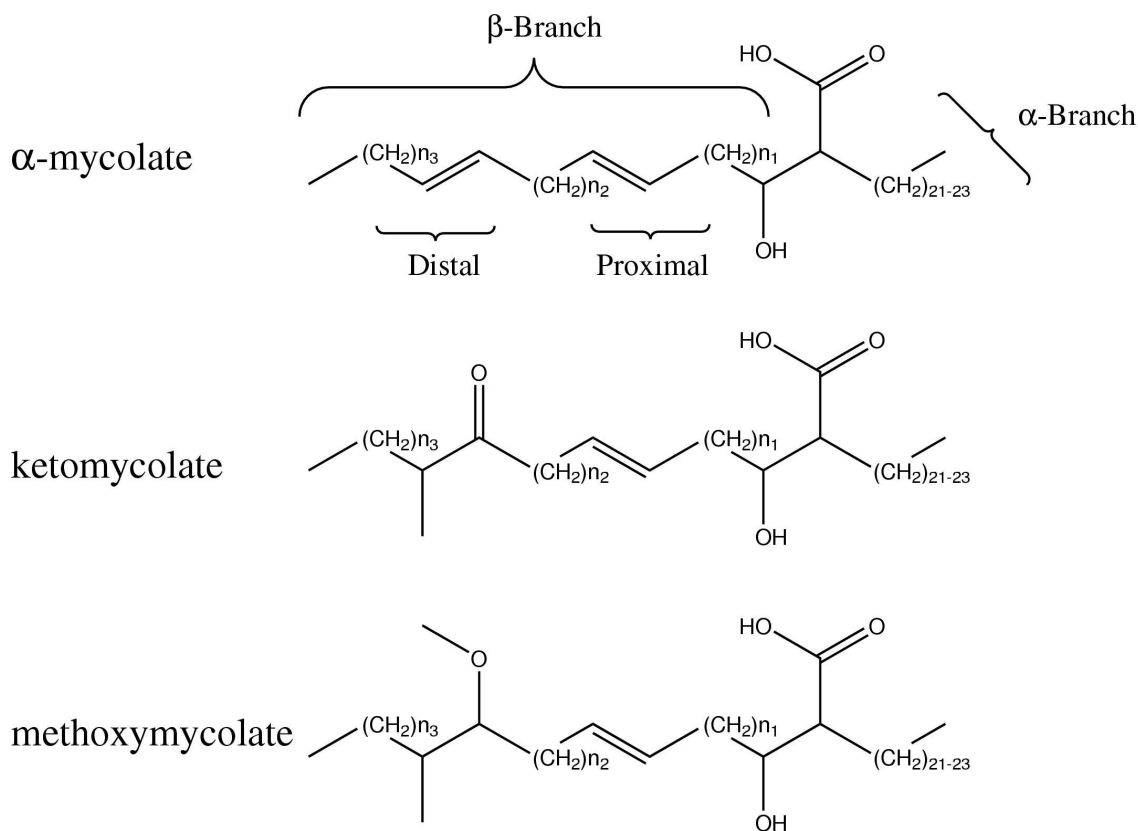


Figure 26: Chemical structures of mycolic acids. There are five forms of mycolic acids in *M. tuberculosis*, illustrated by the three main families of mycolic acids with α -, methoxy-, and keto-mycolates. The α - and β -branches are indicated. Cyclopropane groups may be incorporated into the β -branch. The cyclopropane rings in α -mycolic acids would have the *cis* configuration, while the methoxy- and keto-mycolic acids can have either the *cis* or *trans* configuration on the proximal cyclopropane ring. The length of the n_1 and n_3 units are normally 15,17, or 19 carbons long, while the n_2 units are usually between 12 and 17 carbons, depending on modifications at the proximal and distal sites.

Type I Fatty Acid Biosynthesis

A single gene, *fab*, encodes the multifunctional FAS-I system of *M. tuberculosis*. The 2 MDa protein expressed by this gene forms a homodimer containing all of the required functions of a *de novo* fatty acid synthesis system (Smith *et al.*, 2003). Studies of how *Mycobacterium* synthesize C₁₆ to C₁₈ and C₂₄ to C₂₆ fatty acids date back to the 1970s, when Bloch *et al.* showed that *M. smegmatis* possess both a type I fatty acid synthetase (FAS-I) and a type II fatty acid synthetase (FAS-II) system. The main distinction between the two systems is the arrangement of the enzymes involved, with FAS-I having a large single, multifunctional polypeptide encompassing all of the enzyme activities, whereas the FAS-II system has each enzymatic activity isolated on individual, dissociated proteins. Typically FAS-I systems are found in eukaryotes and advanced prokaryotes, while the FAS-II systems are found in plants and bacteria. Both the FAS-I and FAS-II systems were found in *M. tuberculosis*, and were later shown to be very similar to those from *M. smegmatis*. The FAS-I system synthesizes *de novo* fatty acids from two-carbon units, using acetyl-CoA and malonyl-CoA as substrates, releasing C₂₀ to C₂₆ products. FAS-I also produces hexacosanoyl-CoA (C₂₆) and this fatty acid becomes the short α -alkyl chain and methyl carboxyl segment of all mycolic acids of *M. tuberculosis*.

Type II Fatty Acid Biosynthesis

In *M. tuberculosis*, fatty acid biosynthesis also proceeds through a basic FAS-II elongation cycle shown in Figure 27. It has been proposed that the C₂₀ fatty acid is the starting point where the FAS-II systems take over for the synthesis of the very-long-chain mero segment of α -, methoxy-, and keto-mycolic acids (Takayama *et al.*, 2005). Malonyl-S-acyl carrier protein (malonyl-S-ACP, a co-substrate in reaction 1 of Fig-

ure 27). Through successive cycles by β -ketoacyl-ACP synthase (KasA/KasB) and β -ketoacyl-ACP reductase, R-CO-S-ACP is converted to R-CHOH-CH₂-CO-S-ACP (reactions 1 and 2). This product is then converted to *trans*-R-CH=CH-CO-S-ACP by β -hydroxyacyl-ACP dehydrase (reaction 3). The gene encoding this enzyme has yet to be identified in the *M. tuberculosis* genome. The product of reaction 3 is reduced by 2-*trans*-enoyl-ACP reductase (InhA) to yield R-CH₂-CH₂-CO-S-ACP, which is two carbons longer than the starting substrate. This product can then be utilized in another FAS-II cycle of elongation, and the process begins anew.

Cyclopropane synthases and Methyltransferases

Many interesting modifications are observed within mycolic acids. These functional modifications confer advantageous properties to the cell wall, and contribute to the tight packing of the long-chain mycolates. The cyclopropanation of mycolic acids also conveys resistance to host cell processes, and have profound effects on the resistance of the mycobacteria to oxidative stress and the fluidity and permeability of the cell wall. A few important mycolic acid modifying enzymes have been characterized. MmaA2 is required for the introduction of the distal cyclopropane ring in the formation of α -meroacid. PcaA (UmaA2) is required for the introduction of the proximal distal ring in the formation of α -meroacid. MmaA4 introduces the distal-branch methyl group in the formation of *trans*-oxygenated meroacids. MmaA3 O-methylates the distal secondary alcohol in the formation of *cis*- and *trans*-methoxy-meroacids. MmaA2 and CmaA2 are required for the introduction of the proximal *cis*-cyclopropane ring in methoxy-meroacids, and Mma2 is required for the introduction of the proximal *cis*-cyclopropane ring in keto-meroacids. MmaA1 and CmaA2 are required for the introduction of the proximal-branch methyl group and *trans*-cyclopropane ring in *trans*-oxygenated meroacids.

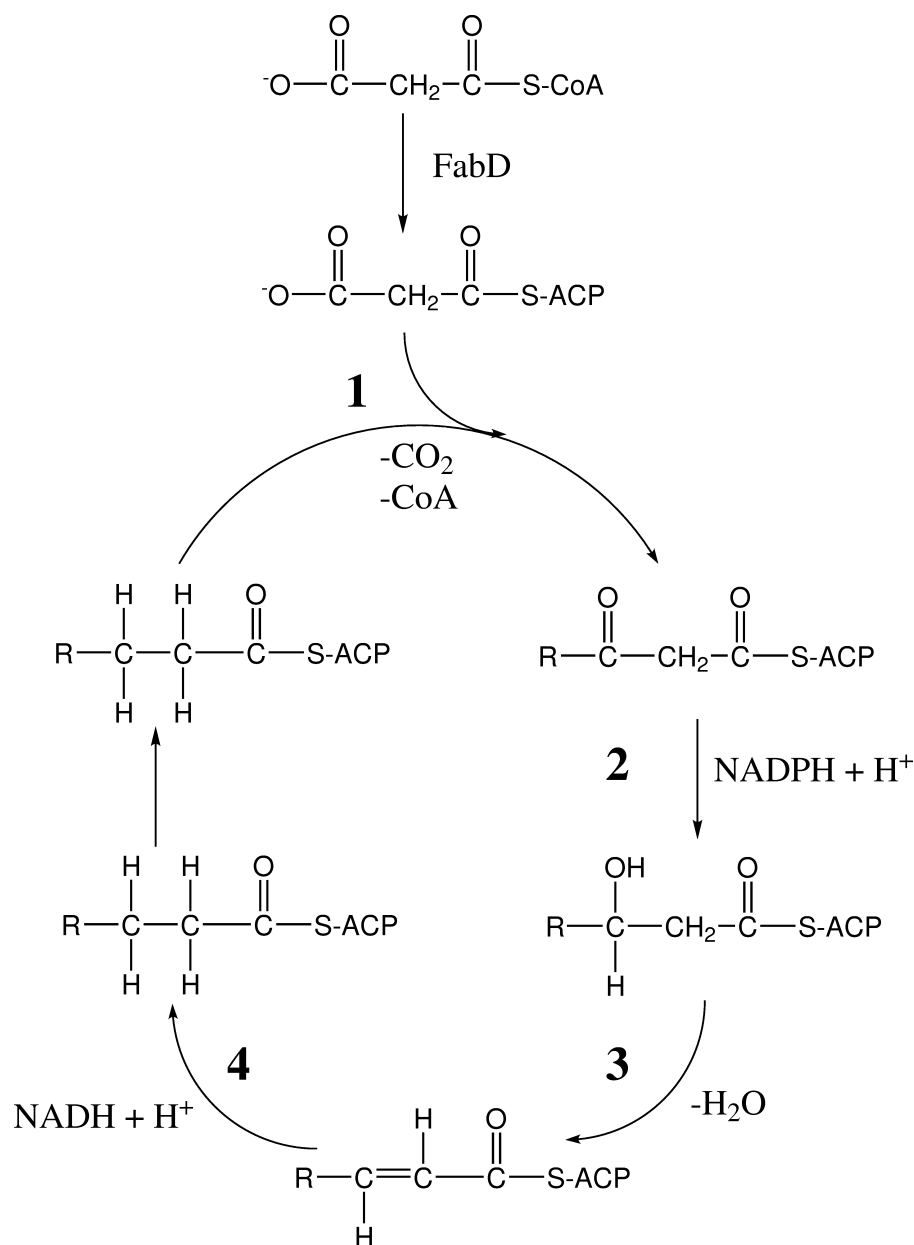


Figure 27: FAS-II fatty acid biosynthesis by *M. tuberculosis*. The substrates are R-CO-S-ACP and malonyl-S-ACP derived from malonyl-S-CoA by FabD. R, long-chain alkyl group. Enzymes involved in these reactions are as follows: **1**, β -ketoacyl-ACP synthase (KasA/KasB); **2**, β -ketoacyl-ACP reductase; **3**, β -hydroxyacyl-ACP dehydrase; **4**, 2-*trans*-enoyl-ACP reductase (InhA). The product of the last reaction undergoes the next cycle of elongation as the ACP derivative on another FAS-II module. This is a long-chain fatty acid elongation system in which the hydrocarbon chain is increased by two carbons with the completion of each cycle.

***M. tuberculosis* Enoyl Acyl-Carrier-Protein Reductase**

As mycolic acids possess such a critical role in the viability of tuberculosis against host cell defenses, the underlying pathways responsible for their synthesis were targeted. The focus of this study, *M. tuberculosis* enoyl-ACP reductase (InhA), is a NADH-dependent that participates in fatty acid biosynthesis. InhA catalyzes the final step of reduction in the FAS-II elongation cycle through the reduction of 2-*trans*-enoyl chains ($> C_{12}$) to yield saturated chains (Figure 28). InhA has been identified as an excellent anti-tubercular target for several reasons. First of all, the first-line anti-tubercular drug isoniazid has been shown to inhibit mycolic acid synthesis, and specifically target InhA (Banerjee *et al.*, 1994). Temperature sensitive inactivation of *M. smegmatis* InhA resulted in inhibition of mycolic acid synthesis and subsequently a drastic change in cell morphology indicative of mycobacterial cell lysis, emphasizing the critical role InhA possesses in tuberculosis viability Vilcheze *et al.*, 2000. Second, there exist several known inhibitors of homologous enoyl-ACP reductases from other organisms, and the underpinnings of the mechanism have been extensively studied, as well as the mode of action of the inhibitors. Third, only one enoyl-ACP reductase is present in *M. tuberculosis*, unlike some of the other enzymes in bacterial FAS-II systems Heath and Rock, 1995. Finally, the longer chain substrate specificity of InhA distinguishes it from the enoyl-ACP reductases from other sources, such as the enoyl-ACP reductase component of the human FAS-I system.

Mechanism

Previous studies with InhA have proposed that substrate reduction occurs via a stepwise mechanism in which hydride transfer precedes protonation (Quemard *et al.*, 1995). In enzymatic experiments conducted by Parikh *et al.* (Parikh *et al.*, 1999),

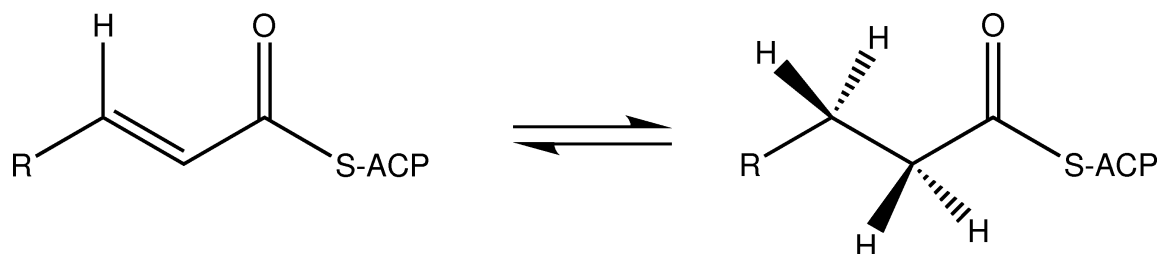


Figure 28: *M. tuberculosis* enoyl-ACP reductase reaction. The substrate is a 2-*trans*-enoyl-ACP, which is reduced to yield a saturated chain in a NADH-dependent manner. The mechanism is via a transfer of a hydride ion from the co-factor to the substrate.

they characterized InhA's mechanism of action through kinetic isotope experiments and mutational analysis. There are two critical conserved residues, Tyr¹⁵⁸ and Lys¹⁶⁵, that form a hydrogen bond to the substrate/inhibitor and cofactor, respectively. Replacement of these residues with Y158F and K165A resulted in a decrease of 24 and 1500-fold in k_{cat} . However, mutation to Y158S restored wild-type activity. Kinetic isotope studies indicated that the transfer of a solvent-exchangeable proton is partially rate-limiting for the wild-type and Y158S enzymes, but not for the Y158A mutant. These data indicated that Tyr¹⁵⁸ does not function formally as a proton donor in the reaction but likely functions as an electrophilic catalyst, stabilizing the transition state for hydride transfer by hydrogen bonding to the substrate carbonyl. It has been suggested that the 2'-hydroxyl oxygen of the nicotinamide ribose of NADH may also stabilize the enolate intermediate through its hydrogen bonding interaction with the fatty acyl substrate carbonyl thioester oxygen (Rozwarski *et al.*, 1999). Replacement of Lys¹⁶⁵ with K165Q or K165R had no effect on the enzyme's catalytic ability to bind NADH, showing that they are able to substitute for lysine. However, K165A and K165M mutations resulted enzymes unable to bind NADH, indicating that Lys¹⁶⁵ has a primary role in co-factor binding. These data are consistent with a mechanism where InhA catalyzes the reduction of the *trans* double bound

between positions C2 and C3 of the fatty acyl substrate through the formation of an enolate intermediate through the direct transfer of a hydride ion from NADH to position C3 of the substrate, followed by protonation at position C2.

Inhibition

Two inhibitors have been well characterized against *M. tuberculosis* InhA, namely isoniazid and triclosan. Several early reports on the mechanism of action of isoniazid suggested an effect on cell wall integrity. It was observed that acid-fastness, an important clinical diagnostic tool for *M. tuberculosis* infection, was lost shortly after treatment with isoniazid, presumably destroying the layer that allows the acid-fast staining property unique to mycobacteria (Koch-Weser *et al.*, 1953). Nearly two decades later, it was demonstrated that isoniazid inhibits the synthesis of mycolic acids in *M. tuberculosis* (Winder *et al.*, 1970), and a direct correlation between isoniazid uptake, viability, and mycolic acid biosynthesis was noted (Takayama *et al.*, 1972; Wang and Takayama, 1972). Isoniazid, the most effective and widely used drug against tuberculosis since the 1950's, has a somewhat complicated mode of action. Isoniazid is a pro-drug that must be converted, via a mycobacterial catalase-peroxidase enzyme KatG, into an activated form of the drug. The activated form of isoniazid, suspected to be an isonicotinic-acyl radical, becomes covalently attached to the nicotinamide ring of the NADH bound within the active site of InhA.

Crystal structures of the isoniazid-inhibited InhA revealed the basis for its tight interaction. The location and orientation of the isonicotinic acyl group are complementary to those of the surrounding InhA side chains, which creates a specific hydrophobic binding pocket for the isonicotinic acyl group. When compared to the crystal structure of the native InhA:NADH complex, the only significant difference in the conformation of the protein is the side chain of Phe¹⁴⁹ rotates approximately

90° to optimize aromatic ring-stacking interactions with the pyridine ring of the isonicotinic acyl group. This NADH adduct acts very potently ($K_i = 0.75$ nM) as a slow, tight-binding inhibitor (Rawat *et al.*, 2003). As it turns out, a substantial fraction of clinical isolates that are resistant to isoniazid are attributable to mutations or deletions of *katG*, so a drug that could circumvent this requirement for activation, but still inhibit InhA, would hold tremendous promise.

Triclosan, unlike isoniazid, does not require activation to achieve inhibition. Triclosan is a broad-spectrum antibacterial agent that enjoys widespread applications in a multitude of consumer products, including soaps, toothpastes, dermatological products, and is even embedded into toys (Bhargava and Leonard, 1996). It had been widely deployed under the assumption that triclosan had a nonspecific mode of action for disrupting bacterial membranes, therefore making it unlikely that resistance could arise (Russell, 2000). However, Heath *et al.* identified the enzyme triclosan specifically targets to be the FAS-II enoyl-ACP reductase in *E. coli*, and triclosan-resistant bacteria have been identified. Early experiments with *E. coli* FabI showed triclosan to be a potent inhibitor, with a $K_i = 38$ pM at saturating NAD^+ concentration (Ward *et al.*, 1999). Subsequent genetic studies have also revealed that mutations in the enoyl reductase from *M. smegmatis* result in resistance to triclosan (McMurry *et al.*, 1999). *M. tuberculosis* InhA is structurally similar to *E. coli* FabI and 87% identical to the *M. smegmatis* enoyl reductase, implying that *M. tuberculosis* InhA could also be inhibited by triclosan. Triclosan was later shown to directly inhibit *M. tuberculosis* InhA in *in vitro* enzyme assays (Parikh *et al.*, 2000). Interestingly, triclosan is a relatively weak inhibitor of InhA compared to the *E. coli* FabI (Parikh *et al.*, 2000), with *M. tuberculosis* InhA having an affinity for triclosan approximately 10,000-fold less than for the *E. coli* FabI ($K_i = 0.22$ μM versus 38 pM).

It has been well documented that mycolic acid and cell wall biosynthesis are excellent targets for anti-tuberculosis drugs. From a rational drug design perspective, the InhA protein in particular is an excellent target, as biochemical and genetic data indicate it is crucial to the viability of the bacillus. Structural information arising from the structures of InhA in complex with various inhibitors will greatly enhance drug discovery efforts by elucidating the key elements of inhibitor binding. Specifically, the structure of InhA with inhibitors that do not require activation, such as triclosan, will be a great weapon against drug-resistant tuberculosis.

CHAPTER VI

CRYSTALLOGRAPHIC STUDIES OF INHA*

Results and Discussion

To facilitate the drug design process, we determined the crystal structure of the ternary complex of InhA, NAD⁺, and triclosan. Triclosan appears to be an analog of an intermediate in catalysis, and is classified as a slow, tight-binding, reversible inhibitor. Triclosan does not require activation, nor does it covalently attach to cofactor. In the previously determined structures of *E. coli* FabI with triclosan (Ward *et al.*, 1999; Qiu *et al.*, 1999; Stewart *et al.*, 1999; Levy *et al.*, 1999), the phenol ring of triclosan stacked above the nicotinamide ring of the coenzyme, which is positively charged for NAD⁺, raising the possibility of a charge-transfer effect, which may contribute to affinity (Ward *et al.*, 1999). This may increase the preference for enzyme-bound NAD⁺ over NADH in the complex with the inhibitor. The C5-C6 bond in the phenolic ring of triclosan seems to be in the position expected for the C2=C3 double bond of the enolate intermediate, with the 2,4-dichlorophenoxy moiety of triclosan being located in the region anticipated to bind the phosphopantothene of ACP. The importance of the hydroxyl group of triclosan is significant, as replacement of the -OH with -H decreases affinity by over 10,000-fold.

*Part of the data reported in this chapter is reprinted with permission from "Structural elucidation of the specificity of the antibacterial agent triclosan for malarial enoyl acyl carrier protein reductase" by Perozzo *et al.*, 2002. *J Biol Chem*, **277**, 13106-14. 2006 by the American Society for Biochemistry and Molecular Biology.

Crystal Structure of InhA with Triclosan

Triclosan has been found to bind noncovalently to *E. coli* FabI (Ward *et al.*, 1999; Qiu *et al.*, 1999; Stewart *et al.*, 1999; Levy *et al.*, 1999), *Plasmodium falciparum* ENR (Perozzo *et al.*, 2002), and *Brassica napus* ENR (Roujeinikova *et al.*, 1999a). Here we determined the structure of *M. tuberculosis* InhA in complex with triclosan, to 2.6 Å resolution. This revealed binding of the triclosan inhibitor in a similar site and orientation within the *M. tuberculosis* enzyme, when compared to the *E. coli* and *B. napus* enzymes. Triclosan binding was found to overlap with the acyl substrate-binding pocket and was quite separate from the site of INH binding. In the crystal structure of the INH-NADH adduct (Rozwarski *et al.*, 1998) bound to InhA, the NAD(H) part of the adduct was maintained in the NAD(H)-binding site, and the INH portion of the adduct projected into a pore formed by the rotation of the side chain of Phe¹⁴⁹. Phe¹⁴⁹ was adjacent to the nicotinamide of NAD⁺ in the substrate-bound form (Rozwarski *et al.*, 1999) and rotated 90° to optimize stacking with the pyridine ring of the isonicotinic acyl group. In contrast, in the InhA:triclosan complex, the hydroxyl-substituted ring of triclosan (the “A” ring) stacked with the nicotinamide ring of NAD⁺ and hydrogen bonded with the 2'-hydroxyl group of NAD⁺ and with Tyr¹⁵⁸ in the catalytic active site (Perozzo *et al.*, 2002; Ward *et al.*, 1999; Qiu *et al.*, 1999; Stewart *et al.*, 1999; Levy *et al.*, 1999; Roujeinikova *et al.*, 1999a) in a manner well-conserved across enoyl reductase structures. Hydrophobic contacts were responsible for the remaining interactions. The dichlorophenyl ring (the “B” ring) of triclosan was oriented orthogonally to the A ring, and the chlorines were projected toward the solvent.

The crystal structure of InhA also revealed a unique binding stoichiometry (Figure 29) compared to other enoyl reductases. In the asymmetric unit, each monomer

of InhA exhibited a significant deviation within the substrate-binding loops from each other. One monomer contained a single molecule of triclosan, that possessed the canonical triclosan hydrogen bonding network seen in enoyl reductases from all known ENR:TCL structures.

This mode of triclosan binding was conserved for the ENRs and for InhA (figure on page 147). However, the second monomer of InhA in the asymmetric unit showed binding of two triclosan molecules to the active site (Figure 29). This had not been observed for any of the triclosan:ENR complexes elucidated to date. In the doubly-bound subunit, the mode of binding of one molecule of triclosan (designated TCN1) was identical to ENR:triclosan structures reported previously (Perozzo *et al.*, 2002; Ward *et al.*, 1999; Qiu *et al.*, 1999; Stewart *et al.*, 1999; Levy *et al.*, 1999; Roujeinikova *et al.*, 1999a) and was also identical to the binding we observed in the singly-bound monomer of *M. tuberculosis* InhA. The second molecule, designated TCN2, resided in an inverted orientation relative to TCN1 in an almost entirely hydrophobic area within the binding cavity. Both TCN1 and TCN2 were in identical low energy conformations and exhibited mostly van der Waals interactions between themselves and the protein. The binding of TCN2 to InhA was primarily mediated by van der Waals interactions with the hydrophobic side chains of residues Met¹⁰³, Gly¹⁰⁴, Phe¹⁴⁹, Ala¹⁵⁷, Met¹⁹⁹, Ile²⁰², Ile²¹⁵, and Leu²¹⁸. The majority of the interactions were from the substrate-binding loop that extended from residues 197 to 226 and that encompassed helices α_6 (residues 197-206) and α_7 (residues 209-226) (Figure 29). The only polar residues within 4 Å were Gln¹⁰⁰ and Tyr¹⁵⁸, which did not hydrogen-bond with TCN2. TCN2 stabilized the substrate-binding loop, resulting in an average B-factor of 54 Å². This loop was only partially ordered (B-factor 70 Å²) in the subunit containing a single molecule of triclosan. Superposition of each subunit (singly- versus doubly-bound forms) revealed significant deviations in

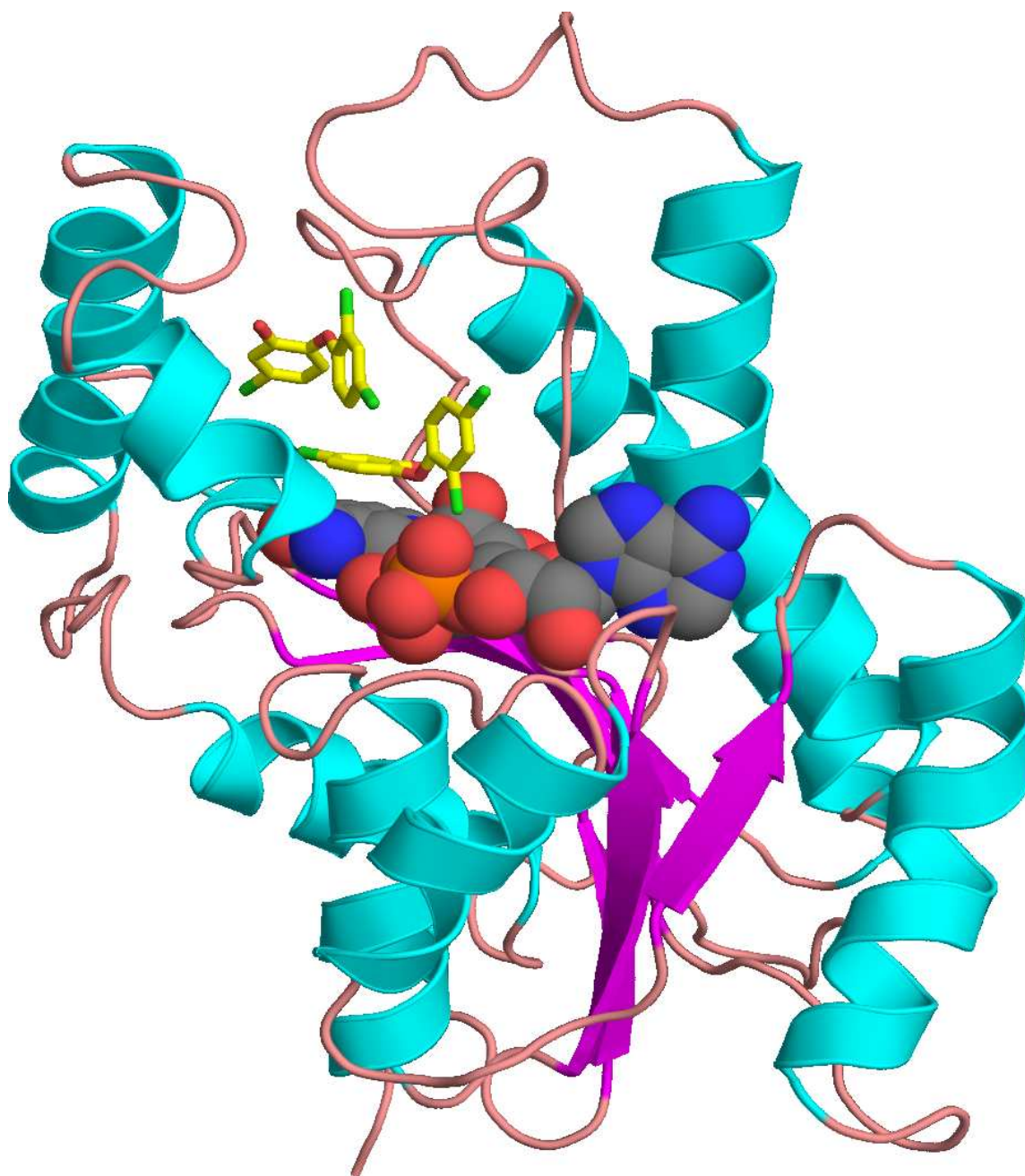


Figure 29: Structure of the InhA:triclosan complex. Helices are depicted in blue, and the β -strands are represented in yellow. The two molecules of triclosan occupied the substrate-binding portion of the active site. The hydroxyl groups of the A rings were oriented in opposing directions, whereas the dichlorophenyl rings (B rings) were in approximately parallel planes but did not stack.

the C α - backbone in the substrate-binding loops that contacted triclosan (Figure 30). The presence of two molecules of triclosan in the active site of InhA can be attributed to the specificity of the *M. tuberculosis* enzyme for long to very long chain (C₁₆ and up to C₆₀) fatty acyl substrates, whereas *E. coli* FabI, *B. napus*, and *P. falciparum* ENR all have specificity for short-chain fatty acyl substrates (C₄ - C₈). To accommodate the growing long-chain fatty acids, InhA possesses a hydrophobic substrate-binding loop (residues 197-226) that is 10 residues longer (residues 203-212) than the corresponding loop in *E. coli* or *B. napus* FabI. The long loop in InhA, comprising one face of the active site, correlated with a substrate-binding cavity that is considerably larger in volume relative to ENRs from other organisms (acyl-binding site volume of 1,551 Å³ for InhA, compared with 1,118 Å³ for *E. coli* FabI and 1,257 Å³ for *B. napus* ENR). These loop regions appeared to be of variable lengths, adjusting to the size of the preferred substrate/inhibitor. Superimposition of the backbones of the doubly-bound inhibitor form of InhA:triclosan and InhA complexed with a fatty acyl substrate analog (C₁₆-N-acetylcysteamine) produced a root mean square deviation of 0.6 Å, showing that the occupancy by two molecules of triclosan approximated a longer length substrate binding fairly well. Further examination revealed that the C₁₆- NAc and the two triclosan molecules showed strikingly similar modes of binding, with the acyl-chain and the two molecules of triclosan adopting a U-shaped or horseshoe conformation. The substrate-binding loops also superimposed well (Figure 31) supporting the observation that two triclosans would appear to mimic the C₁₆ substrate fairly well. These data suggest that selective targeting of *M. tuberculosis* within the human host might be achieved using an inhibitor composed of the dual complex TCN1/TCN2.

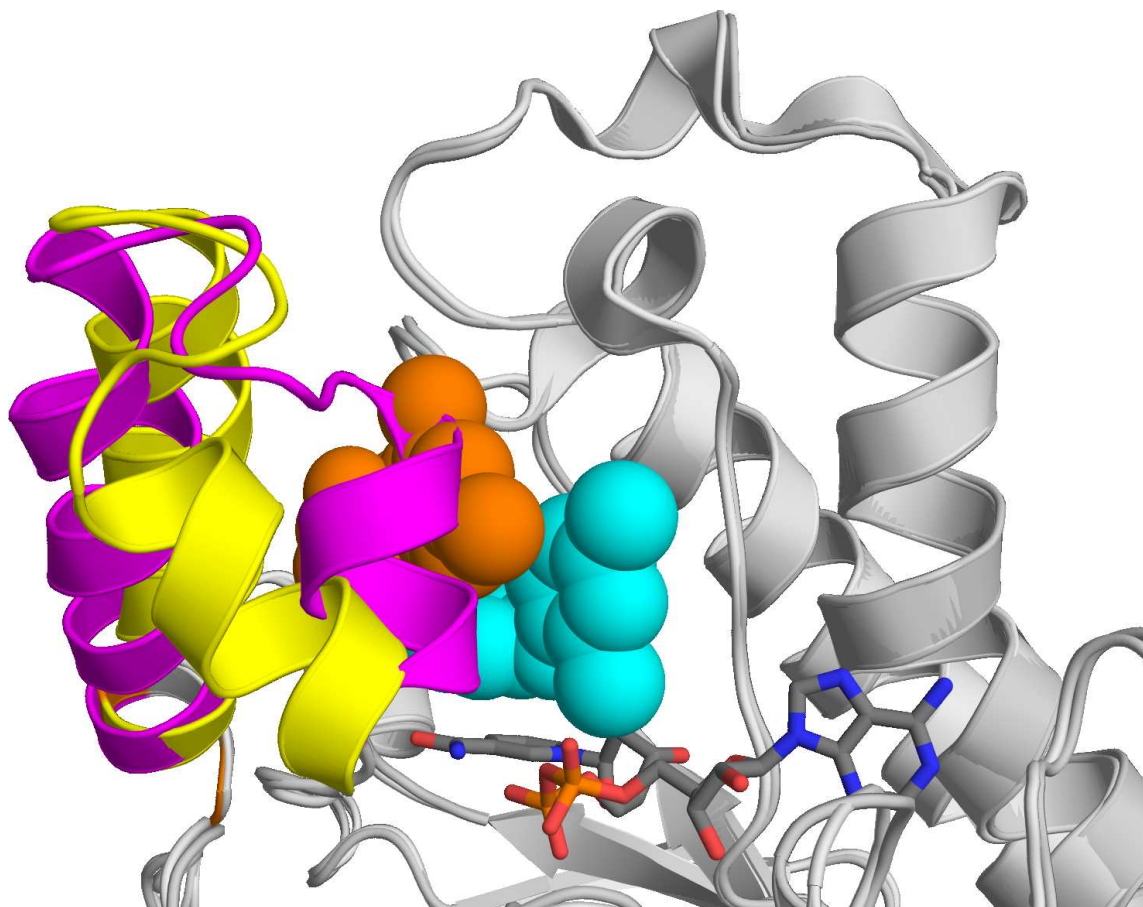


Figure 30: Superposition of the two forms of the InhA:triclosan complex. Superimposed ribbon diagrams representing the backbone of each subunit. The NAD^+ co-factor is depicted in stick form, and triclosan is shown as spheres (TCN1 in cyan and TCN2 in orange). White represents regions of InhA without significant backbone deviations. Colored worms represent the conformation of the substrate-binding loop ($\alpha 6$ and $\alpha 7$) in the singly- (magenta) and doubly- (yellow) bound forms of InhA. The presence of TCN2 results in a pronounced shift of the loop in order to accommodate the second triclosan molecules.

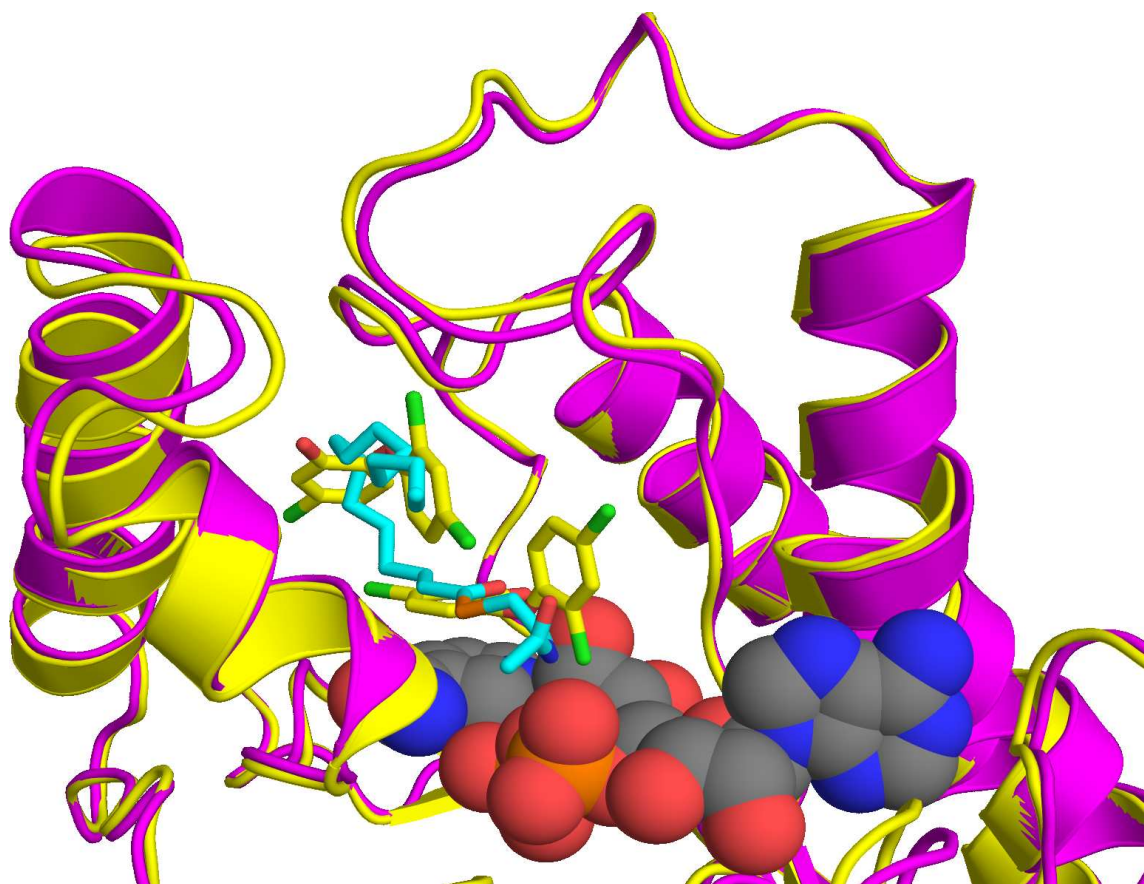


Figure 31: Superposition of the InhA:C₁₆-Nac and InhA:triclosan complexes. Magenta ribbons represent the C_α trace of InhA:C₁₆-Nac, and yellow ribbons represent the C_α trace of the InhA:triclosan structure. The C₁₆-Nac (cyan carbons) and the two molecules of triclosan (yellow carbons) exhibit remarkably similar modes of binding, while the substrate binding loop shifts only slightly.

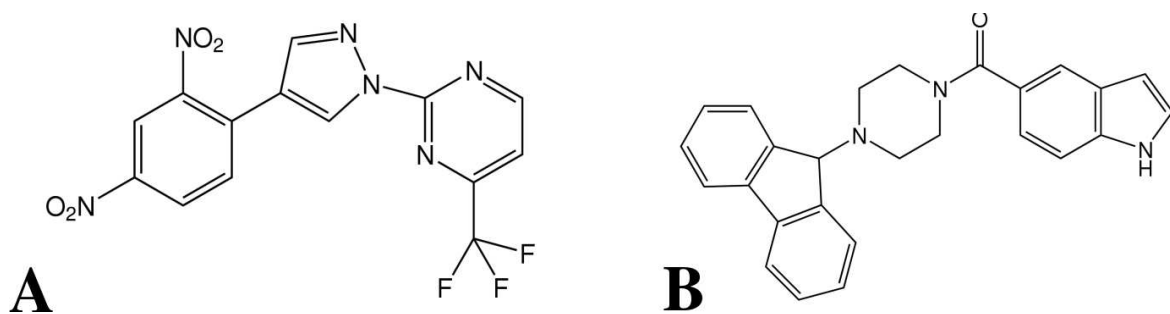
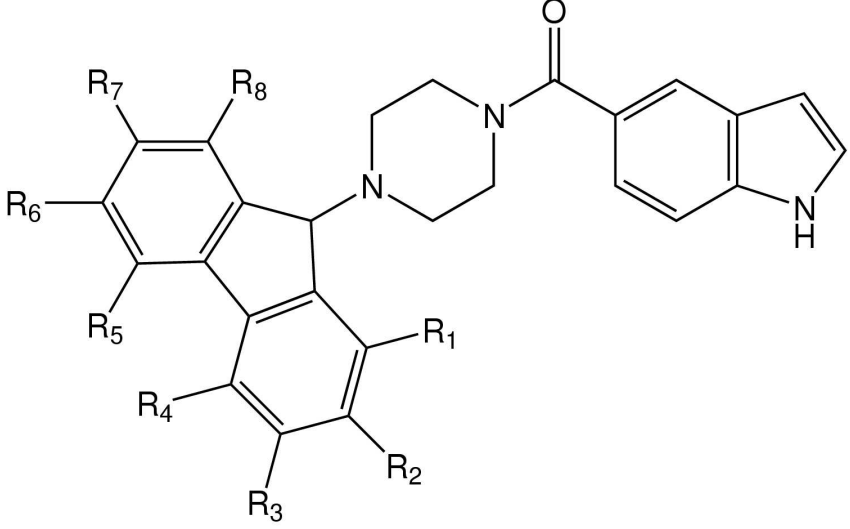


Figure 32: Stick models of newly discovered InhA inhibitors. These inhibitors were discovered from a high throughput combinatorial screen of recombinant *M. tuberculosis* InhA. A, Genz-8575; and B, Genz-10850.

Genzyme Inhibitors

A high-throughput screen of approximately 500,000 compounds from a combinatorial library against InhA resulted in the identification of Genz-8575 and Genz-10850 (Figure 32), two new classes of InhA inhibitors. Enzymatic testing of a series of about 300 Genz-10850 analogs resulted in the generation of a structure-activity relationship where substitution was not allowed at carbon positions 2 or 3 of the piperazine ring (suggesting a steric clash with this part of the molecule) and where polar substitutions were allowed at the 2-position of the fluorenyl group (suggesting that this site is exposed to solvent). Alkylation or acylation of the indole nitrogen was not tolerated, in agreement with the role of this moiety as a hydrogen-bonding group (Table 18). These compounds were synthesized and assayed for their ability to inhibit InhA-mediated, NADH-dependent catalysis of an octenoyl-CoA substrate. The IC₅₀ values in Table 18 refer to the concentration resulting in 50% inhibition of enzyme activity and were the lowest for Genz-10850. For the Genz-8575 analogs, a stringent requirement was detected at the trifluoromethylpyrimidine substituent, with more latitude at the dinitrophenyl site (Table 19). The right columns in Table 19 show the percent inhibition of InhA activity in the presence of 40 μ M of each of

Table 18: InhA:Genz-10850 structure-activity relationship

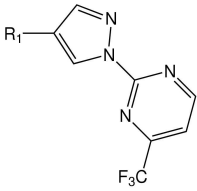
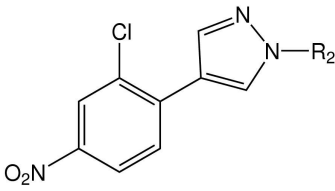
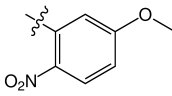
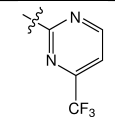
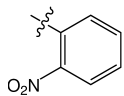
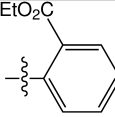
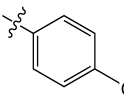
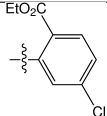
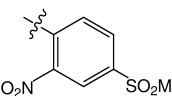
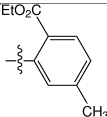
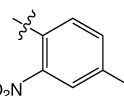
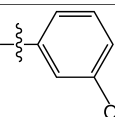
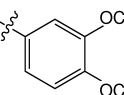
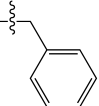
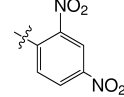
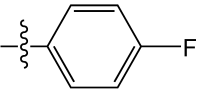
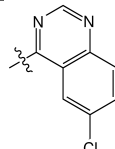


| Genz-# | R _n -group | IC ₅₀ (μM) |
|--------|---|-----------------------|
| 10850 | H | 0.16 |
| 11918 | 1-CO ₂ CH ₃ | 0.34 |
| 12637 | 2-Cl, 3-NHAc | >10 |
| 12638 | 2,7-I ₂ | 0.13 |
| 12639 | 2-NHAc | 0.28 |
| 12640 | 2-NMe ₂ | 0.91 |
| 12641 | 2-NHCHO | 0.18 |
| 12643 | 2,4,7-Cl ₃ | 0.17 |
| 12644 | 2-NO ₂ | 0.13 |
| 12645 | 3-NO ₂ | 0.13 |
| 12646 | 2,7-Br ₂ | 0.12 |
| 13100 | 2-NHCOB | 0.59 |
| 13108 | 2-NHCOCH ₂ CH ₂ CH ₃ | 0.46 |
| 13347 | 2-NEt ₂ | >10 |
| 13348 | 2-OCH ₃ | 0.52 |
| 13349 | 4-OCH ₃ | 0.82 |

these compounds. The best of this initial set of pyrazoles, Genz-5542, was further derived to generate analogs, including Genz-8575, which substituted a chlorine atom with a nitro group and that gave the best inhibition of all compounds in this series. When tested against purified InhA, Genz-8575 and Genz-10850 displayed IC₅₀ values of 2.4 and 0.16 μ M, respectively (Kuo *et al.*, 2003).

To gain insights into the molecular details of how this new group of compounds binds to InhA, we solved the x-ray crystal structure of the InhA:NAD⁺:Genz-10850 ternary complex. Electron density for a single molecule of Genz-10850 was observed in the InhA active site. Comparison of this structure with a previous structure of InhA:NAD⁺:C₁₆-NAc (Dessen *et al.*, 1995; Rozwarski *et al.*, 1998, 1999) suggested that Genz-10850 also occupied a region of the active site that was normally bound by substrate or inhibitor. This interpretation was supported by kinetic studies of members of the two classes of Genzyme compounds, showing that they were competitive with the enoyl-CoA substrate. The Genz-10850 carbonyl group formed a hydrogen-bonding network with the 2'-ribose hydroxyl of the NAD⁺ and the side chain of the catalytic residue Tyr¹⁵⁸, highly reminiscent of the network observed in triclosan binding (Figure 33). Binding of the bulky fluorenyl group occurred within the substrate-binding pocket that normally sees the long acyl chain of the substrate. Genz-10850 binding also resulted in a wider fatty acyl substrate-binding groove (compared with the NAD⁺ bound structure) as well as additional van der Waals interactions with the hydrophobic residues Gly⁹⁶, Met¹⁰³, Phe¹⁴⁹, Met¹⁵⁵, Pro¹⁵⁶, Ala¹⁵⁷, Met¹⁶¹, Pro¹⁹³, Ala¹⁹⁸, Ile²¹⁵, and Leu²¹⁸. This information was in accord with the observed structure-activity relationship for Genz-10850, which indicated that substitutions on the piperazine ring were detrimental to potency (sterically clash with Phe¹⁴⁹), whereas polar substitutions at the 2-position of the fluorene moiety would be tolerated due to its exposure to solvent. Alkylation or acylation of the indole

Table 19: InhA:Genz-8575 structure-activity relationship

|  | | |  | | |
|---|---|--------------|--|---|--------------|
| Genz-# | R ₁ -group | % Inhibition | Genz-# | R ₂ -group | % Inhibition |
| 5537 |  | 17 | 5544 |  | 86 |
| 5538 |  | 14 | 5984 |  | 10 |
| 5539 |  | 8 | 5985 |  | 17 |
| 5540 |  | 10 | 5986 |  | 9 |
| 5542 |  | 82 | 6341 |  | 60 |
| 7466 |  | 11 | 6356 |  | 54 |
| 8575 |  | 91 | 6371 |  | 27 |
| | | | 6386 |  | 5 |

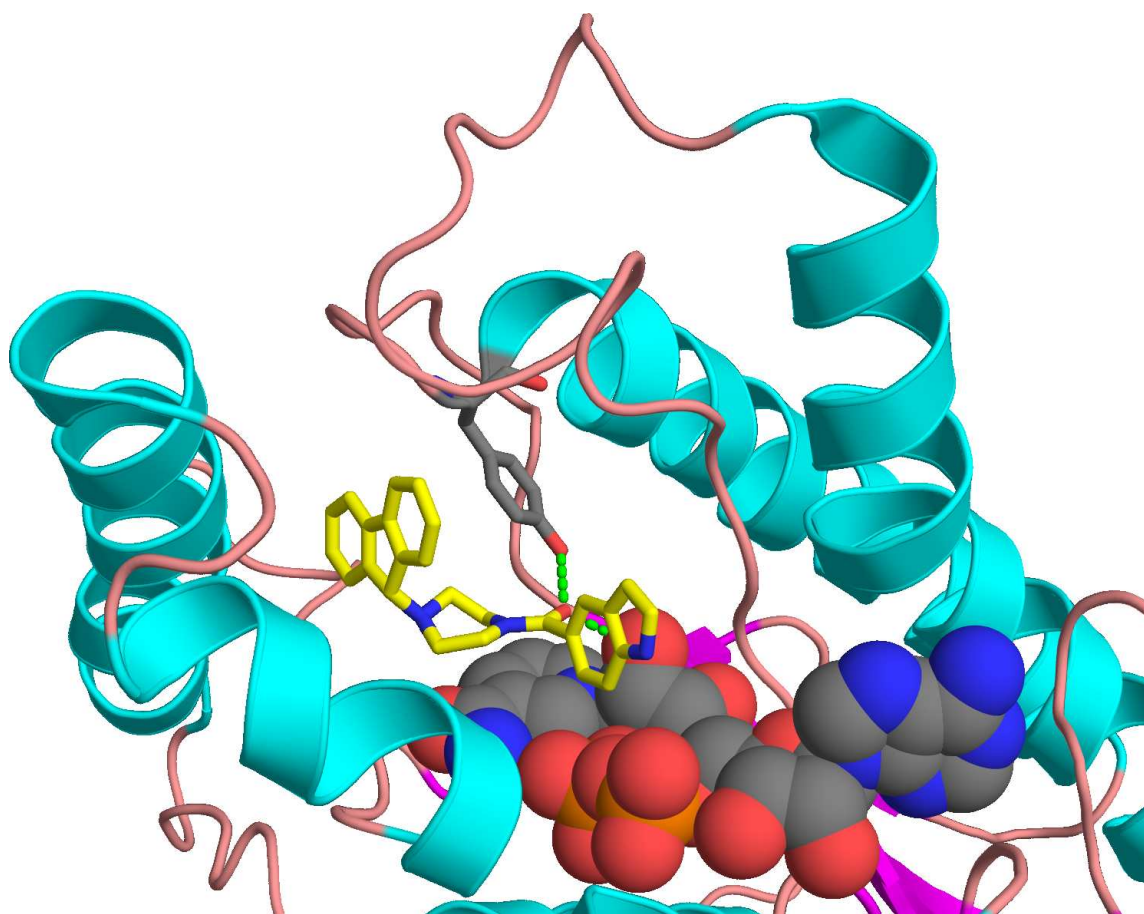


Figure 33: Structure of the InhA:Genz-10850 complex. Helices are depicted in blue, and the loops are represented in pink. NAD⁺ is depicted as spheres. Genz-10850 (yellow carbons) is represented as a stick model, and occupied the substrate-binding portion of the active site. The carbonyl group of Genz-10850 formed hydrogen bonds with Tyr¹⁵⁸ and the 2'-ribose of NAD⁺, in a manner identical to triclosan.

nitrogen would disrupt a weak hydrogen bond between Genz-10850 and a NAD^+ phosphate oxygen.

Comparison of InhA and Other ENR Inhibitors

Superimposition of the backbones of the two InhA inhibitor complexes, triclosan and Genz-10850, revealed that the A and B ring of triclosan overlaid the piperazine and indole groups of Genz-10850, respectively. The triclosan hydroxyl group and the Genz-10850 carbonyl group occupied similar positions and retained a similar hydrogen-bonding network with the 2'-ribose hydroxyl of the dinucleotide co-factor and the Tyr¹⁵⁸ side chain. Van der Waals interactions accounted for the remainder of the interactions between Genz-10850 and protein, and the fluorenyl moiety ordered the substrate-binding loop. Our structural model of the mechanism of action for these inhibitors is consistent with the structure-activity relationships identified in other organisms (Perozzo *et al.*, 2002; Ward *et al.*, 1999; Qiu *et al.*, 1999; Stewart *et al.*, 1999; Levy *et al.*, 1999; Roujeinikova *et al.*, 1999a). Several reports described the mode of binding of triclosan to the ENRs from *E. coli* (Ward *et al.*, 1999; Qiu *et al.*, 1999; Stewart *et al.*, 1999; Levy *et al.*, 1999), *B. napus* (Roujeinikova *et al.*, 1999a), and *P. falciparum* (Perozzo *et al.*, 2002). All maintained the hydrogen-bonding network between the A ring, a catalytic tyrosine, NAD^+ co-factor, and a catalytic lysine (Figure 34). The stacking interactions between the A ring and NAD^+ were also conserved. In addition to triclosan analogs (Heath *et al.*, 1998; Perozzo *et al.*, 2002), other ENR inhibitors have been described, including derivatives of diazaborines (Roujeinikova *et al.*, 1999b), imidazoles (Hearding *et al.*, 2001), indoles (Seefeld *et al.*, 2001), and aminopyridines (Miller *et al.*, 2002). Perozzo *et al.* (Perozzo *et al.*, 2002) reported a series of triclosan derivatives utilized in inhibitor

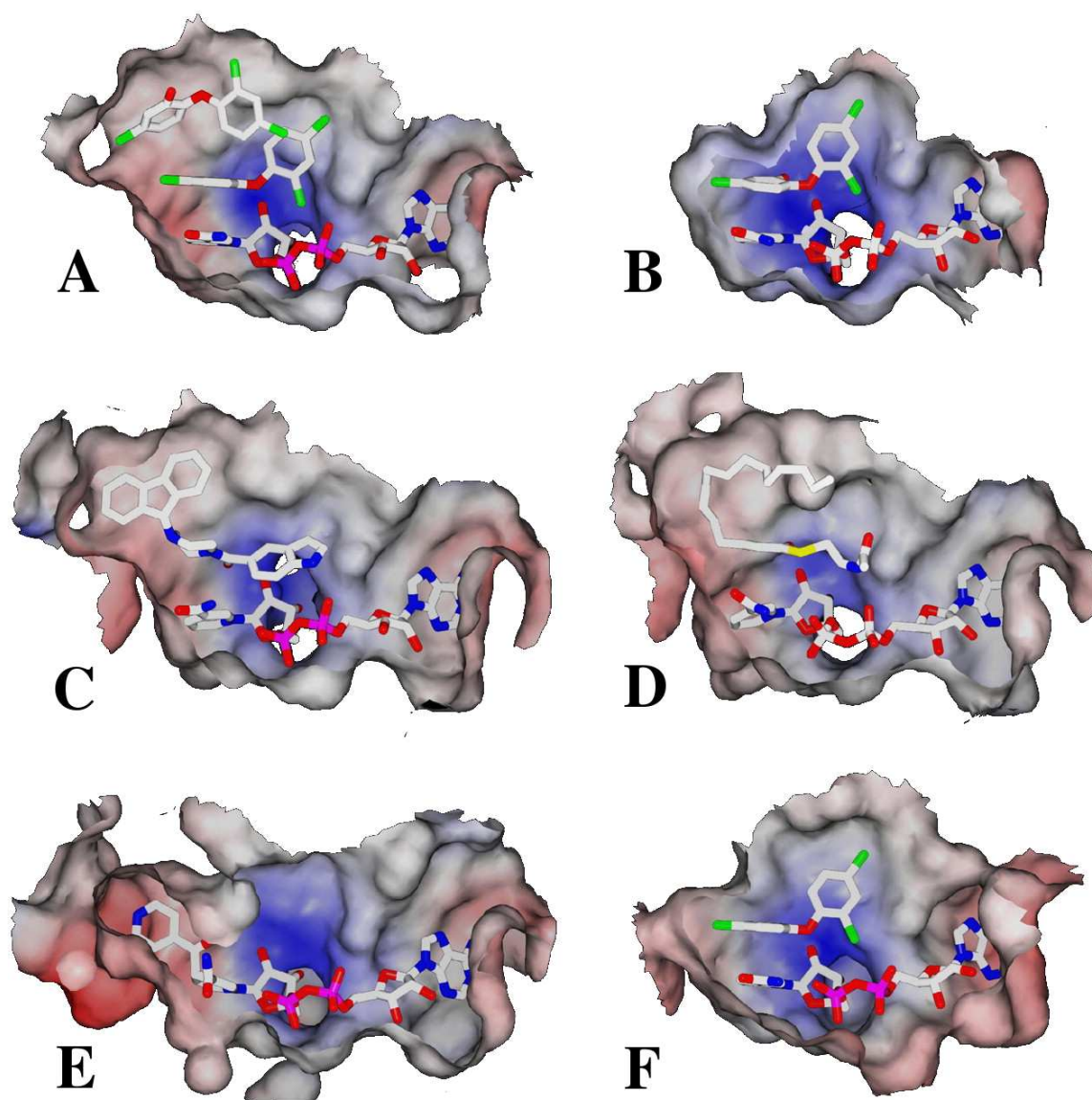


Figure 34: Active sites of *M. tuberculosis* and homologous ENRs. A, cross-section through the surface of the InhA active site with bound triclosan, showing that InhA contains an additional triclosan-binding site compared with other ENRs. B, similar view of *E. coli* FabI with triclosan. C, cross-section through the Genz-10850-binding site in InhA, revealing the bulky fluorenyl group of this inhibitor that widens the fatty acid-binding loop. This is not observed in the NADH-bound structure that lacks an analogous bulky substituent. Note also the interaction of the nitrogen of the Genz-10850 indole ring with a NAD⁺ phosphate oxygen. D, cross-section of the InhA active site with bound C₁₆ fatty acyl substrate. Comparison with the inhibitor-bound forms of InhA shows that both substrate and inhibitor utilize the 2'-OH ribose of NADH as a hydrogen-bonding partner. E, cross-section of the InhA active site with bound INH. The activated form of INH covalently attaches to the nicotinamide ring of NADH. F, cross-section of the *B. napus* active site with bound triclosan.

studies with PfENR. Common features associated with the more potent derivatives included a hydroxyphenyl ring bridged with either a dichlorophenyl or a naphthol ring. Substitution of the hydroxyl group of the A ring was not tolerated, whereas the bridging atom could be either an oxygen or a nitrogen but not a sulfur or a carbon (Heath *et al.*, 1998, 2000b). Variability was allowed in the remainder of the molecule, which tended to be highly hydrophobic. Binding of thienodiazaborine and benzo-diazaborine to *E. coli* FabI has also been described (Baldock *et al.*, 1996). This report showed that the diazaborines covalently modified NAD⁺, whereas the bicyclic rings formed face-to-face stacking interactions with the nicotinamide ring and hydrogen-bonded to Tyr¹⁵⁶. Heerding *et al.* (Heerding *et al.*, 2001) reported the crystal structure of *E. coli* FabI complexed to an inhibitor derived from disubstituted imidazoles (Protein Data Bank entry 1I2Z). In their analysis, the inhibitor stacked with the nicotinamide ring of NAD⁺, whereas the unsubstituted nitrogen of the imidazole interacted with the catalytic tyrosine. The crystal structure of *E. coli* FabI bound to an indole-derived inhibitor has also been described (Seefeld *et al.*, 2001) and showed that the 4-hydroxybenzamide moiety hydrogen-bonded to the catalytic Tyr¹⁵⁶ of FabI and had orthogonal π -stacking interactions with Tyr¹⁴⁶ (Protein Data Bank entry 1I30). Similar results were reported by Miller *et al.* (Miller *et al.*, 2002), who reported the structure of *E. coli* FabI bound to two aminopyridine-based inhibitors. These inhibitors stacked with NAD⁺ and formed hydrogen bonds to a conserved catalytic tyrosine Tyr¹⁵⁶ (the equivalent of Tyr¹⁵⁸ in InhA), as well as additional hydrogen bond interactions with either phosphates on NAD⁺ or two hydrogen bonds to the Ala⁹⁵ backbone. We note that lead optimization studies have been initiated on aminopyridine-based inhibitor hits (Payne *et al.*, 2002), identified through previous high-throughput screens against *S. aureus* FabI (Miller *et al.*, 2002). Iterative medicinal chemistry and structure-based drug design improved the inhibitory

potency of the original lead compound by 350-fold, and the final compound retained the moieties implicated as important for stacking and hydrogen-bonding. In the structure of InhA with bound NAD^+ and the product analog $\text{C}_{16}\text{-NAc}$, a similar hydrogen-bonding pattern was observed for the carbonyl oxygen of the $\text{C}_{16}\text{-NAc}$. The remainder of the product analog interacted with the substrate-binding loop, restoring order to this loop upon binding. These studies, in concert with our crystal structures of InhA:triclosan and InhA:Genz-10850, accentuate the importance of the hydrogen bonding network, aromatic ring stacking interactions with either NAD^+ or catalytic residues, and the presence of a hydrophobic moiety to mimic a fatty acyl substrate.

CHAPTER VII

CONCLUSIONS AND FUTURE WORK

Discussion

The work undertaken in this thesis should greatly enhance inhibitor design efforts against two of the most deadly infectious diseases worldwide, malaria and tuberculosis. Together, these diseases affect over one third of the world's population, and have a mortality rate upwards of 3 million people annually. The insight gained from extensively examining the enoyl-ACP reductases from *Plasmodium falciparum*, *Plasmodium berghei*, and *Mycobacterium tuberculosis*, as well as their complexes with inhibitors, allows for the exploitation of the subtle differences between each of these proteins to produce inhibitors exquisitely specific for each organism. Comprehensive knowledge of inhibitor action also affords the opportunity to optimize protein:inhibitor interactions to develop more potent inhibitors.

Regarding malaria, the identification of the *pfenr* and *pbenr* genes sparked interest into enoyl-ACP reductases as attractive and novel anti-malarial drug targets in *P. falciparum* and *P. berghei*. Examination of the multiple sequence alignment of PfENR and PbENR revealed that these enzymes shared 87% identity, except for the N-terminal bipartite extension and a low-complexity insertion within the putative substrate binding loop. This high degree of similarity had important implications for *in vivo* testing of inhibitors against PfENR. The human parasite *Plasmodium falciparum* and the mouse parasite *Plasmodium berghei* are extremely species-specific, unable to cross-infect other organisms. However, due to the well conserved nature of the FAS-II enzymes in these organisms, it became apparent that inhibitors effective

against *P. falciparum in vitro* should be effective against *P. berghei* as well.

The binary structures of PfENR:NADH and PbENR:NADH allowed for the identification and comparison of the structurally conserved regions of these proteins, as well as the identification of unusual differences such as the differing lengths of the substrate binding loops. PfENR contains a 43 amino acid insertion within the substrate binding loop (residues 325-366), while PbENR possesses only a 10 amino acid insertion (residues 313-323). However, these insertions were not well-ordered in the crystal structures. The comparison verified the nearly identical tertiary structures (< 0.8 angstrom rmsd) of the *Plasmodial* enoyl reductases from the two parasites, supporting our contention that inhibitors that are effective against *P. falciparum* ENR would also be active against *P. berghei* ENR. This allows for the use of *P. berghei* in mice as an *in vivo* model system for testing compounds designed against PfENR, and leaves us reasonably confident that compounds effective in enzyme assays and whole cell assays against the *P. falciparum* enoyl-ACP reductase would have the same mode of action in *P. berghei* studies in mice.

The ternary structures of PfENR:NAD⁺:triclosan and PbENR:NAD⁺:triclosan, while not particularly surprising compared to previous structures of homologous enoyl-ACP reductases complexed with triclosan, allowed us to unequivocally identify the catalytic residues, and therefore confirm the mode of action. For example, the structure of PfENR in complex with triclosan showed unambiguously that Tyr²⁷⁷ was the critical catalytic residue involved in a conserved hydrogen bonding network, while Tyr²⁶² held the same role in the PbENR:triclosan complex. Lys²⁸⁵ in PfENR and Lys²⁷³ in PbENR were assigned roles in co-factor binding, consistent with the works of Ward *et al.* with *E. coli* FabI and triclosan inhibition. The structure of PfENR:triclosan allowed us to infer roles of the residues populating the active site, and possible inhibitor analogs to take advantage of hydrophobic interactions,

hydrogen-bonding interactions, and ring-stacking interactions. Additionally, these structures revealed the location of a second hydrophobic pocket in close proximity to triclosan that could be utilized to provide increased inhibitor efficacy.

The structure of PfENR:isoniazid allowed us to confirm our speculation that the second hydrophobic pocket could be utilized to improve inhibitor potency. The isonicotinyl group of the isoniazid-NADH adduct protruded into a small binding cavity, and formed stacking interactions with Tyr²⁶⁷. This was highly similar to *M. tuberculosis* InhA and its interaction with isoniazid, except that Phe¹⁴⁹ is involved in ring stacking. Although *Plasmodium falciparum* does not contain a catalase-peroxidase enzyme capable of activating isoniazid and forming an INH-NADH adduct, this type of structural information is useful to consider in the design of new drugs.

The structure-activity relationships generated from the several hundred triclosan analogs screened will help narrow down the key protein:inhibitor interactions necessary to generate a potent, high-affinity, bioavailable inhibitor. We were able to determine regions along the triclosan scaffold that were amenable to modification while maintaining inhibitor potency, while also recognizing that modifying certain positions had deleterious effects on inhibitor potency. For example, the 1-position hydroxyl on the A ring of triclosan could not be substituted without destroying the inhibitory activity, while modifications of the 5-position and 6-position were well tolerated. The 5-position on the A ring offered a building point to access the isoniazid binding pocket, while the 6-position could potentially lower the efficiency of glucuronidation or sulfonation at the 1-position, giving the drug better bioavailability. Substitutions on the B ring were allowed at the 2' and 4' position, but substitutions here did not substantially improve inhibitor potency. X-ray crystallography of 4'-substituted triclosan analogs confirmed the presence of additional hydrogen bonds between inhibitor and backbone or side chain atoms of Asn²¹⁸ and Ala²¹⁹. While

these analogs did not significantly enhance inhibitor potency, many of these analogs did not destroy activity either. This knowledge could provide possibilities for modifying the triclosan scaffold to improve the pharmacokinetic profile.

Regarding tuberculosis, the structure of InhA in complex with two compounds that were not derivatives of available anti-tuberculars will be instrumental in advancing research into anti-tuberculars that circumvent existing resistance mechanisms. Isoniazid resistant strains of tuberculosis typically have mutations in the KatG protein, which activates isoniazid. Compounds that do not require this step of activation would immediately offer an advantage in anti-tubercular drug development. Triclosan, Genz-8575, and Genz-10850 fit this criteria.

The *M. tuberculosis* InhA:triclosan crystal structure revealed an additional mode of binding for the inhibitor, one not previously observed in enoyl-ACP reductases from homologous organisms. Triclosan bound to InhA in the configuration normally seen in other enoyl-ACP reductases, with Tyr¹⁵⁸ hydrogen bonding with the hydroxyl group of triclosan, while the A ring stacked with the nicotinamide portion of NAD⁺. However, in addition to seeing triclosan in this commonly observed orientation, there was a second molecule of triclosan in an inverted position adjacent to the first molecule. This had not been reported in the literature previously. The doubly-bound triclosan maintained a conformation that was similar to that of the preferred C₁₆ substrate, and is consistent with the specificity of InhA for long chain substrates. This offers an avenue for engineering an inhibitor that is exquisitely specific for *M. tuberculosis* InhA, while not adversely affecting fatty acid biosynthesis in the host.

Genz-8575 and Genz-10850, discovered through high-throughput screening techniques, offer new chemical scaffolds that are distinct from the mode of action of isoniazid. Genz-8575 and Genz-10850 were found to be effective against InhA in *in vitro* enzyme assays, with IC₅₀ values of 2.4 and 0.16 μ M, respectively. Genz-8575

was also found to be effective against strains of multi-drug resistant tuberculosis, as well as whole cell cultures of *P. falciparum* (Kuo *et al.*, 2003). To gain insight into the molecular details of this class of inhibitors, we determined the crystal structure of the InhA:Genz-10850 complex. Genz-10850 bound in the active site in the area normally occupied by triclosan or substrate, and the Genz-10850 carbonyl group hydrogen-bonded with Tyr¹⁵⁸ and the 2'-hydroxyl of the NAD⁺ co-factor. The fluorenyl group was situated within the binding pocket that normally borders the long acyl chain of the substrate. These compounds offer novel leads for future optimization studies, and provide a foundation on which to aim to develop a new family of compounds for use against tuberculosis.

Future Work

While the investment of time and effort into obtaining structural information concerning *P. falciparum* ENR, *P. berghei* ENR, and *M. tuberculosis* InhA have returned a significant amount of information, research on these important enzymes must continue. Future work will focus on discovering new lead compounds for each of these proteins to increase chemical diversity, obtaining crystal structures of protein:inhibitor complexes, and subsequently the generation of comprehensive structure-activity relationship profiles for the purpose of optimizing lead compounds. Several of these approaches are already in motion.

To generate greater chemical diversity, there are several approaches that can be undertaken. High throughput screens can be conducted to search for more potent, chemically diverse inhibitors. The 50,000 compound high throughput screens initiated against PfENR with Southern Research Institute should be repeated, once the technical problems are corrected. Two problems that could easily be corrected are to

purchase crotonoyl-CoA from a single source, and to run the assays in a reasonable amount of time so that the activity of the enzyme does not change within the duration of the screening. Careful observation of the plate preparation and screening process would allow early detection of problems, and prevent propagation of errors throughout the screening process. Statistical analysis and inspection of the initial velocity plots would filter out false positives, and the resulting list of “hits” would be re-screened and subjected to IC_{50} determination. This procedure would elicit greater accuracy and confidence in the results.

Virtual screening also offers the opportunity to discover new lead compounds. The FlexX docking experiments yielded promising results. vHTS of the 3.3 million compound library indicated 68 top hits, defined as the intersection of the top 2% of scores across five categories of scoring algorithms. Visual inspection of the results revealed five docked compounds that appear to have a mode of action that is consistent with all available PfENR crystal structures. *In vitro* enzyme assays and IC_{50} determination will soon be conducted to verify these results.

After discovery of new and effective inhibitor scaffolds, crystal structures of the enzyme:inhibitor complexes would make available new information regarding important elements in inhibitor potency. Crystal structures have already played a significant role in guiding triclosan analoging efforts, and should continue to do so with any promising inhibitor candidates. One uncertainty is the presence of low-complexity insertions within the substrate binding loops of the *Plasmodial* ENR proteins. Since they border the active site and unusually enriched in polar residues, these insertions could provide another means for tailoring drugs to the active site. However, because they are not visibly ordered in the crystal structure, it remains to be seen whether these low-complexity insertions should be accounted for in the drug design process.

In parallel, optimization of the triclosan scaffold should continue. Based on the

widely disparate affinities of triclosan for the *E. coli*, *M. tuberculosis*, and *P. falciparum* enoyl-ACP reductases, there appears to be room for improvement in tailoring triclosan to the enzyme. *In vivo* tests with *P. berghei* infected mice should be conducted with the 6-position substituted inhibitors to determine if the modification prevents glucuronidation while maintaining inhibitor potency. Genz-8575 and Genz-10850, which have IC₅₀ values of 18 and 32 μ M, respectively, against PfENR, should be co-crystallized to determine the mode of binding. For *M. tuberculosis* InhA, derivatives that mimic the doubly-bound triclosan should be synthesized for *in vitro* testing, and perhaps co-crystallization.

The present body of work and the future objectives combine to give the process of anti-malarial and anti-tuberculosis drug development a promising start. The combination of excellent drug targets, knowledge of current inhibitors, and straightforward *in vitro* enzyme assays, are great advantages in ensuring successful drug discovery and optimization efforts against malaria and tuberculosis.

CHAPTER VIII

EXPERIMENTAL: MATERIALS AND METHODS*

Plasmodium falciparum Enoyl-ACP Reductase*Cloning*

Overlapping pfenr sequences were PCR-amplified from a *P. falciparum* (3D7 strain) gametocyte cDNA pSPORT plasmid library (kindly provided by Dr. Thomas Templeton, Weill Medical College of Cornell University, New York) using vector-specific primers (M13/pUC forward and reverse) combined with the following pfenr primers: 5'-TTT ATT GCT GGT ATA GGA GAT ACA AAT and 5'-ATT TGT ATC TCC TAT ACC AGC AAT AAA, 5'-TGG CCT CCT GTT TAT AAT ATT TTT and 5'-AAA AAT ATT ATA AAC AGG AGG CCA, 5'-GAA GAA ACG AAA AAT AAT AAA AGA TAT AAT and 5'-ATA TCT TTT ATT ATT TTT CGT TTC TTC, 5'-CCA GGC TAT GGT GGA GGT ATG and 5'-CAT ACC TCC ACC ATA GCC TGG, 5'-GAT TAT GCA ATA GAG TAT TCA and 5'-CAT ATT ATT TAA GTG TTT CAT. PCR conditions were: 1× (94 °C for 2 min); 35× (94 °C for 20 s, 48 °C for 10 s, 52 °C for 10 s, and 60 °C for 2 min). Amplified PCR fragments were isolated and directly sequenced using internal primers.

Full-length pfenr gene was amplified using primers W1 (5'-AAC GTC CCATGG ATA AAA TAT CAC AAC GGT TAT TAT TCC TCT TTC TAC AT) and W2 (5'-A TAT GGATCC TCA TTC ATT TTC ATT GCG ATA TAT ATC ATC TGG TAA AAA CAT), which contain NcoI and BamHI sites, respectively (underlined). Four

*Part of the data reported in this chapter is reprinted with permission from "Structural elucidation of the specificity of the antibacterial agent triclosan for malarial enoyl acyl carrier protein reductase" by Perozzo *et al.*, 2002. *J Biol Chem*, **277**, 13106-14. 2006 by the American Society for Biochemistry and Molecular Biology.

silent mutations (shown in lowercase letters) were introduced with mutagenic primers M1 (5'-GA_g AAG GAA GA_g AA_g AA_g AAT TCA GCT AGC CAA AAT TAT ACA TTT ATA GAT TAT) and M2 (5'-GAA TT_c TT_c TT_c TCT TCC TT_c TCA CCT GAA TTG TTC ATA ATA TTA TGA ACA TC) using a two-step mega-primer PCR method. In the first step, the cDNA library was used as a template to amplify both a 5' fragment with the primers W1 and M2 and a 3' fragment with the primers M1 and W2. Both reactions used the PCR conditions: 1× (94 °C for 2 minutes); 30× (94 °C for 20 seconds, 53 °C for 40 seconds, and 60 °C for 3 minutes). For the second step, both fragments were gel-purified and combined in a PCR reaction with primers W1 and W2, yielding the full-length pfenr. After restriction digestion, the gene was ligated into the pET28a vector (Novagen) and transfected into *E. coli* (NovaBlue, Novagen). A construct containing the four silent mutations was identified and verified by restriction digestion, PCR, and automated sequencing with internal primers.

This construct harboring the stabilized pfenr gene was used as a template to prepare a N-terminal and C-terminal truncated version, using expression primers E1 (5'-AC GTC CCATGG TGC ATC ATC ATC ATC ATC ATA ATG AAG ATA TTT GTT TTA TTG CTG GTA TAG G) and E2 (5'-ATAT GGATCC TCA ATC ATC TGG TAA AAA CAT TAT ATT TAA TCC GTT ATC CAC ATA TAT TGT CTG) (NcoI and BamHI sites underlined) and the PCR conditions described above. This gene was ligated into pET28a, and its sequence was verified.

Recently, the full-length pfenr gene sequence also appeared in the *P. falciparum* genome data base as sequence from the *P. falciparum* "blob" chromosomes that co-migrate on pulse-field gels. This has been confirmed independently by two other publications (Surolia and Surolia (2001); McLeod *et al.* (2001)). When compared with these recently published sequences, our data from multiple independent PCR

products show a Gln at position 35 instead of His, and an Asn instead of a Tyr at position 88 of the complete amino acid sequence. Both changes occur at the N-terminus of the enzyme in a region that is structurally distant to the site of enzymatic function.

Purification

BL21(DE3) Codon+RIL cells (Novagen) harboring the expression plasmids were grown in Terrific broth. When the A_{600} reached 0.8, the cells were induced with 1 mM isopropyl-1-thio-D-galactopyranoside for 5 h at 37 °C. Cell pellets were resuspended in buffer A (20 mM Tris/HCl, pH 8.0, 500 mM NaCl, 50 mM imidazole) and disrupted using a French press. The filtered supernatant was applied to a metal chelate affinity column loaded with nickel. The column was washed with buffer B (20 mM Tris/HCl, pH 8.0, 500 mM NaCl, 150 mM imidazole) and eluted with buffer C (20 mM Tris/HCl, pH 8.0, 500 mM NaCl, 400 mM imidazole). The protein was concentrated using Centriprep 30 and applied to a Superdex 75 size-exclusion column equilibrated with buffer D (20 mM Tris/HCl, pH 7.5, 150 mM NaCl).

Crystallization and Data Collection

Using hanging drop and vapor diffusion methods, PfENR was crystallized as a binary complex with NADH bound to the enzyme and as a ternary complex with NAD⁺ and triclosan. The protein in buffer D (20 mg/ml) was incubated with 4 mM NAD⁺ and 1 mM triclosan for the ternary complex and with 4 mM NADH for the binary complex. Two microliters of these mixtures was mixed with 2 μ l of well solution consisting of 2.35 M (NH₄)₂ SO₄ and 100 mM buffer, pH 5.6 (sodium acetate for the ternary, MES for the binary complex) and equilibrated against the reservoir solution at 18 °C. The crystals of both complexes were isomorphous, belonged to the space

group P4₃2₁2 (cell dimensions $a = b = 134.0 \text{ \AA}$, $c = 84.0 \text{ \AA}$), and contained a dimer (half of the functional tetramer) in the asymmetric unit.

Crystals of ternary complexes with NADH and the triclosan analogs B13 and B24 were prepared by soaking binary ENR:NADH crystals. The inhibitors were dissolved in acetonitrile, directly added to the drops containing crystals of binary complexes, and incubated for a week.

To increase protein yield and facilitate the crystallization process, the PfENR protein was expressed without the N-terminal signal and translocation peptide and the following 18 residues, as well as the C-terminal 7 amino acids, which were predicted to extend into solvent and potentially interfere with crystallization but not contribute to enzyme function. When BL21(DE3) Codon⁺-RIL cells (Novagen) were used for expression, the purification typically resulted in 20-30 mg of truncated PfENR per liter of media. The K_m and V_{max} values of the truncated PfENR were indistinguishable from the full-length enzyme carrying silent point mutations.

Diffraction data was collected at room temperature to 2.35 to 2.50 \AA resolution from single crystals using a MacScience DIP2030 image plate detector with double-focusing mirrors coupled to a Rigaku x-ray generator utilizing a copper rotating anode (CuK_α wavelength = 1.54 \AA). The data were processed and scaled using the DENZO/SCALEPACK (Otwinowski and Minor 1997) crystallographic suite of programs.

Enzyme Assays

All experiments were carried out on a Shimadzu UV-1201 UV-visible spectrophotometer at 25 °C in 20 mM Tris/HCl, pH 7.6, 150 mM NaCl. Kinetic parameters were determined spectrophotometrically by following the oxidation of NADH to NAD⁺ at 340 nm ($\epsilon = 6.3 \text{ mM}^{-1}\text{cm}^{-1}$). K_m and V_{max} values for crotonoyl-CoA

were determined at a fixed and saturating concentration of NADH (200 μM) and by varying the substrate concentration (0-500 μM). K_m and V_{max} values for NADH were determined at variable concentrations of NADH and a fixed and saturating concentration of crotonoyl-CoA (500 μM). Kinetic parameters were obtained by fitting the initial velocity data to the Michaelis-Menten equation.

Inhibition constants were determined under conditions of saturating substrate (500 μM crotonoyl-CoA, 200 μM NADH) and variable inhibitor concentration. Values for K_i were determined from the x-intercept of a Dixon plot, assuming uncompetitive inhibition. Mean values of two independent experiments are reported for kinetic parameters and inhibition data.

IC_{50} results were determined by varying the concentration of inhibitor in standardized enzyme assays, and the IC_{50} calculated with the following formula:

$$\frac{v_i}{v_0} = \frac{1}{1 + \frac{[I]}{\text{IC}_{50}}}$$

where v_i/v_0 represents the fractional enzyme activity remaining after the addition of inhibitor, $[I]$ represents the concentration of inhibitor added, and IC_{50} is determined by curve fitting.

Crystallographic Methods

The structure of the ternary ENR:NAD⁺:triclosan complex was solved by molecular replacement with AMORE (Navaza 1994) using only protein coordinates of the *Brassica napus* ENR structure (Protein Data Bank entry 1ENO) as a search model. The initial solution was used as a template for the Automated Protein Modeling Server (available at www.expasy.ch/swissmod) to generate a three-dimensional model of the PfENR sequence. The resulting model was then used to calculate an initial electron

density map at 2.43 Å, which showed strong and continuous density for NAD⁺ and triclosan. Several rounds of model refinement included the addition of missing amino acids. In a later stage, water was automatically added and the final refinement was carried out without any noncrystallographic symmetry restraints. This yielded a final R_{work} of 17.1% and a value for R_{free} of 21.3%. The first 9 amino acids (including the His₆-tag) were not resolved, and 40 of the 43 amino acids comprising an insertion next to the binding loop area did not show any density. There were no additional breaks in the main chain, although the density was weak for residues Ile¹⁵³-Lys¹⁵⁵ and Glu¹⁷⁹-Asn¹⁸³ that form two small loop regions. The average B-value for protein atoms was 36 Å². The final model contained a total of 289 amino acids, one NAD⁺ molecule, one triclosan molecule, and 57 water molecules in each monomer. PROCHECK analysis (Laskowski *et al.* 1993) showed 90% of all residues in the most favored and 10% in the generously allowed regions of the Ramachandran diagram.

Because crystals of the binary complex with NADH were isomorphous to the ternary complex, the protein coordinates of the latter were used to calculate the initial binary complex density maps. The first map calculated at 2.40 Å clearly identified the NADH co-factor with strong and continuous density. Subsequent refinement led to an R_{work} of 17.6% and an R_{free} of 22.4%. Again, no density was observed for the first 9 amino acids and the same 40 amino acids of the binding loop insertion of each monomer, and the same areas for the loops showed weak density. The average B-value for main-chain atom positions of the binary structure was 31 Å². The final model contained a total of 289 amino acids, one NADH molecule, and 77 water molecules in each monomer.

The ternary structures with bound inhibitors B13 and B24 were solved using the method described above. Initial maps showed strong density for NADH, and additional differences in electron density at the inhibitor binding site. Good density

for B13 was only observed in monomer B, whereas B24 showed excellent density in both monomers. The inhibitors were built into the model, and subsequent refinement for B13 led to an R_{work} of 18.7% and an R_{free} of 23.2%, with a total of 289 amino acids, one NADH, and 69 solvent molecules in each monomer and one B13 molecule in subunit B. The ternary structure with bound B24 was refined to an R_{work} of 17.6% and an R_{free} of 22.7%. The model comprised 289 amino acids, one NADH molecule, one B24 molecule, and 64 solvent molecules in each monomer. Both structures lacked density for the initial 9 amino acids and the same residues of the large loop insertion. The density for the two small loops was weak. The average B-values of the main-chain atoms of the ternary PfENR:NAD⁺:B13 and PfENR:NAD⁺:B24 complexes were 33 and 34 Å², respectively. The statistics for all the structural determinations are presented in Table 20.

Crystallographic Programs

The HKL Software Suite (Otwinowski and Minor 1997) is composed of several individual programs for useful for displaying, processing, and scaling x-ray diffraction images. Chief among these applications are the programs DENZO and SCALEPACK. These programs allow for identification of unit cell parameters and crystal indexing of x-ray reflections, necessary for the accurate determination of the crystal space group . The set of parameters a, b, and c are unit cell axes measured in angstroms, while the angles between these axes are defined in degrees and are represented by the variables α , β , and γ , where α is the angle between axes b and c, β is the angle between axes a and c, and γ the angle between axes a and b. Typically, only a single diffraction pattern is necessary for estimates of these values, however, two or more images separated by larger oscillation ranges may be necessary for accurate determination of the unit cell parameters. Additionally, a variety of experimentally-derived x-ray detector

Table 20: PfENR:NADH and PfENR:inhibitor crystallographic statistics

| Data collection | PfENR:NADH | PfENR:Triclosan | PfENR:B13 | PfENR:B24 |
|-------------------------------------|----------------------------------|----------------------------------|----------------------------------|----------------------------------|
| Maximum resolution (Å) | 2.40 | 2.43 | 2.35 | 2.50 |
| Space group | P4 ₃ 2 ₁ 2 | P4 ₃ 2 ₁ 2 | P4 ₃ 2 ₁ 2 | P4 ₃ 2 ₁ 2 |
| a=b (Å) | 133.28 | 133.08 | 133.37 | 133.10 |
| c (Å) | 83.83 | 84.16 | 83.86 | 83.69 |
| $\alpha = \beta = \gamma$ (°) | 90 | 90 | 90 | 90 |
| R _{sym} (%) | 12.3 | 9.5 | 9.9 | 9.8 |
| Completeness (%) | 94.6 | 96.9 | 90.0 | 94.8 |
| Refinement statistics | | | | |
| Resolution range (Å) | 30-2.40 | 30-2.43 | 30-2.35 | 30-2.50 |
| Number of reflections | 28,422 | 28,104 | 28,883 | 25,188 |
| Number of atoms | | | | |
| Protein | 4,574 | 4,574 | 4,574 | 4,574 |
| Water | 154 | 114 | 138 | 128 |
| Ligand(s) | 88 | 122 | 120 | 128 |
| R _{cryst} (%) | 17.6 | 17.1 | 18.7 | 17.6 |
| R _{free} (%) | 22.4 | 21.3 | 23.2 | 22.7 |
| Average B-factors (Å ²) | | | | |
| Protein (subunit A/B) | 32/31 | 35/36 | 34/32 | 35/34 |
| NADH+/NADH (subunit A/B) | 32.3/23.4 | 28.0/28.6 | 56.9/26.8 | 29.7/26.0 |
| Inhibitors (subunit A/B) | | 14.9/13.7 | 77.5/56.1 | 21.3/21.6 |

parameters are necessary to properly index the crystal, the most important factors being the crystal to detector distance, the θ offset, the incident x-ray wavelength, any detector offsets, and the beam center position. The program DENZO utilizes these known parameters to enforce Bravais lattice restrictions consistent with the diffraction pattern of the crystal. Most of the Bravais lattice classes have restrictions on the α , β , and γ angles of the unit cell ($\alpha = \beta = \gamma = 90$, for orthorhombic space groups) and thus a distortion index is calculated to determine the best fit vectors must be slightly distorted to match the diffraction pattern. Thus, a distortion index value is calculated in DENZO that is given in percent values, where the lower the percentage, the better the observed data matches the calculated space group and unit cell. The calculated distortion index as a guideline to select the Bravais lattice that best agrees with the collected crystallographic data. Typically the Bravais lattice with the highest symmetry and a low distortion index is selected as the proper Bravais lattice. Once the unit cell and detector parameters are determined and refined, and all data is collected, DENZO utilizes a weighted profile-fitting algorithm dependent on factors such as spot size and background noise for determining the intensity of each measured reflection. Each frame is processed individually, and each reflection is integrated to calculate the area beneath the peak. The result is a series of files corresponding to each individual frame collected during the experiment, which are ready for the next step in structure determination: scaling of the data.

The SCALEPACK software scales the data resulting from DENZO. This program performs the data reduction, merging, and qualitative analysis of symmetry related reflections of a single data set. Each frame of integrated data contains values of the indices of the reflections along with their intensities, and SCALEPACK assembles all the reflection data into a single text file. The output from SCALEPACK typically consists of the the hkl indices of each unique reflection, the intensity (I) of the unique

reflections, the intensity of the region directly surrounding the measured reflections, and the I/σ value (signal to noise ratio) for each reflection. Statistics are used to assess the quality of the data collection, and are given as χ^2 and R_{sym} . Data from a high quality crystal should yield χ^2 values near 1.0 and R_{sym} values below 10%, and these values are useful in determining the utility of the data as well as whether continuing the process of structure determination is feasible. For example, reflections that do not give a signal-to-noise ratio above background can be used to eliminate a particular resolution shell from future structure determination calculations.

HKL2000 is a program package that provides a graphical user interface for the programs DENZO and SCALEPACK, insulating the user from editing scripts manually. It includes extended functionality such as a strategy program to optimize both data collection speed and data completeness, three-dimensional profile fitting of x-ray data, real-time monitoring of data collection quality and progress, and finally statistical analysis of freshly collected data.

The Crystallography and NMR System (Brünger *et al.*, 1998), abbreviated CNS, is a suite of programs useful for various phasing techniques, Fourier electron density map calculation and manipulation, and model refinement. The components of this suite of programs were used to for simulated-annealing and maximum-likelihood refinements for the models described in this study. Later steps generally included energy minimization, placement of ordered water molecules, and temperature-factor refinement. Several steps of refinement include R_{factor} and an R_{free} calculation for monitoring the progress of protein structure determination. The R_{factor} and R_{free} are both calculated using the following calculation.

$$R_{factor} = \frac{\sum_{hkl} ||F_{obs}| - |F_{calc}||}{\sum_{hkl} |F_{obs}|}$$

The distinction between the R_{factor} and R_{free} lies in their utilization in protein model building. R_{free} is calculated with a small segment of the x-ray data, usually 5-10%, that is excluded from protein model refinement, and serves as a measure of cross-validation to prevent over-fitting of the protein model to the experimental data. As the R_{free} is not biased by the protein model, careful monitoring of this variable prevents “over-fitting” that produces artificially low R_{factor} values.

CCP4 Collaborative Crystallographic Programs Version 5 (Collaborative Computational Project, Number 4, 1994) is a suite of programs utilized for all steps of data reduction, phase determination, electron density map manipulation, protein model building, and model refinement. It contains separate programs that can be unified into a graphical user interface with the front-end CCP4i (Potterton *et al.*, 2003). As a user interface, it simplifies repetitive and error-prone tasks such as manually editing scripts, small molecule model building, changing data formats, and various other menial tasks.

AMORE (Navaza, 1994) is one of the automated molecular replacement search programs included within the CCP4 suite of programs. AMORE performs the rotation and translation searches separately, as it is much more efficient than performing the searches simultaneously. The rotation function searches Patterson space by moving the search model to the origin of the new unit cell and iterating through rotations of the search model. During the search, correlation values are calculated between a table of the model protein structure factors and the observed amplitudes from the x-ray data. This results in a list of peaks that clearly define the most likely rotations, which are then used in translation searches. Correlation coefficients are recalculated as the newly rotated molecule is translated within the unit cell of the new crystal form, and the highest scoring combination of rotations and translations are used to generate the full oligomer of the protein of interest within the unit cell. The contents of this

unit cell are then ready for model refinement.

REFMAC (Murshudov *et al.*, 1997) is a refinement program within the CCP4 suite of programs that uses maximum likelihood refinement as its minimization algorithm. This suite of programs is analogous to CNS.

XtalView (McRee, 1999) is a suite of programs, with the component Xfit being used for visualizing electron density maps, building of protein models, structure validation, and fitting of small molecule inhibitors or substrates. XtalView can also generate high quality figures suitable for publication.

PROCHECK (Laskowski *et al.*, 1993) is a structure validation program used to verify that the protein geometry, bond angles, and lengths lie within historically accepted limits. The various analyses indicate both the degree of agreement with the experimental data and the quality of their geometrical properties.

High Throughput Screening

All 50,000 compounds from the Chemical Diversity Labs compound library were dissolved in 100% DMSO and plated at 1 μ l per well in a 96-well flat bottom plate using a BioMekFX. Test compound concentrations were 10 μ M per inhibitor. All procedures that involved transfer to the HTS platforms began with the transfer of the 96-well plate, using the SAMI NT Method creation software on a Beckman Coulter 2-meter rail system. The assay was further validated through variability testing, which included Z-analyses to incorporate the assay's signal dynamic range and the data variation associated with sample measurement. The final assay (total volume of 100 μ l) included 20 mM Tris-HCl Buffer (pH 7.6), 300 μ M NADH, 150 mM NaCl, 600 μ M crotonoyl-CoA, and 12.0 μ g/ml (340 nM) PfENR. The reagent mix, including the Tris-HCL Buffer, NaCl, NADH, and crotonoyl CoA was combined, protected from light and added to the test plate via a Titertek Multidrop 384. The

reaction was initiated with the addition of PfENR (diluted in Tris-HCl Buffer, pH 7.6) using a Multitek 96. The test plate was then immediately transferred to a Molecular Devices Spectramax Plus 384 where it was shaken for 20 seconds and read kinetically at 340 nm for 12 second intervals over 2 minutes.

ZINC Virtual Screening

The crystal structure of the ternary complex PfENR:NAD⁺:triclosan was used for virtual library screening results with the ZINC library of commercially available small molecules. All crystallographic waters were removed. Atom typing of protein residues and addition of hydrogens to them was carried out by reference to standard Biopolymer libraries keyed to residue type available in SYBYL 7.0. Terminal rotors such as methyl and hydroxyl groups were then relaxed to avoid distortion of scores by spurious steric clashes with the added hydrogen atoms. Charges were assigned to both protein and ligand atoms. Binding sites were defined for all scoring functions as including all atoms in protein residues where at least one atom was within 5 angstroms of an atom in the inhibitor, triclosan, as found in the parent crystal structure. FlexX docking runs utilized the default parameters provided in SYBYL 7.0. Afterwards, they were scored with the consensus scoring technique to give a score in five separate categories. The top hits were selected as the intersection of the top 2% of each of the five categories.

***Plasmodium berghei* Enoyl-ACP Reductase**

Cloning

Full-length *pbenr* was amplified from *Plasmodium berghei* genomic DNA with primers p433 (CC AGATCT ATT GTT AAT AGA ATT TTT ATT GAA TAT ATT C)

including a BglIII restriction site and p434 (CC GCGCGC GAA TAG AGT GAG AAA GAG AAT GAA AGG) containing a BssHII restriction site. A stretch of 10 adenosines was replaced with a sequence enhanced in GC content using the site-directed mutagenesis kit from Invitrogen. The forward primer p435 was CAG AAA AAT ATG CAC CCT TA AA_g AA_g AA_g TTA CTA TCT ACT GAT GTT GG and the reverse primer p436 was CCA ACA TCA GTA GAT AGT AA cTT cTT cTT TAA GGG TGC ATA TTT TTC TG with the silent mutations indicated with underlining.

For cloning into the pET28a expression vector, *pbenr* was PCR amplified from the product containing the silent mutations (lowercase) with the following primers p444 (CC CATATG AA_g AAT GA_g AAT GAA AAT GAA AT_c TGT TT, NdeI site underlined) and p438 (CC GGATCC TCA ATC ATC AGG CCC AAA CAT AAT ATT CAA TC, BamHI site underlined) and TA cloned into pGEM-T Easy (Promega).

Purification

BL21(DE3) cells (Novagen) harboring the expression plasmids were grown in Luria broth. When the A_{600} reached 0.8, the cells were induced with 0.75 mM isopropyl-1-thio-D-galactopyranoside for 12 hours at 16 °C. Cell pellets were resuspended in buffer A (20 mM Tris/HCl, pH 7.5, 50 mM imidazole) and disrupted using a French press. The filtered supernatant was applied to a metal chelate affinity column loaded with nickel. The column was washed with an increasing gradient of buffer B (20 mM Tris/HCl, pH 7.5, 500 mM NaCl, 500 mM imidazole). Fractions containing His₆-MBP fusion protein were pooled and treated with His₆-TEV protease (1:100 v/v) at 16 °C overnight in order to cleave off the fusion protein. The protein/protease mixture was then dialyzed in 4 L of dialysis buffer (20 mM Tris pH 7.5, 100 mM

NaCl) for 12 hours and the extent of cleavage assessed by SDS-PAGE. Subsequently the dialyzed protein/protease mixture was loaded onto an anion exchange column and washed with loading buffer (20 mM Tris/HCl pH 7.5, 100 mM NaCl). A linear gradient from 100 to 400 mM NaCl was utilized to elute the protein. The protein was then dialyzed and concentrated using Centriprep 30 and prepared for crystallization.

Crystallization and Data Collection

Using hanging drop and vapor diffusion methods, PbENR was crystallized as a binary complex with NADH bound to the enzyme and as a ternary complex with NAD⁺ and triclosan. The protein was incubated with 3 mM NAD⁺ and 1 mM triclosan for the ternary complex and with 3 mM NADH for the binary complex. Two microliters of these mixtures was mixed with 2 μ l of well solution consisting of 100 mM Tris pH 7.1, 14% PEG 2000, and 100 mM NaCl, and equilibrated against the reservoir solution at 18 °C. The crystals of both complexes were isomorphous, belonged to the space group P2₁ (cell dimensions a = 64.1 Å, b = 121.1 Å, c = 87.7 Å, $\alpha=\gamma=90$, $\beta=109$), and contained a tetramer in the asymmetric unit.

Crystallographic Methods

The structure of the ternary PbENR:NAD⁺:triclosan complex was solved by molecular replacement with AMORE using only protein coordinates of the *Plasmodium falciparum* ENR structure (Protein Data Bank entry 1NHD) as a search model. The initial solution was used as a template for the Automated Protein Modeling Server (available at www.expasy.ch/swissmod) to generate a three-dimensional model of the PbENR sequence. The resulting model was then used to calculate an initial electron density map at 2.9 Å, which showed strong and continuous density for NAD⁺. Several rounds of model refinement included the addition of missing amino acids. In a

later stage, water was automatically added and the final refinement was carried out without any noncrystallographic symmetry restraints. This yielded a final R_{work} of 19.1% and a value for R_{free} of 25.3%. The first 9 amino acids (including the His₆-tag) were not resolved, and the amino acids comprising an insertion next to the substrate binding loop area did not show any density. The average B-value for protein atoms was 36 Å². The final model contained a total of 289 amino acids, one NAD⁺ molecule, one triclosan molecule, and 57 water molecules in each monomer. PROCHECK analysis showed 90% of all residues in the most favored and 10% in the generously allowed regions of the Ramachandran diagram.

Because crystals of the binary complex with NADH were isomorphous to the ternary complex with triclosan, the protein coordinates of the latter were used to calculate the initial binary complex density maps. The first map calculated at 2.40 Å clearly identified the NADH co-factor with strong and continuous density. Subsequent refinement led to an R_{work} of 17.6% and an R_{free} of 22.4%. Again, no density was observed for the first 9 amino acids and the same amino acids of the binding loop insertion of each monomer, and the same areas for the loops showed weak density. The average B-value for main-chain atom positions of the binary structure was 31 Å². The final model contained a total of 289 amino acids, one NADH molecule, and 77 water molecules in each monomer.

The statistics for all the structural determinations are presented in Table 21.

***Mycobacterium tuberculosis* Enoyl-ACP Reductase**

Cloning

The *inha* gene of *M. tuberculosis* H37Rv was amplified by polymerase chain reaction (PCR), using primers that contained *Nco*I and *Bam*HI restriction sites at the 5' and

Table 21: PbENR:NADH and PbENR:triclosan crystallographic statistics

| Data collection | PbENR:NADH | PbENR:NAD ⁺ :Triclosan |
|-------------------------------------|-----------------|-----------------------------------|
| Maximum resolution (Å) | 2.90 | 2.50 |
| Space group | P2 ₁ | P2 ₁ |
| a (Å) | 64.11 | 64.34 |
| b (Å) | 120.93 | 121.20 |
| c (Å) | 87.69 | 87.83 |
| $\alpha = \gamma$ (°) | 90 | 90 |
| β (°) | 109 | 108.97 |
| Unique reflections | 30,051 | 44,053 |
| R _{sym} (%) | 12.3 | 9.5 |
| Completeness (%) | 94.6 | 92.9 |
| Redundancy | 3.0 | 5.8 |
| I/sigma | 9.1 | 11.5 |
| Refinement statistics | | |
| Resolution range (Å) | 30-2.90 | 30-2.50 |
| Number of reflections | 30,051 | 44,053 |
| Number of atoms | | |
| Protein | 9,072 | 9,072 |
| Water | 77 | 238 |
| Ligand(s) | 166 | 234 |
| R _{cryst} (%) | 17.6 | 19.7 |
| R _{free} (%) | 22.4 | 26.3 |
| Average B-factors (Å ²) | | |
| Protein | 31.5 | 35.3 |
| NADH+/NADH | 32.3/23.4 | 46.0 |
| Inhibitors | | 56.2 |

3' ends, respectively. The PCR product was ligated into the pET-15b expression vector that had been previously treated with *Nco*I and *Bam*HI restriction enzymes, and this plasmid was used to transform the BL21(DE3) *E. coli* strain.

Purification

The *E. coli* BL21(DE3) strain was grown in 4L of Terrific broth in a 37° Celcius shaker, to an OD₆₀₀ of 1 and induced with 1 mM isopropyl-1-thio-D-galactopyranoside for 12 hours. Cells were then harvested by centrifugation. Standard purification protocols were then performed at 4° Celcius, and fractions analyzed by SDS-PAGE. Cells were disrupted with a French press, and the supernatant obtained after centrifugation was dialyzed and applied to a 5 x 40 cm Blue-Sepharose (Pharmacia) affinity column. Proteins were eluted using a linear 0-1 M NaCl gradient, and fractions containing the InhA protein were pooled and applied to a 5 x 40 cm Phenyl-Sepharose (Pharmacia) hydrophobic interaction column. Elution proceeded with a 500 - 5 mM NaCl decreasing linear gradient, and fractions containing the InhA protein were pooled and concentrated, yielding a single 28.5 kDa band on SDS-PAGE stained with Coomassie Blue.

High Throughput Screening and Synthesis of Inhibitors

The high throughput screen measured the NADH-dependent catalysis of an octenoyl (C₈:1 Δ 2)-CoA substrate as a decrease in 340 nm absorbance resulting from conversion of NADH to NAD⁺. This screen was run using samples synthesized as mixtures of up to 100 compounds. For the mixture containing Genz-10850, indole-5-carboxylic acid was reacted with 86 different amines in equimolar and limiting concentration. This mixture showed 40% inhibition when tested at a total concentration of 40 μ M. The 86 compounds in this mixture were then individually synthesized and tested.

The most potent analogs from this mixture were amides of indole-5-carboxylic acid and 4-aryl-substituted piperazines. Subsequent synthesis of an array of piperazine analogs resulted in Genz-10850 (Table 19), which showed potent inhibition of InhA with an IC_{50} value of $0.15 \mu\text{M}$. In the case of Genz-8575 (Table 19), a mixture of 13 malondialdehydes was reacted with an excess of (4-trifluoro-methyl-pyrimidine-2-yl)-hydrazine. The resulting mixture had an inhibition of 38% against InhA at $40 \mu\text{M}$. Deconvolution of this mixture yielded several active pyrazoles, the best of which (Genz-5542, 2-[3-(4-chloro-2-nitrophenyl)-pyrazol-1-yl]-4-trifluoromethyl-pyrimidine) showed 82% inhibition at $40 \mu\text{M}$. Several analogs of this compound were prepared, among them Genz-8575, the result of replacing the chlorine atom with a nitro group. Genz-8575 displayed 91% inhibition at 40 M against InhA. Substrate and coenzyme concentrations in these screens were 250 and 100 M, respectively. IC_{50} values were determined by measuring the initial velocity over a broad range of inhibitor concentrations, plotting the fractional activity as a function of the log of the inhibitor concentration, and curve-fitting with a sigmoidal function. Inhibition constants were determined under conditions of saturating substrate ($200 \mu\text{M}$ substrate and $600 \mu\text{M}$ NADH) and variable inhibitor concentrations. K_i values were determined from the x-intercept of a Dixon plot, assuming uncompetitive inhibition. For triclosan binding of InhA, we found a K_i of $8.5 \mu\text{M}$, which differs from an earlier measurement of $0.22 \mu\text{M}$ (Parikh *et al.* (2000)). These discrepant results may in part be due to differences in the assay conditions, including the use of different chain length acyl-CoA substrates ($C_{12}:1$ CoA versus $C_8:1$ CoA).

Crystallization and Data Collection

Hanging drop methods were utilized to co-crystallize InhA inhibitor complexes. For the InhA:Genz-10850 complex, the product analog was solubilized in 100% Me_2SO

and added dropwise at room temperature to a dilute InhA solution containing NAD^+ . The final molar ratios of the mixture were 1 InhA active site to 100 NAD^+ to 1.5 Genz-10850, in 1% (v/v) Me_2SO . The mixture was concentrated to 10 mg/ml, and the crystals were produced in wells containing 12% polyethylene glycol 3350, 150 mM ammonium acetate, and 100 mM [(carbamoylmethyl)imino]diacetic acid, pH 6.8, using the vapor diffusion method. The crystals were of the space group C2 with unit cell dimensions $a = 101.01 \text{ \AA}$, $b = 83.31 \text{ \AA}$, $c = 193.07 \text{ \AA}$, $\alpha = \gamma = 90^\circ$, $\beta = 95.21^\circ$ and contained 6 molecules per asymmetric unit. X-ray diffraction data of the InhA:Genz-10850 crystal was collected using a MacScience DIP2030 image plate detector coupled to a Rigaku x-ray generator utilizing a copper rotating anode ($\text{CuK}_\alpha = 1.54 \text{ \AA}$). The detector was placed 200 mm from the crystal with no offset in the 2θ angle. Each data frame was exposed for 10 min and consisted of a 1.5° rotation of the crystal. For the InhA:triclosan complex, crystals bound to triclosan were formed in the $\text{I}2_12_12_1$ space group, unit cell $a = 94.8 \text{ \AA}$, $b = 103.9 \text{ \AA}$, $c = 189.6 \text{ \AA}$, $\alpha = \beta = \gamma = 90^\circ$, via hanging drop vapor diffusion experiments, with 100 mM Tris, pH 8.0, in the well solution. InhA was concentrated to 5 mg/ml and crystallized upon the introduction of triclosan to a solution with a 1:2:1 stoichiometric ratio of InhA, NAD^+ , and triclosan. Increasing the concentration of triclosan to yield a 1:2:2 (or higher) stoichiometric ratio resulted in microcrystals that did not diffract. Data were collected to 2.6 \AA resolution at 120° K . X-ray diffraction data of the InhA:triclosan crystal were collected at the Advanced Photon Source (Beamline 14-BM-C) at a wavelength of 1.0 \AA . The detector was placed 200 mm from the crystal. Each data frame was exposed for 30 seconds and consisted of a 1.0° rotation of the crystal. All images were autoindexed, integrated, and scaled together using the DENZO and SCALEPACK software packages .

Crystallographic Methods

Initial phases were obtained using molecular replacement, with a single subunit of InhA derived from the hexagonal crystal form of InhA (Protein Data Bank code 1ENY) as a search model. Molecular replacement solutions for the translation and rotation function were obtained from Crystallography and NMR software (CNS) . The CNS software package was utilized for molecular replacement, rigid-body refinement, simulated annealing, minimization, and B-factor refinement. The nucleotide cofactor was easily identified in a symmetry-averaged difference Fourier ($F_o - F_c$) electron density map, verifying the correctness of the molecular replacement solution. Non-crystallographic symmetry restraints were applied after rigid body refinement and initial simulated annealing. NAD^+ , triclosan, and water molecules were added during several cycles of minimization followed by B-factor refinement, resulting in an R_{factor} of 19% and an R_{free} of 28% for the InhA:Genz-10850 complex, and an R_{factor} of 22.5% and an R_{free} of 28% for the InhA:triclosan complex. Non-crystallographic restraints were removed when significant differences were observed between the individual subunits present in the asymmetric unit. Inspection of $F_o - F_c$ electron density maps calculated from an InhA:NADH model revealed significant additional density in the active sites of some of the subunits in the asymmetric unit. For the InhA Genz-10850 complex, four of the six subunits contained product analog, whereas the remaining subunits lacked bound inhibitor. For the InhA:triclosan complex, two molecules of triclosan were clearly identified and placed in one subunit of the enzyme, whereas the other subunit contained only one molecule of triclosan. The differences may be related to negative cooperativity (Dessen *et al.*, 1995), which may translate into differences in inhibitor occupancy. Data collection statistics are presented in Table 22.

Table 22: InhA:Genz-10850 and InhA:triclosan crystallographic statistics

| Data Collection | InhA:NADH:Genz-10850 | InhA:NAD ⁺ :Triclosan |
|-------------------------------------|----------------------|---|
| Maximum resolution (Å) | 2.7 | 2.6 |
| Space group | C2 | I2 ₁ 2 ₁ 2 ₁ |
| a (Å) | 101.0 | 94.8 |
| b (Å) | 83.3 | 103.9 |
| c (Å) | 193.1 | 189.6 |
| α (°) | 90 | 90 |
| β (°) | 95.2 | 90 |
| γ (°) | 90 | 90 |
| Unique reflections | 38,313 | 27,704 |
| R _{sym} (%) | 8.5 | 8.0 |
| Completeness (%) | 85.2 | 95.1 |
| Redundancy | 2.9 | 4.5 |
| I/ σ | 13.2 | 10.3 |
| Refinement statistics | | |
| Resolution range (Å) | 30-2.7 | 30-2.6 |
| No. reflections | 38,313 | 27,704 |
| No. atoms/subunit | | |
| Protein | 11,964 | 11,964 |
| NAD ⁺ | 44 | 44 |
| Ligand(s) | 30 | 17/34 |
| R _{cryst} (%) | 19.0 | 22.5 |
| R _{free} (%) | 28.8 | 28.2 |
| Average B factors (Å ²) | | |
| Protein | 31.6 | 26.5 |
| NADH/NAD ⁺ | 44.1 | 45.8 |
| Inhibitors | 47.7 | 38/52 |

REFERENCES

- Baldock C, Rafferty J, Sedelnikova S, Baker P, Stuitje A, Slabas A, Hawkes T, Rice D (1996) A mechanism of drug action revealed by structural studies of enoyl reductase. *Science* **274**: 2107–10
- Banerjee A, Dubnau E, Quemard A, Balasubramanian V, Um K, Wilson T, Collins D, de Lisle G, Jacobs W Jr (1994) inhA, a gene encoding a target for isoniazid and ethionamide in *Mycobacterium tuberculosis*. *Science* **263**: 227–30
- Bendtsen J, Nielsen H, von Heijne G, Brunak S (2004) Improved prediction of signal peptides: SignalP 3.0. *J Mol Biol* **340**: 783–95
- Bergler H, Wallner P, Ebeling A, Leitinger B, Fuchsbichler S, Aschauer H, Kollenz G, Hogenauer G, Turnowsky F (1994) Protein EnvM is the NADH-dependent enoyl-ACP reductase (FabI) of *Escherichia coli*. *J Biol Chem* **269**: 5493–6
- Bhargava H, Leonard P (1996) Triclosan: applications and safety. *Am J Infect Control* **24**: 209–18
- Black JG, Howes D, Rutherford T (1975) Percutaneous absorption and metabolism of Irgasan DP300. *Toxicology* **3**: 33–47
- Blanchard CZ, Amspacher D, Strongin R, Waldrop GL (1999) Inhibition of biotin carboxylase by a reaction intermediate analog: implications for the kinetic mechanism. *Biochem Biophys Res Commun* **266**: 466–471
- Brennan PJ (2003) Structure, function, and biogenesis of the cell wall of *Mycobacterium tuberculosis*. *Tuberculosis (Edinb)* **83**: 91–97
- Brünger AT, Adams PD, Clore GM, DeLano WL, Gros P, Grosse-Kunstleve RW, Jiang JS, Kuszewski J, Nilges M, Pannu NS, Read RJ, Rice LM, Simonson T, Warren GL (1998) Crystallography & NMR system: A new software suite for macromolecular structure determination. *Acta Crystallogr D Biol Crystallogr* **54** (Pt 5): 905–921
- Clark RD, Strizhev A, Leonard JM, Blake JF, Matthew JB (2002) Consensus scoring for ligand/protein interactions. *J Mol Graph Model* **20**: 281–295
- Claros MG, Brunak S, von Heijne G (1997) Prediction of N-terminal protein sorting signals. *Curr Opin Struct Biol* **7**: 394–8
- Cole S, Brosch R, Parkhill J, Garnier T, Churcher C, Harris D, Gordon S, Eiglmeier K, Gas S, Barry C 3rd, Tekaia F, Badcock K, Basham D, Brown D, Chillingworth T, Connor R, Davies R, Devlin K, Feltwell T, Gentles S, Hamlin N, Holroyd S,

- Hornsby T, Jagels K, Barrell B, et al (1998) Deciphering the biology of *Mycobacterium tuberculosis* from the complete genome sequence. *Nature* **393**: 537–44
- Collaborative Computational Project, Number 4 (1994) The CCP4 suite: programs for protein crystallography. *Acta Crystallogr D Biol Crystallogr* **50**: 760–763
- Crofton J, Chaulet P, Maher D, Grosset J, Harris W, Norman H, Iseman M, Watt B (1997) Guidelines for the management of drug resistant tuberculosis. *WHO/TB/96210 Rev. 1*: World Health Organization, Geneva, Switzerland
- Daffé M, Etienne G (1999) The capsule of *Mycobacterium tuberculosis* and its implications for pathogenicity. *Tuber Lung Dis* **79**: 153–169
- Deng L, Mikusová K, Robuck KG, Scherman M, Brennan PJ, McNeil MR (1995) Recognition of multiple effects of ethambutol on metabolism of mycobacterial cell envelope. *Antimicrob Agents Chemother* **39**: 694–701
- Dessen A, Quemard A, Blanchard J, Jacobs W Jr, Sacchettini J (1995) Crystal structure and function of the isoniazid target of *Mycobacterium tuberculosis*. *Science* **267**: 1638–41
- Djimdé A, Doumbo OK, Cortese JF, Kayentao K, Doumbo S, Diourté Y, Dicko A, Su XZ, Nomura T, Fidock DA, Wellems TE, Plowe CV, Coulibaly D (2001a) A molecular marker for chloroquine-resistant falciparum malaria. *N Engl J Med* **344**: 257–263
- Djimdé A, Doumbo OK, Steketee RW, Plowe CV (2001b) Application of a molecular marker for surveillance of chloroquine-resistant falciparum malaria. *Lancet* **358**: 890–891
- Egan A, Russell R (1973) Conditional mutations affecting the cell envelope of *Escherichia coli* K-12. *Genet Res* **21**: 139–52
- Eldridge MD, Murray CW, Auton TR, Paolini GV, Mee RP (1997) Empirical scoring functions: I. The development of a fast empirical scoring function to estimate the binding affinity of ligands in receptor complexes. *J Comput Aided Mol Des* **11**: 425–445
- Enserink M (2005) Infectious diseases. Source of new hope against malaria is in short supply. *Science* **307**: 33
- Espitia C, Elinos M, Hernández-Pando R, Mancilla R (1992) Phosphate starvation enhances expression of the immunodominant 38-kilodalton protein antigen of *Mycobacterium tuberculosis*: demonstration by immunogold electron microscopy. *Infect Immun* **60**: 2998–3001

- Fan F, Yan K, Wallis N, Reed S, Moore T, Rittenhouse S, DeWolf W Jr, Huang J, McDevitt D, Miller W, Seefeld M, Newlander K, Jakas D, Head M, Payne D (2002) Defining and combating the mechanisms of triclosan resistance in clinical isolates of *Staphylococcus aureus*. *Antimicrob Agents Chemother* **46**: 3343–7
- Fichera M, Bhopale M, Roos D (1995) *In vitro* assays elucidate peculiar kinetics of clindamycin action against *Toxoplasma gondii*. *Antimicrob Agents Chemother* **39**: 1530–7
- Fichera M, Roos D (1997) A plastid organelle as a drug target in apicomplexan parasites. *Nature* **390**: 407–9
- Fidock DA, Nomura T, Talley AK, Cooper RA, Dzekunov SM, Ferdig MT, Ursos LM, Sidhu AB, Naudé B, Deitsch KW, Su XZ, Wootton JC, Roepe PD, Wellems TE (2000) Mutations in the *P. falciparum* digestive vacuole transmembrane protein PfCRT and evidence for their role in chloroquine resistance. *Mol Cell* **6**: 861–871
- Foote SJ, Galatis D, Cowman AF (1990) Amino acids in the dihydrofolate reductase-thymidylate synthase gene of *Plasmodium falciparum* involved in cycloguanil resistance differ from those involved in pyrimethamine resistance. *Proc Natl Acad Sci U S A* **87**: 3014–3017
- Foth B, Ralph S, Tonkin C, Struck N, Fraunholz M, Roos D, Cowman A, McFadden G (2003) Dissecting apicoplast targeting in the malaria parasite *Plasmodium falciparum*. *Science* **299**: 705–8
- Freundlich JS, Anderson JW, Sarantakis D, Shieh HM, Yu M, Valderramos JC, Lucumi E, Kuo M, Jacobs WR, Fidock DA, Schiehser GA, Jacobus DP, Sacchettini JC (2005) Synthesis, biological activity, and X-ray crystal structural analysis of diaryl ether inhibitors of malarial enoyl acyl carrier protein reductase. Part 1: 4'-substituted triclosan derivatives. *Bioorg Med Chem Lett* **15**: 5247–5252
- Freundlich JS, Yu M, Lucumi E, Kuo M, Tsai HC, Valderramos JC, Karagyozov L, Jacobs WR, Schiehser GA, Fidock DA, Jacobus DP, Sacchettini JC (2006) Synthesis and biological activity of diaryl ether inhibitors of malarial enoyl acyl carrier protein reductase. Part 2: 2'-substituted triclosan derivatives. *Bioorg Med Chem Lett* **16**: 2163–2169
- Gardner M, Hall N, Fung E, White O, Berriman M, Hyman R, Carlton J, Pain A, Nelson K, Bowman S, Paulsen I, James K, Eisen J, Rutherford K, Salzberg S, Craig A, Kyes S, Chan M, Nene V, Shallom S, Suh B, Peterson J, Angiuoli S, Perteau M, Allen J, Selengut J, Haft D, Mather M, Vaidya A, Martin D, Fairlamb A, Fraunholz M, Roos D, Ralph S, McFadden G, Cummings L, Subramanian G, Mungall C, Venter J, Carucci D, Hoffman S, Newbold C, Davis R, Fraser C, Barrell

- B (2002) Genome sequence of the human malaria parasite *Plasmodium falciparum*. *Nature* **419**: 498–511
- Gardner MJ, Tettelin H, Carucci DJ, Cummings LM, Aravind L, Koonin EV, Shalom S, Mason T, Yu K, Fujii C, Pederson J, Shen K, Jing J, Aston C, Lai Z, Schwartz DC, Perteza M, Salzberg S, Zhou L, Sutton GG, Clayton R, White O, Smith HO, Fraser CM, Adams MD, Venter JC, Hoffman SL (1998) Chromosome 2 sequence of the human malaria parasite *Plasmodium falciparum*. *Science* **282**: 1126–32
- Gilberger TW, Schirmer RH, Walter RD, Müller S (2000) Deletion of the parasite-specific insertions and mutation of the catalytic triad in glutathione reductase from chloroquine-sensitive *Plasmodium falciparum* 3D7. *Mol Biochem Parasitol* **107**: 169–79
- Gornicki P (2003) Apicoplast fatty acid biosynthesis as a target for medical intervention in apicomplexan parasites. *Int J Parasitol* **33**: 885–96
- Harwood J (1996) Recent advances in the biosynthesis of plant fatty acids. *Biochim Biophys Acta* **1301**: 7–56
- He C, Shaw M, Pletcher C, Striepen B, Tilney L, Roos D (2001) A plastid segregation defect in the protozoan parasite *Toxoplasma gondii*. *EMBO J* **20**: 330–9
- Heath R, Rock C (1995) Enoyl-acyl carrier protein reductase (fabI) plays a determinant role in completing cycles of fatty acid elongation in *Escherichia coli*. *J Biol Chem* **270**: 26538–42
- Heath R, Su N, Murphy C, Rock C (2000a) The enoyl-[acyl-carrier-protein] reductases FabI and FabL from *Bacillus subtilis*. *J Biol Chem* **275**: 40128–33
- Heath R, Yu Y, Shapiro M, Olson E, Rock C (1998) Broad spectrum antimicrobial biocides target the FabI component of fatty acid synthesis. *J Biol Chem* **273**: 30316–20
- Heath RJ, Li J, Roland GE, Rock CO (2000b) Inhibition of the *Staphylococcus aureus* NADPH-dependent enoyl-acyl carrier protein reductase by triclosan and hexachlorophene. *J Biol Chem* **275**: 4654–9
- Heerding D, Chan G, DeWolf W, Fosberry A, Janson C, Jaworski D, McManus E, Miller W, Moore T, Payne D, Qiu X, Rittenhouse S, Slater-Radosti C, Smith W, Takata D, Vaidya K, Yuan C, Huffman W (2001) 1,4-Disubstituted imidazoles are potential antibacterial agents functioning as inhibitors of enoyl acyl carrier protein reductase (FabI). *Bioorg Med Chem Lett* **11**: 2061–5

- Heym B, Honoré N, Truffot-Pernot C, Banerjee A, Schurra C, Jacobs WR, van Embden JD, Grosset JH, Cole ST (1994) Implications of multidrug resistance for the future of short-course chemotherapy of tuberculosis: a molecular study. *Lancet* **344**: 293–298
- Hoang T, Schweizer H (1999) Characterization of *Pseudomonas aeruginosa* enoyl-acyl carrier protein reductase (FabI): a target for the antimicrobial triclosan and its role in acylated homoserine lactone synthesis. *J Bacteriol* **181**: 5489–97
- Irwin JJ, Shoichet BK (2005) ZINC—a free database of commercially available compounds for virtual screening. *J Chem Inf Model* **45**: 177–182
- Jackowski S, Murphy C, Cronan J Jr, Rock C (1989) Acetoacetyl-acyl carrier protein synthase. A target for the antibiotic thiolactomycin. *J Biol Chem* **264**: 7624–9
- Jambou R, Legrand E, Niang M, Khim N, Lim P, Volney B, Ekala MT, Bouchier C, Esterre P, Fandeur T, Mercereau-Puijalon O (2005) Resistance of *Plasmodium falciparum* field isolates to *in-vitro* artemether and point mutations of the SERCA-type PfATPase6. *Lancet* **366**: 1960–1963
- Jones G, Willett P, Glen RC (1995) Molecular recognition of receptor sites using a genetic algorithm with a description of desolvation. *J Mol Biol* **245**: 43–53
- Jones G, Willett P, Glen RC, Leach AR, Taylor R (1997) Development and validation of a genetic algorithm for flexible docking. *J Mol Biol* **267**: 727–748
- Jones R, Jampani H, Newman J, Lee A (2000) Triclosan: a review of effectiveness and safety in health care settings. *Am J Infect Control* **28**: 184–96
- Kabsch W, Sander C (1983) *Biopolymers* **22**: 2577–2637
- Kapoor M, Reddy C, Krishnasastri M, Surolia N, Surolia A (2004) Slow-tight-binding inhibition of enoyl-acyl carrier protein reductase from *Plasmodium falciparum* by triclosan. *Biochem J* **381**: 719–24
- Kater MM, Koningstein GM, Nijkamp HJ, Stuitje AR (1994) The use of a hybrid genetic system to study the functional relationship between prokaryotic and plant multi-enzyme fatty acid synthetase complexes. *Plant Mol Biol* **25**: 771–90
- Koch-Weser D, Ebert RH, Barclay WR, Lee VS (1953) Studies on the metabolic significance of acid-fastness of tubercle bacilli. *J Lab Clin Med* **42**: 828–829
- Kohler S, Delwiche C, Denny P, Tilney L, Webster P, Wilson R, Palmer J, Roos D (1997) A plastid of probable green algal origin in Apicomplexan parasites. *Science* **275**: 1485–9

- Kremer L, Douglas JD, Baulard AR, Morehouse C, Guy MR, Alland D, Dover LG, Lakey JH, Jacobs WR, Brennan PJ, Minnikin DE, Besra GS (2000) Thiolactomycin and related analogues as novel anti-mycobacterial agents targeting KasA and KasB condensing enzymes in *Mycobacterium tuberculosis*. *J Biol Chem* **275**: 16857–16864
- Kuo M, Morbidoni H, Alland D, Sneddon S, Gourlie B, Staveski M, Leonard M, Gregory J, Janjigian A, Yee C, Musser J, Kreiswirth B, Iwamoto H, Perozzo R, Jacobs W Jr, Sacchettini J, Fidock D (2003) Targeting tuberculosis and malaria through inhibition of enoyl reductase: compound activity and structural data. *J Biol Chem* **278**: 20851–9
- Laskowski RA, MacArthur MW, Moss DS, Thornton JM (1993) PROCHECK: a program to check the stereochemical quality of protein structures. *J Appl Cryst* **26**: 283–291
- Levy C, Roujeinikova A, Sedelnikova S, Baker P, Stuitje A, Slabas A, Rice D, Rafferty J (1999) Molecular basis of triclosan activity. *Nature* **398**: 383–4
- Li Q, Lee J, Castillo R, Hixon M, Pujol C, Doppalapudi V, Shepard H, Wahl G, Lobl T, Chan M (2002) NB2001, a novel antibacterial agent with broad-spectrum activity and enhanced potency against beta-lactamase-producing strains. *Antimicrob Agents Chemother* **46**: 1262–8
- Magnuson K, Jackowski S, Rock C, Cronan J Jr (1993) Regulation of fatty acid biosynthesis in *Escherichia coli*. *Microbiol Rev* **57**: 522–42
- Marcinkeviciene J, Jiang W, Kopcho L, Locke G, Luo Y, Copeland R (2001) Enoyl-ACP reductase (FabI) of *Haemophilus influenzae*: steady-state kinetic mechanism and inhibition by triclosan and hexachlorophene. *Arch Biochem Biophys* **390**: 101–8
- McFadden G, Reith M, Munholland J, Lang-Unnasch N (1996) Plastid in human parasites. *Nature* **381**: 482
- McFadden G, Waller R (1997) Plastids in parasites of humans. *Bioessays* **19**: 1033–40
- McKinney JD, Jacobs W, Bloom BR (1998) *Emerging Infections*. New York, Academic Press
- McLeod R, Muench S, Rafferty J, Kyle D, Mui E, Kirisits M, Mack D, Roberts C, Samuel B, Lyons R, Dorris M, Milhous W, Rice D (2001) Triclosan inhibits the growth of *Plasmodium falciparum* and *Toxoplasma gondii* by inhibition of apicomplexan FabI. *Int J Parasitol* **31**: 109–13

- McMurry L, McDermott P, Levy S (1999) Genetic evidence that InhA of *Mycobacterium smegmatis* is a target for triclosan. *Antimicrob Agents Chemother* **43**: 711–3
- McRee DE (1999) XtalView/Xfit—A versatile program for manipulating atomic coordinates and electron density. *J Struct Biol* **125**: 156–165
- Meng EC, Gschwend DA, Blaney JM, Kuntz ID (1993) Orientational sampling and rigid-body minimization in molecular docking. *Proteins* **17**: 266–278
- Middlebrook G (1954) Isoniazid-resistance and catalase activity of tubercle bacilli; a preliminary report. *Am Rev Tuberc* **69**: 471–472
- Miller R, Ikram S, Armelagos G, Walker R, Harer W, Shiff C, Baggett D, Carrigan M, Maret S (1994) Diagnosis of *Plasmodium falciparum* infections in mummies using the rapid manual ParaSight-F test. *Trans R Soc Trop Med Hyg* **88**: 31–2
- Miller W, Seefeld M, Newlander K, Uzinskas I, Burgess W, Heerding D, Yuan C, Head M, Payne D, Rittenhouse S, Moore T, Pearson S, Berry V, DeWolf W Jr, Keller P, Polizzi B, Qiu X, Janson C, Huffman W (2002) Discovery of aminopyridine-based inhibitors of bacterial enoyl-ACP reductase (FabI). *J Med Chem* **45**: 3246–56
- Morris S, Bai GH, Suffys P, Portillo-Gomez L, Fairchok M, Rouse D (1995) Molecular mechanisms of multiple drug resistance in clinical isolates of *Mycobacterium tuberculosis*. *J Infect Dis* **171**: 954–960
- Moss T, Howes D, Williams F (2000) Percutaneous penetration and dermal metabolism of triclosan (2,4,4'-trichloro-2'-hydroxydiphenyl ether). *Food Chem Toxicol* **38**: 361–370
- Muegge I, Martin YC (1999) A general and fast scoring function for protein-ligand interactions: a simplified potential approach. *J Med Chem* **42**: 791–804
- Murshudov GN, Vagin AA, Dodson EJ (1997) Refinement of macromolecular structures by the maximum-likelihood method. *Acta Crystallogr D Biol Crystallogr* **53**: 240–255
- Musser JM, Kapur V, Williams DL, Kreiswirth BN, van Soolingen D, van Embden JD (1996) Characterization of the catalase-peroxidase gene (katG) and inhA locus in isoniazid-resistant and -susceptible strains of *Mycobacterium tuberculosis* by automated DNA sequencing: restricted array of mutations associated with drug resistance. *J Infect Dis* **173**: 196–202
- Nakai K, Horton P (1999) PSORT: a program for detecting sorting signals in proteins and predicting their subcellular localization. *Trends Biochem Sci* **24**: 34–6

- Navaza J (1994) AMoRe: an automated package for molecular replacement. *Acta Crystallogr* **A50**: 157–163
- Nielsen H, Engelbrecht J, Brunak S, von Heijne G (1997) Identification of prokaryotic and eukaryotic signal peptides and prediction of their cleavage sites. *Protein Eng* **10**: 1–6
- Nishida I, Kawaguchi A, Yamada M (1986) Effect of thiolactomycin on the individual enzymes of the fatty acid synthase system in *Escherichia coli*. *J Biochem (Tokyo)* **99**: 1447–54
- Oaks J S C, Mitchell VS, Pearson GW, Carpenter CJ (1999) *Malaria*. National Academy Press
- Omura S, Katagiri M, Nakagawa A, Sano Y, Nomura S (1967) Studies on cerulenin. V. Structure of cerulenin. *J Antibiot (Tokyo)* **20**: 349–354
- Otwinowski Z, Minor W (1997) Processing of x-ray diffraction data collected in oscillation mode. *Methods in Enzymology: Macromolecular Crystallography, part A* **276**: 307–326
- Palmer J, Delwiche C (1996) Second-hand chloroplasts and the case of the disappearing nucleus. *Proc Natl Acad Sci U S A* **93**: 7432–5
- Parikh S, Moynihan DP, Xiao G, Tonge PJ (1999) Roles of tyrosine 158 and lysine 165 in the catalytic mechanism of InhA, the enoyl-ACP reductase from *Mycobacterium tuberculosis*. *Biochemistry* **38**: 13623–34
- Parikh S, Xiao G, Tonge P (2000) Inhibition of InhA, the enoyl reductase from *Mycobacterium tuberculosis*, by triclosan and isoniazid. *Biochemistry* **39**: 7645–50
- Payne D, Miller W, Berry V, Brosky J, Burgess W, Chen E, DeWolf Jr W Jr, Fosberry A, Greenwood R, Head M, Heerding D, Janson C, Jaworski D, Keller P, Manley P, Moore T, Newlander K, Pearson S, Polizzi B, Qiu X, Rittenhouse S, Slater-Radosti C, Salyers K, Seefeld M, Smyth M, Takata D, Uzinskas I, Vaidya K, Wallis N, Winram S, Yuan C, Huffman W (2002) Discovery of a novel and potent class of FabI-directed antibacterial agents. *Antimicrob Agents Chemother* **46**: 3118–24
- Perozzo R, Kuo M, Sidhu A, Valiyaveetil J, Bittman R, Jacobs W Jr, Fidock D, Sacchettini J (2002) Structural elucidation of the specificity of the antibacterial agent triclosan for malarial enoyl acyl carrier protein reductase. *J Biol Chem* **277**: 13106–14
- Potterton E, Briggs P, Turkenburg M, Dodson E (2003) A graphical user interface to the CCP4 program suite. *Acta Crystallogr D Biol Crystallogr* **59**: 1131–1137

- Qiu X, Janson C, Court R, Smyth M, Payne D, Abdel-Meguid S (1999) Molecular basis for triclosan activity involves a flipping loop in the active site. *Protein Sci* **8**: 2529–32
- Quemard A, Sacchettini JC, Dessen A, Vilcheze C, Bittman R, Jacobs WR Jr, Blanchard JS (1995) Enzymatic characterization of the target for isoniazid in *Mycobacterium tuberculosis*. *Biochemistry* **34**: 8235–41
- Rafferty J, Simon J, Baldock C, Artymiuk P, Baker P, Stuitje A, Slabas A, Rice D (1995) Common themes in redox chemistry emerge from the X-ray structure of oilseed rape (*Brassica napus*) enoyl acyl carrier protein reductase. *Structure* **3**: 927–38
- Ralph S, D’Ombrain M, McFadden G (2001) The apicoplast as an antimalarial drug target. *Drug Resist Updat* **4**: 145–51
- Ralph S, van Dooren G, Waller R, Crawford M, Fraunholz M, Foth B, Tonkin C, Roos D, McFadden G (2004) Tropical infectious diseases: metabolic maps and functions of the *Plasmodium falciparum* apicoplast. *Nat Rev Microbiol* **2**: 203–16
- Ramaswamy SV, Amin AG, Göksel S, Stager CE, Dou SJ, Sahly HE, Moghazeh SL, Kreiswirth BN, Musser JM (2000) Molecular genetic analysis of nucleotide polymorphisms associated with ethambutol resistance in human isolates of *Mycobacterium tuberculosis*. *Antimicrob Agents Chemother* **44**: 326–336
- Rarey M, Kramer B, Lengauer T, Klebe G (1996) A fast flexible docking method using an incremental construction algorithm. *J Mol Biol* **261**: 470–489
- Rawat R, Whitty A, Tonge P (2003) The isoniazid-NAD adduct is a slow, tight-binding inhibitor of InhA, the *Mycobacterium tuberculosis* enoyl reductase: adduct affinity and drug resistance. *Proc Natl Acad Sci U S A* **100**: 13881–6
- Raynaud C, Lanéelle MA, Senaratne RH, Draper P, Lanéelle G, Daffé M (1999) Mechanisms of pyrazinamide resistance in mycobacteria: importance of lack of uptake in addition to lack of pyrazinamidase activity. *Microbiology* **145** (Pt 6): 1359–1367
- Ristow M, Möhlig M, Rifai M, Schatz H, Feldmann K, Pfeiffer A (1995) New isoniazid/ethionamide resistance gene mutation and screening for multidrug-resistant *Mycobacterium tuberculosis* strains. *Lancet* **346**: 502–503
- Robert A, Benoit-Vical F, Claparols C, Meunier B (2005) The antimalarial drug artemisinin alkylates heme in infected mice. *Proc Natl Acad Sci U S A* **102**: 13676–13680

- Rock C, Cronan J (1996) *Escherichia coli* as a model for the regulation of dissociable (type II) fatty acid biosynthesis. *Biochim Biophys Acta* **1302**: 1–16
- Ross R (1923) *Memoirs—with a Full Account of the Great Malaria Problem and Its Solution*. London, United Kingdom, Murray
- Rossmann MG, Blow DM (1962) The detection of subunits within the crystallographic asymmetric unit. *Acta Crystallogr D Biol Crystallogr* **15**: 24–31
- Rossmann MG, Moras D, Olsen KW (1974) Chemical and biological evolution of nucleotide-binding protein. *Nature* **250**: 194–9
- Roujeinikova A, Levy C, Rowsell S, Sedelnikova S, Baker P, Minshull C, Mistry A, Colls J, Camble R, Stuitje A, Slabas A, Rafferty J, Pauptit R, Viner R, Rice D (1999a) Crystallographic analysis of triclosan bound to enoyl reductase. *J Mol Biol* **294**: 527–35
- Roujeinikova A, Sedelnikova S, de Boer G, Stuitje A, Slabas A, Rafferty J, Rice D (1999b) Inhibitor binding studies on enoyl reductase reveal conformational changes related to substrate recognition. *J Biol Chem* **274**: 30811–7
- Rozwarski D, Grant G, Barton D, Jacobs W Jr, Sacchettini J (1998) Modification of the NADH of the isoniazid target (InhA) from *Mycobacterium tuberculosis*. *Science* **279**: 98–102
- Rozwarski DA, Vilcheze C, Sugantino M, Bittman R, Sacchettini JC (1999) Crystal structure of the *Mycobacterium tuberculosis* enoyl-ACP reductase, InhA, in complex with NAD⁺ and a C16 fatty acyl substrate. *J Biol Chem* **274**: 15582–9
- Russell AD (2000) Do biocides select for antibiotic resistance? *J Pharm Pharmacol* **52**: 227–233
- Sacco J, James M (2005) Sulfonation of environmental chemicals and their metabolites in the polar bear (*Ursus maritimus*). *Drug Metab Dispos* **33**: 1341–1348
- Schroeder EK, de Souza N, Santos DS, Blanchard JS, Basso LA (2002) Drugs that inhibit mycolic acid biosynthesis in *Mycobacterium tuberculosis*. *Curr Pharm Biotechnol* **3**: 197–225
- Scior T, Morales IM, Eisele SJG, Domeyer D, Laufer S (2002) Antitubercular isoniazid and drug resistance of *Mycobacterium tuberculosis*—a review. *Arch Pharm (Weinheim)* **335**: 511–525
- Seefeld M, Miller W, Newlander K, Burgess W, Payne D, Rittenhouse S, Moore T, DeWolf W Jr, Keller P, Qiu X, Janson C, Vaidya K, Fosberry A, Smyth M, Jaworski D, Slater-Radosti C, Huffman W (2001) Inhibitors of bacterial enoyl acyl

- carrier protein reductase (FabI): 2,9-disubstituted 1,2,3,4-tetrahydropyrido[3,4-b]indoles as potential antibacterial agents. *Bioorg Med Chem Lett* **11**: 2241–4
- Sherman IW (1998) *Malaria: Parasite Biology, Pathogenesis, and Protection*. Washington, D.C., ASM Press
- Sidhu ABS, Valderramos SG, Fidock DA (2005) pfmdr1 mutations contribute to quinine resistance and enhance mefloquine and artemisinin sensitivity in *Plasmodium falciparum*. *Mol Microbiol* **57**: 913–926
- Sidhu ABS, Verdier-Pinard D, Fidock DA (2002) Chloroquine resistance in *Plasmodium falciparum* malaria parasites conferred by pfcr1 mutations. *Science* **298**: 210–213
- Sivaraman S, Zwahlen J, Bell A, Hedstrom L, Tonge P (2003) Structure-activity studies of the inhibition of FabI, the enoyl reductase from *Escherichia coli*, by triclosan: kinetic analysis of mutant FabIs. *Biochemistry* **42**: 4406–13
- Smith S (1994) The animal fatty acid synthase: one gene, one polypeptide, seven enzymes. *FASEB J* **8**: 1248–59
- Smith S, Witkowski A, Joshi A (2003) Structural and functional organization of the animal fatty acid synthase. *Prog Lipid Res* **42**: 289–317
- Snider DE Jr, Roper WL (1992) The new tuberculosis. *N Engl J Med* **326**: 703–5
- Snow R, Guerra C, Noor A, Myint H, Hay S (2005) The global distribution of clinical episodes of *Plasmodium falciparum* malaria. *Nature* **434**: 214–7
- Stewart M, Parikh S, Xiao G, Tonge P, Kisker C (1999) Structural basis and mechanism of enoyl reductase inhibition by triclosan. *J Mol Biol* **290**: 859–65
- Stoeckle MY, Guan L, Riegler N, Weitzman I, Kreiswirth B, Kornblum J, Laraque F, Riley LW (1993) Catalase-peroxidase gene sequences in isoniazid-sensitive and -resistant strains of *Mycobacterium tuberculosis* from New York City. *J Infect Dis* **168**: 1063–1065
- Surolia N, Surolia A (2001) Triclosan offers protection against blood stages of malaria by inhibiting enoyl-ACP reductase of *Plasmodium falciparum*. *Nat Med* **7**: 167–73
- Syafruddin D, Asih PBS, Casey GJ, Maguire J, Baird JK, Nagesha HS, Cowman AF, Reeder JC (2005) Molecular epidemiology of *Plasmodium falciparum* resistance to antimalarial drugs in Indonesia. *Am J Trop Med Hyg* **72**: 174–81
- Takayama K, Wang C, Besra G (2005) Pathway to synthesis and processing of mycolic acids in *Mycobacterium tuberculosis*. *Clin Microbiol Rev* **18**: 81–101

- Takayama K, Wang L, David HL (1972) Effect of isoniazid on the *in vivo* mycolic acid synthesis, cell growth, and viability of *Mycobacterium tuberculosis*. *Antimicrob Agents Chemother* **2**: 29–35
- Telenti A, Honoré N, Bernasconi C, March J, Ortega A, Heym B, Takiff HE, Cole ST (1997) Genotypic assessment of isoniazid and rifampin resistance in *Mycobacterium tuberculosis*: a blind study at reference laboratory level. *J Clin Microbiol* **35**: 719–723
- Tsay J, Rock C, Jackowski S (1992) Overproduction of beta-ketoacyl-acyl carrier protein synthase I imparts thiolactomycin resistance to *Escherichia coli* K-12. *J Bacteriol* **174**: 508–13
- van Dooren G, Su V, D’Ombrain M, McFadden G (2002) Processing of an apicoplast leader sequence in *Plasmodium falciparum* and the identification of a putative leader cleavage enzyme. *J Biol Chem* **277**: 23612–9
- Vilcheze C, Morbidoni H, Weisbrod T, Iwamoto H, Kuo M, Sacchettini J, Jacobs W Jr (2000) Inactivation of the *inhA*-encoded fatty acid synthase II (FASII) enoyl-acyl carrier protein reductase induces accumulation of the FASI end products and cell lysis of *Mycobacterium smegmatis*. *J Bacteriol* **182**: 4059–67
- Waller R, Keeling P, Donald R, Striepen B, Handman E, Lang-Unnasch N, Cowman A, Besra G, Roos D, McFadden G (1998) Nuclear-encoded proteins target to the plastid in *Toxoplasma gondii* and *Plasmodium falciparum*. *Proc Natl Acad Sci U S A* **95**: 12352–7
- Waller R, Reed M, Cowman A, McFadden G (2000) Protein trafficking to the plastid of *Plasmodium falciparum* is via the secretory pathway. *EMBO J* **19**: 1794–802
- Wang L, Falany C, James M (2004) Triclosan as a substrate and inhibitor of 3'-phosphoadenosine 5'-phosphosulfate-sulfotransferase and UDP-glucuronosyl transferase in human liver fractions. *Drug Metab Dispos* **32**: 1162–9
- Wang L, Takayama K (1972) Relationship between the uptake of isoniazid and its action on *in vivo* mycolic acid synthesis in *Mycobacterium tuberculosis*. *Antimicrob Agents Chemother* **2**: 438–441
- Ward W, Holdgate G, Rowsell S, McLean E, Pauptit R, Clayton E, Nichols W, Colls J, Minshull C, Jude D, Mistry A, Timms D, Camble R, Hales N, Britton C, Taylor I (1999) Kinetic and structural characteristics of the inhibition of enoyl (acyl carrier protein) reductase by triclosan. *Biochemistry* **38**: 12514–25
- Warrell DA, Gilles HM (2002) *Essential Malariology*. London, New York, Arnold
- Wierenga RK, De Maeyer MCH, Hol WGJ (1985) *Biochemistry* **24**: 1346–1357

- Wilson R, Denny P, Preiser P, Rangachari K, Roberts K, Roy A, Whyte A, Strath M, Moore D, Moore P, Williamson D (1996) Complete gene map of the plastid-like DNA of the malaria parasite *Plasmodium falciparum*. *J Mol Biol* **261**: 155–72
- Winder FG, Collins P, Rooney SA (1970) Effects of isoniazid on mycolic acid synthesis in *Mycobacterium tuberculosis* and on its cell envelope. *Biochem J* **117**: 27P
- Winstanley P (2002) Coping with malaria in the face of resistance. *Int J Infect Dis* **6**: 246–52
- Wongsrichanalai C, Sirichaisinthop J, Karwacki JJ, Congpuong K, Miller RS, Pang L, Thimasarn K (2001) Drug resistant malaria on the Thai-Myanmar and Thai-Cambodian borders. *Southeast Asian J Trop Med Public Health* **32**: 41–49
- Zhang Y, Cronan J Jr (1998) Transcriptional analysis of essential genes of the *Escherichia coli* fatty acid biosynthesis gene cluster by functional replacement with the analogous *Salmonella typhimurium* gene cluster. *J Bacteriol* **180**: 3295–303
- Zhang Y, Heym B, Allen B, Young D, Cole S (1992) The catalase-peroxidase gene and isoniazid resistance of *Mycobacterium tuberculosis*. *Nature* **358**: 591–593
- Zhang Y, Permar S, Sun Z (2002) Conditions that may affect the results of susceptibility testing of *Mycobacterium tuberculosis* to pyrazinamide. *J Med Microbiol* **51**: 42–49
- Zhang Y, Wade MM, Scorpio A, Zhang H, Sun Z (2003) Mode of action of pyrazinamide: disruption of *Mycobacterium tuberculosis* membrane transport and energetics by pyrazinoic acid. *J Antimicrob Chemother* **52**: 790–795
- Zuegge J, Ralph S, Schmuker M, McFadden G, Schneider G (2001) Deciphering apicoplast targeting signals—feature extraction from nuclear-encoded precursors of *Plasmodium falciparum* apicoplast proteins. *Gene* **280**: 19–26

VITA

Mack Ryan Kuo received his Bachelor of Science degree in biology from Baylor University at Waco in 1995. He received his Doctor of Philosophy degree in 2006. Mr. Kuo may be reached at Texas A&M University, Department of Biochemistry & Biophysics, College Station, TX 77843. His email address is mack@usa.net.